Global modeling of comets: Nucleus, neutral and ionized coma of comets 67P/Churyumov-Gerasimenko and 46P/Wirtanen

Preparations for the ROSETTA Radio Science Investigations

INAUGURAL–DISSERTATION
ZUR
ERLANGUNG DES DOKTORGRADES
DER MATHEMATISCH–NATURWISSENSCHAFTLICHEN FAKULTÄT
DER UNIVERSITÄT ZU KÖLN

VORGELEGT VON
JÖRG VON OERTZEN
AUS BÖBLINGEN

KÖLN 2003

Berichterstatter: Prof. Dr. F. M. Neubauer

Hochsch.-Doz. Dr. M. Pätzold

Tag der mündlichen Prüfung: 4. Dezember 2003

Contents

List of Figures

CHAPTER 1

INTRODUCTION

1.1 Kurzzusammenfassung

Das thermische Verhalten eines Kometenkernes, die Entstehung und Entwicklung der Neutralgasumgebung (der sogenannten kometaren Koma), der Plasmaumgebung des Kometen, sowie seine Interaktion mit dem Sonnenwind werden in dieser Arbeit studiert. Das Ziel ist es, ein umfassendes Modell eines Kometen und seiner Umgebung zu entwickeln. Mit diesem Modell lassen sich dann physikalische Parameter in der Kometenumgebung und deren Entwicklung in Abhängigkeit vom heliozentrischen Abstand der Kometen 46P/Wirtanen und 67P/Churyumov-Gerasimenko bestimmen. Insbesondere soll untersucht werden, welche Effekte die Kometenumgebung auf das Radiosondierungs-Experiment (RSI = Radio Science Investigations) auf der Raumsonde ROSETTA haben wird. Die Mission ROSETTA soll im Februar 2004 gestartet werden und etwa 10 Jahre später den Kometen 67P/Churyumov-Gerasimenko bei einem Abstand von ca. 4 Astronomischen Einheiten (AE) erreichen, und ihn dann auf seiner Bahn begleiten. Ursprünglich war Komet 46P/Wirtanen als Zielkomet für die Mission vorgesehen. Nachdem der Start von ROSETTA im Januar 2003 aufgrund von Problemen mit der vorgesehenen Startrakete verschoben werden musste, war der Zeitplan der Mission nicht einzuhalten und es wurde ein neuer Zielkomet ausgewählt. Komet 46P/Wirtanen dient nun noch als mögliches Ersatzziel, falls in der nächsten Startphase wieder Probleme auftauchen sollten. Die hier entwickelten Modelle beziehen sich im allgemeinen auf beide Kometen, da diese sich in vielen Dingen ähnlich sind, wie zum Beispiel Orbitparameter, Größenordnung des Kometenkerns und Zusammensetzung. Im Einzelnen werden die Unterschiede in der Diskussion der Ergebnisse ausgearbeitet.
Die Wärmediffusion im Kometenkern wird hier mit einem eindimensionalen Modell beschrieben. Um eine Aussage über die Temperaturverteilung und das Sublimationsverhalten für die gesamte Oberfläche des Kometen machen zu können, wird ein Gitter von eindimen-

sionalen Modellen über den Kometenkern verteilt. Die physikalischen Bedingungen an der Oberfläche werden durch ein Energiegleichgewicht beschrieben und gehen als Randbedingung in die Modellrechnungen ein. Viele der in den Modellen zu berücksichtigenden Parameter sind derzeit nur ungenau bekannt. Diese nicht zu vermeidende Ungenauigkeit spiegelt sich in der Variationsbreite der Ergebnisse wieder. Die Wärmediffusion im Kometenkern wird mit einer Energie-Erhaltungsgleichung beschrieben. Diese beinhaltet Wärmeleitung durch das poröse Kometenmaterial und Wärmetransport in Form von latenter Wärme durch den Fluss von Gas innerhalb des Kometenkerns. Die Anwendbarkeit der einzelnen Modellstudien lässt sich zur Zeit wohl am Besten überprüfen, indem man die Gasproduktionsrate mit beobachteten Daten vergleicht. Die Ergebnisse der Modelle beinhalten auch Karten der Oberfläche des Kometenkerns mit der Temperaturverteilung oder der Verteilung der lokalen Gasproduktionsrate an bestimmten heliozentrischen Abständen.
Das Neutralgas in der kometaren Koma wird mit den Methoden der Hydrodynamik beschrieben. Dieses Vorgehen ist gerechtfertigt, wenn das Verhalten des Neutralgases in der Koma durch Teilchenstöße dominiert ist. Dieses stoßdominierte Regime kann je nach Gasproduktionsverhalten des Kometen sehr unterschiedlich ausgedehnt sein. Bei heliozentrischen Abständen von mehr als $r_h \approx 2.5$ AE und einem Gasproduktionsverhalten, wie es für die Kometen 46P/Wirtanen und 67P/Churyumov-Gerasimenko abgeschätzt wird, wird das hydrodynamische Regime den Kometenkern möglicherweise nicht vollständig umschließen. Bei kleineren Abständen von der Sonne dehnt sich der Bereich voraussichtlich über mehrere hundert bis tausend Kilometer um den Kometen aus. Der Massenfluss des expandierenden Staub-Gas-Gemisches wird die Bahn eines Raumfahrzeuges in der Umgebung des Kometen stören. Die Beschleunigung, die ein Raumfahrzeug aufgrund des Gas-Massenflusses erfährt, wird mit den Modellergebnissen abgeschätzt. Die sich ergebende Änderung der Geschwindigkeit verursacht eine Dopplerverschiebung der Frequenz des von dem Raumfahrzeug ausgesendeten Radiosignals. Diese Dopplerverschiebung ist eine der Messgrößen des Experimentes RSI. Aufgrund der großen Rechenzeit, die einzelne Modellstudien benötigen, werden Fallstudien an bestimmten heliozentrischen Abständen diskutiert. Es ergibt sich, dass die Beschleunigung von ROSETTA durch den Gasfluss selbst bei $r_h \approx 3$ AE noch so groß sein kann, dass die mit dem RSI-Experiment geplanten Messungen der Koeffizienten des Gravitationspotentials des Kometenkernes gestört werden können.
Der ionisierte Anteil der Kometenumgebung kann auch mit dem RSI-Experiment untersucht werden. Die Änderungen und der Absolutwert des Elektroneninhaltes in der Sichtlinie zwischen ROSETTA und dem Beobachter auf der Erde sind die entsprechenden Messgrößen. Die Dichte des kometaren Plasmas wird mit einem eindimensionalen Modell abgeschätzt. Dieses Modell bezieht sich auf die Achse Komet-Sonne und entspricht in etwa der Beobachtungsrichtung in der Hauptmissionsphase der ROSETTA Mission. Die bei früheren Arbeiten bei dem Kometen 1P/Halley angewendete Annahme des photochemischen Gleichgewichts im ionisierten Teil der inneren Koma lässt sich nicht ohne Weiteres auf Kometen mit einer schwächeren Gasproduktionsrate übertragen. Das Temperaturprofil der Elektronen entlang der Achse Komet-Sonne wird in dem Zusammenhang ebenfalls mit einigen Annahmen abgeschätzt. Die sich ergebenden Plasma- und Elektronendichten lassen einen nur geringen Effekt der ionisierten Koma auf das Radioträgersignal erwarten.
Abschließend wird noch die Wechselwirkung des Kometen mit dem Sonnenwind untersucht. Dabei werden aus der Theorie der Magneto-Hydrodynamik abgeleitete Formeln eingesetzt,

die die Abstände der Bugstoßwelle, der Ionopause (bzw. Grenzfläche der magnetischen Kavität) und den Abstand des Überganges vom stoßfreien Sonnenwindregime zu der von Stößen mit dem Neutralgas dominierten Kometenumgebung bestimmen. Diese Abstände werden in Abhängigkeit vom jeweiligen heliozentrischen Abstand für 67P/Churyumov-Gerasimenko und 46P/Wirtanen berechnet. Dabei wird auch die Variation der Parameter des Sonnenwindes und des interplanetaren Magnetfeldes mit dem Abstand von der Sonne berücksichtigt. Es ergibt sich, dass nur mit geringfügigen Effekten auf das Radioträgersignal von ROSETTA zu rechnen ist. Um die Lage und das Verhalten der Plasmagrenzflächen mit dem RSI-Experiment zu untersuchen, müssen daher geeignete Strategien insbesondere mit Bezug auf die Umlaufbahn von ROSETTA um den Kometen entwickelt werden.

1.2 Abstract

Models of the thermal behaviour of a cometary nucleus, the evolution of the neutral gas coma, the ionized cometary coma and of the interaction of the cometary plasma with the solar wind are studied in this work. The general aim is to develop a global model of the comet and its environment in order to characterize the physical conditions around comets 67P/Churyumov-Gerasimenko and 46P/Wirtanen with respect to the heliocentric distance. The results also provide estimates of the effects of the cometary environment on the radio science investigations experiment (RSI) aboard the spacecraft ROSETTA. After the launch that is scheduled for February 2004, the ROSETTA mission is planned to encounter comet 67P/Churyumov-Gerasimenko and accompany it on its orbit. Comet 46P/Wirtanen has been the original target comet, but serves now as back-up target due to the postponement of the ROSETTA launch in January 2003.

The model of the heat diffusion within the cometary nucleus is one-dimensional. A grid of one-dimensional models is distributed over the nucleus in order to determine the temperature distribution and the sublimation characteristics of the comet on the whole surface of the comet. A heat balance equation is applied as boundary condition on the surface. Many parameters that have to be accounted for in a heat diffusion model are not precisely known to date. The variation of these parameters within reasonable limits yields a wide range of possible results. The heat diffusion within the cometary nucleus is derived from an energy conservation equation that includes heat conduction through the porous cometary material and heat convection due to the transport of latent heat by the gas phase within the nucleus. Model results are evaluated by a comparison of modeled and observed global gas production rates. Exemplary maps of the local temperature distribution and local sublimation rates at particular heliocentric distances are also provided.

The neutral gas coma of the comet is modeled with a hydrodynamic approximation. This method is justified within a collision dominated regime. Due to the expected weak gas production of a comet at large heliocentric distances, this hydrodynamic regime might be small and might not enclose the whole nucleus. When the comet approaches the sun and the gas production increases, the hydrodynamic regime extends to cometocentric distances of several hundred or thousand kilometer. The gas mass flux within the coma perturbs an orbiting spacecraft. The acceleration of the spacecraft due to the gas mass flux is evaluated with the model

results. The resulting change in velocity can be measured as a Doppler shift of the recorded frequency of the carrier signal. Case studies at several heliocentric distances are carried out. It turns out that even at heliocentric distances of ≈ 3 AU the drag force of the gas can become strong enough to perturb the measurements of the second order gravity coefficients, which is a primary science objective of RSI.
The ionized coma of a comet can also have an effect on the carrier signal. Changes of the electron content in the line of sight between spacecraft and observer at earth are in principle observable. A one-dimensional model of the plasma density at the comet-sun axis is developed. The assumption of photochemical equilibrium is not necessarily justified within the coma of weak outgassing comets. The continuity equation of the plasma density has to be solved without this simplifying assumption. A model of the electron temperature profile is also generated. The transition from a regime where electrons are effectively cooled to a region with temperatures of the electron fluid similar to solar wind levels is assumed to set in at the position of the thermal electron collisionopause. The plasma densities obtained from the ionospheric model indicate only minor effects on the carrier signal.
The interaction of the cometary plasma with the solar wind is also studied. The respective standoff distances of the bow shock, the cavity surface and the collisionopause of comets 67P/Churyumov-Gerasimenko and 46P/Wirtanen are determined with respect to the heliocentric distance. The variation of the solar wind parameters with heliocentric distance is accounted for. Effects of transient solar events, such as solar flares or coronal mass ejections, are discussed. It can be concluded that the plasma environment of comets 67P/Churyumov-Gerasimenko and 46P/Wirtanen and their interaction with the solar wind will have only a minor effect on the carrier signal. Special scenarios might be needed in order to locate plasma boundaries within the cometary environment with RSI.

1.3 Motivation

The general motivation of the ROSETTA mission is the study of the comet and its environment and the implications to the origin of comets, origin of the solar system and the relationship between cometary and interstellar material. The special mission scenario distinguishes ROSETTA clearly from other cometary missions. The target comet will be studied for many months while it approaches the sun on its orbit. This provides the opportunity to study the dependency of the cometary parameters on the heliocentric distance. With the planned landing on the nucleus, the cometary material can be studied in-situ for the first time. The difference to other missions that usually provide snapshot-like impressions of comets comes at the cost of a long mission duration (mainly due to the interplanetary traveltime) and a large budget.

Besides the general interest in comets and their relationship to the origin of the solar system, the cometary environment needs to be studied in order to evaluate the effects on a spacecraft and its navigation at a comet. Therefore the information on comets and their environment available to date is gathered and combined to develop a comprehensive model of comets. Many physical effects need to be simplified or parameterized in order to keep the model manageable.

The model results therefore provide general estimates of the physical conditions of the comet and its environment and estimates of the effects on the carrier signal that are to be expected for ROSETTA at 67P/Churyumov-Gerasimenko. Special attention is given to the variation of the results with respect to the variation of the heliocentric distance during the planned prime mission of ROSETTA.

1.4 Cometary missions

First in-situ observations of the cometary environment were provided by the ICE encounter at 21P/Giacobini-Zinner in September 1985. In 1986 a swarm of spacecraft flew by comet 1P/Halley with the european GIOTTO mission being the highlight. The flyby distance of GIOTTO was less than 600 km at March, 13 1986, and it provided the first images of a cometary nucleus. Two russian spacecraft (VEGA 1+2) and two spacecraft from Japan (SAKIGAKE and SUISEI) also visited 1P/Halley in March 1986. Other successful encounters with comets to date are GIOTTO at 26P/Grigg-Skjellerup in July 1992 and DEEP-SPACE-1 at 19P/Borrelly in September 2001. All encounters took place at approximately the same heliocentric distance of 1 AU. ROSETTA will be the first spacecraft to accompany a comet on its orbital path and study the cometary environment with respect to the variation of the heliocentric distance of a comet. Comet 67P/Churyumov-Gerasimenko is selected as the target comet for the ROSETTA mission.
The spacecraft CONTOUR has been scheduled to meet at least two comets, but this mission has been lost after launch. Other encounters that are currently planned are a flyby of the spacecraft STARDUST at comet 81P/Wild-2 in January 2004, and a flyby and collision of an impactor of the mission DEEP IMPACT at comet 9P/Tempel-1 in July 2005.

CHAPTER 2

THE ROSETTA MISSION

The ROSETTA mission has been selected as a planetary corner stone mission by an ESA committee in 1993. The objective is a rendezvous with a comet and a landing on its nucleus. Therefore the space probe needs to reach the same orbit around the sun as the comet. ROSETTA has originally been scheduled to launch in January 2003. Due to a failure of a previous Ariane launcher, the launch has been postponed and the optimal launch window to reach the original target comet 46P/Wirtanen could not be used. Due to this postponement, the project had to chose a new scenario to reach its mission objectives. Comet 67P/Churyumov-Gerasimenko has been selected as the new target for ROSETTA.

The main scientific objectives of the ROSETTA mission are the study of the origin of comets, the relationship between cometary and interstellar material and its implications with regard to the origin of the Solar System. The aim is the global characterization of the nucleus, the determination of dynamic properties, surface morphology and composition, and the determination of the chemical, mineralogical and isotopic compositions of volatiles and refractory elements in a cometary nucleus. The study of the development of cometary activity and the processes in the surface layer of the nucleus and the inner coma (dust/gas interaction) are further goals of the mission. The evolution of cometary activity with respect to the heliocentric distance will also be studied[1].

2.1 The ROSETTA Spacecraft

Most scientific instruments on the orbiter need to be accommodated on one side of the spacecraft, which must permanently face the comet during the operational phase of the mission.

[1] see http://sci.esa.int/rosetta for more details

The maximum launch mass is $m_{sc} \approx 2900$ kg, with a propellant portion of more than 50%. This mass limit is governed by the launch capability of the Ariane-5 launcher.

The ROSETTA design is based on a box-type central structure, $2.8m\ x\ 2.1m\ x\ 2.0m$, on which all subsystems and payload equipments are mounted. Two solar panels, each of 32 m^2, are giving a total span of about 32 m. The maximum cross section of the spacecraft therefore is $A_{sc} \approx 70m^2$, which has to be considered when estimating non-gravitational forces on the spacecraft, such as the drag force of the neutral gas sublimating from the comet surface or the solar radiation pressure.
The two solar wings extend from the 'side' faces. The instrument panel should point almost always towards the comet, while the antenna and solar arrays are directed towards earth and sun, respectively.

2.2 Radio Science Investigations

Radio Science Investigations (RSI) use the radio subsystem onboard the spacecraft for scientific studies. The analysis of frequency shifts, signal power and the polarization of the radio carrier waves are examined. The variation of these parameters allows conclusions concerning the motion of the spacecraft, perturbing forces acting on the spacecraft and the propagation medium of the carrier signal [*Pätzold et al.*, 2000]. RSI uses two radio link modes. The two-way radio link with an uplink radio signal and a simultaneous downlink at different frequencies, and the one-way mode with a dual-frequency downlink. The latter mode is only intended for occultation experiments.

2.2.1 Scientific Objectives

The primary science objectives of RSI at the comet are the determination of [*Pätzold et al.*, 2000]:

- the mass and the bulk density,
- the second order and degree gravity field coefficients,
- the gas and dust mass flux on the spacecraft,
- the abundance of mm-dm size cometary dust,
- the size, shape and internal structure of the nucleus,
- and the plasma content in the line-of-sight.

Additionally, a search for gravitational waves and the sounding of the solar corona is proposed. The mass and the density of asteroids can also be determined, when the flyby geometry is favorable.

2.2.2 Radio Subsystem

The spacecraft has three antenna systems: a fully steerable parabolic high gain antenna (HGA) with 2.2 m diameter, a fixed parabolic medium gain antenna of 0.6 m diameter and

two low gain antennas. The HGA is the main antenna for receiving and transmitting communication signals. The transponder consist each of S-band and X-band transmitter and receiver.
The carrier frequencies, the signal amplitudes and the polarization of the radio signals are monitored at the ground station.

2.3 Other Experiments

The Orbiters scientific payload includes 11 experiments and a Lander which is equipped with its own payload of scientific instruments. The scientific instruments on the orbiter include:

- an UV spectrometer (ALICE),
- a radio sounding experiment, intended for a tomography of the nucleus (CONSERT),
- a dust mass spectrometer (COSIMA),
- dust velocity and impact measurements (GIADA),
- micro-imaging dust analysis (MIDAS),
- a microwave spectrometer (MIRO),
- an imaging experiment (OSIRIS),
- a neutral gas and ion mass spectrometer (ROSINA),
- plasma measurements (RPC),
- radio science investigations (RSI),
- and a visible and infrared thermal imaging spectrometer (VIRTIS).

The ROSETTA Lander carries nine experiments and a drilling system to take samples of subsurface material. The Lander instruments are designed to study the composition and structure of the nucleus material. A detailed description and current status can be found on the webpages of the mission[1].

[1] http://sci.esa.int/rosetta

CHAPTER 3

POSSIBLE TARGET COMETS

Due to the postponement of the ROSETTA launch, comet 67P/Churyumov-Gerasimenko has been selected as the new target comet, with a rendezvous in 2014. Comet 46P/Wirtanen is intended as back-up target if problems with the next launch option should arise. The general properties currently known for both comets are summarized below.

3.1 46P/Wirtanen

Comet 46P/Wirtanen was discovered in 1948 during examination of photographic plates by C. Wirtanen of the Lick Observatory in California. With the exception of 1980 Comet 46P/Wirtanen has been observed during every close approach to the Sun since its discovery. It was particularly closely monitored during the observational campaign in 1996 and 1997, after the comet was chosen as the target for the Rosetta mission in 1995. The 1996 apparition has been used for a better determination of the orbit and the activity throughout the orbit has been studied.

The nucleus spin period of 46P/Wirtanen is estimated from the analysis of the observed lightcurve as $\sim$ 6 h. The estimate of the radius of the nucleus is 550 m (e.g. *Lamy et al.* [1998]; *Boehnhardt et al.* [2002]). The assumed bond albedo for this size estimate is 0.04.

3.2 67P/Churyumov-Gerasimenko

Comet 67P/Churyumov-Gerasimenko was discovered on a photograph by K. I. Churyumov in 1969. The plate was originally exposed for a different comet by S. I. Gerasimenko. The comet

has been observed in several apparitions since, with probably the best observing conditions during 1982.
Comet 67P/Churyumov-Gerasimenko shows an asymmetry about perihelion in observed gas production rates, with peak productivity occurring shortly after perihelion [*Osip et al.*, 1992]. The estimated radius of 67P/Churyumov-Gerasimenko is 1.98 km and the spin period of the nucleus is estimated as 12.3 h (unpublished results by P. Lamy [2003]).

3.3 Orbital Elements

The osculating orbital elements (heliocentric, ecliptic, J2000) for both comets given in Table 3.1 are taken from the JPL DASTCOM Database Browser[1].

	46P/Wirtanen	**67P/C-G**
Orbital period [years]	5.44	6.57
Perihelion distance [AU]	1.06	1.29
Aphelion distance [AU]	5.13	5.72
Orbital eccentricity [deg]	0.658	0.632
Orbital inclination [deg]	11.72	7.12
Semi-major axis *a* [AU]	3.094	3.507
Longitude of the Ascending Node Ω [deg]	82.17	50.95
Year of discovery	1948	1969

Table 3.1: *Orbital elements for comets 46P/Wirtanen and 67P/Churyumov-Gerasimenko*

3.4 Timeline and Geometric Considerations

The mission scenarios at comets 46P/Wirtanen and 67P/Churyumov-Gerasimenko have differences mainly in time of the prime mission and in observational geometry. At comet 67P/Churyumov-Gerasimenko the prime mission is planned for the perihelion passage of the comet in the year 2015. With the orbital elements listed in Table 3.1 the corresponding distances between comet, sun and earth can be derived. In Figure 3.1 the resulting distances for the scenario at 67P/Churyumov-Gerasimenko are plotted. The solid line represents the distance between the comet and the sun. The perihelion passage is expected to occur in October 2015. The rendezvous of ROSETTA with the comet is planned for November 2014. At this time the comet will be approximately at 3.5 AU distance from the sun. The closest distance between the line of sight (or the ray path between earth and comet/spacecraft) and the sun, indicated by the dotted line, decreases significantly during a solar conjunction. If the distance becomes less than ≈ 40 solar radii (or ≈ 0.2 AU), the solar corona can be sounded by the radio signal. This is a secondary science objective of the RSI experiment [*Pätzold et al.*, 2000]. At the same time, the solar corona can perturb radio science measurements at the

[1] http://ssd.jpl.nasa.gov/dastcom.html

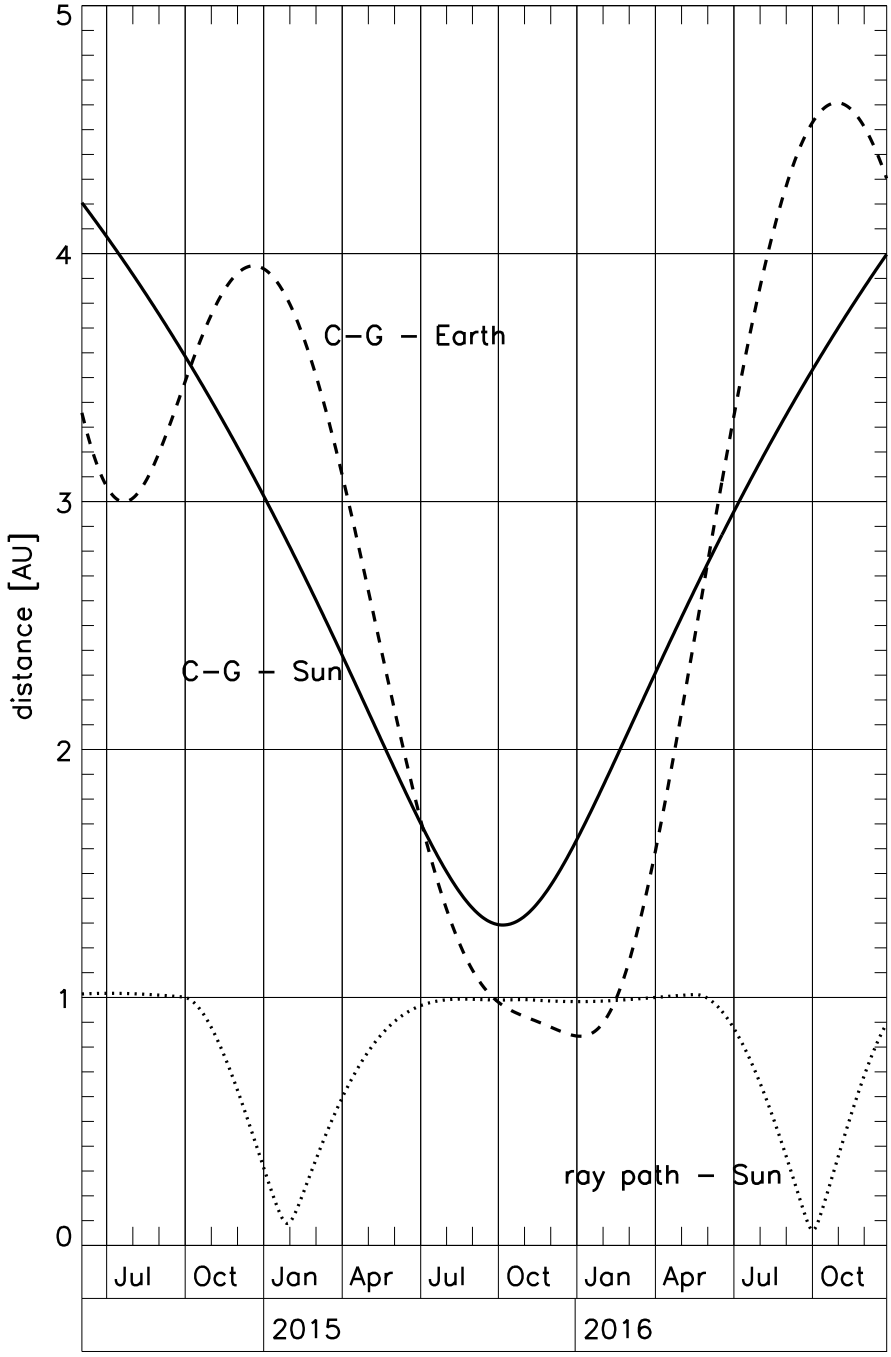

Figure 3.1: *Distances between comet 67P/Churyumov-Gerasimenko and sun (solid line), 67P/Churyumov-Gerasimenko and earth (dashed line), and closest distance between the line of sight and the sun (dotted line) at the time of the proposed prime mission.*

comet during a solar conjunction. A corresponding situation is expected in January/February 2015 and again in September/October 2016 for the 67P/Churyumov-Gerasimenko scenario (see Figure 3.1).

The scenario at 46P/Wirtanen is plotted in Figure 3.2. A solar conjunction does occur in this scenario in December 2011/January 2012, and from February to April 2013. The perihelion

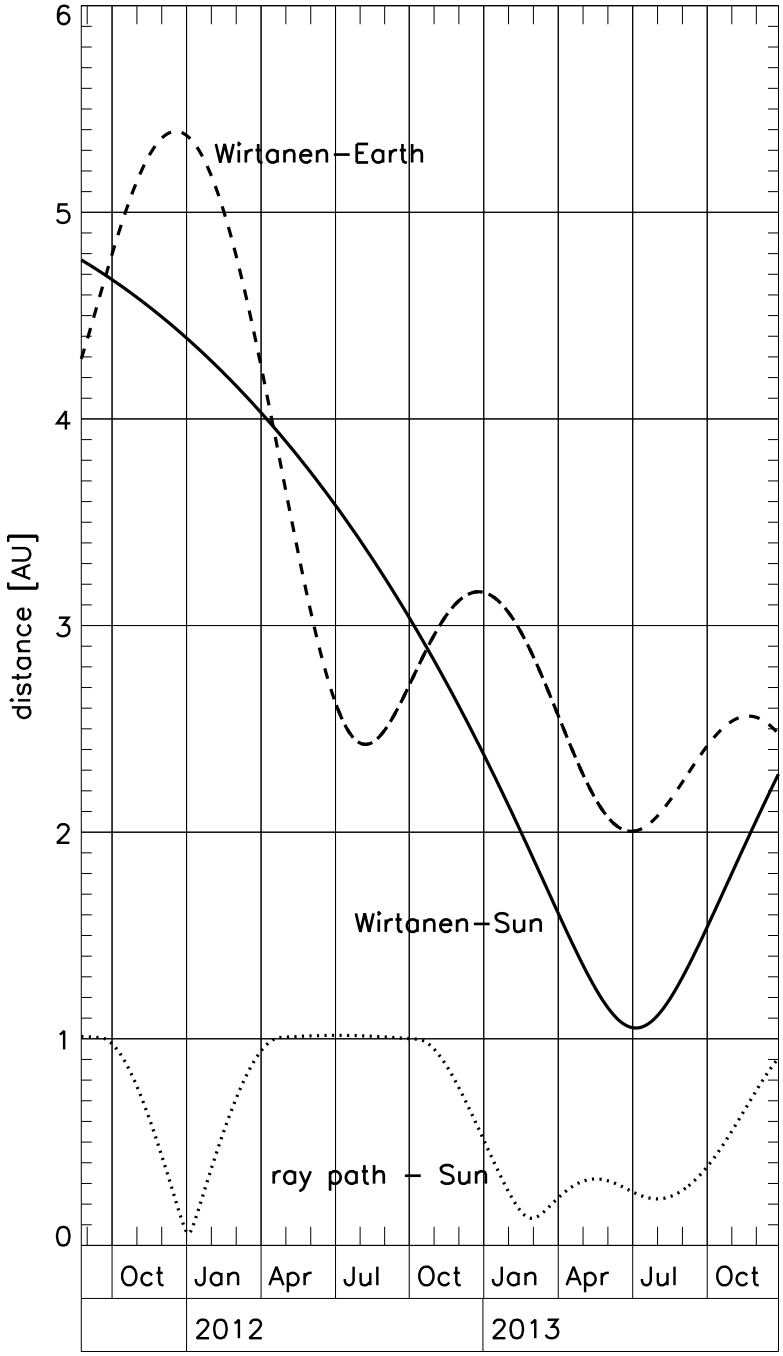

Figure 3.2: *Distances between comet 46P/Wirtanen , sun and earth at the time of the proposed prime mission. Line styles are chosen similar as in Figure 3.1.*

passage of 46P/Wirtanen is expected in July 2013. The geocentric distance of 46P/Wirtanen during the intended prime mission is always larger than 2 AU, indicating poorer conditions for earth-bound observations of comet 46P/Wirtanen (when compared with the intended scenario at comet 67P/Churyumov-Gerasimenko). See also Appendix E for more details of the observational geometry.

CHAPTER 4

THERMAL MODEL OF A COMETARY NUCLEUS

In the following sections information on cometary nuclei and the theory for a thermal one-dimensional model of a cometary nucleus with emphasis on the surface boundary is presented. The developed theory is applied to model comets in the orbit of 46P/Wirtanen and 67P/Churyumov-Gerasimenko and present the results.

4.1 Introduction

The interpretation of the few existing comet images leads to the following general assumptions: A comet nucleus is of irregular shape, the surface is very dark with a mean bond albedo of $0.01 - 0.04$. The surface varies in topography, roughness, structure and albedo. There are only very few craters visible (compared to images of asteroids) [*Keller et al.*, 1988; *Soderblom et al.*, 2002], indicating a young and active surface. The low bulk density of the nucleus (estimates range from ≈ 100 kg/m^{-3} to ≈ 1500 kg/m^{-3}) indicates a high porosity of the cometary material (see e.g. [*Sagdeev et al.*, 1988] or *Hughes* [1996]). The dark appearance of the surface may be caused by organic and silicate components, as *Thompson et al.* [1987] propose. They also mention that surface roughness and porosity of the matrix of the near-surface material are important for the understanding of the low albedo. The porosity also has an effect on the heat diffusion within the nucleus since the convective transport of heat is attenuated when the material is not compact. In fact, the transport of energy by gas diffusion may be an equally important process and enhance the transport of heat by convection within the porous material [*Kehse*, 1994].

The initial parameters for the one-dimensional thermal model of the cometary nucleus are summarized and applied to a grid of models distributed over the surface of the model comet. Boundary conditions variable in space and time are therefore accounted for. The results

provide maps of local surface temperatures, local gas production rates and, when integrating over the surface, the total gas production rate. Estimates of the total gas production rates for various heliocentric distances exist from observations, which allows calibration of parameters and confirmation of model results.

The main task of the model is to provide estimates of the total gas production rates and initial conditions for a hydrodynamic simulation of the inner coma of the considered comet. Special care is therefore taken for the surface boundary of the nucleus and the interior is modeled as simply as possible.

4.2 The Cometary Nucleus

The expected general features of cometary nuclei are discussed in this section. The structure, composition, and detailed model assumptions are presented. The ranges for important model parameters are given. A short overview of existing models of the heat diffusion within cometary nuclei is given.

4.2.1 Observations of Cometary Nuclei

The observation of comets with telescopes has some limitations. Only the dust and gas envelope can currently be observed with earth-bound telescopes. At large heliocentric distances, where the dust envelope may disappear, the resolution of the telescopes is too low to observe the nucleus in detail. So only in-situ observations provide direct information of a cometary nucleus.

Only two cometary nuclei are known from imaging experiments. GIOTTO took images with the best resolution of the nucleus of 1P/Halley from a distance of approximately 600 km in 1986 [*Keller et al.*, 1986]. These images were the first direct observations of a cometary nucleus. Shape, morphology and photometric characteristics could be studied for the first time. Most comet models today are based on these observations. Recently, on September 22, 2001, has another comet been imaged: the probe DEEP SPACE 1 flew by 19P/Borrelly within 2170 km distance [*Soderblom et al.*, 2002].
Other encounters with comets did not provide images of cometary nuclei. ICE at comet 21P/Giacobini-Zinner did not have a camera and when GIOTTO reached comet 26P/Grigg-Skjellerup in 1992, the camera experiment had already been destroyed from dust grain impacts during the encounter with 1P/Halley.

4.2.2 Structure

The detailed structure of cometary nuclei is not yet known. There are several models of the structure of the interior of a comet (see also Figure 4.1): from the so called icy conglomerate or *dirty snow ball* [*Whipple*, 1950], or the *primordial rubble pile* [*Weissman*, 1986], to the *icy-glue* model by *Gombosi and Houpis* [1986] and the *fluffy aggregate* model by *Donn* [1991].

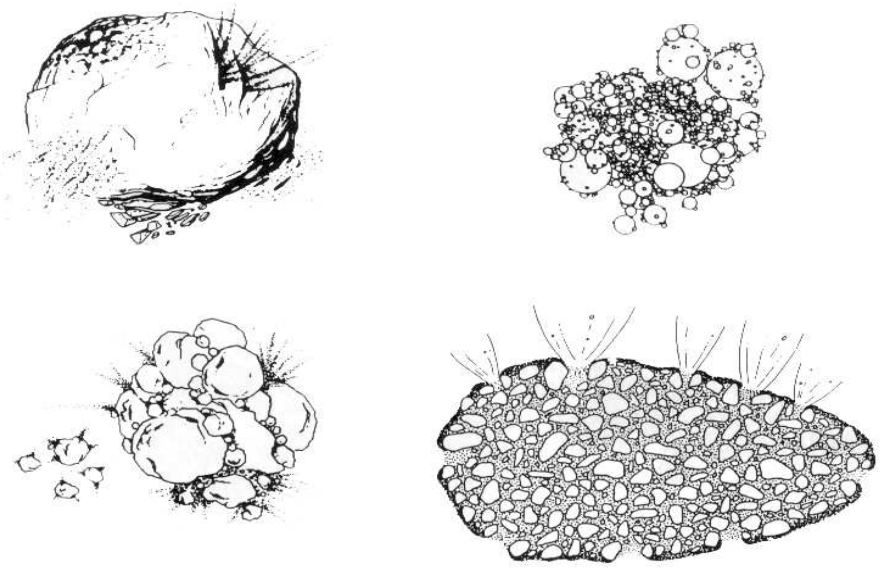

Figure 4.1: *Various models of cometary nuclei: (top left) dirty snowball [Whipple, 1950], (top right) fluffy aggregate [Donn, 1991], (bottom left) primordial rubble pile [Weissman, 1986], (bottom right) icy-glue model [Gombosi and Houpis, 1986] (image reproduced from Donn [1991]).*

So far no model can be excluded by observations because only remote observations exist. Images from GIOTTO seem to favor the icy-conglomerate model. The ROSETTA mission (especially the Lander) should be helpful to distinguish between these models.
A homogeneous structure of a porous matrix in the inner part of the nucleus is assumed in the model developed here, with possible stratification close to the surface due to the depletion of volatile species by sublimation in this region.

4.2.3 Composition

The composition of cometary surface material has never been measured directly. Therefore only indirect methods can be used to determine the composition of a comet nucleus. Spectral analysis and satellite measurements of the dust, gas and plasma environment provide the best clues to the basic cometary material to date. Dust is dragged by the gas from the surface and reflects the sunlight, therefore absorption lines in the reflected light can be studied to determine the dust composition. Gas can be released directly from the surface by sublimation, by diffusion of sublimated gas through porous material from within the nucleus, or from grains of dust that are in the coma and still contain volatile species (e.g. *Huebner and Benkhoff* [1999]). Photochemistry is assumed to have strong influence on the neutral gas. The original species dissociate and become ionized. Mainly daughter products of the original molecules can therefore be observed. They absorb and re-emit photons and can therefore be studied in emission lines. Since the 1970s cometary comae have been studied with UV spectroscopy from space. This way the major volatile constituents of many comets have been observed.

Although the observed comets have differences with respect to gas production rate, gas/dust ratio, heliocentric distance and observation geometry. Their ultraviolet spectra appear approximately similar. This indicates a common chemical composition. See e.g. *Huebner and Benkhoff* [1999] for more details.

The compositions of the gas and the plasma environment at 1P/Halley have been measured directly by a neutral mass spectrometer (NMS) on board the GIOTTO spacecraft. Results show that water vapor and daughter products dominate the inner coma of the comet [*Krankowsky et al.*, 1986].
Besides water typical elements are: Carbon Monoxide (the second most abundant gas in the coma of 1P/Halley), Carbon Dioxyde, Methanol(CH_3OH), Methane (CH_4), Ammonia (NH_3), molecular Nitrogen (N_2), Formaldehyde (H_2CO), Hydrogen Cyanide (HCN) and Methyl Cyanide (CH_3CN). Other possible components are e.g. H_2S, C_2H_2 [*Krankowsky*, 1991; *Rickman*, 1991].

A possible chemical differentiation in the surface layers would enable any comet to appear to have an H_2O dominated ice component due to the depletion of more volatile elements by sublimation. This appearance therefore does not reflect the initial composition which may be found in deeper layers under the surface (e.g. *Houpis et al.* [1985]). A process that mitigates the chemical differentiation is the loss of surface material during the orbit. *Capria et al.* [1996] estimate a loss of material at the surface of a 46P/Wirtanen model comet that reduces the radius by up to 10 m during one orbit. It may therefore be possible that a significant amount of ice components more volatile than water appear at or close to the surface.

A body composed of one dust component (for simplicity), H_2O as the major ice component and possible minor components of higher volatility (e.g. CO, CO_2) below the surface is assumed in the model developed here. Thermal conductivity varies with depth. Gas flux of highly volatile species from sublimation fronts below the surface layer of the nucleus into the coma is not explicitly modeled.

The release of heat due to H_2O ice crystallization will be neglected in the calculations. It is assumed that the main part of the ice close to the surface has already changed from the initially amorphous state to a crystalline structure, which is consistent with an estimation made for comet 67P/Churyumov-Gerasimenko by *Espinasse et al.* [1991]. This should be a reasonable assumption for most short period comets.

The dust/ice mass ratio R_{di} is an initially free parameter in the model. The estimated order of magnitude of the dust/gas ratio by the GIOTTO-DIDSY experiment at 1P/Halley was close to unity [*McDonnell et al.*, 1987]. This experiment was not sensitive to the higher mass range in which a large amount of the cometary dust is expected to be emitted, as *Hughes* [1996] points out. From the cosmic abundance of elements a dust/ice mass ratio of $R_{di} = 1/2.2$ is expected [*Hughes*, 1996]. Other theoretical estimates of the dust/gas ratio at comets give the same order of magnitude (e.g. *Greenberg* [1982]; *Delsemme* [1982; 1991]). Since the surface layer of comets may be depleted of volatiles, the dust to ice mass ratio can locally be significantly larger and a dust mantle might exist.

4.2.4 Albedo

The surface of comets appears to be very dark in the visible range. The mean bond albedo a at 1P/Halley was estimated to be $a = 0.02 - 0.04$ [*Keller et al.*, 1986] and even lower at 19P/Borrelly ($a = 0.01 - 0.03$ [*Soderblom et al.*, 2002]).

The dark appearance of the surface may be due to organic and silicate components, as *Thompson et al.* [1987] propose. They also mention that surface roughness and the porosity of the matrix of the material are important for understanding the low albedo. The low albedo of cometary grains has also been deduced by e.g. *McDonnell et al.* [1991].

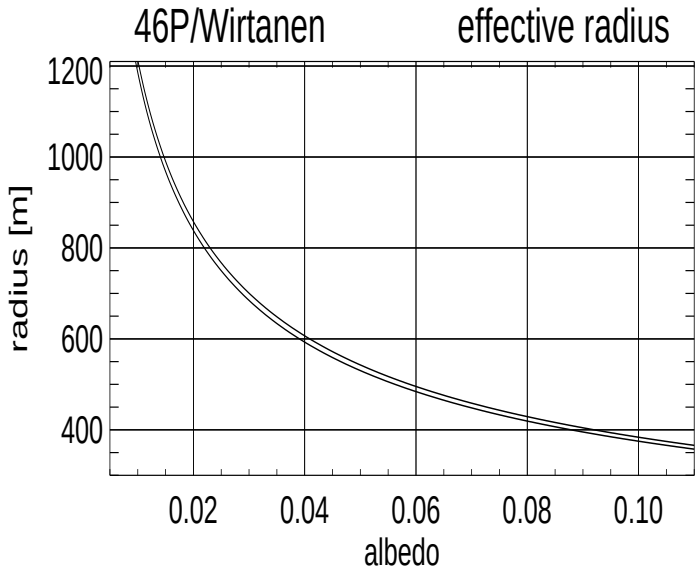

Figure 4.2: *Effective radius of 46P/Wirtanen versus assumed values of the comets mean bond albedo*

A value of $a = 0.03 - 0.04$ for the mean bond albedo is applied in the calculations. The uncertainty in the mean bond albedo is of particular interest when determining the size of a cometary nucleus from images taken by telescopes in the visible range. Following *Keller* [1990], the effective radius of a comet R_c is derived from the normalized (to a heliocentric and geocentric distance of $1AU$) measured magnitude of the nucleus m_c as:

$$\log R_c \;=\; 2.14 - 0.2 m_c - 0.5 \log a \quad . \tag{4.1}$$

In Figure 4.2 the variation of the effective radius of comet 46P/Wirtanen with assumed values for the mean bond albedo are plotted, as derived from Equation (4.1). The radius is assumed to be $R_c = 600$m for $a = 0.04$, which is consistent with the results from observations (see *Lamy et al.* [1998]; *Boehnhardt et al.* [2002]). This indicates the uncertainty of the derived radius of the nucleus R_c, since in the case of 46P/Wirtanen a value of $a = 0.02$ instead of $a = 0.04$ would change the derived radius R_c by ≈ 30 %. A similar uncertainty exists for comet 67P/Churyumov-Gerasimenko . The radius of the model comet has therefore to be varied when varying the mean bond albedo.

4.2.5 Thermal Skin Depth

The application of a one-dimensional model is justified only when volume effects in the interior can be neglected. It turns out that the skin depth of thermal signals is expected to be so low that the simplification is acceptable, as shown below.

When constant thermal conductivity k, density ρ and heat capacity c are assumed for the cometary material, Equation (4.9) can be written as $\frac{\partial T}{\partial t} = \kappa \Delta T$, with the thermal diffusivity $\kappa = k/\rho c$. The thermal diffusivity therefore controls the heat diffusion within the considered medium. The thermal skin depth δ_{th} of the heat wave generated during a full orbit of a comet can then be estimated as [*McKay et al.*, 1986]:

$$\delta_{th} \approx \sqrt{\frac{\kappa \Pi}{\pi}} \quad , \tag{4.2}$$

with the duration of the heat pulse Π. The thermal skin depth is the depth at which the amplitude of a sinusoidal temperature variation with a period Π equal to the orbit period is reduced by the factor $1/e$.

For a general estimate of δ_{th} one can apply the orbit periods of comets 46P/Wirtanen $\Pi_W = 5.43a$ and 67P/Churyumov-Gerasimenko $\Pi_{CG} = 6.57a$. With a mean density of the nucleus $\rho = 600$ kg/m^3, a value for the thermal conductivity of the order $h \cdot k \approx 0.1$ W/(m K) (see Section 4.3.3) and $c \approx 1350$ J/(kg K) (see Section 4.4), and get for both comets $\kappa \approx 1.2 \times 10^{-7}$ m^2/s.

The skin depth of the heat wave then is $\delta_{th} \approx 2.6$ m for 46P/Wirtanen and $\delta_{th} \approx 2.8$ m for 67P/Churyumov-Gerasimenko . The temperature in the interior of such a homogeneous structured comet approximately 10 m below the surface should therefore be uniform and depend only on the average thermal conditions. The time scale τ_T for a temperature signal to reach a certain depth d can be estimated as $\tau_T = d^2/\kappa$. An average temperature in a depth of 50 m is with the above approximation of thermal diffusivity established after ~ 680 years. Since it is not known if a particular comet has a stable orbit over that period of time, the knowledge of the temperature profile in the comet nucleus would in principle provide clues to possible previous major changes in orbit parameters.
A constant mean temperature below a depth of 50 m is assumed in the model comet. The lower boundary of the nucleus model can therefore be placed at a depth of 50 m.

This estimate neglects surface erosion which would tend to reduce the thickness of the shell of variable temperatures. It also neglects possible heat transport by vapor flow into the interior which would increase the layer of temperature variability and accelerate the heat transport into the interior. Changes in the chosen parameters with depth due to possible changes in composition or compactness of the body (a dust mantle or more volatile ice species in deeper layers) are also neglected.

The uncertainty of the deviation of the thermal skin depth due to the choice of parameters is very large. The variation of e.g. the Hertz factor h, which has an estimated range of several orders of magnitude (see Section 4.4), is therefore able to change the estimate of the thermal skin depth by a factor of the square root of its magnitude range.

It can be concluded that a skin depth of the order $\delta_{th} \approx 1 - 10$ m is a reasonable first order approximation. For a heat diffusion model of the comet it is implied that volume effects due to the assumed spherical shape can be neglected for the timescales considered in this work. A one-dimensional model is a good first order approximation to derive heat diffusion within the nucleus.

With the above estimate, the thermal skin depth of the diurnal temperature variation is of the order of 0.01 m, if the rotation period of the nucleus is of the order of 10 h. This corresponds to the current estimate for comets 46P/Wirtanen and 67P/Churyumov-Gerasimenko (see Section 4.4). The derived values of the thermal skin depth are in agreement with computations by e.g. *Rodionov et al.* [2002]

4.2.6 Heat and Gas Diffusion Models

As described in the previous sections, cometary nuclei are assumed to be composed of various ices and dust. Silicate and organic materials are expected in the dust. The ice consists initially of mainly H_2O and one can include several minor components of higher volatility, like e.g. CO, or CO_2. The heat from solar irradiation is either reflected, re-radiated, used to evaporate ices, or penetrates into the nucleus where it can also evaporate ices. In general, the heat transport mechanism into the nucleus is either solid-state heat conduction of the porous ice-dust matrix, vapor flow through the pores of the matrix including re-deposition, or thermal radiation [*Benkhoff*, 1999*a*; *Orosei et al.*, 1999]. Heat transport by vapor flow is only effective at high temperatures - for water vapor the effect is only minor below $T \approx 180$ K [*Kehse*, 1994] and becomes dominant at temperatures above $T \approx 210$ K [*Tancredi et al.*, 1994]. The gas flux usually is described in the Knudsen regime, which is a first approximation that seems reasonable in comparison to the uncertainties of other parameters of the models, like dust to ice ratio, porosity or heat conductivity of the porous matrix [*Benkhoff and Boice*, 1996; *Benkhoff*, 1999*a*]. Detailed studies of the near surface layer of a cometary nucleus were carried out by e.g. *Markiewicz et al.* [1998]; *Skorov and Rickman* [1995; 1999]; *Skorov et al.* [1999]; *Gutiérrez et al.* [2001; 2003].

The vapor from the sublimation of the ices diffuses through the pores of the nucleus and can be re-deposited in lower temperature areas, like the deep interior of the nucleus, or escape into the coma. A chemical differentiation might occur due to the different volatility of the ice components [*Espinasse et al.*, 1991; 1993].

The thermal evolution of a comet nucleus has been modeled by many authors with comparable assumptions. The earliest concept of the comet nucleus suggested a compact ice-dust mixture, as *Whipple* [1950] proposed. Therefore the first models only considered heat conduction as an energy transport mechanism, e.g. *Smoluchowski* [1981]; *Weissman and Kieffer* [1981]; *Klinger* [1983]; *Podolak and Herman* [1985]; *Herman and Weissman* [1987]. The additional energy transport due to gas diffusion within the nucleus was first implemented in models by *Smoluchowski* [1982] and *Squyres et al.* [1985]. Most models were used to study the surface temperatures and resulting sublimation rates. The sublimation rate (or gas production rate) has been derived by spacecraft measurements and has been estimated from ground based observations, so these model results can be verified [*Benkhoff*, 1999*b*]. The more recent model calculations, like e.g. *Benkhoff and Huebner* [1996]; *Benkhoff* [1999*b*]; *Orosei et al.* [1999], also include a variation of mixing ratios and an evolution of the surface (build-up of a dust mantle or surface erosion).
Laboratory experiments also simulated cometary material in an interplanetary environment and helped to assess the importance of processes involved, like the so called *KOSI*-experiments

[*Grün et al.*, 1991], or experiments by other groups like *Bar-Nun et al.* [1985]; *Bar-Nun and Laufer* [2003]. Thermal results from the KOSI-experiments have been modeled e.g. by *Spohn and Benkhoff* [1990]. Based on these models *Kehse* [1994] studied latitude dependent irradiation by adding a second dimension, but only porous water ice bodies were studied in that work.

Huebner et al. [1999] compared various published state-of-the-art models and their results and concluded that there is no general agreement on the parameterization of processes: *"We must conclude that at present nucleus models have only limited credibility"* (*Huebner et al.* [1999], p.1297). Included in this work of the so called *Comet Nucleus Model Team* were models by *Benkhoff and Boice* [1996]; *Coradini et al.* [1997]; *Enzian et al.* [1997]; *Kührt and Keller* [1994]; *Orosei et al.* [1999]; *Prialnik* [1992] and *Tancredi et al.* [1994]. Only the very simple model of a pure porous water ice body leads to an agreement in the resulting surface temperatures and gas release rates. When more volatile ice components and dust are added, the results differ by as much as $3-4$ orders of magnitude for local sublimation rates (only one point at the surface was compared) [*Huebner et al.*, 1999]. In order to understand these huge differences further investigations have been announced, with the intention to publish a reference model in the future. These further investigations include the application of the following processes [*Huebner et al.*, 1999]: the power balance, temperature profiles in the interior of the nucleus, determination of the effective thermal conductivity, energy flow profiles in the nucleus, gas flux profiles in the nucleus, porosity profiles in the nucleus, and density profiles in the nucleus. Not included in their work are effects of irregular shape or topography effects, which was studied in more detail by e.g. *Gutiérrez et al.* [2001].

This highlights the uncertainties when modeling a comet nucleus and indicates the need for detailed measurements on a real comet nucleus. With this in mind, the estimates from the previous sections are used to develop a thermal model that yields gas production rates which match observed gas production rates of comets 67P/Churyumov-Gerasimenko and 46P/Wirtanen .

4.3 Thermal Model of a Cometary Nucleus

The model of the nucleus is assumed for simplicity to be spherical. A grid of one-dimensional models of the heat and gas distribution, with grid points every 5° in latitude and longitude is used to cover the whole surface. The initial free parameters are the mean density of the nucleus ρ_n, the dust to ice mass ratio R_{di}, the radius of the pores r_{po} and the Hertz parameter h. The general behavior of the comet nucleus can also be chosen in terms of orbital elements, spin period, obliquity of the spin axis and radius of the comet. Some processes are parameterized in the model, such as the evolution of the surface (dust mantle), the gas flux within the nucleus, the attenuation of the solar radiation by the coma, or the energy input from gas particles from the coma that are deposited at the surface. The physical context is described in the following sections.

4.3.1 Energy and Mass Conservation in a Porous Medium

The model nucleus is assumed to be a porous mixture of dust and ice. The pores contain vapor of the sublimated ice components. The dust to ice ratio of the solid matrix is defined as

$$R_{di} = \frac{\rho_d}{\sum_i \rho_i} \ , \tag{4.3}$$

with the specific densities of the dust component ρ_d and the ice components ρ_i. The total bulk density of the matrix ρ_t can then be written as $\rho_t = \rho_d + \rho_i$. It is assumed that $\rho_n = \rho_t$, neglecting at this point the specific density of the gas component within the nucleus $\tilde{\rho}_g = \Psi\rho_g$, where Ψ is the porosity of the material. The ice component can be split into different specific ice densities, i.e. $\rho_i = \rho_{H_2O} + \rho_{CO} + \rho_{CO_2} + ...$ The specific densities are derived from the dust to ice ratio as:

$$\rho_i = \frac{\rho_n}{R_{di}+1} \tag{4.4a}$$

$$\rho_d = \rho_n - \rho_i \ . \tag{4.4b}$$

The porosity Ψ is the fraction of a unit volume that contains pores. The solid material then fills the fraction $1-\Psi$ of a unit volume. In this work, the porosity of the material is found by relating the specific densities ρ_d, ρ_i to the corresponding densities of compact material $\rho_{d,c}, \rho_{i,c}$ (e.g. *Tancredi et al.* [1994]):

$$\Psi \ = \ 1 - \frac{\rho_d}{\rho_{d,c}} - \frac{\rho_i}{\rho_{i,c}} \ . \tag{4.5}$$

The local icy area fraction of the surface of the material is derived as (e.g.*Crifo* [1997]):

$$A_0 = \frac{1}{1 \ + \ R_{di} \ \ (\rho_{i,c}/\rho_{d,c})} \ . \tag{4.6}$$

Using the densities of the compact material implies that the porosity can be neglected when determining the illuminated icy fraction at the surface layer. The consequence of applying the densities of the compact materials is that with a dust-to-ice mass ratio of $R_{di} = 1$ the icy area fraction of the surface is larger than 0.5 due to the smaller mass per volume of the compact ice component.
In order to vary the amount of dust at the surface without explicitly tracking the mass balance, a dusty layer at the surface is parameterized by assuming that the value of A_0 at the surface varies with heliocentric distance.

The conservation of mass leads to the continuity equation for the density ρ, if only gas is assumed to escape from the matrix:

$$\frac{\partial \rho}{\partial t} \ + \ \nabla \left(\tilde{\rho}_g v_g\right) \ = \ 0 \ , \tag{4.7}$$

where $\tilde{\rho}_g v_g$ is the gas flux within the pores, with the specific gas density $\tilde{\rho}_g = \Psi\rho_{g,n}$, where $\rho_{g,n}$ is the density of the considered gas and the velocity of the gas v_g. Equation (4.7) can be split into a continuity equation for the gas and a continuity equation for the dust/ice matrix:

$$\frac{\partial \tilde{\rho}_g}{\partial t} \ = \ -\nabla \, \tilde{\rho}_g v_g \ + \ q_g^{\pm} \ , \tag{4.8a}$$

$$\frac{\partial \rho_{d,i}}{\partial t} \ = \ q_g^{\pm} \ , \tag{4.8b}$$

with the net sublimating or depositing mass flux rate $q_g^{\pm}$.
Local thermal equilibrium between the gas and the solid matrix is assumed. For the temperature of the gas T_g and the solid matrix T_m therefore applies $T_g = T_m$.
The conservation of energy in one dimension (with depth z), neglecting gravity and viscous effects, can then be written as (e.g. *Steiner and Kömle* [1991]):

$$[\rho_n c(T) + \tilde{\rho}_g c_g] \frac{\partial T}{\partial t} = \frac{\partial}{\partial z}\left[k(T)\frac{\partial T}{\partial z}\right] - c_g \tilde{\rho}_g v_g \frac{\partial T}{\partial z} - L_h q_g^{\pm} \ , \tag{4.9}$$

with the specific heat of the solid phase $c(T)$ and the gas component c_g, the thermal conductivity k, the latent heat of sublimation L_h and the net sublimating or depositing flux rate $q_g^{\pm}$. The first term on the right-hand side is energy transport due to heat conduction, and the second and third terms are energy transport by the gas phase caused by advection and transport of latent heat.

The second term on the left-hand side will be neglected, since the energy necessary to heat the gas phase and build up the vapor pressure is negligible compared with the energy needed to heat the solid matrix, when water ice is the dominant ice species ($\rho_i \gg \tilde{\rho}_g$). This assumption may be incorrect when more volatile species are major ice components, as *Steiner and Kömle* [1991] point out. The second term on the right-hand side, the energy transport due to advection, has been shown to be negligible in a porous ice matrix when compared to the transport of latent heat [*Fanale et al.*, 1990; *Steiner and Kömle*, 1991], hence will be neglected in this work.

4.3.2 Sublimation Rate

In order to derive the flux rate of sublimated molecules q_g from a homogeneous icy surface, the kinetic theory model described e.g. by *Delsemme and Miller* [1971] is applied:
When the saturated pressure of the neutral gas p_s is at equilibrium with the sublimating ice $p_s = nkT$ is used, with the number density n and the homogeneous surface temperature T. The kinetic model of deposition implies that all molecules that collide with the surface are deposited, and when assuming steady state the depositing flux rate q_g^- at equilibrium equals the sublimating flux rate q_g^+. If now the gas pressure is assumed to be zero (vacuum), the depositing flux drops to zero, but the sublimating flux does not change, which has been verified experimentally as *Delsemme and Miller* [1971] state. The sublimation rate into vacuum can now be predicted from q_g^- at equilibrium, which is known in terms of flux density from kinetic theory in the Knudsen-Regime (e.g. *Kittel and Krömer* [1993]):

$$q_g(\text{vacuum}) = q_g^-(\text{eq}) \, (= q_g^+(\text{eq})) \ = \frac{1}{4} n \bar{v} \ , \tag{4.10}$$

with $n = p_s/kT$ and the mean speed of molecules $\bar{v}$. For a Maxwell velocity distribution at temperature T the mean speed is

$$\bar{v} = \sqrt{\frac{8kT}{\pi m}} \ , \tag{4.11}$$

with the mass of a molecule m. The temperature is assumed to be the temperature of the considered surface element $T = T_s$. Applying the ideal gas law and Equation (4.11), one gets

for Equation (4.10) [particles/(m^2 s)]:

$$q_g \;=\; \frac{p_s}{\sqrt{2\pi mkT}} \;, \tag{4.12a}$$

or in terms of the mass flow rate mq_g one gets in units of [kg/(m^2 s)]:

$$mq_g \;=\; p_s \sqrt{\frac{m}{2\pi kT}} \;, \tag{4.12b}$$

or the also often used term $\tilde{q}_g$ in units of [mol/(m^2 s)]:

$$\tilde{q}_g \;=\; p_s \sqrt{\frac{\mu}{2\pi RT}} \;, \tag{4.12c}$$

with the molar mass of a molecule μ. With the assumption of thermal equilibrium the gas pressure p_s above an ice surface is often derived with an approximate expression from the Clausius-Clapeyron equation (e.g. *Fanale and Salvail* [1984]):

$$p_s \;=\; p_0\, e^{-L_h/(RT)} \quad [Pa] \;. \tag{4.13}$$

The parameters $a = p_0$ and $b = L_h/R$ are derived from laboratory experiments and have values of $a = 3.56 \times 10^{12}$ Pa and $b = 6141.667$ K [*Fanale and Salvail*, 1984]. This kind of approximation to the gas pressure implies that the latent heat of sublimation does not depend on the temperature in the considered temperature regime and has the value $L_h = bR_{gas} \approx 5.1 \times 10^4$ J/mol $\approx 2.8 \times 10^6$ J/kg. The latent heat of sublimation of water ice is, however, not independent of temperature (see Section 4.4). An empirical formulation for the saturated water vapor pressure over ice is provided by e.g. *Benkhoff and Huebner* [1995]:

$$\log(\tilde{p}_s) \;=\; 4.07023 - 2484.986 \,/\, T + 3.56654 \log(T) - 0.00320981\, T \quad [Pa] \;. \tag{4.14}$$

In Figure 4.3 the ratio of the saturated vapor pressures over water ice from Equation (4.14) and (4.13) are plotted. It can be concluded that in the temperature regime of $\sim$ 120K $-$220K the difference is only marginal, while at lower temperatures the difference becomes significant. The error made by using Equation (4.13) to derive the saturated pressure of water is not significant, since the results for temperatures below $T \approx 120$K indicate a negligible water production rate. Equation (4.13) is therefore applied in the model calculations and the latent heat of water sublimation is considered as depending on temperature (see Section 4.4). The use of Equation (4.13) has the advantage of providing a simple analytical expression for the thermal conductivity of the pores (see Section 4.3.3).

If the modeled ice contains more than just one component, sublimation rates for each component have to be calculated. Stationary sublimation from a homogeneous plane surface with a homogeneous mixture of ice components is assumed in this case, with mainly water and additional minor CO_2 or CO components. If e.g. CO_2 is considered as an additional component, the saturated vapor pressure is derived from Equation (4.13) with parameters $a = 1.2264 \times 10^{12}$ Pa and $b = 3167.8$ K [*Fanale and Salvail*, 1987]. For CO ice the parameters are $a = 1.2631 \times 10^9$ Pa and $b = 764.16$ K [*Fanale and Salvail*, 1990]. This corresponds to a constant latent heat of $L_h(CO_2) \approx 2.63 \times 10^4$ J/mol and $L_h(CO) \approx 0.6 \times 10^4$ J/mol.

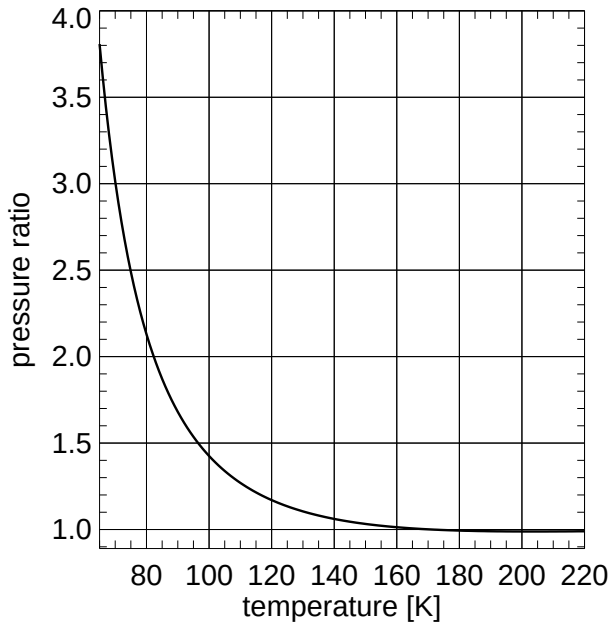

Figure 4.3: *Pressure ratio $\tilde{p}_s/p_s$ from Equations (4.14) and (4.13) versus temperature*

Water ice is assumed to be the single ice species in the surface layer of the nucleus, implying that all more volatile species were already depleted in the surface layer during previous orbits.

The assumptions concerning the sublimation are simplifying. The nucleus surface and the pore walls are not expected to be plane homogeneous surfaces. At least within the pores the sublimation into vacuum is a reasonable assumption. When considering the surface of the nucleus, the return flux from the collision dominated inner coma has to be accounted for, which influences the thermal balance at the surface. This is discussed by e.g. *Crifo* [1987]; *Skorov and Rickman* [1998], who consider a thin non-equilibrium layer next to the surface before the gas reaches a temperature T_g and a pressure p_g at the inner coma boundary. The resulting effects are taken into consideration when determining the energy balance at the surface (Section 4.3.4) and when determining the inner boundary conditions for the hydrodynamic model of the neutral gas environment (Chapter 5).

4.3.3 Thermal Conductivity and Gas Flux

The thermal conductivity of the matrix material $k(T)$ is a combination of the thermal conductivity of the considered ice species and the dust component. The values are given in Section 4.4. The energy transport due to transport of latent heat by the gas phase within the pores will now be defined as thermal conductivity of the pores $k_{\mathrm{po}}(T)$. The effective thermal conductivity k_{eff} of the porous medium will be derived. In general, k_{eff} is a function of temperature, composition, and porosity.

The energy conservation equation (4.9) includes the source term $L_h q_g^{\pm}$ (the last term on the right-hand side). The source term can be derived by multiplying the equation of the conservation of mass (4.8a) with the latent heat of sublimation L_h and one gets:

$$L_h q_g^{\pm} \;=\; L_h \frac{\partial \tilde{\rho}_g}{\partial t} + L_h \nabla \tilde{\rho}_g v_g \quad . \tag{4.15}$$

The first term on the right-hand side can be neglected in the considered temperature regime, as e.g. *Hagermann* [1996] shows. The term can therefore be written as $L_h q_g^{\pm} = L_h \nabla \tilde{\rho}_g v_g$.

The mean free path Λ of molecules in the pore system is derived as:

$$\Lambda = \frac{1}{\sqrt{2} n \sigma} \quad . \tag{4.16}$$

Water ice is assumed to be the dominant species. A temperature of the ice of 200 K, with the collision cross section for water $\sigma \approx 5 \times 10^{-19}$ m^{-2} [*Crovisier*, 1984], and applying the ideal gas law, assuming the pressure in the pores to be saturated (by applying Equation (4.14)) to determine the number density n, yields a mean free path of $\Lambda = 0.17$ m which is larger than the typical assumed pore diameter of $d \approx 10 - 1000$ μm (e.g. *Horányi et al.* [1984]; *Klinger et al.* [1996]).

If the Knudsen Number $Kn = \Lambda / d > 1$, the collisions between gas molecules and pore walls are more frequent than collisions between molecules. The gas flow through the porous medium is then best described as a diffusion process, and viscous flow, where particle collisions are dominant, can be neglected. Therefore the concept of the *Knudsen-Regime* is applied.

The mass flux $\tilde{\rho}_g v_g$ depends in the Knudsen-Regime on the pressure gradient $\partial P / \partial z$ and can be described as depending on the gradient of the sublimation rate $\tilde{q}_g$ (e.g. *Kehse* [1994]), which for a dust-ice mixture can be written as:

$$\tilde{\rho}_g v_g \;=\; - f A_0 r_{\mathrm{po}} \nabla \tilde{q}_g(T) \quad , \tag{4.17}$$

with the radius of the pores r_{po} and the structural parameter f. The parameter f describes the effective flow area for the gas phase per unit cross section. The parameter f is defined in different ways by various authors (e.g. *Fanale and Salvail* [1984]; *Mekler et al.* [1990]; *Espinasse et al.* [1991]; *Steiner and Kömle* [1991]). The choice of f can lead to over- or under-estimation of the effect of the gas phase on the energy transport. The discussion of *Steiner and Kömle* [1991] is followed in this work with:

$$f \;=\; 1 - \sqrt{1 - \Psi} \quad . \tag{4.18}$$

When applying Equations (4.12c) and (4.13), and using $\partial q_g / \partial z = \partial q_g / \partial T \;\; \partial T / \partial z$, one gets

$$\tilde{\rho}_g v_g \;=\; - f A_0 r_{\mathrm{po}} \tilde{q}_g(T) \left(-\frac{1}{2} + \frac{b}{T} \right) \frac{1}{T} \frac{\partial T}{\partial z} \quad . \tag{4.19}$$

In the considered temperature regime one has $b/T \gg 1/2$, one can therefore neglect the first term in the brackets. The energy transport of the gas phase can now be written as:

$$L_h q_g^{\pm} \;=\; - k_{\mathrm{po}}(T) \nabla T \quad , \tag{4.20}$$

with the *thermal conductivity of the pores*

$$k_{\mathrm{po}}(T) \;=\; f \, A_0 \, r_{\mathrm{po}} \, \tilde{q}_g(T) \, \frac{b}{T^2} \, L_h \quad . \tag{4.21}$$

In general, the effective thermal conductivity $k_{\mathrm{eff}}(T)$, which could be measured experimentally, should be a function of the individual thermal conductivities. $k_{\mathrm{eff}}(T)$ is approximated in this work by adding the individual thermal conductivities $k_{\mathrm{eff}}(T) = k(T) + k_{\mathrm{po}}(T)$. This can be viewed as an upper boundary of the real effective thermal conductivity as *Hagermann* [1996] and references therein point out.

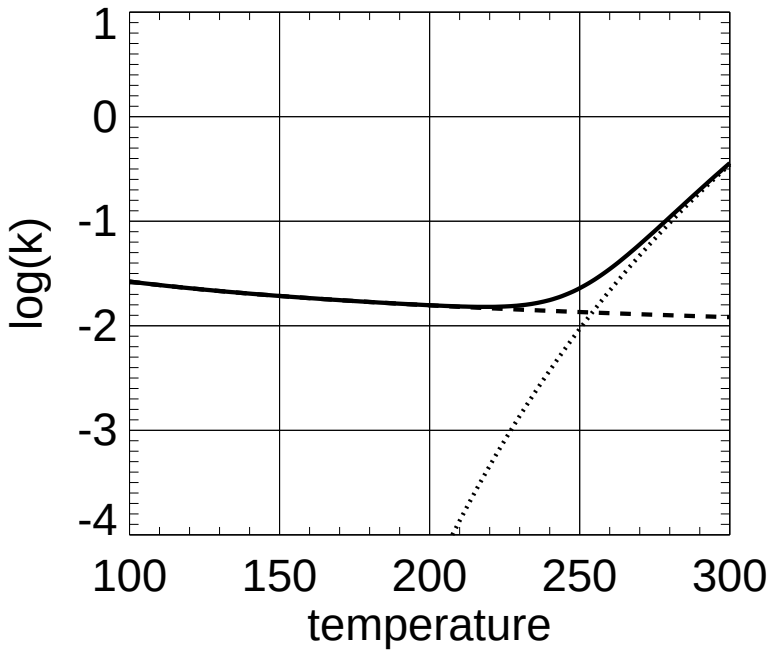

Figure 4.4: *Typical thermal conductivities of the matrix material (dashed), the gas phase within the pores (dotted) and the effective thermal conductivity (solid)*

Typical thermal conductivities are plotted in Figure 4.4. The assumed parameters for this example are: pore radius $r_{\mathrm{po}} = 100\mu$m, porosity $\Psi = 0.5$, Hertz factor $h = 10^{-2}$ and dust to ice mass ratio $R_{di} = 1.0$. The assumed pore radius has a strong effect on the resulting thermal conductivity of the pores k_{po}, which is plotted as dotted line in Figure 4.4. The dashed line is the thermal conductivity of the dust-ice mixture of the matrix material. In the given example, a significant effect of k_{po} on k_{eff} is visible above a temperature of $T \approx$ 220K.

Instead of solving the coupled differential equations of heat and gas diffusion within the comet nucleus, the heat equation in the following version is solved in this work:

$$\rho_n c(T)\,\frac{\partial T}{\partial t} \;=\; \frac{\partial}{\partial z}\left[(k_{\mathrm{eff}}(T))\,\frac{\partial T}{\partial z}\right] \quad . \tag{4.22}$$

4.3.4 Boundary Conditions

The energy due to insolation of the cometary surface is balanced by various different processes. The low albedo of cometary nuclei (see Section 4.2.4) reflects only about 1%-4% of the solar energy back into interplanetary space. Other processes are the heating of the material at the surface and phase changes of cometary material. The energy at the surface is also balanced by transport processes, like thermal re-radiation, heat conduction within the solid material of the comet, heat convection due to gas flux within the nucleus and thermal radiation inside the pores of the nucleus material. The thermal radiation inside the pores is the least effective transport process in the considered temperature regime (e.g. *Horányi et al.* [1984]) and will be neglected in this work.

In Figure 4.5 a schematic view of the energy balance for a surface element is plotted. A possible stratification below the surface is indicated by the different grayscales. Some important parameters are assigned to the physical processes for convenience.

The surface temperature of a modeled dust/ice-body is derived from the energy balance equation for the considered surface cell i:

$$\frac{S_{\mathrm{eff}}(1-a_i)\cos\theta_i C_i}{r_h^2} \;=\; \varepsilon_i\sigma T_{s,i}^4 + A_i L_h \Phi_{s,i}(T_{s,i}) + k_{\mathrm{eff}}(T)\,\left.\frac{\partial T_s}{\partial z}\right|_i \quad , \tag{4.23}$$

with the effective solar radiation at the surface S_{eff}, the bond albedo a_i, the zenith angle of the sun θ, $C_i = 1/0$ if the cell is / is not illuminated, the infrared emissivity ε, the surface Temperature T, the Stefan-Boltzman constant σ, the latent heat of sublimation L_h, the thermal conductivity $k(T)$, the local icy area fraction at the surface A (see Equation (4.6)), the normal direction to the surface z and the sublimating gas mass flux rate $\Phi = (1-\alpha)mq_g$[1]. The value of α in this trans-sonic regime has been derived by e.g *Crifo* [1987] and has the recommended value of $\alpha \approx 0.25$, which is adopted in the model calculations.

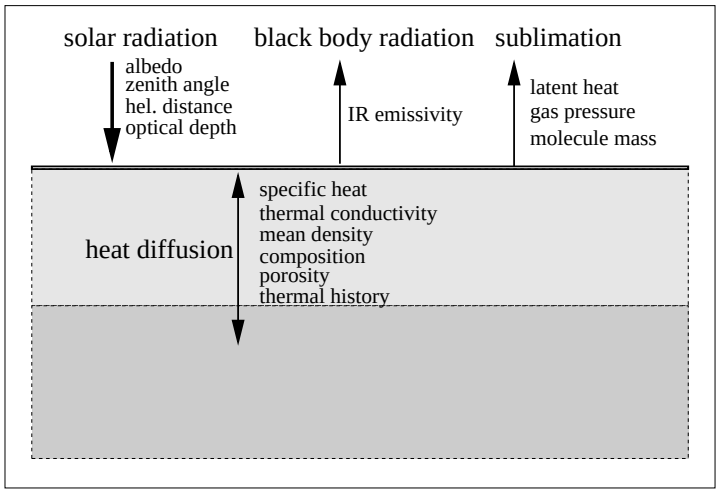

Figure 4.5: *A schematic view of the energy balance and the important parameters at each surface element*

The term on the left-hand side of equation (4.23) is the solar energy input. The radiative transfer properties of the inner coma are parameterized. The effective solar radiation at the surface is determined as $S_{\text{eff}} = S_0 \cdot e^{-\tau} + s_c$, with the solar constant S_0, the optical depth τ and the flux of indirect light scattered onto the nucleus by the coma s_c. For simplicity the parameters τ and s_c are set to zero in this work. This can be easily changed for detailed parameter studies with the provided model routines.

The right-hand side of equation (4.23) includes the terms of thermal re-radiation, sublimation of the ice component at the surface and diffusion of heat to/from the interior of the nucleus. The heat diffusion is solved as described in Section 4.3.1. The mass flux into the coma is in this model derived from the sublimation rate at the surface. Gas diffusion within the porous medium is only considered as a mechanism to transport energy. This implies that any molecule sublimated within the pores is re-deposited. This assumption therefore restricts the model to just one sublimation front at the surface when considering the global gas production rate.

[1]The term $(1-\alpha)$ is included to account for the energy provided by the re-depositing flux from the coma, as proposed by *Crifo* [1987]. The value of α is correlated to the Mach number M of the sublimated gas emerging from the surface. The velocity v_0 of the emerging gas depends on the characteristics of the surface. *Delsemme and Miller* [1971] obtain a value of $v_0 = 0.6\bar{v}$, with the mean speed of a Maxwell distribution $\bar{v}$. This is the mean value for v_0 as a compromise between the case of a solid plane sublimating surface without any pores down to the molecular level and the case of a surface with deep and narrow pores oriented at random. With the speed of sound $v_s = (\gamma kT_g/m)^{1/2}$, the temperature of the gas T_g and the heat capacity ratio γ, one gets an estimated value of $M \approx 0.8$ for water vapor. *Huebner and Markiewicz* [2000] derive the Mach number of the gas when the Maxwell distribution is reestablished a few mean free path lengths above the surface. The derived Mach numbers have a value slightly larger than one ($M \approx 1.08 - 1.14$), depending on the degrees of freedom of the considered gas. *Skorov and Rickman* [1998] use a direct simulation Monte Carlo method to model gas flow in a Knudsen layer above a cometary surface and obtain a value of $M \approx 1.2$ at the exterior boundary of the Knudsen layer.

At the inner boundary the heat flux has to vanish:

$$\left.\frac{\partial T}{\partial z}\right|_{z=0} = 0 \quad . \tag{4.24}$$

The inner boundary can be either the center of the comet nucleus or the lower boundary of the layer of variable temperatures.

4.3.5 Numerical Scheme

To solve the partial differential equation (4.22) numerically, a finite difference approximation with an FTCS scheme is used (e.g. *Press et al.* [1986]). See Appendix B for details.

The computations start at aphelion with a constant initial temperature throughout the nucleus. The respective heliocentric distance is derived from the standard formulas for orbit determinations (e.g. *Green* [1985]) by calculating the mean anomaly, the eccentric anomaly (using the Newton-Raphson formula), and then the heliocentric distance at each time step. The osculating orbital elements of each considered comet were used as input (see Section 3.3). With the obliquity, the angle between the ascending node and the subsolar point at perihelion and the eccentric anomaly, the latitude of the subsolar point and the zenith angle at each point can be derived at each time step.
Case studies for model comets in the orbits of 46P/Wirtanen and 67P/Churyumov-Gerasimenko are computed. The osculating orbital elements and general estimates for both comets are given in Chapter 3. The obliquity (the angle between orbit normal and spin axis) is a free parameter of the model. Most model runs were initiated with zero obliquity.

The number of grid points in the space domain is of the order 10^3 and can be varied. The corresponding spatial resolution depends on the size of the considered nucleus or layer of temperature variability, respectively. The spatial resolution close to the surface is at maximum of the order 10^{-1} m, which is approximately the thermal skin depth of the daily temperature variations (see Section 4.2.5).
One-dimensional thermal diffusion models are allocated to equidistant points along a meridian and are computed with the appointed time step. The temperature distribution and gas production rate for the whole surface is derived by storing results of a full rotation at the considered orbit position. This strategy reduces computational resources and makes the model computations faster than a complete coverage of the surface.
One time step in the model calculations is the rotation period of the considered comet divided by the number of grid points of the hydrodynamic model in the longitudinal direction. With a longitudinal resolution of five degree, the resulting time step is about 500 s for comet 67P/Churyumov-Gerasimenko and about 300 s for comet 46P/Wirtanen.

4.4 Physical Parameters

The model comet is assumed to be of spherical shape. Other shapes have been studied by e.g. *Gutiérrez et al.* [2001], who pointed out that the topography can have a significant effect

on the energy balance at the surface. Since the shape of the target comet of the ROSETTA mission is not yet known, topography effects are neglected.

When modeling the structure of the nucleus one can either use the porosity Ψ and the dust/ice ratio R_{di} as free parameters and determine the mean density of the nucleus via Equation (4.5), or derive the porosity from an assumed mean density of the nucleus ρ_n and the dust/ice ratio R_{di}. The latter way is used in this work (see Table 4.1), since ρ_n and R_{di} will hopefully be provided by the experiments aboard ROSETTA. The Hertz factor h is used to correct the effective area of the matrix material through which heat flows. It is assessed with the assumption of two spheres of radius R that are pressed together and have a contact area of radius r_c, so $h \approx r_c^2/R^2$. The estimated value of h (e.g. *Huebner et al.* [1999]) has a large range and can be used to effectively dim or amplify the heat diffusion by the solid matrix within the nucleus.

ρ_n	mean density of the nucleus	$500-1000$ kg/m^3
R_{di}	dust/ice mass ratio	$0.1-100$
h	Hertz factor	$10^{-5}-10^{-2}$
r_{po}	mean pore radius [m]	$10^{-6}-10^{-4}$

Table 4.1: *Range of free parameters used in the model calculations*

In Table 4.2 some physical parameters with respect to the considered components are listed. Following *Huebner et al.* [1999], the specific heat c and the heat conductivity k of a *CO* ice component is assumed to be the same as for the H_2O component. The specific heat and the heat conductivity of water ice is taken from *Klinger* [1981]. The specific heat and the heat conductivity of the dust component and the density of the compact ice $\rho_{i,c}$ is taken from *Ellsworth and Schubert* [1983]. The compact density of the dust material is an average of the considered species as listed in *Grün and Jessberger* [1990].

	Parameter	H_2O	CO	Dust
$c(T)$	specific heat [J kg^{-1} K^{-1}]	$7.5T+90$K	$7.5T+90$K	1200
$k(T)$	heat conductivity [W m^{-1} K^{-1}]	$h567/T$	$h567/T$	$h4.2$
ρ_c	density of compact material [kg/m^3]	930	930	3000

Table 4.2: *Physical parameters for the ice and dust components*

For water ice the latent heat of sublimation is given as (e.g. *Espinasse et al.* [1993]:

$$L_h = 2.888 \times 10^6 - 1116\,T \quad [J/kg] \quad . \tag{4.25}$$

This represents the energy to release water molecules (in kg) from an ice surface. The lower limit of latent heat of sublimation of a *CO* molecule in a water ice matrix is given by *Enzian et al.* [1998] as $L_h(CO) = 2.3 \times 10^5$ J/kg.

Since only a homogeneous surface is considered in this work, the local icy area fraction A_0 equals the total icy area fraction of the nucleus A_n. In some model calculations A_n is varied with respect to the heliocentric distance. This parameterizes a variation of the dust to ice

mass ratio R_{di} that might occur due to the possible build-up of a dusty layer at the surface when the ice is sublimated. Comet images suggest a strong variation of A_0 across the surface of a comet. The results here can be viewed as the corresponding homogeneous comet with an averaged icy area fraction.

4.5 Calibration and Results

The thermal model provides the temperature distribution within the comet nucleus as well as temperatures and sublimation rates at the surface for discrete surface elements evenly distributed over the nucleus.
As soon as ROSETTA reaches its target the validity of the assumptions and the reliability of the results can be tested in detail. With presently available datasets only the general behavior and global results of the model can be verified. The quantity that can be currently used best to evaluate model results is the global gas production rate of a comet, which can be obtained from remote sensing measurements. These measurements usually involve additional assumptions about the gas distribution within the cometary coma, such as symmetrical radial outflow, exponential decay of the species, or a constant outflow velocity (e.g. *Feldman* [1982]).
It should also be noted that a particular sublimation rate from a comet surface can be obtained by thermal models with different parameter settings. Resulting gas production rates that are consistent with observations therefore only indicate the applicability of a particular model.

Results of 4 different exemplary cases for comet 67P/Churyumov-Gerasimenko and 2 different cases for comet 46P/Wirtanen are presented. Many more case studies were carried out. They are consistent with the conclusions drawn here. The chosen parameter settings for the models with the orbit parameters of comet 46P/Wirtanen are summarized in Table 4.3. The difference between model W1 and W2 is the assumed dust to ice mass ratio and a decreasing icy area fraction A_n at the surface with heliocentric distance for model W2.

46P/Wirtanen		model W1	model W2
ρ_n [kg/m^3]	mean density of the nucleus	500	500
R_{di}	Dust/ice mass ratio	1	10
h	Hertz factor	10^{-2}	10^{-2}
r_{po}	mean pore radius [m]	10^{-4}	10^{-4}
A	icy area fraction	A_0	$A_n(r_h)$
ω	Obliquity of spin axis	0°	0°

Table 4.3: *Parameter settings for 46P/Wirtanen -like model comets*

The variation with heliocentric distance r_h is derived as $A_n(r_h) = A_0(R_{ph}/r_h)^2$, with the initial value A_0 as derived from Equation (4.6) and the perihelion distance R_{ph} of the comet. This variation was derived empirically by comparing modeled and observed gas production rates (see below).

H_2O production rates derived from observations at 46P/Wirtanen and results from models W1 and W2 are plotted in Figure 4.6. Observed production rates are taken from *Schulz and*

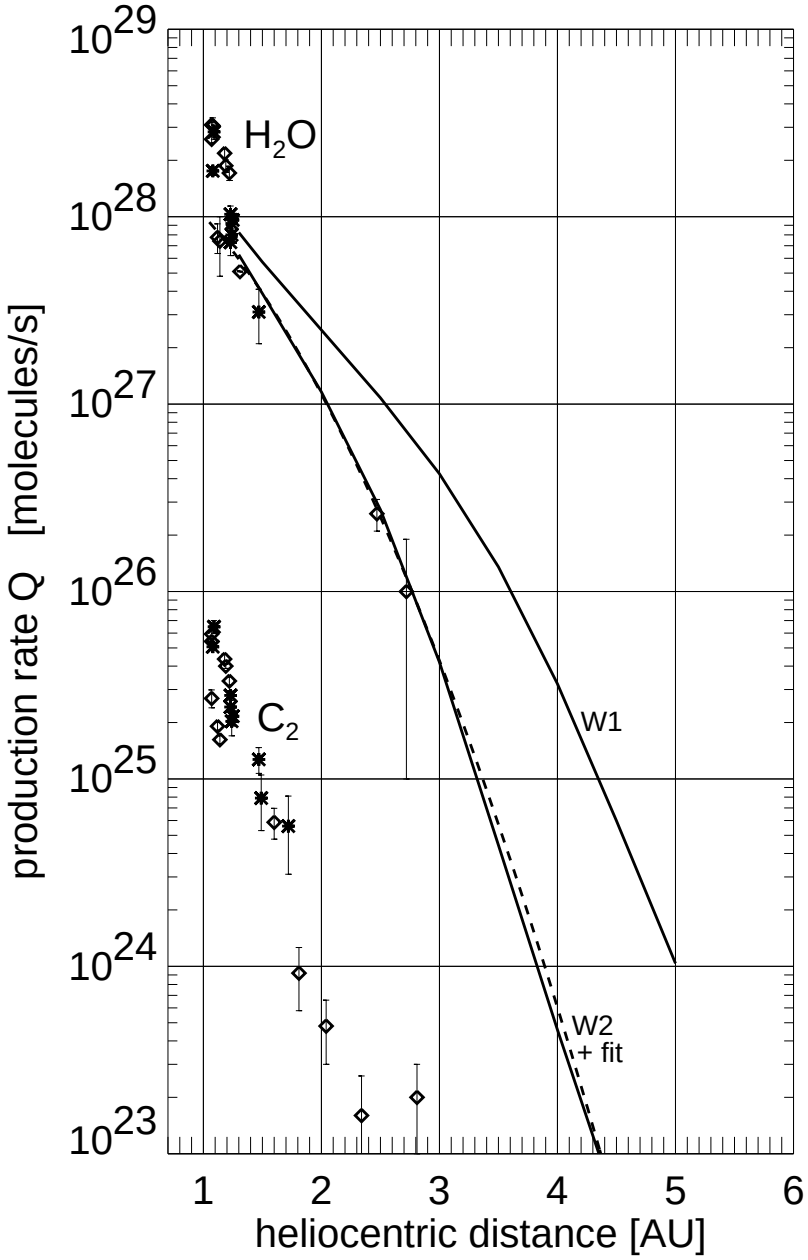

Figure 4.6: *Observed and modeled production rates at comet 46P/Wirtanen, see text for details.*

Schwehm [1999]. Observed C_2 production rates are plotted as an example for other observed species at 46P/Wirtanen, which have at most the order of magnitude of the C_2 component (see *Schulz and Schwehm* [1999]). Data obtained on the inbound part of the orbit (pre-perihelion) are indicated by diamonds. Data from post-perihelion are represented by asterisk symbols. No general difference between pre- and post-perihelion is visible in the data.

The gas production rate from the model comet is derived by adding up the calculated local gas production rates of each surface element. The two model results for comet 46P/Wirtanen produce a comparable amount of gas at perihelion (see Figure 4.6), with slightly lower gas production Q_g from model W2 caused by a larger dust to ice mass ratio (see Table 4.3). The steeper decrease with heliocentric distance in model W2 is obtained by the variation of the icy

area fraction as described above. The variation with r_h^{-2} is empirically derived by comparing results with the observed gas production rate at distances $r_h > 2$AU. This dependence indicates and parameterizes the stepwise blow-off of a dust mantle at the surface with increasing gas production at pre-perihelion, or the build-up of a dust mantle due to the attenuation of the gas production with increasing heliocentric distance at post-perihelion, respectively.

The largest observed gas production rates of H_2O around perihelion are not reproduced in the models. In order to match these production rates, a significantly larger amount of sublimating ice would be required at the surface. This can be obtained by an additional blow-off of parts of a dusty surface crust, which uncovers a fresh icy surface. This process is not explicitly included in the models.

In order to obtain a quick method to determine the gas production rate Q_g of 46P/Wirtanen consistent with the model results at a particular heliocentric distance, a function is fitted to model W2. This model reproduces the observed H_2O production rates at distances larger than ≈ 1.3 AU better than model W1 (see Figure 4.6). The fit plotted with a dashed line in Figure 4.6 is calculated as:

$$Q_g(\text{46P/Wirtanen }) = 2.5 \times 10^{28}\ exp\left[-\left(\frac{r_h}{1.06AU}\right)^{1.78}\right]\ [1/s], \tag{4.26}$$

and has only small deviations from the results of model W2. The deviations are less than the range of errors of the observations indicated by the error bars in Figure 4.6. Therefore Equation 4.26 is an acceptable fit. This approximation is used when the gas production rate Q_g of 46P/Wirtanen is needed in other model computations, especially in Chapter 6.

Since the estimated radius of 67P/Churyumov-Gerasimenko is larger by a factor of 3.3 than the radius of 46P/Wirtanen, the total surface area of 67P/Churyumov-Gerasimenko is larger by a factor of 10.9 (assuming spherical nuclei). The observed gas production rates have the same order of magnitude at 1.3 AU of up to 10^{28} 1/s (see Figures 4.6 and 4.7). From this it can be concluded that the amount of ice available for sublimation must be smaller at comet 67P/Churyumov-Gerasimenko, or that a different process consumes much of the incoming energy (such as a more effective heat transport into deeper layers).

67P/C-G		M1	M2	M3	M4
ρ_n [kg/m^3]	mean density of the nucleus	800	800	800	600
R_{di}	Dust/ice mass ratio	10	100	100	100
h	Hertz factor	10^{-2}	10^{-3}	10^{-3}	10^{-3}
r_{po}	mean pore radius [m]	10^{-4}	10^{-4}	10^{-4}	10^{-4}
A	icy area fraction	A_0	$A_n(r_h)$	$0.1 \cdot A_n(r_h)$	$0.5 \cdot A_n(r_h)$
ω	Obliquity of spin axis	0°	0°	0°	30°

Table 4.4: *Parameter settings for 67P/Churyumov-Gerasimenko -like model comets*

Lower gas production rates can be obtained for example by increasing the dust to ice mass ratio, by increasing the obliquity of the spin axis to reduce the area per rotation that is reached by solar radiation, by assuming an irregular shape that creates shadows on the day-side hemisphere, or by increasing the effective thermal conductivity. The latter procedure would require the inner nucleus to be relatively cold, but also thermally well coupled to the surface.

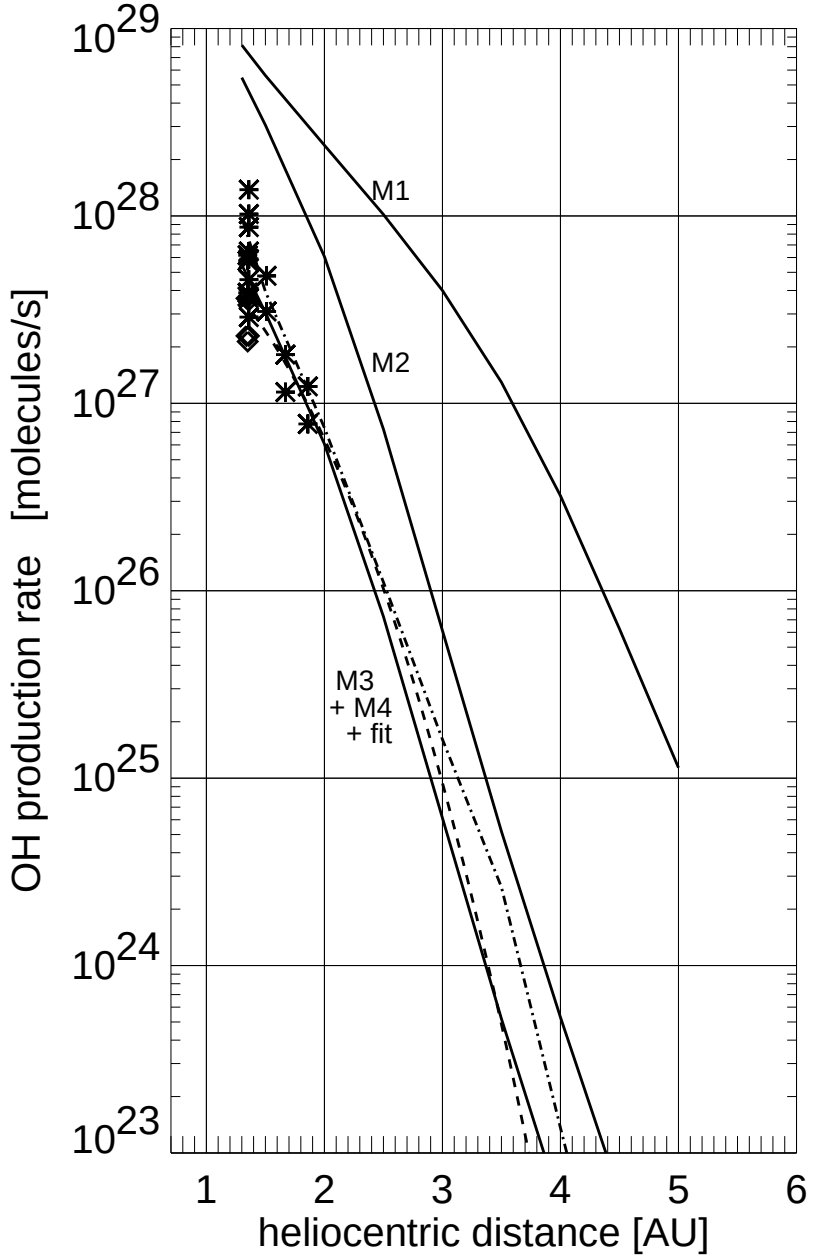

Figure 4.7: *Observed and modeled production rates at comet 67P/Churyumov-Gerasimenko; M3=solid, M4=dashed-dotted, fit = dashed, see text for details.*

The varied parameters in the models for comet 67P/Churyumov-Gerasimenko presented here are: the dust to ice mass ratio, the Hertz factor, the icy area fraction at the surface and the obliquity of the spin axis. Details are listed in Table 4.4.

Results from different models of comet 67P/Churyumov-Gerasimenko are plotted in Figure 4.7. Also included are observed gas production rates. Remotely measured gas production rates at various heliocentric distances are available inside $r_h \approx 1.9$ AU for comet 67P/Churyumov-Gerasimenko. The summarized gas production rates were provided by the 'Group of Cometary Atmospheres and Extra-Solar Planets' from the DLR in Berlin, Germany[1].

[1] http://berlinadmin.dlr.de/Missions/corot/caesp/comet_db.shtml

Observed production rates of the *OH* molecule at comet 67P/Churyumov-Gerasimenko vary over approximately an order of magnitude at perihelion distance, as can be seen in Figure 4.7. This is probably a consequence of the recurrent observed sudden brightening of the comet at or shortly after perihelion[1]. The *OH* production rate is assumed to be equal to the H_2O production rate when comparing observations with model results.

Models M1 and M2 overestimate the gas production rate by about an order of magnitude inside 2 AU (see Figure 4.7). From the results at comet 46P/Wirtanen the variation of the icy area fraction A_n with heliocentric distance is adopted in model M2, which also includes a dust to ice mass ratio enhancement by a factor of ten when compared with model M1. The progression of the modeled gas production rate with heliocentric distance seems reasonable for model M2, with an overestimation of the absolute values. The icy area fraction at the surface A_n is therefore reduced by a factor of 10 in model M3, which produces results that correspond well with the observed production rates. The large variation at perihelion distance is not reproduced by the model. Since model M3 matches the observed production rates inside 2 AU, this model is used as a reference model for other calculations where the gas production rate is involved (especially in Chapter 6).

Model M4 is used to demonstrate that the set of parameters to reproduce observed gas production rates is not unique. The resulting gas production rates of model M4 are indicated by the dashed-dotted line in Figure 4.7. The main difference with the other models is the assumed obliquity of the spin axis of $\omega = 30^\circ$. Also varied are the mean density of the model comet ρ_n and the icy area fraction at the surface A_n (see Table 4.4). The observed gas production rates are reproduced with accuracy similar to model M3. With increasing heliocentric distances models M3 and M4 have larger differences. The modeled gas production rates at 3 AU distance are $Q_g \approx 6 \times 10^{24}$ 1/s for model M3 and $Q_g \approx 3 \times 10^{25}$ 1/s for model M4 respectively. This indicates the large factor of uncertainty in the modeled gas production rates, which was also concluded by *Huebner et al.* [1999].

A fit consistent with results from model M3 and M4 and with observations was derived as

$$Q_g(\text{67P/Churyumov-Gerasimenko }) \approx 1.0 \times 10^{28}\ exp\left[-\left(\frac{r_h}{1.29AU}\right)^{2.3}\right]\ [1/s]. \quad (4.27)$$

This fit is represented by the dashed line in Figure 4.7. This formula is used to derive gas production rates of 67P/Churyumov-Gerasimenko at particular heliocentric distances.

Results from models W2 for 46P/Wirtanen and M3 or M4 for 67P/Churyumov-Gerasimenko therefore represent reasonable conditions at the surface of the respective comet. Figures 4.8 (M3), 4.9 (W2) and 4.10(M4) show maps of the resulting surface temperatures of these models at heliocentric distances of 5.0 AU, 2.0 AU and 1.3 AU. Isotherms are plotted at equidistant levels of 10 K. The subsolar point in each map is at 180 degree longitude. In Figures 4.8 and 4.9 the subsolar point is at the equator.

The general appearance shows a steep temperature increase on the surface shortly after local sunrise (90 degree longitude), a temperature maximum at the latitude of the sub solar point, which trails local noon (180 degree longitude) due to the thermal inertia of the material, and

[1] see e.g. http://berlinadmin.dlr.de/Missions/corot/caesp/comet_db.shtml

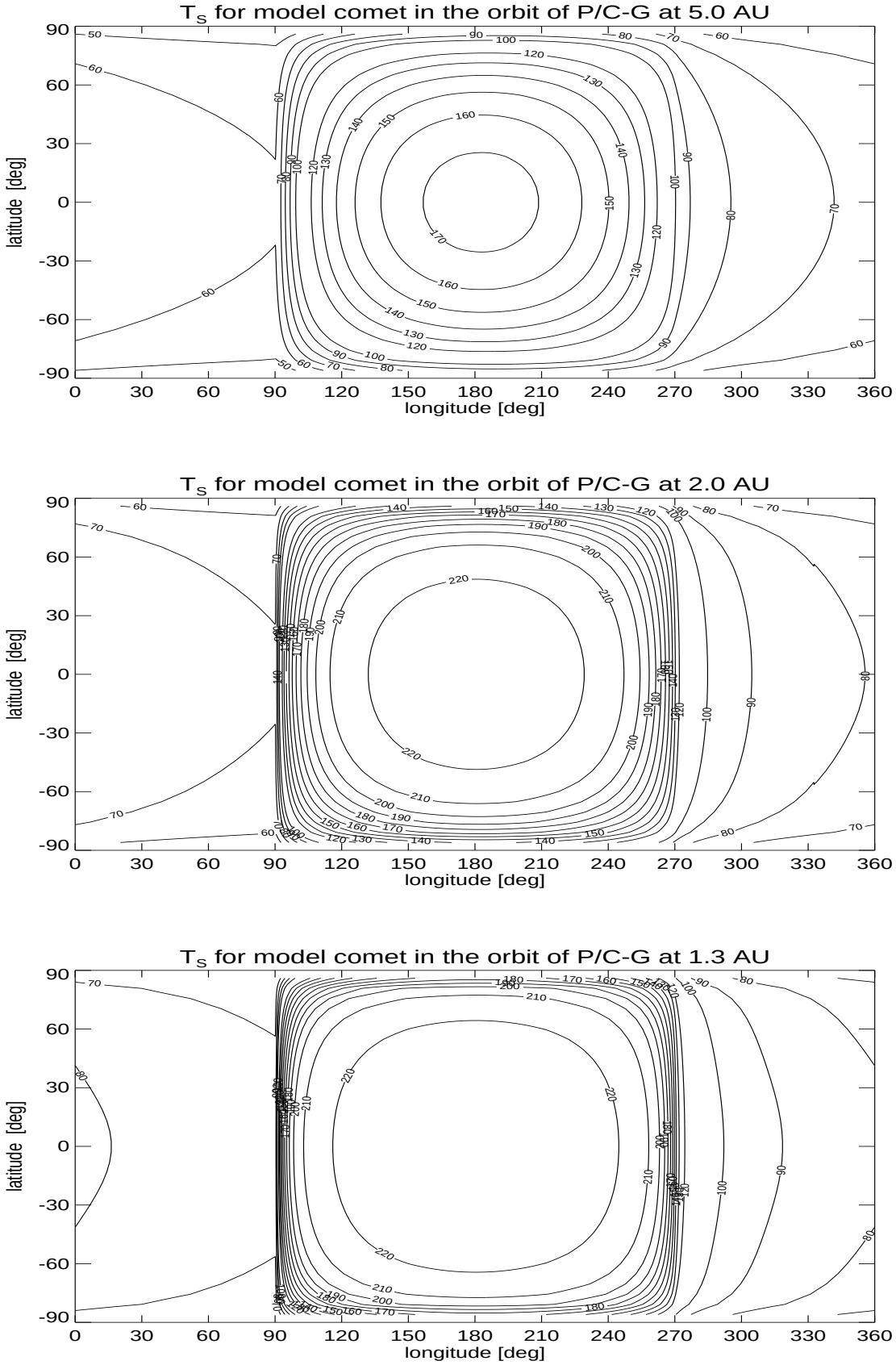

Figure 4.8: *Contour plot of surface temperatures [K] of the model nucleus in the orbit of 67P/Churyumov-Gerasimenko, model M3.*

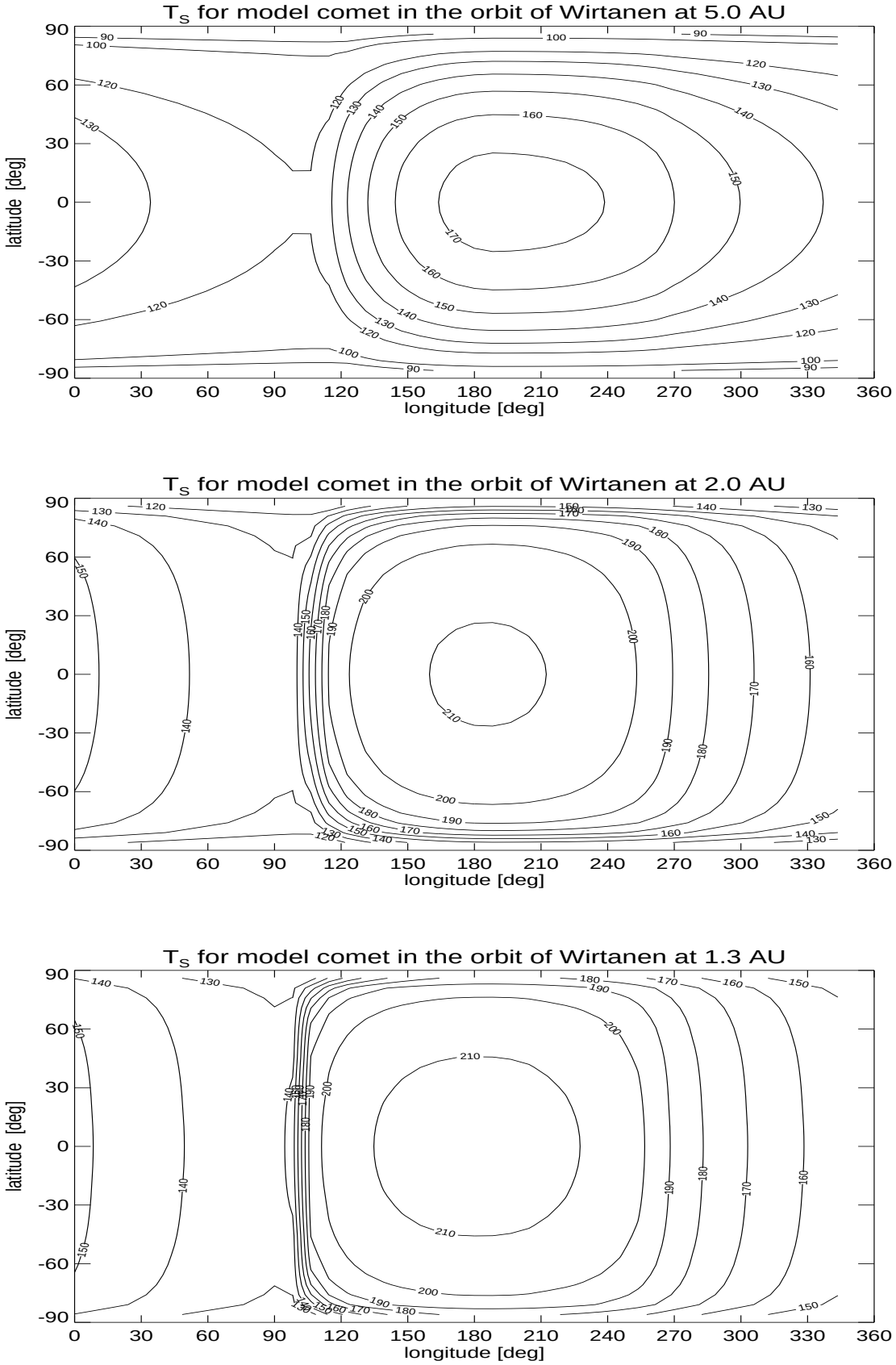

Figure 4.9: *Contour plot of surface temperatures [K] of the model nucleus in the orbit of 46P/Wirtanen, exemplary from model W2.*

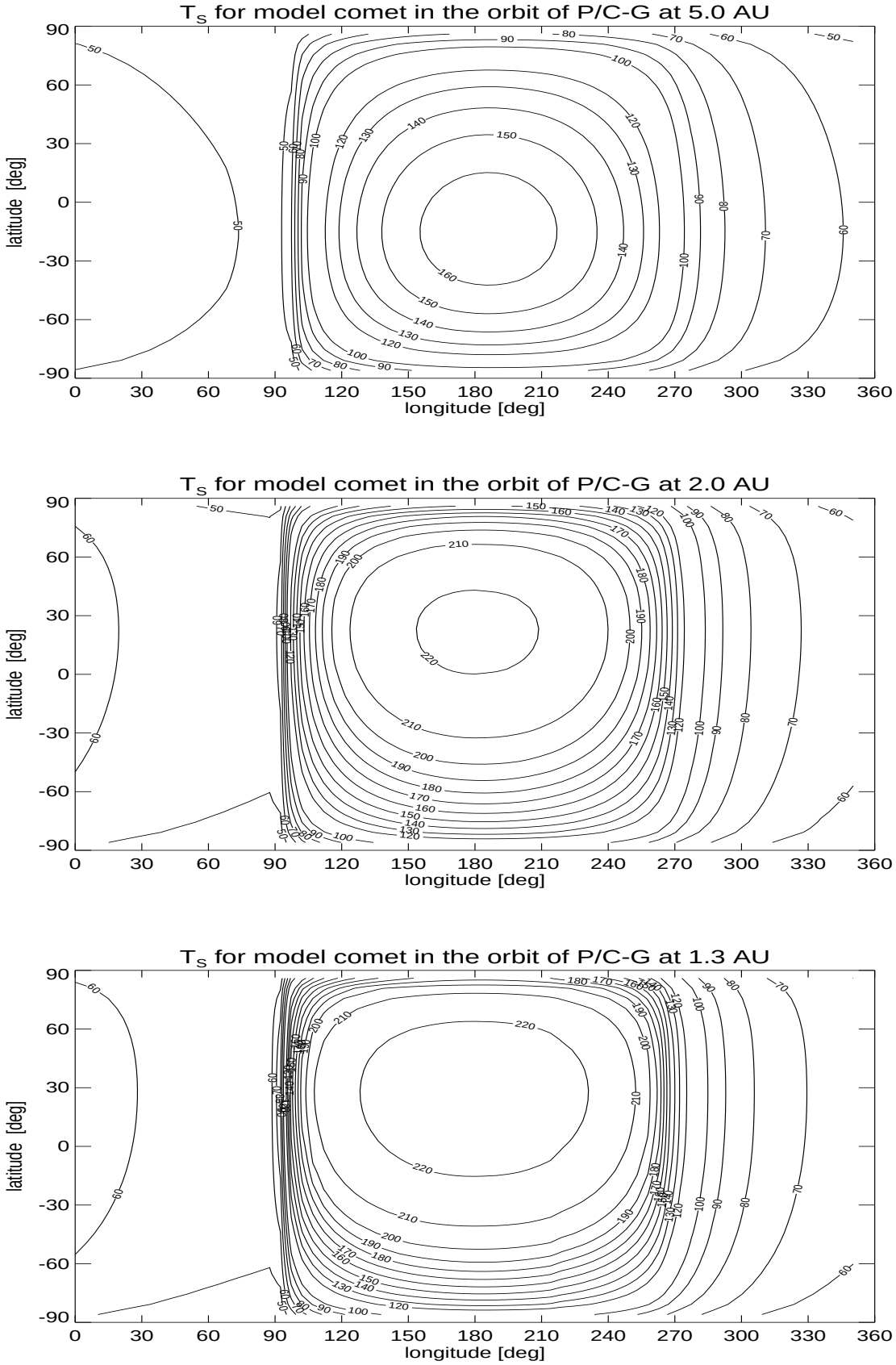

Figure 4.10: *Contour plot of surface temperatures [K] of the model nucleus in the orbit of comet 67P/Churyumov-Gerasimenko with an obliquity of the spin axis of* 30°*, model M4.*

a relatively slower, more gradual decay of the temperature during local evening and night hours. The polar regions remain at low temperatures when zero obliquity is assumed. The lowest temperatures occur just before local sunrise. The temperature maximum and the maximum difference between day and night temperatures increases with decreasing heliocentric distance. The absolute value of the temperature inside $r_h \approx 2$ AU is controlled by the dust to ice ratio at the surface. Dusty surfaces reach significantly higher temperatures, while icy surfaces use much of the incoming energy for the sublimation process. The absolute temperatures at the surface can therefore not be directly connected to local sublimation rates. The icy fraction area has to be taken into account.

The differences between Figures 4.8 and 4.9 are caused by the smaller rotation period of comet 46P/Wirtanen and the differences in the assumed mean density of the nucleus and in the dust to ice mass ratio. The differences between Figures 4.8 and 4.10 are mainly caused by the assumed tilt of the spin axis versus normal of the orbital plane.

One conclusion that can be drawn concerning the temperatures at the surface is that almost any temperature between 80 K and the black body temperature at the considered heliocentric distance can be computed with the considered range of the free parameters for comet models. The results are principally in agreement with results obtained by e.g. *Enzian et al.* [1999] who derive similar maps of surface temperatures for comet 46P/Wirtanen. They used a different composition of the nucleus, so the absolute values are not directly comparable. The differences can become very large with different model approaches or different parameter settings, as *Huebner et al.* [1999] point out. A direct comparison with other models is therefore expected to result in large differences. The local production rate of a point on the equator, as given in the work of *Huebner et al.* [1999] for reference, can be reproduced with the same order of magnitude. The models discussed in *Huebner et al.* [1999] account for surface evolution which is parameterized in this work. Absolute values are therefore not expected to be exactly reproducible.

The local sublimation rates q_g can be plotted in the same way as the local temperatures. As an example, a result from model M3 is discussed with Figure 4.11. The surface grid is identical to the maps of the temperatures, with the subsolar point at 180° longitude. The heliocentric distance in this example is 2 AU. Figure 4.11 represents the corresponding sublimation rates to the temperatures at 2 AU presented in Figure 4.8. The largest sublimation rates occurring are of the order $q_g \approx 10^{21}$ $\mathrm{m}^{-2}\mathrm{s}^{-1}$ in the subsolar region. Isolines of the gas production rate are not at equidistant levels. The wave-like pattern of the isolines at high latitudes is an artificial effect of the resolution of the grid. The global pattern is comparable to the behavior of the temperatures on the surface, with much larger variations across the surface due to the exponential dependence of the sublimation rate on the temperature. The gas production is slightly asymmetric to the sun direction in accordance with the asymmetric temperature distribution. Concluding can be noted that the gas production is expected to be primarily on the day-side and negligible on the night-side of a cometary nucleus at this heliocentric distance. This is also valid for other heliocentric distances, if the only ice species within the surface layer of the nucleus is water ice, as can be concluded from the presented temperature distributions.

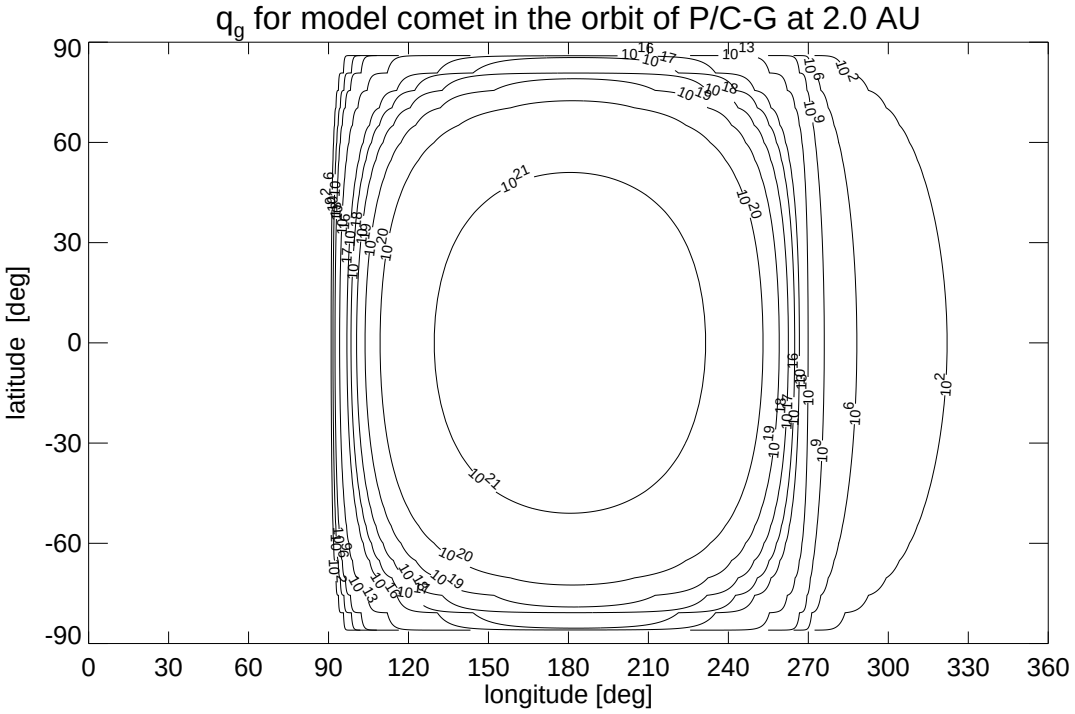

Figure 4.11: *Local gas production rates in $[m^{-2}s^{-1}]$ for model M3*

In conclusion it can be noted that observed gas production rates are reproduced for both comets. The parameter settings required to reproduce observed gas production rates are different for 46P/Wirtanen and 67P/Churyumov-Gerasimenko models. The observed production rates are matched mainly by varying the icy area fraction at the surface. Since the model comets are homogeneous, this variation dims or amplifies the gas production in every surface element. It should be possible to obtain the same result by varying the icy area fraction locally, which would create more or less active area fractions on the surface. An irregularly shaped nucleus could also reduce sublimation rates by shadowing parts of the surface (e.g. *Gutiérrez et al.* [2001]). Other parameters that affect results significantly are the Hertz factor h and the obliquity of the spin axis. The variation of the albedo or the infrared emissivity within reasonable limits has only minor effects on the results. It should be noted that a variation of the albedo has an effect on the estimated size of the nucleus, hence modifying the modeled global gas production rate by modifying the total surface area. This effect has not been studied in detail.

The results indicate a higher abundance of dust on the surface of comet 67P/Churyumov-Gerasimenko which is in accordance with observations. The amount of dust on the surface is expected to vary significantly with heliocentric distance. The icy area fraction in model M3 reaches maximum values of $A_n \approx 0.003$ at perihelion distance.
The large observed gas production rates of 46P/Wirtanen at perihelion distance indicate activity of a large fraction of the surface. A variation with heliocentric distance is also expected at 46P/Wirtanen. Model W2 has a maximum icy area fraction of $A_n \approx 0.24$ at perihelion distance. To obtain gas production rates similar to the maximum of the observed rates, a significantly larger amount of the surface needs to sublimate gas, or additional sublimation from below the surface needs to be assumed.

Gas or dust jets that are observed in the cometary coma seem to indicate inhomogeneities of the sublimation process. These jets can be produced by local active areas due to inhomogeneities at the surface or by an irregular shaped nucleus, as e.g. *Crifo and Rodionov* [1997*a*;*b*] point out. A jet-like feature could also be produced by locally enhancing the quantity of dust grains which are dragged away by the sublimating gas. Model results obtained here do not provide inhomogeneities at the surface that produce any jets. If jets are to be modeled, the dust to ice mass ratio could for example be varied at any surface element which would produce regions of different activity on the surface. This can be done in future work.

The thermal model has also been applied to a model comet in the orbit of 1P/Halley. Results from a model run compared with observed gas production rates are presented in Appendix C. The gas production rates could be reproduced with reasonable parameter settings for comet 1P/Halley.

An improvement concerning the range of the considered parameters can be expected from the ROSETTA mission. The uncertainties concerning the results from thermal models are shared in neutral gas models of the cometary environment when thermal models are used to derive boundary conditions. The calibration of thermal models with observed gas production rates is therefore a reasonable method to derive plausible boundary conditions for the cometary coma.

CHAPTER 5

THE NEUTRAL COMA

In this chapter a model of the neutral gas environment (or *coma*) of the comet is developed and discussed. The gas production of the nucleus is expected to be weak at large heliocentric distances. Collisions between emerging molecules can then be neglected and the evolution of the gas coma can be described as free molecular flow. Collisions between molecules become more and more important when the comet approaches the sun due to larger gas production rates. The gas flow can be described by using hydrodynamic principles when molecular collisions become a dominant process in the coma. The hydrodynamic regime of the coma will be studied in more detail in this chapter, and model results will be discussed. At the inner radial boundary of the hydrodynamic regime, which is located at a distance of a few mean free paths of the emerging gas particles above the surface of the nucleus, physical conditions based on the results from the thermal model of the nucleus are defined. The effect of the hydrodynamic gas flow on the ROSETTA spacecraft will also be studied. The ZEUS code, which has been developed at the Laboratory of Computational Astrophysics at the University of Illinois, is used to model the hydrodynamic part of the neutral gas coma.

5.1 Introduction

The sublimation of gas and the detaching of dust grains from the surface of the comet nucleus results in an emerging flux of neutral particles. The gravitational field of the comet is weak, the gas flux expands almost freely into the ambient space. Neutral molecules become dissociated and ionized and the dust may fragmentate and release trapped volatile components. They also interact with the solar wind. When the outgassing of the nucleus is strong enough, it creates a hydrodynamic regime where collisions between molecules dominate, eventually surrounding the nucleus. The term *collisional coma* is applied in the sense of the importance

of collisions between molecules. The collision dominated part of the coma is, in this work, referred to as the collisional coma.

At the time ROSETTA reaches its target comet the heliocentric distance will be approximately $3-4$ AU. The first aim will be to characterize the nucleus as precisely as possible so that the lander can be deployed successfully. This task will be achieved by mapping the surface with cameras and by determining the gravity field of the nucleus. To map the gravity field, it is important to determine the orbit of the spacecraft around the nucleus to high precision. In order to do so, all perturbing forces have to be evaluated. The orbit of ROSETTA is planned to be in the range of a few kilometer cometocentric distance in early mission phases [*Pätzold et al.*, 2001]. Non-gravitational perturbing forces are e.g. the radiation pressure and drag force due to the emerging gas flux. The latter can be computed from a model of the collisional inner coma. The coma is expected to be mainly collisionless at $3-4$ AU heliocentric distance, although the gas production rate of water and more volatile components is not exactly known. Using results from the thermal model, the water production rate can be estimated to be in the range of $Q_g \approx 10^{25} - 10^{26}$ 1/s for both potential target comets at 3 AU.
The extension of the collisional coma needs to be evaluated in order to obtain a reasonable estimate of the size of the volume that can be modeled with a hydrodynamic approximation. The deviation from a Maxwellian velocity distribution function of the expanding gas increases with decreasing density due to the declining importance of thermalizing collisions. The assumption of a sharp transition from collision dominated regime to free molecular flow yields a rough estimate of the cometocentric distance of this transition. In reality this transition is expected to be more gradual and to depend on the chemical composition of the collisional coma. The justification of the assumption of the dominance of collisions in the modeled volume will be tested a-posteriori with model results. For simplicity, the size of the collision dominated regime R_{HD} is assumed to be quantified by the distance at which the mean free path of the molecules equals their radial distance [*Wallis*, 1974]. Alternate definitions determine the radius of the collisional coma as distance where the probability of an outflowing particle to escape to infinity without another collision is 0.5 or 1 (e.g. *Festou* [1981]; *A'Hearn and Festou* [1990]; *Hodges Jr.* [1990]). This approach leads results of the same order of magnitude, if the outflow velocity is assumed to remain constant [*A'Hearn and Festou*, 1990].
As first order approximation a spherical symmetric coma with radial emerging gas flux, dominated by water vapor, is assumed. The density of the neutral gas n_n can then be written as (neglecting losses caused by ionization) $n_n = Q_g/(4\pi v_n r^2)$, with the radial velocity of the emerging molecules v_n and the cometocentric distance r. Typical velocities v_n measured by GIOTTO at comet 1P/Halley are of the order 1 km/s [*Krankowsky et al.*, 1986]. The velocity is lower closer to the nucleus in the case of an adiabatic spherical expansion. Depending on the temperature of the gas, the modeled velocity has typical values of the order of a few hundred meter per second. For a sketchy estimate of the size of the hydrodynamic regime R_{HD} one can therefore write (e.g. *Wallis* [1974]):

$$R_{HD} = \frac{\sqrt{2}\sigma\, Q_g}{4\,\pi\, v_n} \quad , \tag{5.1}$$

with the collision cross section $\sigma = 5 \times 10^{-19}$ m^2 for water molecules [*Crovisier*, 1984]. With the determined gas production rates of 67P/Churyumov-Gerasimenko or 46P/Wirtanen

at $3-4$ AU (see Section 4.5) and assuming $v_n \approx 500$ m/s, one gets $R_{HD} \approx 1-10$ km. With a gas production of $Q_g \approx 10^{28}$ 1/s for comet 67P/Churyumov-Gerasimenko at perihelion one gets $R_{HD} \approx 1000$ km. It is therefore clear that the size of the part of the coma where a hydrodynamic model can be applied is relatively small at *large* heliocentric distances. Using this model, one can only a-posteriori determine to which cometocentric distance the hydrodynamic approach is correctly applicable, as mentioned above.

The emerging fluid from the nucleus is initially a mixture of gas (containing probably many different species) and dust particles of various sizes. Since the gravity of the nucleus is expected to be negligible, the fluid expands freely into the ambient space, with a velocity that is expected to be close to sound velocity. It is expected that chemical and photo-chemical reactions, dust fragmentation and gas/dust grain interactions are important processes close to the nucleus. As *Crifo* [1991] points out, this regime can be described in hydrodynamic terms as an underexpanded jet. The gradual transition to a collisionless regime, where the distribution function of the gas velocity deviates from the Maxwell-Boltzmann shape, will have effects on the fluid components not to be reproduced in this model.

The shape of the nucleus can also have an effect on the gas flow in the coma, as can be concluded from e.g. *Crifo and Rodionov* [1997*b*]. Since the shape of comets 67P/Churyumov-Gerasimenko and 46P/Wirtanen is not yet known, this effect can be neglected here. The overall appearance of the collisional gas coma is likely not to be predictable to a high accuracy with this model, due to the increasing deviation from the hydrodynamic assumptions that comes with increasing cometocentric distance that is not accounted for. The aim of the model is to evaluate the effects of the gas coma on the radio science experiment (RSI). The strongest effect expected is the drag force due to the combined gas and dust mass flux, which will perturb the orbital motion of the spacecraft and will therefore be directly measurable as Doppler effect on the carrier signal. As long as the orbit is well within R_{HD}, the model can be used to estimate orbit perturbations caused by gas drag.

5.1.1 Composition of the Coma

Since the physical and chemical conditions vary considerably within the coma, measurements of the composition usually face large uncertainties. In-situ measurements by spacecraft provide local quantities at specific times. Even remote measurements usually cover only fractions of the coma and use models to extrapolate the measurements. Some species may not be observable at all by remote techniques due to their spectral emission characteristics, or the resolution constraints of the used instrument.

It becomes evident from many comet observations that the H_2O molecule is the dominant gas species in the inner coma of comets in the inner solar system (e.g. *Shimizu* [1991]). Its relative abundance may change at larger heliocentric distances. A general introduction to the chemistry and solar wind interaction of the coma is provided by e.g. *Huebner et al.* [1991].

At comet 46P/Wirtanen the neutral species $OH, CN, C_3, C_2, NH, NH_2, CS, H$ and O have been observed, with the relative abundance of OH typically 3 to 4 orders of magnitude larger than all other species observed [*Schulz and Schwehm,* 1999]. The same can be concluded from

observations of comet 67P/Churyumov-Gerasimenko , as can be seen from the data base for comet 67P/Churyumov-Gerasimenko provided by the 'Group of Cometary Atmospheres and Extra-Solar Planets' at the DLR[1].
The dust component in the coma is dominating the appearance of remotely observed comets in the visible range. Dust grains are dragged by the gas from the cometary nucleus. The typical size of the grains is assumed to range from $10^{-7} - 10^{-2}$ m. The dust to gas mass ratio is in general estimated to be of the order of unity [*Grün and Jessberger*, 1990].
In the model developed here it is assumed that H_2O is the dominant gas species in the hydrodynamic regime and dust has no significant effect on the gas flow.

5.1.2 Models of the cometary coma

Models of the inner coma differ mainly in the considered processes. The general task is an estimation of the distribution of matter within the coma, the dynamical properties of the constituents, and the chemical composition. A comprehensive coma model, including all relevant physical processes, has not yet been successfully developed. Many published works concentrate on particular details within cometary comae. Some take special care of the interface between nucleus and coma. The sublimating gas is not in thermal equilibrium within a boundary layer, which has to be accounted for by either simplifying assumptions or by modeling these conditions (e.g. *Crifo* [1987]; *Crifo and Rodionov* [1997*a*]; *Skorov and Rickman* [1998; 1999]; *Rodionov et al.* [2002]).
Other models give special attention to the interaction of the gas and the dust component within the cometary coma. Examples can be found in e.g. *Marconi and Mendis* [1983]; *Gombosi et al.* [1985]; *Kitamura* [1986]; *Kömle and Ip* [1987]; *Körösmezey and Gombosi* [1990]; *Sekanina* [1991]; *Crifo et al.* [1995]; *Combi et al.* [1997]; *Müller* [1999].
Chemical reactions of constituent within the coma are considered in greater detail by e.g. *Oppenheimer* [1975]; *Schmidt et al.* [1988], and the interaction with the solar wind is contained in e.g. *Mendis and Houpis* [1982]; *Wegmann et al.* [1987].
The collisionless regime where the hydrodynamic approximation can not be used is modeled by e.g. *Festou* [1981]; *Huebner and Keady* [1984]; *Combi and Smyth* [1988*a*]; *Hodges Jr.* [1990]; *Xie and Mumma* [1996]. A regime where collisions between particles are rare is usually approximated with the so called *Monte-Carlo* models, as discussed in e.g. *Combi and Smyth* [1988*a*].

In this work the collision dominated regime of the inner coma is modeled with a hydrodynamic approximation, as e.g. in *Crifo et al.* [1995]. The aim is an estimation of physical conditions in the collisional coma in order to evaluate effects on the RSI experiment. The model developed here can therefore be assigned to the category of hydrodynamic models with emphasis on the cometary boundary layer, since a thermal model of the nucleus is used to determine boundary conditions at the nucleus-coma interface, and since effects from dust and species other than H_2O are neglected. The details are described in the following sections.

[1] http://berlinadmin.dlr.de/Missions/corot/caesp/comet_db.shtml

5.2 Hydrodynamic Simulation of the Neutral Coma

The procedure applied to model the neutral gas coma is presented in this section. Special attention is given to the interface between results from the thermal model of the nucleus and the inner boundary of the neutral gas coma.

5.2.1 Hydrodynamic Approximation

The velocity distribution becomes a local Maxwellian distribution function, if collisions within the gas are dominant. Due to the fast decrease of the neutral gas density with cometocentric distance, the assumption of local thermal equilibrium of the gas phase becomes critical. The velocity distribution function of the neutral particles within a sphere of radius R_{HD} is assumed to be Maxwellian. The gas can then be described with the macroscopic terms mass density ρ, scalar pressure p and bulk velocity $\mathbf{v}$. The fluid in the coma is assumed to be isentropic and compressible. If one neglects viscosity, thermal conductivity and relaxation effects, the temporal and spatial evolution can be described in the following form of the continuity equations for mass, momentum, and energy, which is also referred to as the 5-moment approximation (e.g. *Schunk* [1977]). The equations of hydrodynamics can then be written as (e.g. *Landau and Lifschitz* [1991]):

$$\frac{\partial \rho}{\partial t} + \nabla \cdot (\rho \mathbf{v}) = Q_\rho \quad , \tag{5.2a}$$

$$\frac{\partial}{\partial t}(\rho \mathbf{v}) + \nabla \cdot (\rho \mathbf{v}\mathbf{v}) + \nabla p + \rho \nabla \Phi = Q_m \quad , \tag{5.2b}$$

$$\frac{\partial}{\partial t}\left(\frac{1}{2}\rho \mathbf{v}^2 + \rho\varepsilon\right) + \nabla \cdot \left[\rho \mathbf{v}\left(\frac{v^2}{2} + w\right)\right] = Q_e \quad , \tag{5.2c}$$

with the gravitational potential Φ, the specific internal energy ε, and the specific enthalpy $w = \varepsilon + pV = \varepsilon + p/\rho$. The inhomogeneous terms are source/sink terms for mass (Q_ρ), momentum (Q_m) and energy (Q_e). The first term in brackets on the left-hand side of Equation (5.2c) is the energy per unit volume for a volume element of the considered fluid as sum of the kinetic energy and internal energy density (per unit volume) $e = \rho\varepsilon$.
The inhomogeneity terms might be due to e.g. condensation or vaporization of grains (Q_ρ), radiation pressure or gas to dust momentum transfer (Q_m), also to photolytic heating, radiative cooling or gas to dust energy transfer (Q_e) (e.g. *A'Hearn and Festou* [1990]; *Gombosi* [1991]). Equations (5.2) are simplified in this work by neglecting these inhomogeneous terms. The gas flux is assumed to be adiabatic and the dust component and effects from solar radiation are neglected for simplicity. The gas component within the coma is expected to have a larger effect on the spacecraft than the dust due to low relative velocities. A distributed source of gas from grains within the coma that include volatile elements is also neglected. The photodissociation of water molecules is expected to be the major external energy source in the innermost coma [*Gombosi*, 1991]. The photodissociation rate for water molecules is of the order of 10^{-5} 1/s (see Table 6.1). The scale length for photodissociation then is $L_{pd} = v_n / I_{pd} \approx 5 \times 10^4$ km, when the mean radial velocity of the particles is assumed to be 500 m/s. This is at least one order of magnitude larger than the range to which the hydrodynamic approximation is applied at comets 46P/Wirtanen or 67P/Churyumov-Gerasimenko

(see Section 5.1). It is therefore sustainable to neglect the energy source term. A set of coupled hyperbolic partial differential equations has now to be solved. The hyperbolic character of the equations allows discontinuous solutions, such as e.g. shocks.

5.2.2 The ZEUS Code

The ZEUS code has been developed as magneto-hydrodynamical (MHD) code for astrophysical purposes at the Laboratory of Computational Astrophysics, National Center for Supercomputing Applications, University of Illinois. The three-dimensional version ZEUS-3D, which is an ideal (non-resistive, non-viscous, adiabatic, non-relativistic) MHD equation solver, using the method of finite differences, is applied in this work. ZEUS allows explicitly to reduce the code to hydrodynamic equations by excluding all terms that involve magnetic fields, making the code also efficient for HD applications. An introduction to the two-dimensional version and studied test cases are provided by *Stone and Norman* [1992]. The coupled partial differential equations of hydrodynamics solved by the ZEUS code are:

$$\frac{\partial \rho}{\partial t} + \nabla \cdot (\rho \mathbf{v}) = 0 \quad , \tag{5.3a}$$

$$\frac{\partial}{\partial t}(\rho \mathbf{v}) + \nabla \cdot (\rho \mathbf{v}\mathbf{v}) + \nabla p + \rho \nabla \Phi = 0 \quad , \tag{5.3b}$$

$$\frac{\partial e}{\partial t} + \nabla \cdot e\mathbf{v} = -p \nabla \mathbf{v} \quad . \tag{5.3c}$$

These equations correspond to Equations (5.2) when neglecting the inhomogeneous terms and when assuming the gas flow in the coma to be adiabatic. An internal energy equation (5.3c) is applied instead of the conservation law for the total energy, which improves the accuracy of the code for supersonic flows [*Stone and Norman*, 1992].
Gravitational effects in the collisional coma are neglected and the set of equations is closed with the ideal gas law. For an ideal gas with constant specific heat, one has:

$$p = n\, k_B\, T \;, \qquad e = \frac{1}{\gamma - 1}\, p \quad , \tag{5.4}$$

with the number density n, the Boltzmann constant k_B, the ratio of specific heats γ, and the internal energy density e.

Spherical coordinates are used in the model calculations. The applied grid usually has a resolution of $34 \times 72 \times 100$ grid points (latitude x longitude x radial distance) plus additional ghost zones, which are needed to apply the boundary conditions correctly. In some cases a resolution of $86 \times 179 \times 100$ was used. The surface grid points are equidistant, the grid is *ratioed* in radial direction, with each zone growing by $2-5$ % of the previous inner zone.

The second-order accurate *van Leer*-method is applied as interpolation scheme in this work. This scheme uses a piecewise linear function to represent the distribution of a quantity within a zone. It has improved accuracy when compared with the first-order accurate donor-cell scheme, and does not consume as much CPU time as the piecewise parabolic advection (PPA) scheme, which is third-order accurate [*Stone and Norman*, 1992].

An artificial viscosity is included in the simulation in order to provide correct jump conditions and shock velocities at shocks within the computed domain. The approach of *von Neumann and Richtmyer* as described in *Stone and Norman* [1992] is applied. Coefficients of viscosity are defined in each direction and a separate scalar artificial pressure is defined in each step.

5.2.3 Boundary Conditions

The gas emerging from the surface of the nucleus is initially not in thermal equilibrium. The velocity distribution does not obey a Maxwell distribution function. The inner radial boundary of the hydrodynamic regime of the coma is therefore not the nucleus itself, but is located at a distance of a few mean free paths of the emerging molecules above the surface where a Maxwellian velocity distribution is established. The outer boundary in radial direction is nominally located at the distance where the mean free path of the molecules becomes larger than the radial distance. This boundary is estimated to be at the radial distance R_{HD} (see Equation (5.1)).
The applicability of the hydrodynamic approach within this region can only be confirmed a-posteriori, when the local number density in each modeled volume is known. The applied spherical coordinate system has its origin in the center of the nucleus, zero degree longitude in anti-solar direction, and zero degree latitude at the north pole. In this work, only cases where the spin axis of the nucleus is parallel to the normal of the orbital plane of the comet are studied.
The boundary of the grid in longitudinal direction is set to periodic boundary conditions. Since the polar regions are problematic to model with a spherical coordinate system, a cone with an aperture angle of 5° at each pole is cut out of the model volume, and outflowing boundary conditions at the cone are assigned (following e.g. *Crifo and Rodionov* [1997*a*]).

Outflowing boundary conditions are applied for the outer radial boundary. The values at the inner radial boundary (inflowing boundary conditions) are derived from the results of the thermal model of the comet nucleus. The values are not transferred directly, but with a correction that is due to the conditions in the near-surface boundary layer. Within this boundary layer, which is expected to have the thickness of a few lengths of the mean free path of the emerging molecules, the gas flux is best described in the Knudsen regime. *Skorov and Rickman* [1998; 1999] have modeled this Knudsen layer with a Monte Carlo type method. They use the following relations for a single species fluid, corresponding to earlier applications by e.g. *Crifo* [1987]; *Crifo and Rodionov* [1997*a*]:

$$\sqrt{\frac{T_g}{T_s}} = \sqrt{1+\left(\frac{S\sqrt{\pi}}{2}\,\frac{\gamma-1}{\gamma+1}\right)^2} - \frac{S\sqrt{\pi}}{2}\,\frac{\gamma-1}{\gamma+1} \quad , \tag{5.5a}$$

$$\frac{p_g}{p_r} = \frac{1}{2} - S\sqrt{\frac{T_g}{\pi\,T_s}} + \left[\left(S^2+\frac{1}{2}\right)\sqrt{\frac{T_g}{T_s}} - \frac{S\sqrt{\pi}}{2}\right]\,\mathrm{erfc}(S)\,\exp\left(S^2\right) \quad , \tag{5.5b}$$

where the subscript g indicates values at the inner boundary of the hydrodynamic regime, T_s is the temperature at the surface of the nucleus, p_r is a convenient reference pressure at the surface [*Crifo*, 1987], and where erfc is the error function. $S = M\sqrt{\gamma/2}$ is a dimensionless

speed, with the Mach number M and the heat capacity ratio of the molecules γ. The assumption of a constant γ implies rotational modes of the H_2O molecule to be in local thermal equilibrium and vibrational modes to be unexcited (e.g. *Crifo and Rodionov* [1999]). A different treatment would require a treatment of radiative transfer within the coma, the effect on the thermodynamics of the collisional inner coma is expected to be minor [*Crovisier*, 1984]. Using the saturation pressure p_s (Equation (4.13)) as reference pressure p_r in Equation (5.5b) would imply a surface of plain ice (e.g. *Crifo* [1987]; *Crifo and Rodionov* [1997*a*]). This overestimates the density and the pressure of the coma gas in the case of a dust-ice mixture at the surface. In this case only a fraction of each surface element contains ice available for sublimation. The local icy area fraction A_0 (Equation (4.6)) is used to determine the reference pressure at the surface as $p_r = A_0\ p_s$.

The dust component can 'mass load' the gas phase by fragmentation or by releasing initially trapped volatiles, hence delay the transition to sonic velocities and increase the lateral flow of the gas [*Keller et al.*, 1990]. Such effects are neglected in this work for simplicity.
A numerical model of the non-equilibrium layer above a plane surface of water ice by *Skorov and Rickman* [1998] implies a maxwellization of the gas flow within a range of about $10-12$ mean free paths. The derived relations between the macroparameters of the flow at this distance are:

$$\frac{T_g}{T_s} \approx 0.6 \quad \frac{p_g}{P_r} \approx 0.2\ . \tag{5.6}$$

The derived local Mach number is $M \approx 1.2$. These values are adopted when determining the boundary conditions at the inner radial boundary in the model developed here. The assigned positions of the one-dimensional thermal models at the surface of the nucleus are located at the same latitude and longitude as the grid points of the inner radial boundary of the coma model.

5.2.4 Non-Gravitational Forces acting on ROSETTA

Effects of solar radiation pressure and gas drag force acting on the spacecraft are discussed in this section. These effects are expected to be the most important non-gravitational forces on a spacecraft in low orbit (with a low relative velocity to the comet). Additional effects, e.g. due to thermal radiation from the comet, scattered radiation from within the coma, reflected radiation from the nucleus, or dust mass flux are not considered here.
The orbit perturbation of a spacecraft caused by gas drag is difficult to model in great detail, since the interaction of the gas particles varies with different spacecraft surfaces. The varying orientation of the spacecraft with respect to the gas flux has also to be taken into account [*Montenbruck and Gill*, 2000]. The interaction is simplified in this work by assuming an average drag coefficient for the whole spacecraft. The drag force is directed mainly in radial direction due to the radial outgassing of the comet. Since the orbital velocity of the spacecraft is expected to be significant less than 1 m/s for an orbital radius of less than 10 km (e.g. *Pätzold et al.* [2001]), the velocity of the spacecraft can be neglected here. The acceleration of the spacecraft due to gas drag a_{drag} can then be estimated as [*Montenbruck and Gill*, 2000]:

$$a_{\mathrm{drag}} = \frac{1}{2}\, C_D \frac{A_{sc}}{m_{sc}} \rho v^2 \mathbf{e}_v\ , \tag{5.7}$$

with the drag coefficient C_D, the total cross sectional area of the spacecraft A_{sc}, the mass of the spacecraft m_{sc}, the velocity of the gas v and the direction vector of the velocity $\mathbf{e}_v = \mathbf{v}/v$, which is directed mainly radially away from the nucleus. The drag coefficient C_D is dimensionless and describes the interaction of the gas with the surface material of the spacecraft. For free molecular flow conditions (when the mean free path of particles is much larger than the dimension of the spacecraft), typical values of C_D range from $1.5-3.0$. In the case of continuum flow C_D is reduced to about unity [*Montenbruck and Gill*, 2000]. The value $C_D = 1$ is assumed in this work, since orbital distances of a few kilometer are considered, where the mean free path of the particles is about or less than the scale size of the spacecraft. The cross sectional area of the spacecraft is $A_{sc} \approx 70$ m^2 (see Section 2.1), with solar panels of ≈ 34 m^2. The launch mass of the spacecraft will be $m_{sc} \approx 2900$kg. The mass is reduced to $m_{sc} \approx 2000$ kg by the time ROSETTA reaches the comet. A mass of $m_{sc} = 2000$ kg is assumed for estimates of the non-gravitational forces acting on ROSETTA.

The magnitude of orbit perturbations caused by gas drag is compared with perturbations due to solar radiation pressure. The solar radiation pressure is determined by the energy of the solar flux Φ that passes through an area per unit time. Hence, the solar radiation pressure acting on a satellite is $P = \Phi/c$ with the velocity of light c, if it is assumed that the surface of the satellite absorbs all incoming photons. With $\Phi = S_0$ at 1 AU and $S_0 = 1367$ W/m^2 (see Appendix A) $P_\odot$ is defined as the solar radiation pressure at 1 AU:

$$P_\odot \;=\; \frac{S_0}{c} \;\approx 4.56 \times 10^{-6} [\mathrm{N/m^2}] \;\; . \tag{5.8}$$

However, in reality the incoming radiation is partly absorbed and partly reflected. When assuming that the solar panels of the spacecraft are always directed towards the sun, the acceleration $a_\odot$ of the spacecraft can be determined as [*Montenbruck and Gill*, 2000]:

$$a_\odot \;=\; -P_\odot \, C_R \, \frac{A_{sc}}{m_{sc}} \left(\frac{r_0}{r_h} \right)^2 \;\; , \tag{5.9}$$

with $r_0 = 1$ AU, and the heliocentric distance of the spacecraft r_h in AU. The radiation pressure coefficient C_R depends on the material and is derived from $C_R = 1 + \varepsilon$, with the reflectivity ε. The reflectivity of solar panels is given as $\varepsilon = 0.21$, the reflectivity of e.g. a high-gain antenna as $\varepsilon = 0.30$ [*Montenbruck and Gill*, 2000]. When determining the acceleration due to solar radiation, a total cross sectional area of 70 m^2 and a radiation pressure coefficient of $C_R = 1.21$ is assumed in this work to keep calculations simple.

The resulting acceleration of ROSETTA in the considered range of heliocentric distances is plotted in Figure 5.1. The absolute value around the perihelion distance of

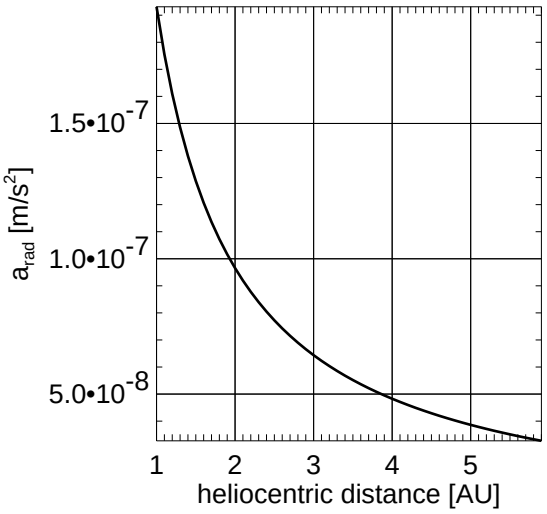

Figure 5.1: *Acceleration of* ROSETTA *due to solar radiation pressure in the range* $1-6$ *AU.*

comets 67P/Churyumov-Gerasimenko or 46P/Wirtanen is slightly underestimated due to the assumption of a constant mass of the spacecraft. The variation shown in Figure 5.1 is controlled by the inverse square dependency on the heliocentric distance.

5.3 Results

Results from the hydrodynamic model and the implied effects on a spacecraft in low orbit around the comet are presented here. Many model runs were carried out for comet 46P/Wirtanen before the postponement of the ROSETTA mission in January 2003. However, since the conditions at the surface of 67P/Churyumov-Gerasimenko and 46P/Wirtanen do not differ too much at a certain heliocentric distance (see Section 4.5), the results for the coma are comparable. Probably the most important difference is the smaller size of the nucleus of 46P/Wirtanen. Since the gas production rate of both comets has about the same order of magnitude at a particular heliocentric distance, the number density of the gas close to the surface is larger for comet 46P/Wirtanen if a spherically symmetric coma is assumed. If the estimate of the sizes of the nuclei of 67P/Churyumov-Gerasimenko and 46P/Wirtanen is correct, it can be inferred that the amount of ice available for sublimation must be significantly smaller at comet 67P/Churyumov-Gerasimenko.
Two different cases are presented here: Case 1 is a model of the coma of 67P/Churyumov-Gerasimenko at 3 AU heliocentric distance. It is assumed that H_2O is the only ice component in the surface layer. The day-side of the nucleus then strongly dominates the gas production as results of the thermal model show. In case 2 the coma of 46P/Wirtanen is modeled at a heliocentric distance of 2 AU. An additional constant source of gas is added to the H_2O sublimation, accounting for possible more volatile species sublimating from deeper layers at a constant rate. All computations are terminated when a steady state within the modeled volume is established. Additional case studies of 67P/Churyumov-Gerasimenko and 46P/Wirtanen at their respective perihelion distance are added in Appendix D.

5.3.1 Case 1: H_2O Sublimation at 3 AU, 67P/C-G

Results from model M3 of the thermal model of the cometary nucleus are used to derive the physical conditions at the inner radial boundary (see Table 4.4 and Figures 4.8). The initial state of the coma is a spherically symmetric thin gas distribution that decreases with the inverse square of the cometocentric distance. The initial velocity is purely radial at the speed of sound. The computed volume is a sphere with a radius of 20 km centered on the cometary nucleus, excluding the polar cones. Results are provided on a grid of $100 \times 36 \times 72$ (r, θ, ϕ) points. Sublimation is assumed to be controlled by H_2O as the only ice component in the dust-ice mixture at the surface. The sublimation is dominant on the day-side of the nucleus and yields a collisional coma restricted to the day-side part of the coma. For simplicity, results in the equatorial plane of the comet are discussed. The spin axis of the comet is assumed to be perpendicular to the orbital plane of 67P/Churyumov-Gerasimenko, the equatorial plane therefore coincides with the orbital plane of the comet.

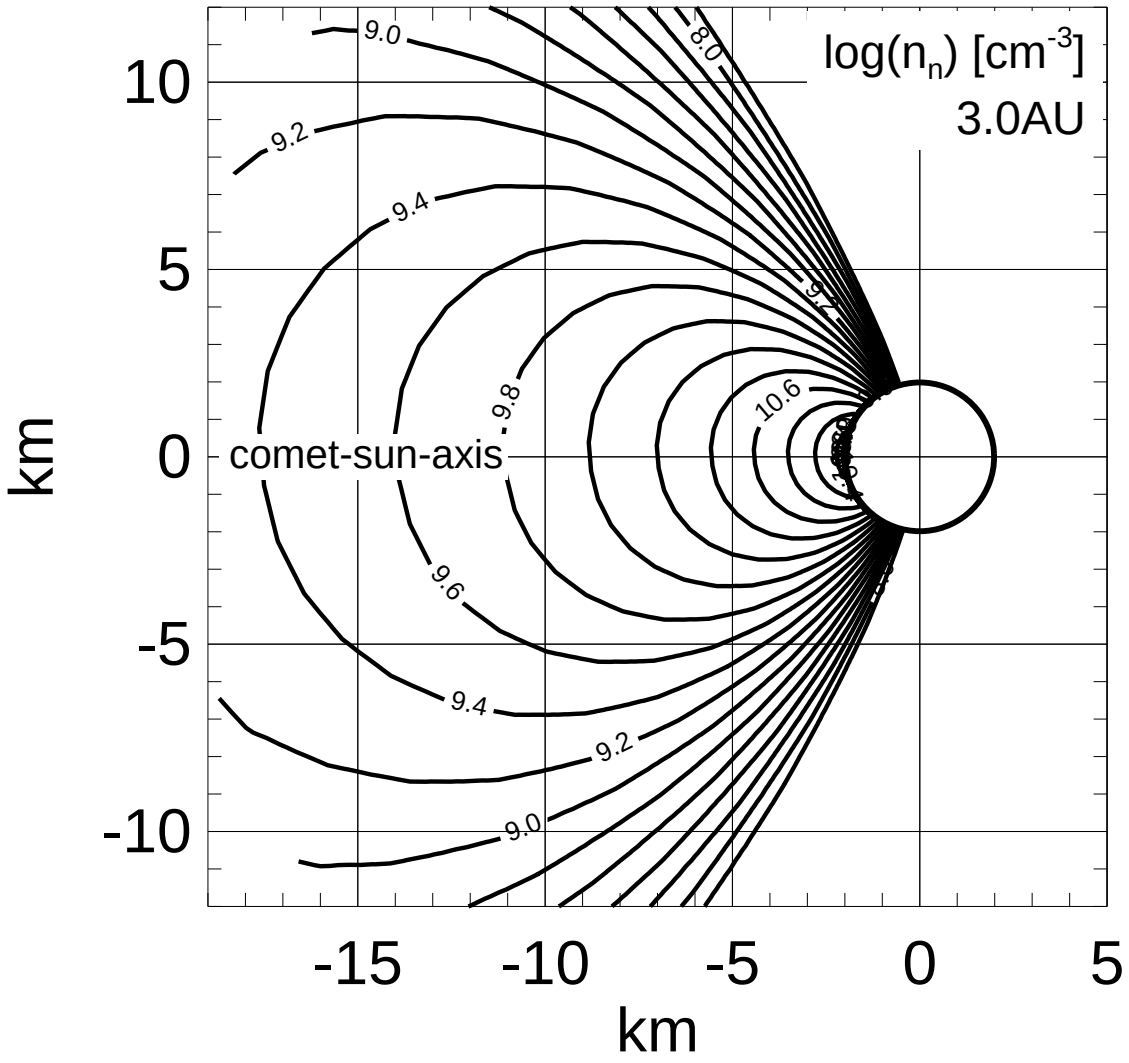

Figure 5.2: *Number density n_n [cm^{-3}] of the neutral gas in the equatorial plane, logarithmically scaled. Isolines indicate the distribution of the number density at levels spaced by an uniformly distance of* 0.2*. Exemplary result for 67P/Churyumov-Gerasimenko at* 3 *AU.*

In Figure 5.2 the resulting number density in the equatorial plane is plotted for a heliocentric distance of 3 AU. At this heliocentric distance the ROSETTA mission is expected to have started scientific operations. The sun is on the left-hand side of the picture. The spin of the comet nucleus is anti clockwise, the terminator (the plane perpendicular to the comet-sun axis that includes the center of the comet) is perpendicular to the plotted plane in *north-south* direction. The highest number densities ($n_n \approx 1.9 \times 10^{11}\mathrm{cm}^{-3}$) occur close to the surface in the subsolar region. The low number densities on the night-side of the comet in this example yield a deviation from the assumption that this region is collision dominated. The strong decrease of the local sublimation rate in the terminator region with increasing longitudinal and latitudinal distance from the subsolar point results in a discontinuous transition to the night-side coma. The resulting radial flow of the neutral gas is comparable to a jet with a very wide aperture angle. The size of the hydrodynamic regime is estimated to be of

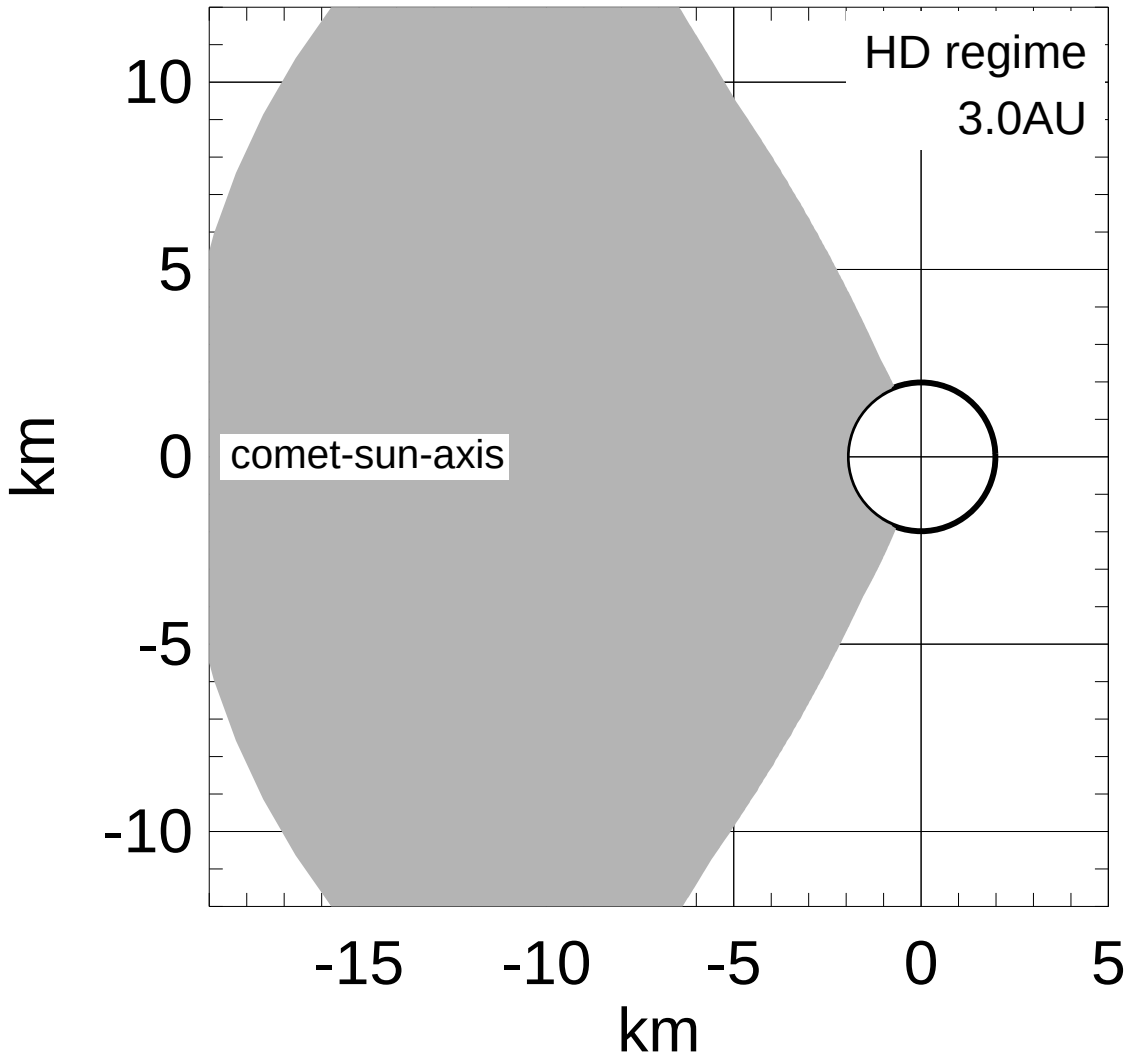

Figure 5.3: *Extent of the collisional coma in the equatorial plane. The shaded area is dominated by collisions. Collisions are negligible in the night-side coma. Exemplary result for 67P/Churyumov-Gerasimenko at* 3 *AU.*

the order $R_{HD} \approx 1 - 10$ km (see Equation (5.1)) for a spherically symmetric neutral coma of 67P/Churyumov-Gerasimenko at a distance of 3 AU from the sun. The approximately axial-symmetry of the sublimation process with respect to the comet-sun axis yields a similar distribution of the number density of the gas particles on the day-side of the collisional coma. A better resolution of the grid in the terminator region might produce different results, because the transition from day-side to night-side conditions would become more gradual. Gas flux from the day-side to the night-side coma would probably arise.

The respective mean free path of the particles within the modeled volume can be determined with the knowledge of the distribution of the number density. The shaded area in Figure 5.3 indicates the extent of the hydrodynamic regime for this particular scenario at 3 AU heliocentric distance. The mean free path of the particles at the boundary of the shaded area equals their cometocentric distance. The collision dominated regime does not enclose the

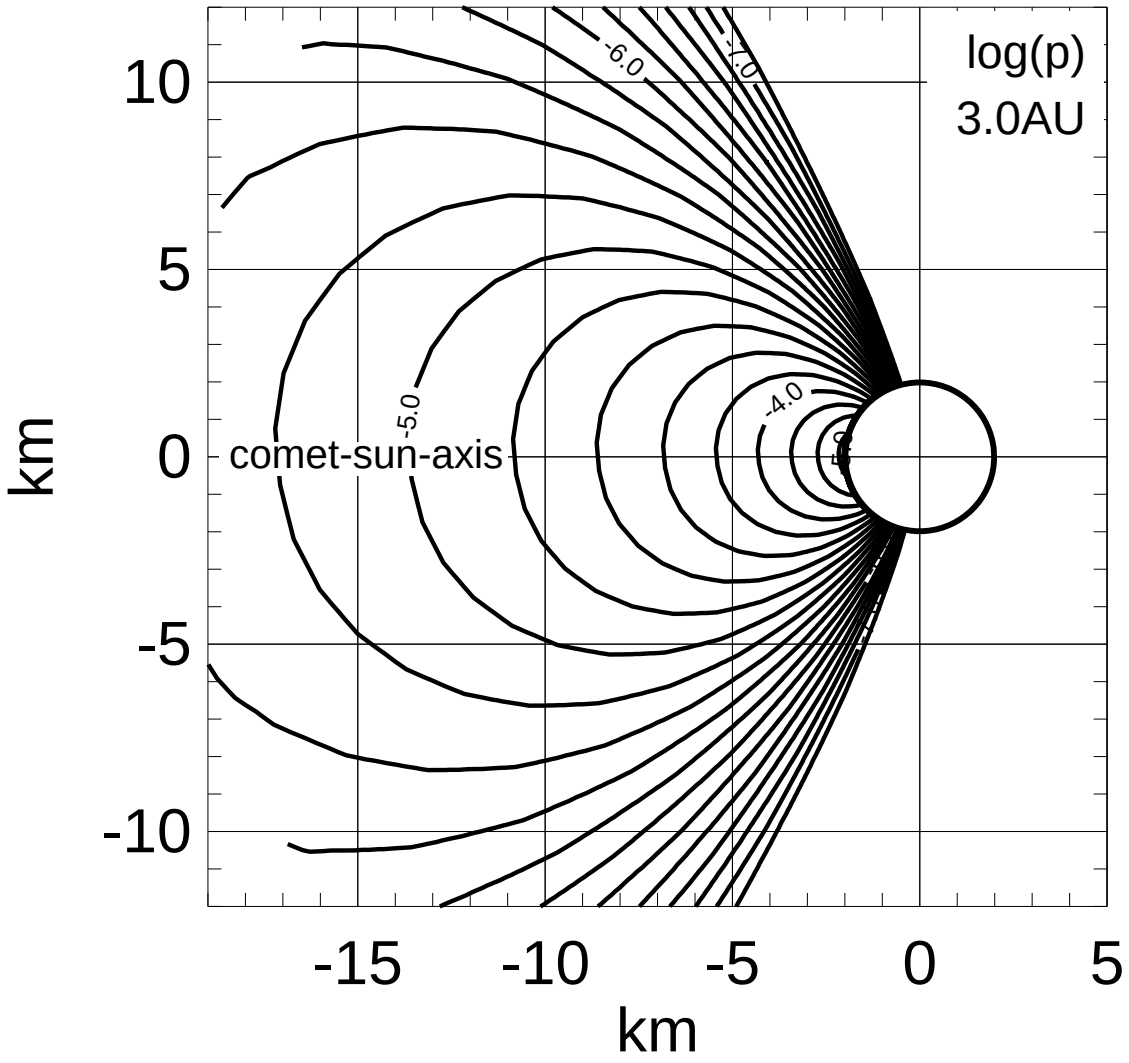

Figure 5.4: *Gas pressure p [Pa] in the equatorial plane, logarithmically scaled. Exemplary result for 67P/Churyumov-Gerasimenko at* 3 *AU.*

whole cometary nucleus. It is restricted to the day-side neutral coma and has a size of a few kilometers. Its outer radial boundary is not resolved with this model due to the restriction to 20 km around the nucleus. The outer radial boundary of the modeled volume is visible in the corners on the left-hand side of Figure 5.3. The model results are not reliable outside the hydrodynamic regime. Conclusions from this model, such as the acceleration of a spacecraft due to gas drag, can therefore refer only to the day-side part of the coma.

In Figure 5.4 isolines of the logarithmically scaled pressure in the equatorial plane at 3 AU heliocentric distance are plotted. The pattern corresponds in principle to the distribution of the number density, as expected. The highest values of the pressure ($p_{\max} \approx 4.5 \times 10^{-4}$ Pa) appear in the subsolar region close to the surface. The variation of the pressure is almost symmetric to the comet-sun axis. The difference between the transition to the night-side from local morning (upper part) and local evening (lower part) is not resolved in this plot.

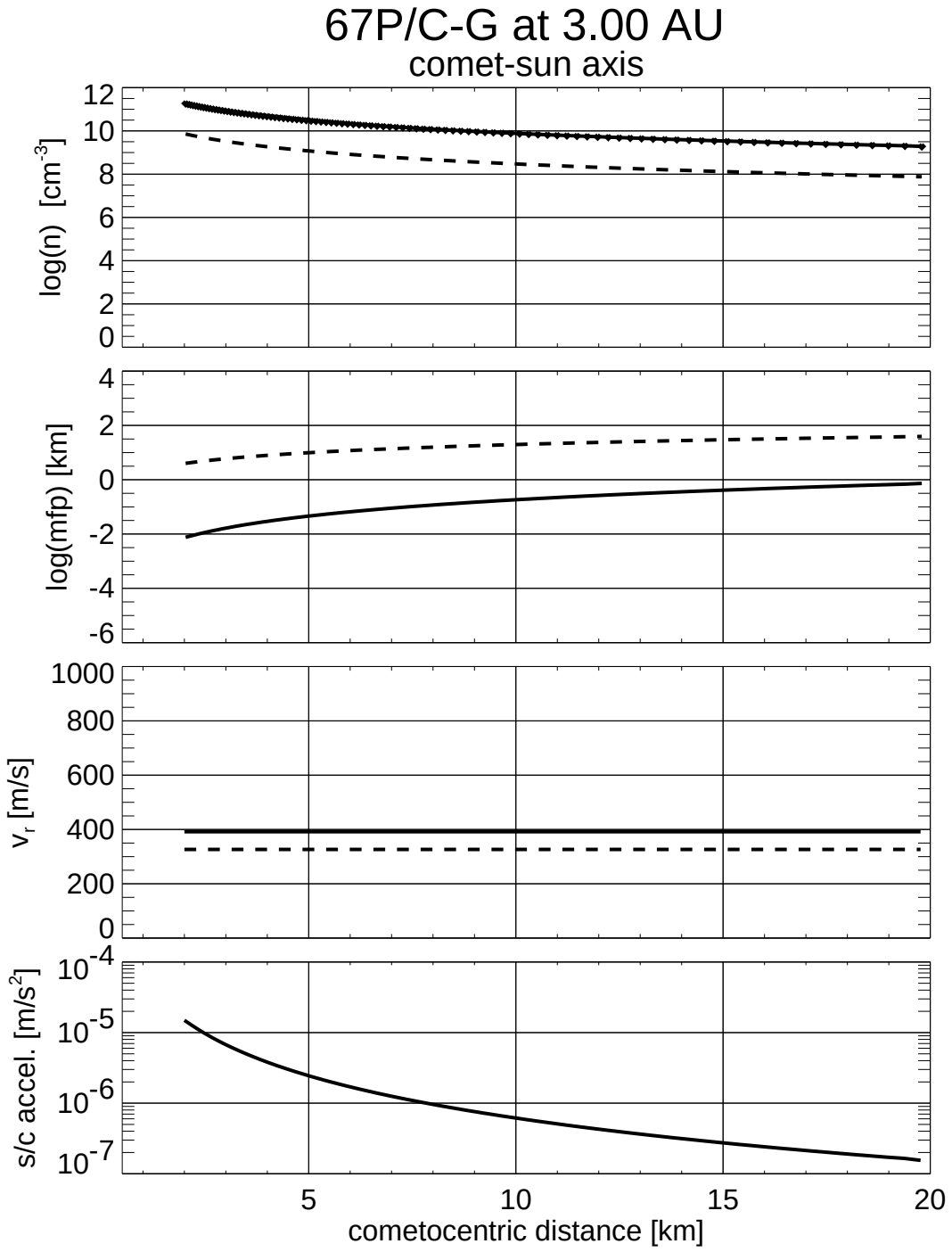

Figure 5.5: *Radial profile at the comet-sun axis of the logarithmically scaled number density n_n and the mean free path (mfp) of particles, the radial velocity v_r and the resulting acceleration of the spacecraft. Exemplary result at a heliocentric distance of* 3 *AU.*

In order to estimate the effects of the coma on a spacecraft at the model comet, the physical conditions along the comet-sun axis are studied. Profiles of the number density, the mean free path, the radial velocity and the resulting acceleration of an orbiting spacecraft with the specifications of the ROSETTA probe that crosses the comet-sun axis are plotted in Figure 5.5. The number density and the mean free path are logarithmically scaled. The dots on the line of the number density indicate the position of the modeled cells.
Several quantities are included in Figure 5.5, making a comparison more convenient. The corresponding number density of a spherical symmetric coma with an equal gas production

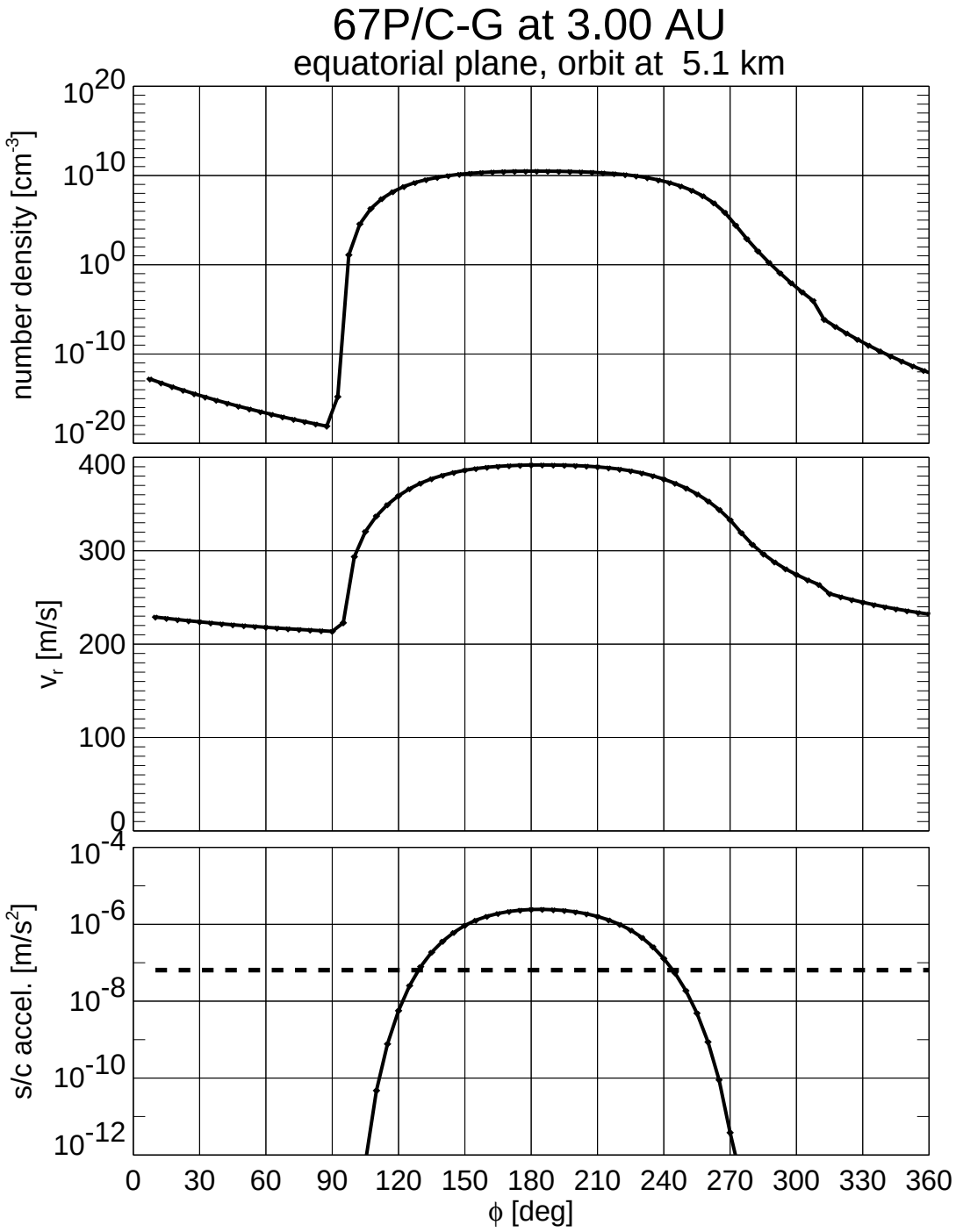

Figure 5.6: *Profile of the number density n_n, radial velocity v_r and the resulting acceleration of a spacecraft with an orbital distance of* 5 *km. Exemplary result at a heliocentric distance of* 3 *AU.*

rate is plotted with a dashed line on the panel of the number density. The number density at the comet-sun axis of the model comet is significantly higher due to the sublimation limited to the day-side part of the nucleus. Only about a quarter of the surface contributes significantly to the gas production of the nucleus (see e.g. 4.11). The variation with cometocentric distance indicates an inverse square dependency of the neutral gas number density. Gas number densities that locally match a dependency with the inverse square on the cometocentric distance are therefore not necessarily the result of a spherically symmetric sublimation process.

The dashed line in the panel of the mean free path in Figure 5.5 indicates the corresponding

cometocentric distance. The intersection of these lines would indicate the outer boundary of the collision dominated hydrodynamic regime. In the case studied here this boundary is outside the modeled range of the comet-sun axis.
The panel of the radial velocity includes the corresponding sound velocity, indicated by the dashed line. It can be concluded that the gas expansion remains supersonic throughout the collisional coma. The resulting acceleration of a spacecraft that crosses the comet-sun axis is plotted in the lowest panel in Figure 5.5. The model results yield a maximum acceleration of $a_{\text{drag}} \approx 10^{-5}$ m/s^2 close to the nucleus.

The physical conditions for a spacecraft with an orbital distance of 5.1 km are plotted in Figure 5.6. The subsolar point is at 180° longitude (Φ), local sunrise at $\Phi = 90°$ and local sunset at $\Phi = 270°$. The dominant feature is the difference between day and night. The number density is plotted in the top panel. The right-hand side of the panel (local afternoon and evening) reflects the decrease of the sublimation rate with decreasing surface temperatures (see Section 4.5). The steep increase of the number density at $\Phi = 90°$ corresponds to the steep rise of the surface temperature at local sunrise on the nucleus. The kink in the line at $\Phi \approx 310°$ corresponds to the actual boundary of the modeled surface, as stored for this particular heliocentric distance (see Section 4.3.5 for details).

The radial velocity component at the orbital distance is plotted in the second panel. The variation of the velocity between day and night is the result of the initialization with constant Mach number, hence depending on the temperature distribution on the surface.

The resulting acceleration of a spacecraft orbiting at a cometocentric distance of 5.1 km is plotted in the third panel. The dashed line indicates the acceleration due to solar radiation pressure at 3 AU heliocentric distance. The spacecraft is assumed to have a cross section of 70 m^2 and a mass of 2000 kg. The resulting acceleration due to solar radiation pressure is 6.4×10^{-8} m/s^2 (see Equation (5.9)). The acceleration due to gas drag is larger in the subsolar region of the orbit and much lower in the night side coma. In the subsolar region the forces are acting in opposite directions. These non-gravitational forces have to be considered from two points of view. The stability of the orbit is not only interesting for exact measurements from the instruments, but also for the safety of the ROSETTA mission (see e.g. *Schwinger* [2001]). Also, effects of the second order gravity coefficient can be weaker than the acceleration due to non-gravitational forces for orbital distances larger than $r \approx 5$km (e.g. *Pätzold et al.* [2001]). The gravity mapping campaign therefore needs a good estimate of the non-gravitational forces to optimize the orbital strategy.

5.3.2 Case 2: Strong Sublimation at 2 AU, 46P/Wirtanen

Comet 46P/Wirtanen at a heliocentric distance of 2 AU is modeled in this second scenario. The H_2O gas production rate as computed in the thermal model W2 is used to determine the conditions at the inner radial boundary of the coma model, with a global gas production rate of $Q_g \approx 10^{27}$1/s. A constant spherically symmetric gas production of 10^{26}1/s is added in order to account for possible more volatile species producing gas from a sublimation front below the surface. This magnitude of gas production was proposed by e.g. *Enzian et al.* [1999]

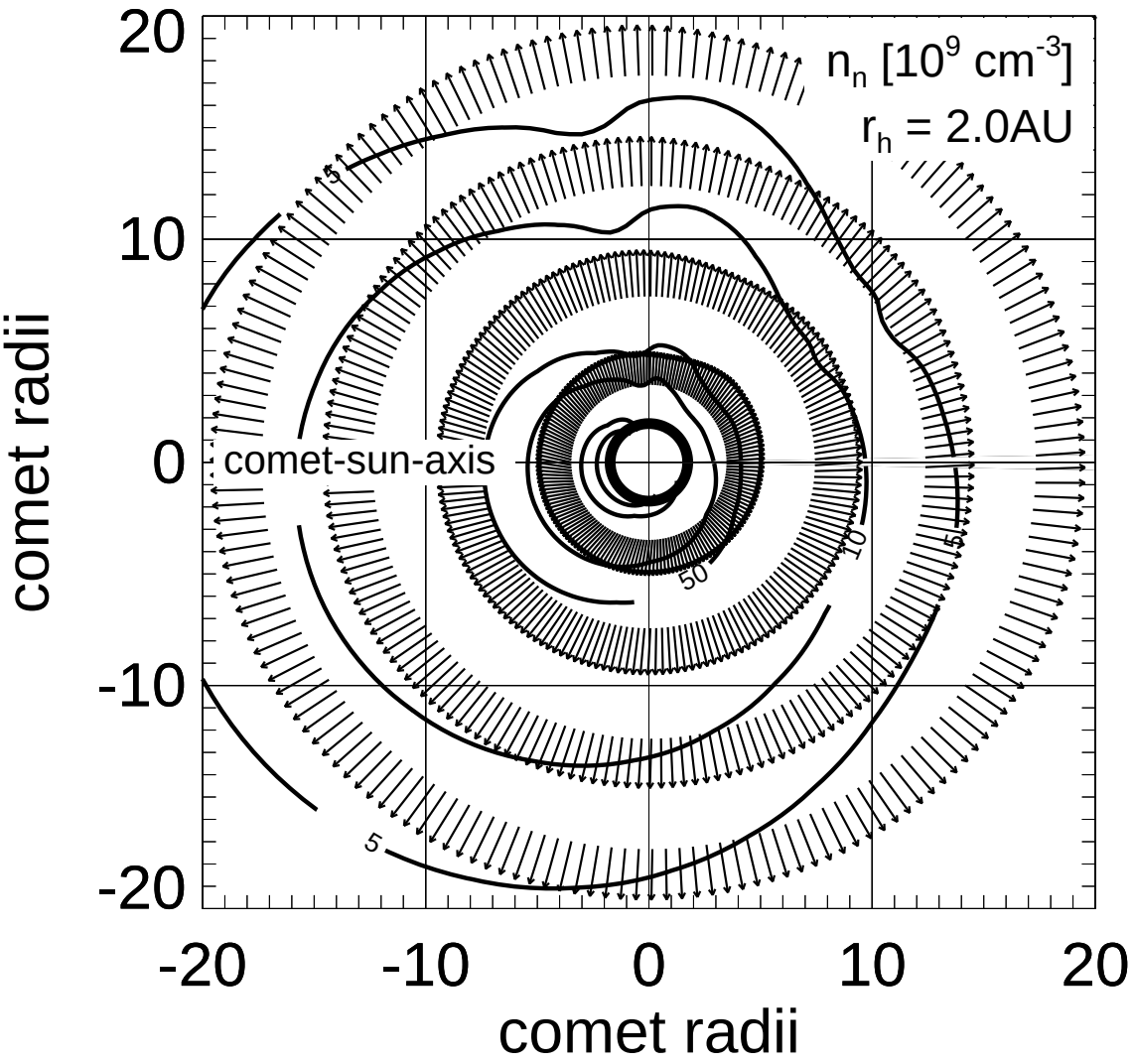

Figure 5.7: *Isolines of the number density n_n in $[10^9 cm^{-3}]$ of the neutral gas at levels* $1, 5, 10, 50, 100, 500, 1000$. *Velocities are projected in the equatorial plane. The respective length of the plotted arrows indicates the velocity in units of (km/s)*$\times 4$. *Exemplary result for 46P/Wirtanen at* 2 *AU.*

for the production of carbon-monoxide for a model comet in the orbit of 46P/Wirtanen. The initial state of the coma is a thin spherically symmetric density distribution with a constant radial expansion velocity. The outer radial boundary of the modeled volume is at 100 comet radii.

In Figure 5.7 the number density of the neutral gas and velocity vectors of the gas in the equatorial plane within 20 comet radii are plotted. Isolines of the number density n_n in units $10^9 \mathrm{cm}^{-3}$ are plotted. The vectors of the velocities are projected in the equatorial plane. The overall appearance of the number density is almost spherically symmetric, but not centered on the origin of the cometocentric coordinate system. The center of this distribution has a slight offset in the sun direction. This is a result of the stronger outgassing of the comet in sun direction. The velocity field is almost radial. A slight tendency towards the point of local

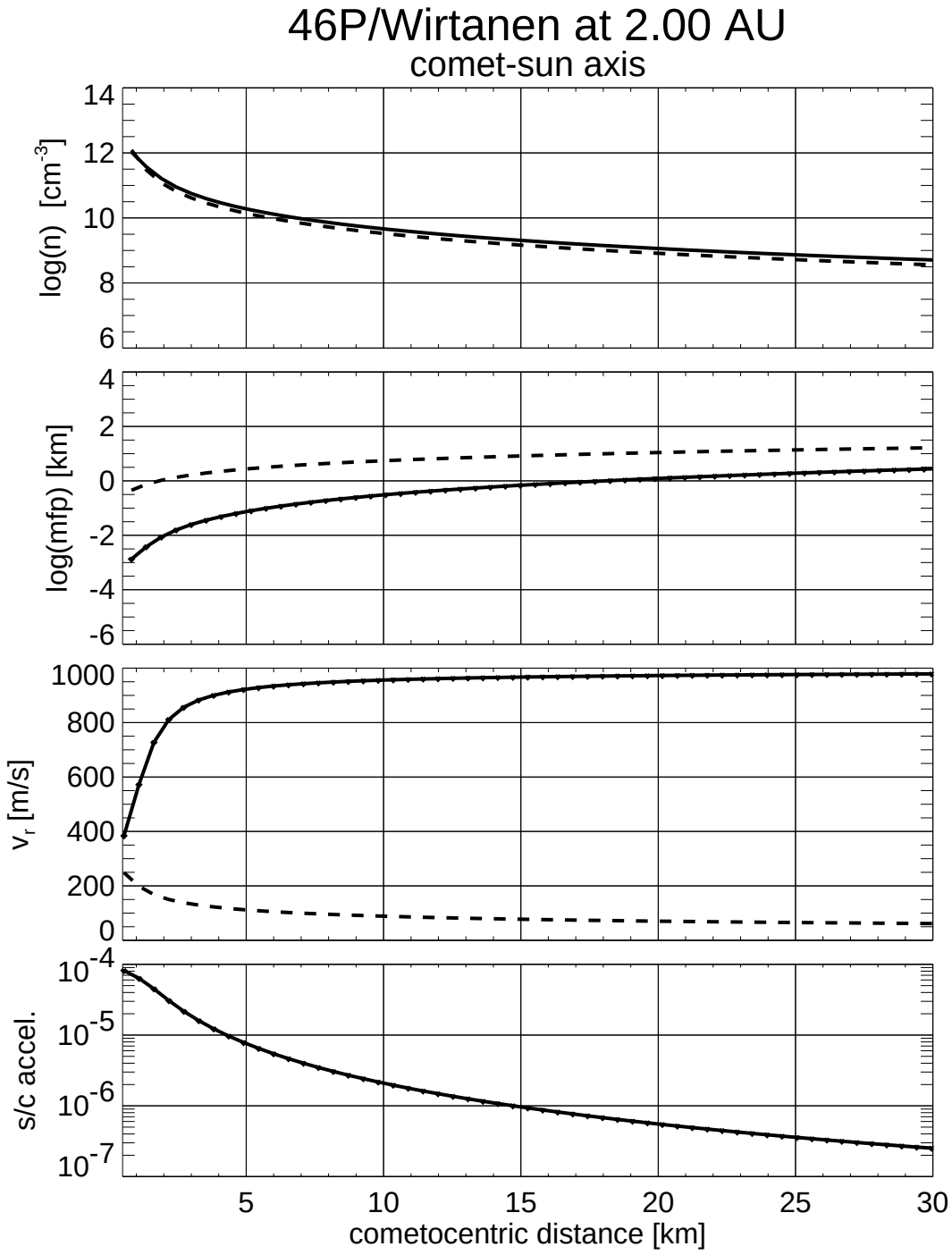

Figure 5.8: *Radial profile at the comet-sun axis of the logarithmically scaled number density n_n and mean free path of particles mfp, the radial velocity v_r and the resulting acceleration of the spacecraft. Exemplary result at a heliocentric distance of 2 AU for 46P/Wirtanen .*

sunrise is identifiable, which is towards the top of the image. This is the initially least dense region due to the smallest sublimation rates on the surface.

Figure 5.8 shows radial profiles along the comet-sun axis of the logarithmically scaled number density n_n and mean free path of particles mfp, the radial velocity v_r and the resulting acceleration of the spacecraft.
Included in Figure 5.8 are the corresponding number density of the spherically symmetric coma with equal gas production rate (dashed line in first panel), the cometocentric distance

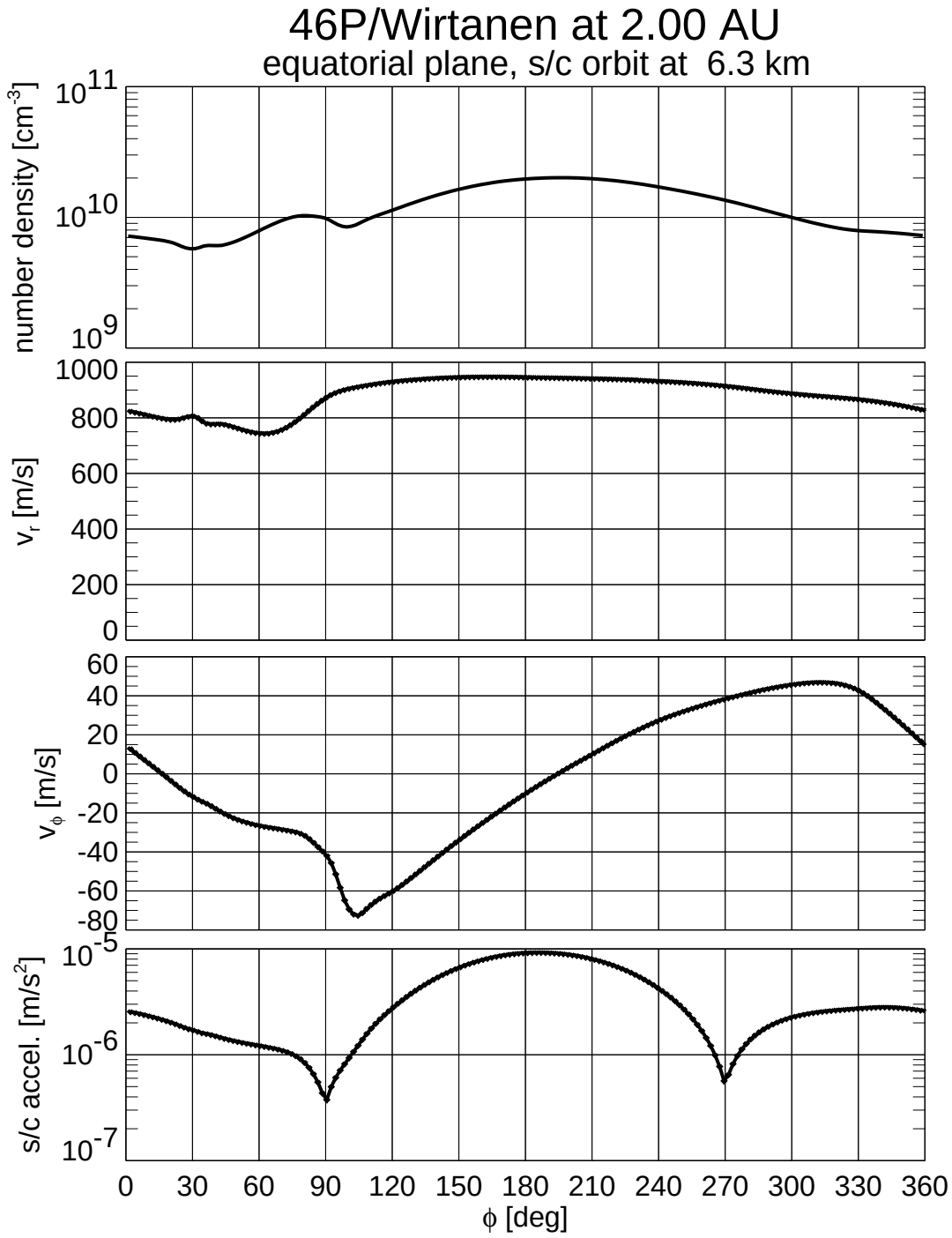

Figure 5.9: *Profile in the equatorial plane of 46P/Wirtanen of the number density n, the radial velocity component v_r, the longitudinal velocity component v_Φ and the resulting acceleration of the spacecraft. Exemplary result at a heliocentric distance of 2AU.*

(dashed line in second panel) and the local speed of sound (dashed line in third panel). The distribution of the number density has an inverse square dependency on the cometocentric distance, almost matching the spherically symmetric distribution. This is a result of the strong outgassing of more volatile species on the night-side of the nucleus, reducing the variation of the density distribution close to the surface.

The computed volume remains dominated by collisions. The local mean free path of particles remains below the cometocentric distance, as the second panel of Figure 5.8 shows. The radial velocity of the expanding gas is plotted in the third panel. The gas expands with super-

sonic velocities and reaches values of about $v_r \approx 1$km/s at $r \approx 10$ km cometocentric distance. The results are in principle agreement with model results of e.g. *Combi and Smyth* [1988*b*].

The acceleration of the spacecraft due to solar radiation pressure at 2 AU heliocentric distance is $a_\odot \approx 9.7 \times 10^{-8}$m/s^2 (see Equation (5.9)). The acceleration due to gas drag therefore exceeds the acceleration caused by solar radiation pressure within the considered range of the comet-sun axis.
In Figure 5.9 the conditions along a virtual orbit in the equatorial plane at a cometocentric distance of $r \approx 6$km are plotted. The day-night variation of the number density is visible in the first panel. The variations of the number density and the radial velocity component (second panel) between day and night are relatively small when compared with the results for 67P/Churyumov-Gerasimenko at 3 AU (see Figure 5.6). The velocity component in longitudinal direction is plotted in the third panel of Figure 5.9 (positive in the direction of increasing Φ). A flow from the day-side to the night-side coma is indicated. The tangential velocity components reach values of $\sim 5\%$ of the radial velocity at this cometocentric distance. The fourth panel in Figure 5.9 shows the resulting absolute of the acceleration of an orbiting spacecraft. The orientation of the solar panels towards the sun and the tangential gas mass flux is taken into account in the computations. The acceleration has a maximum in the subsolar region of the coma and two local minima at the terminator, where the orientation of the solar panels is perpendicular to the surface. The acceleration of the spacecraft is then derived from the size of the main body of the spacecraft. The acceleration due to gas drag exceeds 10^{-7}m/s^2 throughout the orbit.

5.3.3 Consequences for RSI

The acceleration of the spacecraft can be measured with the RSI experiment, if the velocity change has a component in the direction of the line-of-sight. A terminator orbit might be an interesting choice as long as the angle between orbit normal and line-of-sight is large enough. The orientation of the solar panels would minimize the cross section of the spacecraft in the direction of the gas flux. This would be interesting for the gravity mapping campaign in early phases of the mission. During a solar opposition (line up of sun - earth - comet) this configuration is not favorable. The acceleration due to gravity then is mainly perpendicular to the line-of-sight, minimizing the effect on the carrier signal. The angle between line-of-sight for an earth observer and comet-sun axis is given in Appendix E.

An alternative strategy might be as follows: The spacecraft revolution period for an orbital radius of $r \approx 5$ km has the order of 100 hours [*Pätzold et al.*, 2001]. The estimated spin periods of comets 67P/Churyumov-Gerasimenko and 46P/Wirtanen are of the order of 10 hours. The best way to minimize the perturbation due to gas drag without losing the information of the gravity coefficients therefore probably is a polar orbit perpendicular to the terminator orbit, with measurements on the night-side part of the orbit while the nucleus spins under the spacecraft. This would allow to map the gravity of the whole nucleus within a few orbits [*Pätzold et al.*, 2001].

The maximum of the gas and dust mass flux can be obtained with the same orbital strategy, i.e. on the day-side part of the same orbit, where the effect of the mass flux is expected to

be maximal. The perturbation of the orbit can become strong enough to make operation and navigation of a spacecraft challenging, as e.g. *Pätzold et al.* [2001] mentions.

5.3.4 Discussion

The developed model provides the physical conditions of the collision dominated inner coma. The application of the results derived from the thermal model, which were used to determine the conditions at the inner radial boundary, yields reasonable estimates of the conditions in the coma that will be encountered by the ROSETTA mission. The modeling of jets is not included in this work, but can be carried out with the developed model by adjusting the parameters at the inner radial boundary, or by further developing the thermal model of the cometary nucleus. The results presented here therefore represent average conditions in the cometary coma at particular heliocentric distances. The implications for the RSI experiment on ROSETTA are: Firstly, the orbit strategy for the gravity mapping campaign needs to be carefully developed, secondly the drag force due to the gas mass flux can reach (and exceed) the order of magnitude of the solar radiation pressure at heliocentric distances of 3AU. Finally, the collisional coma of a comet might be significantly different if gas production from more volatile species than water is present.
The determination of the boundary conditions is in principle in accordance with the proceeding proposed by e.g. *Crifo and Rodionov* [1997*a*]. The reference pressure used at the surface is adjusted in order to account for the dust-ice mixture present on the surface. Instead of using the saturation pressure $p_s(T)$ as reference, as proposed by e.g. *Crifo and Rodionov* [1997*a*] or *Rodionov et al.* [2002], the reference pressure is adjusted with the local icy area fraction of each surface element A_0.

In general, one can conclude that the gas distribution has a dependence on the inverse square of the cometocentric distance. A spherically symmetric coma observed remotely does not necessarily indicate a spherically symmetric sublimation process. Therefore the total gas production rates derived from remote observations may be overestimated. The matching of the modeled density distribution within the coma with observed densities is possible, however. This can be achieved by iteratively adjusting the thermal model of the cometary nucleus and then adjust the inner boundary conditions of the coma model. This proceeding would probably provide a more realistic computation of the total gas production rate, albeit on the cost of much modeling work.

The model results are in principle agreement with other models of the neutral gas coma of comets. Differences result from different assumptions concerning the boundary condition on the surface of the nucleus. The combination of a thermal model of the cometary nucleus with a hydrodynamic simulation of the neutral gas coma was also modeled by e.g. *Rodionov et al.* [2002]. Their model is also able to account for various shapes of cometary nuclei and gas-dust interaction. It was successfully applied to the coma of comet 1P/Halley (e.g. *Szegö et al.* [2002]). The application to comet 46P/Wirtanen with a homogeneous spherical nucleus (e.g. *Crifo and Rodionov* [1997*a*]) provides comparable results to the model developed in this work, although no thermal model of the cometary interior is used in the work of *Crifo and Rodionov* [1997*a*].

Two additional cases are added in Appendix D. Results for 67P/Churyumov-Gerasimenko and 46P/Wirtanen at their respective perihelion distance are shown. The results indicate the variability of possible conditions in the cometary coma.

CHAPTER 6

IONIZED COMA AND INTERACTION WITH THE SOLAR WIND

The cometary plasma environment and its interaction with the solar wind is studied in this chapter. The general pattern of the interaction, the production and loss of plasma particles, and a simplified model of the ionized coma are discussed.

6.1 Introduction

The RSI experiment can be affected by the ionized component of the cometary coma. The absolute value of the total electron content in the line of sight can be determined from the differential propagation delay of a carrier signal in a two-way mode [*Pätzold et al.*, 2000]. A phase shift of the frequency of the carrier signal is expected when the radio wave propagates through an ionized medium. An estimate of the number density of ions (and electrons) is needed in order to evaluate the effect of the ionized cometary coma on the carrier signal.

In-situ observations of the cometary plasma environment have so far been made only at heliocentric distances around 1 AU from four different comets (chronologically ordered): 21P/Giacobini-Zinner in 1985 (e.g. *Ogilvie et al.* [1986]), 1P/Halley in 1986, 26P/Grigg-Skjellerup in 1992 (e.g. *Johnstone et al.* [1993]; *Neubauer et al.* [1993]) and 19P/Borrelly in 2001 (e.g. *Reisenfeld et al.* [2002]; *Young et al.* [2003]). At this distance from the sun active comets have developed a complex interaction pattern with the solar wind due to large gas production rates and high ionization rates.

The expanding neutral gas of the coma is ionized mainly by photoionization caused by solar UV- and EUV- radiation, as well as by impact ionization or by charge exchange reactions with solar wind particles (mainly H^+). The assumption of photochemical equilibrium, which

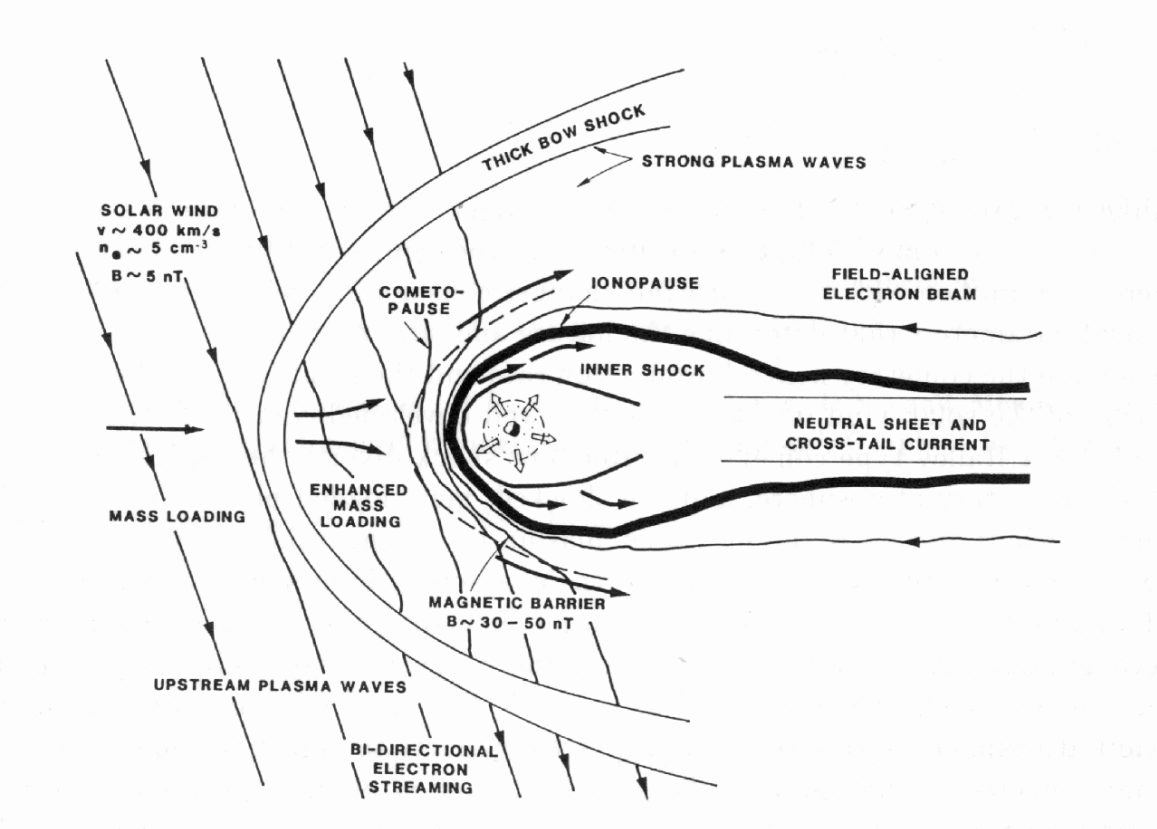

Figure 6.1: *A schematic view of the global pattern of the comet - solar wind interaction at 1 AU for active comets (from Flammer [1991])*

produces reasonable results for comet 1P/Halley at the time of the GIOTTO encounter (e.g. *Cravens* [1989]), is not necessarily justified at comets with a weaker gas production. If photochemical equilibrium can not be assumed, a continuity equation for the cometary ions has to be solved to estimate the plasma densities with respect to the cometocentric distance. A simple one-dimensional model of the plasma densities with respect to the comet-sun axis is developed in Section 6.4. The variation with heliocentric distance and solar activity conditions is also studied.

The global pattern of the interaction of a comet with the solar wind is sketched in Figure 6.1 (reproduced from *Flammer* [1991]). In a reference frame at rest with the comet, the cometary ions are in general much slower than the solar wind and have more mass than average solar wind particles. The solar wind picks up the cometary plasma particles, hence is mass loaded and decelerated. When this mass loading reaches a critical value a shock forms upwind of the comet, according to magneto-hydrodynamic theory. Inside this bow shock the solar wind is further decelerated and enhanced mass loading occurs. Additional important features that are expected at a comet are the collisionopause (also named cometopause by some authors), and a magnetic barrier with the magnetic pile up boundary (MPB) as outer boundary and the cavity surface as inner boundary around the magnetic-field-free cavity. At the collisionopause the regime changes from the collisionless solar wind flow to a regime dominated by collisions with neutral gas particles.
The interplanetary magnetic field is enhanced in the magnetic barrier and the field lines are draped around the comet in this region. The formation of these features depends on the

production rate of neutral gas and the solar wind parameters and therefore varies at different comets and with heliocentric distance.

The cavity surface (or ionopause) forms where the magnetic pressure of the solar wind and the draped magnetic field is balanced by the drag force of the radial outflowing neutral cometary particles on the stagnant ions [*Ip and Axford*, 1987]. The development of the cavity surface therefore depends strongly on the outgassing of the cometary nucleus. The cavity surface is the outer boundary of a magnetic field free region around the cometary nucleus. Inside the cavity surface only plasma of cometary origin exists. If the gas production of the comet is too low to maintain a cavity, the solar wind plasma can reach the surface of the nucleus.
An inner shock was predicted as the supersonic to subsonic transition feature of the velocity of the cometary ions inside the cavity surface (see Figure 6.1), but has not been observed by GIOTTO, see e.g. *Goldstein et al.* [1992]. A piling up of the cometary ions just inside the cavity surface, which would enhance the electron - ion recombination rate and neutralize the plasma instead of decelerating it to subsonic velocities, has been proposed as an explanation by *Cravens* [1989]. See *Flammer* [1991] for a review of this region.

In order to study the ionized cometary coma, the variation of the general physical conditions due to varying heliocentric distance and due to varying solar activity has to be characterized. The modeling of the parameters of the solar wind and the variations due to the state of solar activity are described in the following sections. In Section 6.6 the different interaction features will be discussed.

6.2 Solar Wind Parameters

The spatial and temporal variation of the solar wind parameters is studied by many authors. A straightforward approach is used to model solar wind parameters between 1 AU and 6 AU, principally consistent with the Parker model [*Parker*, 1958]. Many dynamic features of the solar wind are neglected for simplicity. Plasma density, magnetic field and temperature of protons and electrons are expressed with simple power laws. Their respective dependence on heliocentric distance is plotted in Figure 6.2.

Plasma Density

The plasma density of the solar wind is assumed to fall off with the inverse square of the heliocentric distance r_h, complying with a spherical expanding gas at constant velocity. Data analysis shows a small deviation from a pure r_h^{-2} dependency [*Schwenn*, 1990; *Richardson et al.*, 1995], but fluctuations and small deviations are neglected here for simplicity. Therefore the number density n_{sw} of protons in the solar wind is modeled as:

$$n_{sw} = \frac{n_0}{\hat{r}^2} \quad , \tag{6.1}$$

with $n_0 =$ number density at 1 AU, typically $3-10$ cm^{-3} [*Schwenn*, 1991] and the heliocentric distance in astronomical units $\hat{r} = r_h/1\text{AU}$.

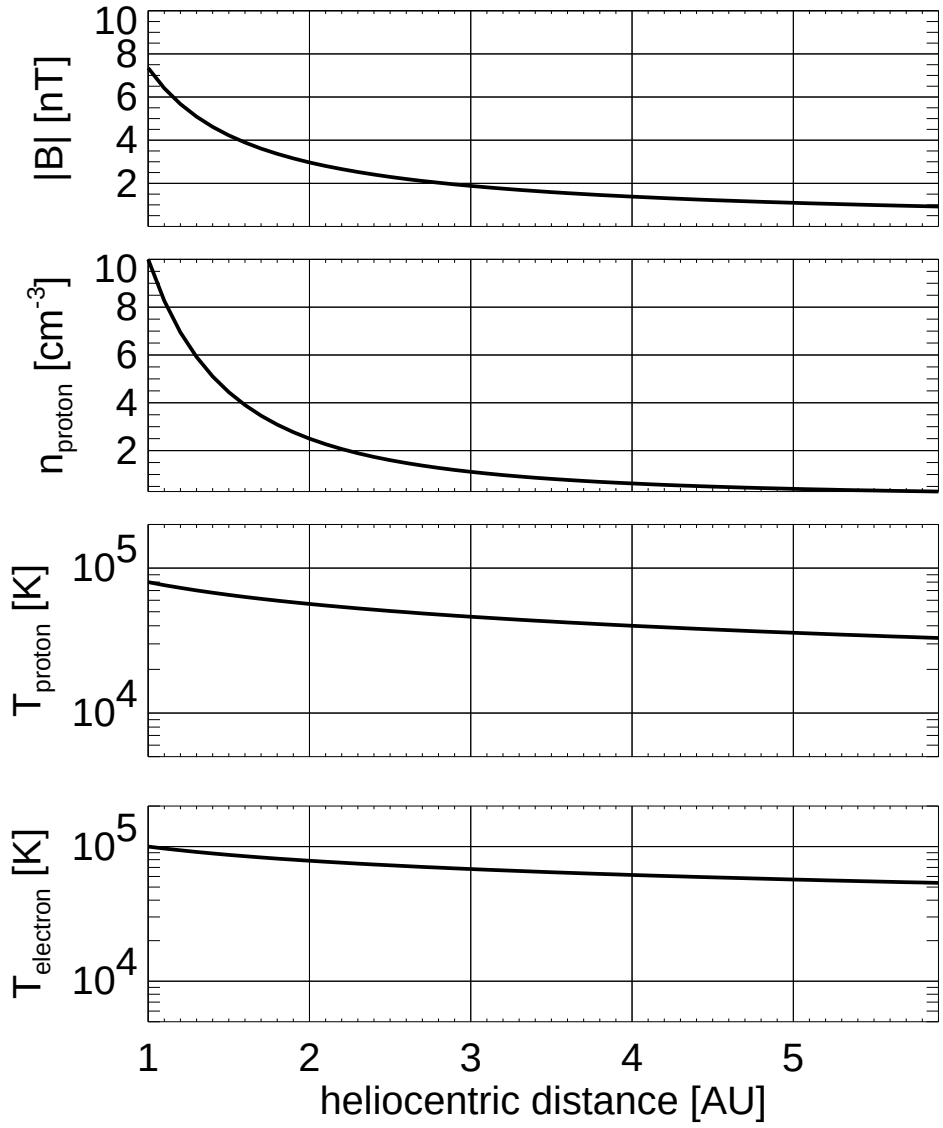

Figure 6.2: *Variation of solar wind parameters with distance between 1 and 6 AU*

Velocity

The flow speed of the solar wind is assumed to be constant over the range of 1 to 6 AU. An increase with increasing distance of a few percent in the inner heliosphere was predicted by *Schwenn* [1990]. Analysis by *Richardson et al.* [1995] showed no general radial gradient in the velocity data observed by IMP 8 at 1 AU and VOYAGER 2 between $5-40$ AU. An average solar wind speed of $v_{sw} = 350$ km/s is usually assumed in the calculations made here. This corresponds to conditions in an average slow solar wind in the ecliptical plane. The variability of the solar wind velocity is neglected here.

Interplanetary Magnetic Field

The general features and predictions of the Parker model have been confirmed by data analysis of many spacecraft. Although certain deviations exist [*Mariani and Neubauer*, 1990], the approach of the Parker model is used in this work. Fluctuations and dynamic effects are

neglected, since the general behavior of the comet - solar wind interaction is studied. The radial variation of the radial component of the magnetic field is therefore computed as :

$$B_r(r) = \frac{B_{r0}}{\hat{r}^2} \ , \tag{6.2}$$

with B_{r0} = radial field component at 1 AU, typically in the range of $2-10$ nT. The heliocentric variation of the field magnitude B depends on the solar angular rotation rate Ω and is derived as:

$$B(r) = B_r(r) \ \sqrt{1+\left(\frac{\Omega r}{v_{sw}}\right)} \ . \tag{6.3}$$

Proton and Electron Temperatures

For the heliocentric variation of the proton temperature in the solar wind, observational results from the work of *Richardson et al.* [1995] are applied. IMP 8 and VOYAGER 2-Data is used to derive the power law fit

$$T_p = \alpha \, \hat{r}^{-0.53\pm0.02} \ , \tag{6.4}$$

with $\alpha = 3.77 \times 10^4$ K, when using data obtained inside 19 AU.

In order to model the temperature of the solar wind electrons with respect to the heliocentric distance, an empirical polytrope law for thermal electrons that has been derived by *Sittler Jr. and Scudder* [1980] from VOYAGER 2 and MARINER 10 measurements is applied:

$$T_e = 5.5 \times 10^4 \ \cdot \ \hat{r}^{-0.185}\mathrm{K} \ . \tag{6.5}$$

6.3 Solar Activity & Predictions

The 11-year activity cycle of the sun is visible, for example, in the number of sunspots which have been observed daily since 1749 at the Zurich Observatory. Monthly averages of the sunspot numbers (officially named the *Boulder sunspot number* and computed by the NOAA Space Environment Center[1]) are plotted in Figure 6.3.

[1] http://sec.noaa.gov

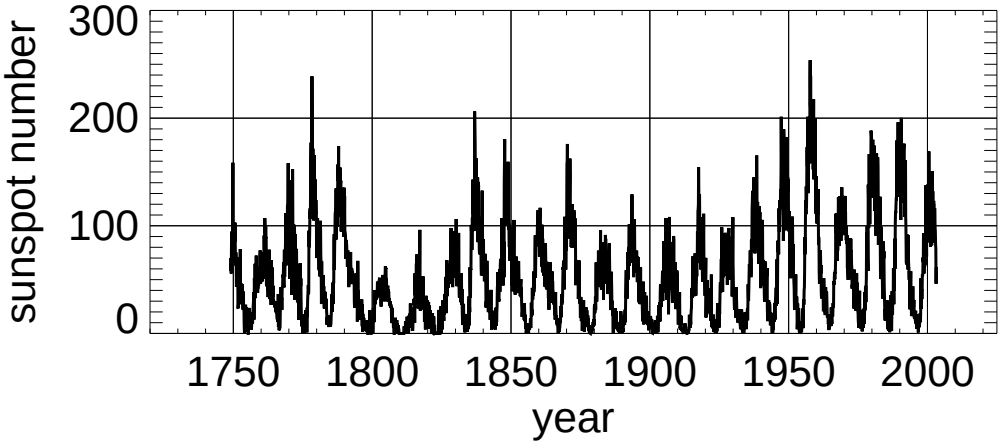

Figure 6.3: *Monthly averaged sunspot numbers, computed by the NOAA Space Environment Center*

In order to estimate the state of activity during the time of the prime mission of ROSETTA, which would be 2012-2013 for comet 46P/Wirtanen and 2015 for comet 67P/Churyumov-Gerasimenko, predictions of the 10.7cm solar flux as computed by K. Schatten and provided by the NASA Goddard Space Flight Center[1] are used. For details about the prediction technique see *Schatten and Pesnell* [1993] and references therein. The 10.7 cm solar flux measures the integrated emission at a wavelength of 10.7 cm from all sources present on the solar disc. It is of thermal origin and related to the amount of magnetic flux. An advantage over other indices of solar activity is the independence of terrestrial weather conditions. The quantity of the flux is given in solar flux units (sfu $= 10^{-22}$ m^{-2} Hz^{-2}).

Three datasets are plotted in Figure 6.4. The upper curve represents monthly averages of the flare activity index. This quantitative daily flare index is defined as $FI = i \cdot t$, where i represents the optical importance coefficient of a flare in H_α (spectral line at 121.567 nm) and t the duration of the flare in minutes (in H_α). The daily sums of the index are divided by the total observation time per day. For more details see Section 6.7.1 and e.g. *Özgüc et al.* [2002] and references therein. The data plotted was provided by the National Geophysical Data Center (NGDC) in Boulder, USA[2].
The curve below is a composite of measured solar 10.7 cm flux, provided by the Dominion Radio Astrophysical Observatory, Canada[3], and the predictions of solar 10.7cm flux.
The state of solar activity is well represented in the solar flux data and as can be seen in Figure 6.4 it correlates well with the flare index. Therefore strong flares should be expected mainly during solar maximum conditions and only few strong flares during solar minimum conditions. With reference to the prime mission of the ROSETTA mission, the predictions of the solar flux are plotted. The three curves represent mean fluxes with *early* (dash-dotted), *nominal* (dotted), and *late* (dashed) timing, taking into account the uncertainty in the timing

[1]The original source (http://denali.gsfc.nasa.gov/926/schatten/sunpredlatest.htm) has been disappeared from the web by the time this work is published. Results consistent with the data used here are published by *Sello* [2003].

[2]ftp://ftp.ngdc.noaa.gov/STP/SOLAR_DATA/SOLAR_FLARES/INDEX

[3]http://www.drao-ofr.hia-iha.nrc-cnrc.gc.ca/index_eng.shtml

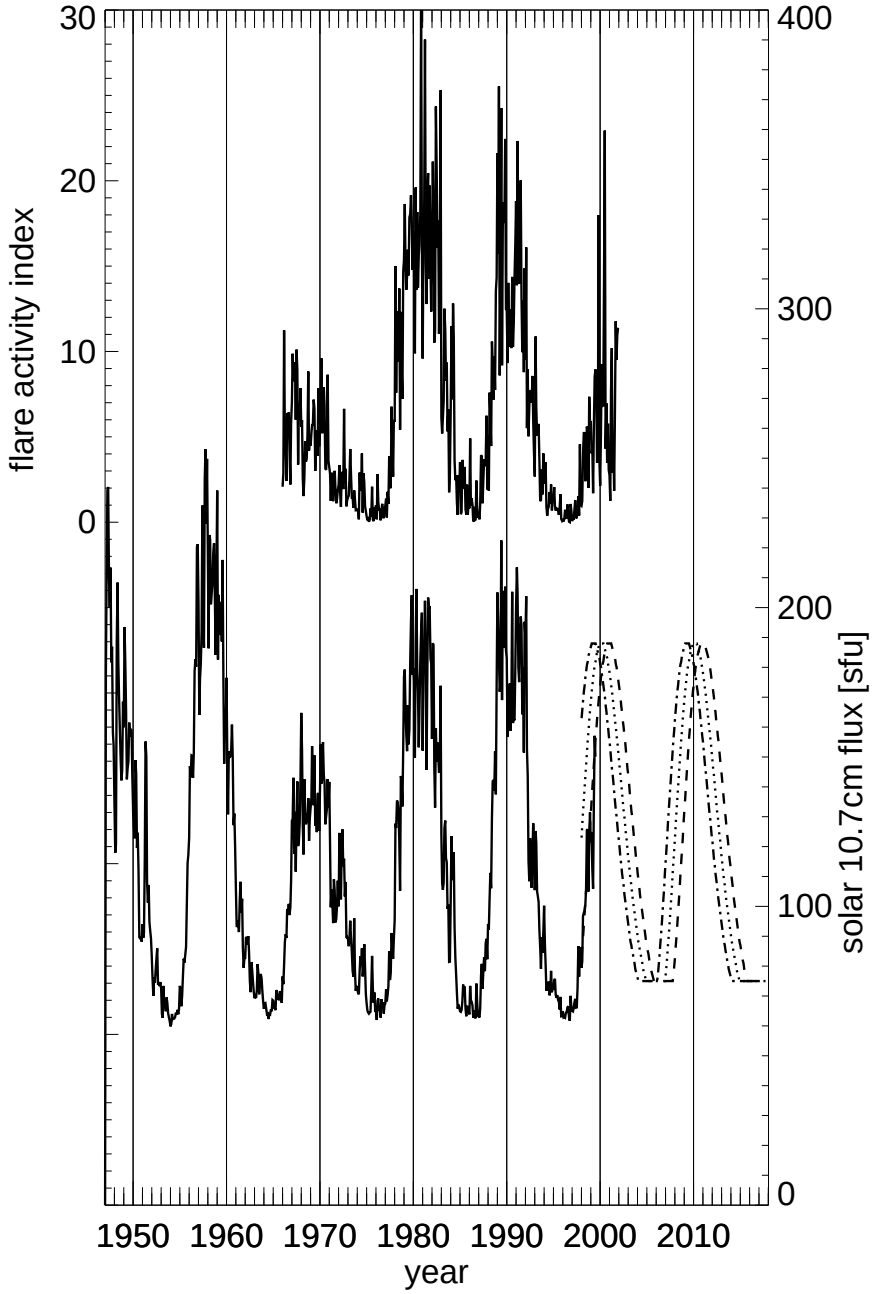

Figure 6.4: *Flare activity, solar 10.7cm flux and predictions. The flare activity index (upper solid line) corresponds well with the measured solar flux data (lower solid line). The dashed and dotted lines indicate predicted solar radio flux, see text.*

of the cycles at the time the predictions were made (1998). From these predictions one would expect maximum to intermediate activity conditions for the 46P/Wirtanen mission scenario and minimum conditions for the mission scenario at 67P/Churyumov-Gerasimenko . Therefore the chances of seeing effects of solar flares in the environment of comet 67P/Churyumov-Gerasimenko during the ROSETTA mission are low, while 46P/Wirtanen would have been a better target from this point of view.

6.4 Cometary Plasma

In this section the cometary plasma environment will be studied. The solar radiation as the main ionization source and important processes within the ionized cometary coma, such as impact ionization and dissociative recombination, are discussed. A model for the electron temperature profile along the comet-sun axis is developed.

In the outward directed flow of neutral particles with a velocity of the order of 1 km/s, collisions and reactions decrease with the distance to the comet. The most important subsequent process for the particles is ionization. The ionization process for cometary neutrals is dominated by photoionization (solar UV), followed by charge exchange and impact ionization. Photoionization takes place throughout the cometary atmosphere (see also Section 6.4.2), and charge exchange and impact ionization are strongest upwind of the comet. Typical reactions with a cometary neutral particle M, such as H_2O, CO, O, H are [*Huebner et al.*, 1991; *Cravens*, 1991*b*]:

$$\begin{array}{llllll} \mathrm{M} + & h\nu & \longrightarrow & M^+ + & e^- & \textit{photoionization,} \\ \mathrm{M} + & H^+_{sw} & \longrightarrow & M^+ + & H_{fast} & \textit{charge exchange,} \\ \mathrm{M} + & e^- & \longrightarrow & M^+ + & e^- + e^- & \textit{impact ionization.} \end{array}$$

The time scale for ionization is of the order of 10^6 s at 1 AU, which results in a characteristic ionization length scale of 10^6 km from the nucleus at 1 AU [*Huddleston et al.*, 1990].

Processes involving solar radiation such as ionization and dissociation vary with the solar activity. For the model computations, the solar activity of the particular time frame has to be estimated. As discussed in Section 6.3, the sun should be shortly after activity maximum at the time of the prime mission at 46P/Wirtanen (2011-2013), and is expected near activity minimum at the time of the prime mission at comet 67P/Churyumov-Gerasimenko (2014/2015).

Only water reactions will be considered in this work. This is a reasonable simplification, since water is supposed to be by far the most dominant species in the inner coma of comet 46P/Wirtanen (see e.g. *Fink et al.* [1998]; *Stern et al.* [1998]; *Schulz and Schwehm* [1999]). At 1P/Halley, the proportion of H_2O was about 80% or more [*Cravens*, 1989].

The ions formed from H_2O molecules in the cometary coma are mainly H_2O^+, H_3O^+, H^+, OH^+ and O^+ (e.g. *Schmidt et al.* [1988]; *Wegmann et al.* [1999]). The processes involved are discussed in the following sections.

6.4.1 Solar UV Spectrum

The photochemical processes involved in the cometary environment are dominated by solar UV radiation of wavelengths shorter than $200nm$. In this wavelength region dust has to be considered only as an absorber, and multiple scattering or thermal re-radiation can be neglected [*Gombosi et al.*, 1986]. The detailed photon flux for many wavelength intervals in the UV range (most in $5-10nm$ bins) can be found in the literature (e.g. *White* [1977]; *Gombosi et al.* [1986]; *Huebner et al.* [1992] and references therein).

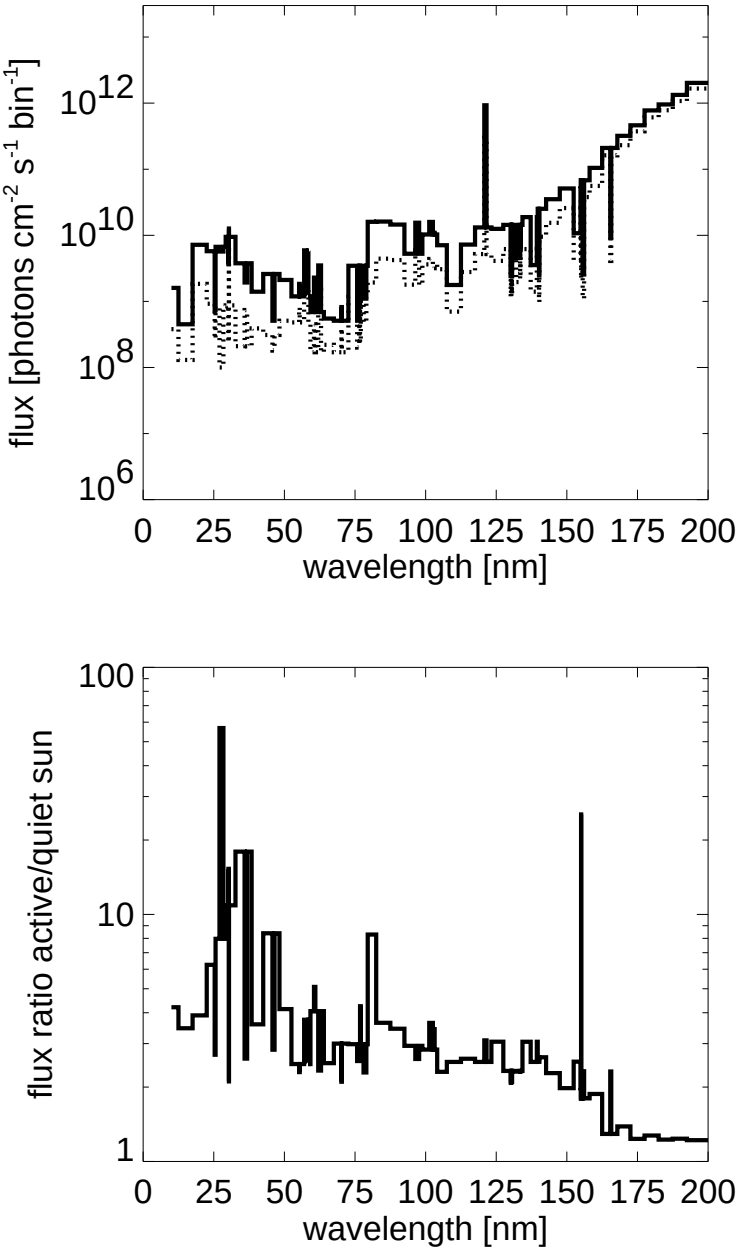

Figure 6.5: *Top: The solar UV flux at 1 AU for maximum conditions (solid) and minimum conditions (dotted), Bottom: max/min solar UV flux ratio; data taken from Gombosi et al. [1986]*

The variation with solar activity is large for some wavelength regions in the UV range. In Figure 6.5 (top) the solar UV flux is plotted. The data is taken from *Gombosi et al.* [1986]. For active solar conditions (solid line), the flux is essentially larger. The UV flux varies by a factor of typically 2 - 3, for some wavelength regions by more than an order of magnitude, as can be seen in Figure 6.5 (bottom), which effects the lifetimes of neutral gas particles within the coma [*Oppenheimer and Downey*, 1980; *Budzien et al.*, 1994]. Since no adequate observational database exists, empirical models have been used to consider the variability with the solar 11-year cycle, usually by correlation between measured solar irradiances and solar activity data (see e.g. *Lean et al.* [1992]; *Richards et al.* [1994]).

As pointed out by *Häberli et al.* [1997], the detailed ionizing spectrum does not necessarily have to be considered when the coma is expected to remain optically thin, which is a reasonable assumption at comets 46P/Wirtanen and 67P/Churyumov-Gerasimenko (see Section 6.4.2). Since the attenuation of particular spectral lines does not have to be taken into account in such a scenario, one can use wavelength-integrated ionization rates (see Section 6.4.3). Additionally it should be noted that the solar radiation is not emitted isotropically, and therefore the observed spectrum at earth may not be the same at a comet [*Stix*, 1989; *Rousselot et al.*, 1993]. For example, the variation with the rotational period of the sun reaches 25% at 120*nm* [*Stix*, 1989]. This kind of variation is neglected in the model, because the aim of this work is only to model the general behavior of the comet - solar wind interaction.

Solar maximum conditions are assumed in the model calculations for the scenario at comet 46P/Wirtanen and solar minimum conditions are assumed for the comet 67P/Churyumov-Gerasimenko scenario for simplicity.

6.4.2 Optical Depth of the Coma in the UV Range

In order to derive the optical depth of the coma in the UV range, the density distribution of the neutral gas and the absorption cross sections of these particles in the UV range have to be known. For simplicity, a spherically symmetric neutral gas coma is assumed here to estimate the optical depth. This simplification is widely used in cometary studies. It is a basic assumption in the so called *Haser* model (e.g. *Festou* [1981]; *Cochran* [1985]). The realistic pattern in the coma should differ from this assumption in the innermost region. Without the appearance of strong jets, spherically symmetry is a good approximation, as can be seen in the results from the hydrodynamic simulations of the neutral gas environment of 46P/Wirtanen (see Chapter 5). Using the HD-model, a more realistic and detailed profile of the number density and the outflow velocity can be constructed. This should be done if a strong asymmetry in the coma due to jets or other asymmetric flow patterns is expected, as for example at comet 67P/Churyumov-Gerasimenko. This will not be evaluated further at this point, since only the general behavior is studied here. In Figure 6.6 the

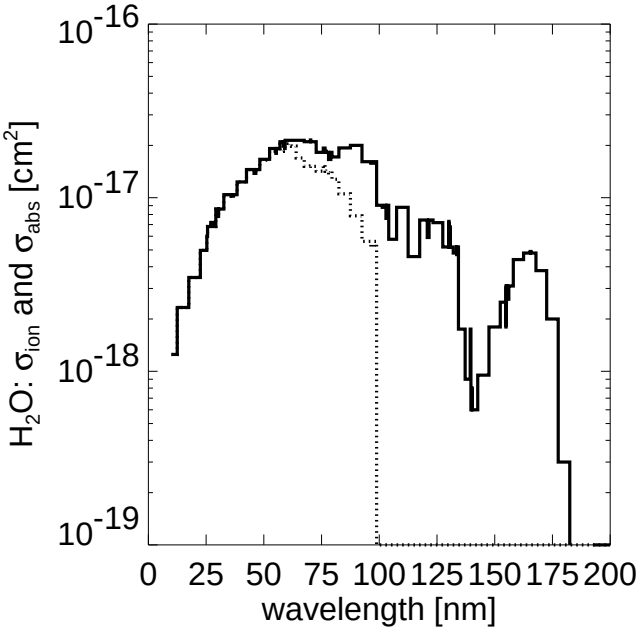

Figure 6.6: *Absorption (solid) and ionization (dotted) cross sections for H_2O molecules in the UV range, data taken from Gombosi et al. [1986]*

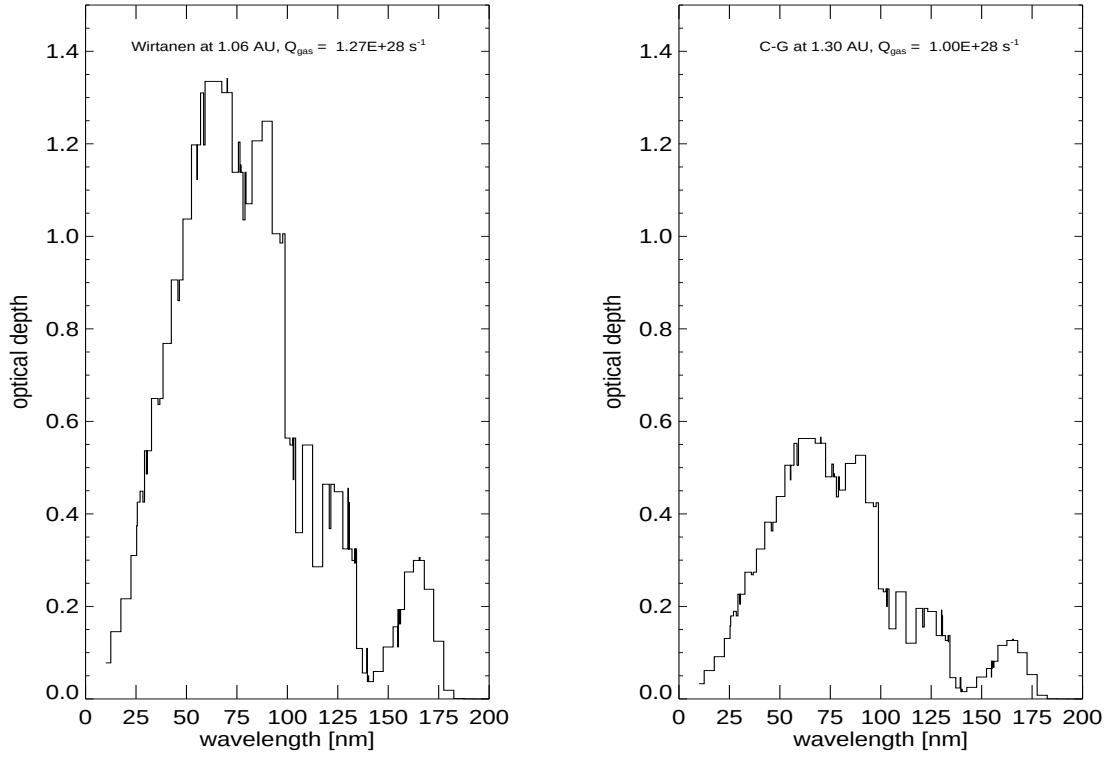

(a) optical depth at 46P/Wirtanen

(b) optical depth at 67P/Churyumov-Gerasimenko

Figure 6.7: *Derived optical depth at the sub solar point for 46P/Wirtanen at perihelion and for solar maximum conditions (a), and for comet 67P/Churyumov-Gerasimenko at perihelion for solar minimum conditions (b)*

cross section of absorption (solid line) and photoionization (dotted line) is plotted. Direct ionization is important for wavelengths up to 100 nm, while dissociation and subsequent ionization occurs mainly at longer wavelength (see also Section 6.4.3). The cross sections for H_2O have typical values of $10^{-18} - 10^{-17}$ cm^2 in the UV range.

If the number density $n_n(r)$ of neutral particles n as a function of radial distance r and the total absorption cross section of these particles $\sigma_{abs}(\lambda)$ as a function of wavelength λ are known, the optical depth $\tau(\lambda, r)$ can be calculated as:

$$\tau(\lambda, r) = \sum_n \sigma_{abs}(\lambda) \int_r^\infty n_n(r)\, dr' \qquad . \tag{6.6}$$

Assuming spherical symmetry, which is a reasonable first order approximation (see also Section 5.3), the density distribution in the coma is derived as (e.g. *Galeev et al.* [1985]):

$$n_n(r) = \frac{Q_g}{4\pi v_n r^2} \exp(-\frac{r\, I_i}{v_n}) \qquad , \tag{6.7}$$

where I_i is the total ionization rate. With the largest observed production rate at 46P/Wirtanen (1.06AU) of $Q_g \approx 3 \times 10^{28}$ s^{-1} [*Fink et al.*, 1998; *Schulz and Schwehm*, 1999] and $Q_g \approx 1 \times 10^{28}$ s^{-1} at comet 67P/Churyumov-Gerasimenko (1.36 AU) [*Osip et al.*, 1992], a typical

outflow velocity of the order $v_n \approx 1$ km/s [*Krankowsky et al.*, 1986] and an ionization frequency as derived in Section 6.4.5, the calculated column density of the neutral gas becomes 6.24×10^{16} cm^{-2} along the comet-sun axis at the perihelion of comet 46P/Wirtanen for solar maximum conditions, and 2.63×10^{16} cm^{-2} for the perihelion of comet 67P/Churyumov-Gerasimenko at solar minimum. These values are derived from the integral of Equation (6.6), truncating the integration at 10^9 km cometocentric distance, well beyond the exponential drop off of the neutral gas density due to the ionization process (see Equation (6.7)). The derived optical depth from Equation (6.6) for the subsolar point of 46P/Wirtanen and 67P/Churyumov-Gerasimenko at perihelion is plotted in Figure 6.7. For comet 46P/Wirtanen solar maximum conditions were applied, while minimum conditions were used for comet 67P/Churyumov-Gerasimenko.
At 46P/Wirtanen, between approximately 50 nm and 100 nm, the optical depth reaches values larger than unity and the irradiation therefore has to be considered as attenuated (see Figure 6.7(a)). The largest ionization rates for these wavelengths are therefore not at the surface, but approximately at that cometocentric distance where $\tau(\lambda, r) = 1$, which still is deep in the inner coma at approximately 2 km distance. However, the optical depth at 67P/Churyumov-Gerasimenko is well below unity for all wavelength bins in the UV-range, as can be seen in Figure 6.7(b). The difference to comet 46P/Wirtanen is mainly caused by the larger radius of the comet nucleus and the lower gas production rate of 67P/Churyumov-Gerasimenko (about a factor 3), resulting in a lower number density close to the surface. The difference in solar activity has only a minor effect in these calculations, altering the exponential part of Equation (6.7). The coma is therefore assumed to be optically thin in the model calculations.

The optical depth of the dust component at 1P/Halley during the GIOTTO encounter has been estimated as $\tau_{dust} = 0.28$ [*Keller et al.*, 1987]. The optical thickness of the dust component is therefore assumed to be < 1 everywhere in the models developed here, due to the lower dust production rate in smaller comets - about a factor of 120 at 46P/Wirtanen [*Jockers et al.*, 1998], and a factor of 40 at comet 67P/Churyumov-Gerasimenko [*Osip et al.*, 1992].

6.4.3 Photoionization and Photodissociation

In Section 6.4.2 it is shown that the coma can be considered optically thin for the solar UV radiation in most cases. Absorption effects within the coma can therefore be neglected. *Häberli et al.* [1997] point out that in this case the spectrum of the ionizing radiation does not have to be considered in detail, and wavelength-integrated ionization frequencies can be used.

Listed in Table 6.1 are wavelength-integrated ionization and dissociation frequencies, given by *Gombosi et al.* [1986]; *Huebner et al.* [1992] and *Schunk and Nagy* [2000]. The chemical reaction rates are taken from *Marconi and Mendis* [1982] and *Gombosi et al.* [1996]. Additional reactions are listed in *Schmidt et al.* [1988] and *Häberli et al.* [1997].

The resulting total photoionization frequency ν_{ph} for H_2O at 1 AU, including the branches leading to H_2O^+, OH^+ and H^+, is $\nu_{ph} = 4.03 \times 10^{-7}$ s^{-1} for solar minimum conditions and $\nu_{ph} = 1.02 \times 10^{-6}$ s^{-1} for solar maximum conditions.

			$[10^{-6}$ s$^{-1}]$	$[10^{-6}$ s$^{-1}]$
			solar min	solar max
photoionization frequencies				
$H_2O + h\nu$	$\longrightarrow$	$H_2O^+ + e$	0.334	0.828
	$\longrightarrow$	$H^+ + OH + e$	0.0131	0.0407
	$\longrightarrow$	$OH^+ + H + e$	0.0554	0.151
$OH + h\nu$	$\longrightarrow$	$OH^+ + e$	0.247	0.652
$O + h\nu$	$\longrightarrow$	$O^+ + e$	0.212	0.588
$H_2 + h\nu$	$\longrightarrow$	$H_2^+ + e$	0.0541	0.115
	$\longrightarrow$	$H^+ + H + e$	0.00952	0.0279
$H + h\nu$	$\longrightarrow$	$H^+ + e$	0.0726	0.172
photodissociation frequencies				
$H_2O + h\nu$	$\longrightarrow$	$OH + H$	10.3	17.6
$H_2O + h\nu$	$\longrightarrow$	$H + H + O$	0.755	1.91
chemical reaction rates				$[10^{-6}$ cm^{-3} s$^{-1}]$
$H_2O + H_2O^+$	$\longrightarrow$	$H_3O^+ + OH$		0.00205
$H_2O + OH^+$	$\longrightarrow$	$H_3O^+ + O$		0.0013
	$\longrightarrow$	$H_2O^+ + OH$		0.0016
$H_2O + H^+$	$\longrightarrow$	$H_2O^+ + H$		0.0082
$H_2O + O^+$	$\longrightarrow$	$H_2O^+ + O$		0.0023
$H_2 + H_2O^+$	$\longrightarrow$	$H_3O^+ + H$		0.0014
$H_2 + OH^+$	$\longrightarrow$	$H_2O^+ + H$		0.00105
$OH + OH^+$	$\longrightarrow$	$H_2O^+ + O$		0.0007

Table 6.1: *Photoionization and photodissociation frequencies of H_2O and daughter products (from Huebner et al. [1992]) and chemical reaction rates in the cometary environment (from Marconi and Mendis [1982]; Gombosi et al. [1986]).*

6.4.4 Impact Ionization and Charge Exchange

Neutral molecules can be ionized by hot cometary electrons or solar wind electrons if the energy of the electrons exceeds the ionization energy of the neutral molecules. Electron impact ionization should be strongest around the thermal electron collisionosphere (see Section 6.4.9), where the temperature of the electrons is high enough (almost at solar wind level, see Section 6.4.8) to cause ionization and the number density of the electrons is large. Further away from the nucleus the electron density drops to solar wind levels and this ionization process becomes negligible [*Gombosi et al.*, 1996]. The time scale for electron impact ionization is in general a function of the electron temperature, number density and distribution function. *Cravens et al.* [1987] conclude that the impact ionization rate reaches values as high as 50% of the photoionization rate for solar minimum conditions at 1 AU. The importance of impact ionization decreases when the photoionization rates are 2-3 times larger during solar maximum conditions. In particular regions around the comet, impact ionization may still be a dominant process, probably due to an energy peak in the electron flux [*Cravens et al.*, 1987].

Körösmezey et al. [1987] calculate steady state photoelectron fluxes in order to derive secondary ionization and electron heating rates due to photoelectrons. Two limiting cases are studied: one without any photoelectron transport (local energy deposition), which is applicable where collisions of electrons with neutrals are frequent (see Section 6.4.9), and one with electron transport along a stationary parallel magnetic field, which can be applied outside this collision zone. If photoelectron transport is accounted for, the impact ionization rates of photoelectrons are reduced by about a factor of 2. The secondary impact ionization rates ν_{imp} for H_2O without photoelectron transport, as derived by *Körösmezey et al.* [1987], are listed in Table 6.2. The impact ionization rate is assumed to be coupled to the photoionization rate in the calculations of this work, since the occurrence of photoelectrons depends on the solar irradiation. With respect to the ionization rates given in Table 6.2 and the conclusion for the photoionization rates in Section 6.4.3 the impact ionization rate is assumed to be $\nu_{imp} = 0.2\nu_{ph}$ everywhere in the coma. Since ionization rates due to solar wind electrons are not derived here, which would require a more sophisticated model that considers variations with cometocentric distance, this approach seems reasonable as a first order approximation of the total ionization rate due to impacts of cometary and solar wind electrons. Local effects, such as high energy electrons that reach regions of high neutral particle number densities and may locally enhance the importance of impact ionization, are neglected.

Solar Activity Conditions	H_2O^+	OH^+	H^+
min	5.77×10^{-8}	6.16×10^{-9}	4.37×10^{-9}
max	1.88×10^{-7}	1.98×10^{-8}	1.39×10^{-8}

Table 6.2: *Secondary impact ionization rates by photoelectrons at 1 AU as derived by Körösmezey et al. [1987]. The ionization rates are given in [s^{-1}].*

Cometary ions can also be created by charge exchange with ions from the solar wind. Charge exchange may become an important solar wind ion loss process around the collisionopause, as *Shelley et al.* [1987] point out. *Gombosi* [1987] proposes an *avalanche* of charge exchange in this region. The rate of charge exchange ν_{cx} between the neutrals and the solar wind ions is determined as $\nu_{cx} = \sigma_{cx} n_{sw} v_{sw}$. For a solar wind velocity v_{sw} of 350 km/s, a charge exchange cross section σ_{cx} of 2.1×10^{-15} cm^2 [*Huddleston et al.*, 1990], and a number density n_{sw} of 5 cm^{-3}, this would result in a rate of charge exchange of $\nu_{cx} = 3.7 \times 10^{-7}$ s^{-1}.
If considered in detail in the cometary environment, the variation with velocity of the charge exchange cross section σ_{cx} has to be taken into account (e.g. *Wallis and Ong* [1975]). In general, the process of charge exchange is variable within the cometary environment, since the mass flux varies with cometocentric distance. At a certain point within the coma the charge exchange effect can become important. In this work this effect is neglected and a constant ionization rate is applied to determine the general comet - solar wind interaction. A rate of ionization caused by charge exchange processes is assumed to be at a level of 10% of the photoionization rate in this work.

6.4.5 Total Ionization Frequency

The total H_2O ionization frequency I_i is a combination of the wavelength integrated photoionization frequencies (see Section 6.4.3), impact ionization and charge exchange processes.

$$I_i = \nu_{ph} + \nu_{imp} + \nu_{cx} \quad , \tag{6.8}$$

where ν_{ph} is the photoionization rate, ν_{imp} is the impact ionization rate and ν_{cx} is the rate of charge exchange between the neutrals and the solar wind ion flux. For solar maximum conditions the resulting total ionization frequency at 1 AU is $I_i = 1.33 \times 10^{-6}$ s^{-1}, while for solar minimum conditions the frequency at 1 AU is $I_i = 5.24 \times 10^{-7}$ s^{-1}. For different heliocentric distances r_h the total ionization frequency is scaled with $1/r_h^2$. This neglects a possible different behavior with heliocentric distance of the respective ionization processes. It is nevertheless a reasonable first order approximation, since only the general behavior is studied here.

6.4.6 Ion-Molecule Reactions

The ion H_3O^+ was the most abundant observed ion in the inner coma at comet 1P/Halley out to $r \approx 2.5 \times 10^4$ km [*Balsiger et al.*, 1986; *Eberhardt and Krankowsky*, 1995]. The chemical formation of H_3O^+ is mainly due to the reaction of H_2O^+ with neutral water molecules:

$$H_2O^+ + H_2O \longrightarrow H_3O^+ + OH. \tag{6.9}$$

Other chemical reactions with reaction rates are listed in Table 6.1 and discussed in the work of *Wegmann et al.* [1999], for example. They are not further evaluated here, since in this work only a water dominant inner coma and H_3O^+ as the dominant ion species is considered. Outside the collision dominated regime these reactions can be neglected and other ions become more abundant. Ion densities then follow an r^{-x} dependency, with $x \geq 2$ for all ion species [*Altwegg et al.*, 1993].

6.4.7 Recombination

Within the ionosphere the lifetime of an H_2O^+ ion is about 100 s. Mainly H_2O^+, OH^+ and H^+ ions are created due to dissociation and ionization processes, and almost all of them are converted to H_3O^+ ions via ion-neutral reactions [*Cravens*, 1989]. The main loss process for H_3O^+ ions is dissociative recombination:

$$H_3O^+ + e^- \longrightarrow H_2O + H. \tag{6.10}$$

Following e.g. *Cravens* [1989], the dissociative recombination rate coefficient α is given as:

$$\alpha = \alpha_0 \sqrt{\frac{300}{T_e}} \, ,$$

where T_e is the electron temperature and $\alpha_0 = 7 \times 10^{-7}$ cm^3/s is the recombination rate coefficient. *Mul et al.* [1983] have measured the temperature dependency of α_0 in laboratory experiments, concluding that the recombination rate deviates from the $T_e^{-0.5}$ dependency for polyatomic ions. In order to correctly approximate the recombination rate this work uses (following e.g. *Eberhardt and Krankowsky* [1995]; *Gombosi et al.* [1996]):

$$\alpha(T_e) = \alpha_0 \sqrt{\frac{300}{T_e}} \qquad T_e \leq 200\,\mathrm{K} \tag{6.11a}$$

$$\alpha(T_e) = 2.342\,\alpha_0\,T_e^{0.2553-0.1633\,\log T_e} \qquad T_e > 200\,\mathrm{K}\ . \tag{6.11b}$$

This recombination rate is applicable for the two most abundant ions in a water dominated coma, H_2O^+ and H_3O^+, as laboratory experiments show [*Heppner et al.*, 1976; *Mul et al.*, 1983]. The uncertainty of this recombination rate is estimated as $\pm 15\%$. Recombination rates for other ions can be found in e.g. *Schunk and Nagy* [2000].

The total loss rate L_i of ions (and electrons) due to dissociative recombination is a function of the number density of ions n_i:

$$L_i = \alpha(T_e)\ n_i^2\ . \tag{6.12}$$

6.4.8 Electron Temperature

The recombination rate of the ions within the coma is coupled to the temperature of the electrons. Lower electron temperature results in a higher recombination rate as can be seen from Equations (6.11a) and (6.11b). The ion density in the coma therefore also depends on the electron temperature.

The electron population in the cometary environment has three sources: solar wind electrons, electrons from the photoionization of cometary gases, and secondary electrons from the ionization of cometary molecules by electrons, fast neutrals and ions. The solar wind electrons represent the hot component in the electron distribution and correspond to a Maxwellian energy distribution with a temperature of about 10^5 K at 1 AU (see Section 6.2).

Since the electron temperature profile can not be calculated self-consistently in an ideal single-fluid MHD-approach, a temperature profile with a simple scaling approach is derived in this work. In general, the electron temperature in the cometary coma will not be the same as the ion temperature [*Gombosi et al.*, 1996].

The excess energy in the photoionization process with solar UV radiation is of the order of $10-15$ eV [*Huebner et al.*, 1992]. Secondary electrons also have energies of the order of a few tens of eV [*Eberhardt and Krankowsky*, 1995]. Cooling mechanisms for electrons in the cometary environment are electron-neutral elastic collisions, electron-ion Coulomb collisions, dissociative recombination with ions, rotational and vibrational excitation of neutral molecules by electron impact, and electronic excitation [*Cravens and Körösmezey*, 1986; *Cravens*, 1991*a*]. Within the inner coma, the electrons are effectively cooled to about the temperature of the neutral gas, as has been modeled by various authors, such as *Marconi and Mendis* [1983]; *Körösmezey et al.* [1987]; *Gan and Cravens* [1990]; *Eberhardt and Krankowsky* [1995]; *Häberli et al.* [1995], as shown in Figure 6.8. GIOTTO observations

at 1P/Halley show that the ion and gas temperatures within the cavity surface are low and approximately constant [*Lämmerzahl et al.*, 1987; *Schwenn et al.*, 1987]. At the cavity surface the measured ion temperature increases rapidly, while the gas temperature shows no discontinuity [*Lämmerzahl et al.*, 1987; *Schwenn et al.*, 1987]. The ion density then significantly piles up by a factor of about $3-4$ near a cometocentric distance of 10^4 km [*Balsiger et al.*, 1986; *Altwegg et al.*, 1993]. The nature of this pile up is still not fully understood. Possible explanations are a reduced ion recombination rate caused by an increasing electron temperature, dynamical pile-up, or enhanced ionization rates due to electron impact [*Ip and Axford*, 1987; *Cravens*, 1989]. This enhancement of the ion density - and the derived electron temperature profile - is not only a short-lived transient phenomenon which can be assumed due to in-situ observations of the VEGA-1 spacecraft [*Vaisberg et al.*, 1987] and due to an analysis of the radio signals of both VEGA missions [*Andreev and Gavrik*, 1993; *Pätzold et al.*, 1997].

Several theoretical approaches to the electron temperature profile, such as *Marconi and Mendis* [1983]; *Körösmezey et al.* [1987]; *Gan and Cravens* [1990]; *Huebner et al.* [1991], show a good agreement inside the cavity surface, but large differences outside (see Figure 6.8). *Häberli et al.* [1996] conclude that photoionization can not be the only important energy source for the electrons outside the cavity surface and show that at least additional heating by solar wind electrons has to be considered. They propose an enhancement in the solar wind electron density that is proportional to the compression of the interplanetary magnetic field in front of the cavity surface. This would provide enough energy for the electrons to reach a temperature that can explain the ion pile-up.

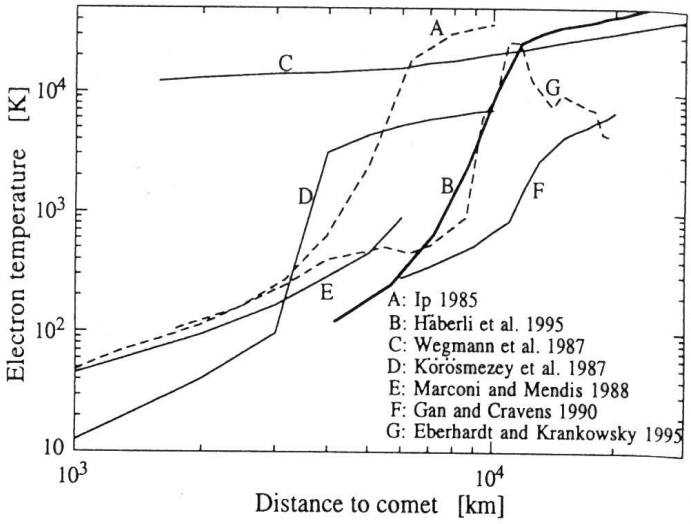

Figure 6.8: *Electron temperature profiles at 1P/Halley, published by various authors. Chart reproduced from Häberli et al. [1996]*

An additional possible heating mechanism for electrons is magnetic field reconnection that can occur in the region of the magnetic barrier and in the plasma tail. Magnetic reconnection at comets is discussed by *Niedner, Jr.* [1984], for example. However, cold electrons (below an energy limit of 10 eV) could not be measured by the GIOTTO electron analyzer and therefore the total energy distribution of the electrons in that region could not be determined.

If the electron thermal pressure has to remain sufficiently small to avoid seriously distorting the magnetic field profile, the increased electron temperature should not immediately reach solar wind levels [*Cravens*, 1989]. Therefore other effects should be considered additionally to explain this ion pile up. *Cravens* [1989] favor an enhanced ionization frequency due to impact ionization, while *Altwegg et al.* [1993] indicate a significant dynamic pile up process as

an

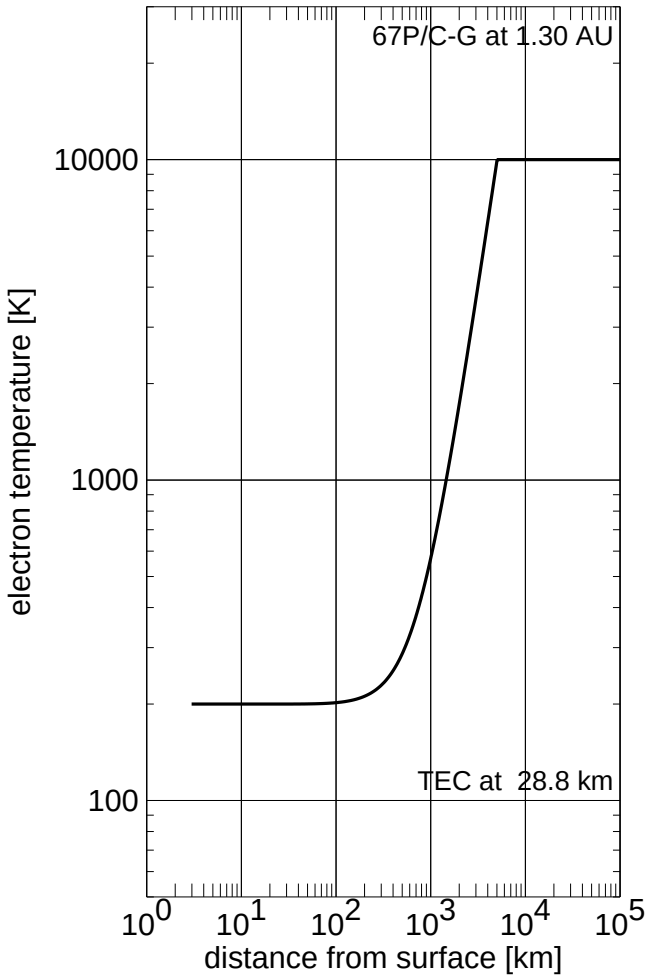

Figure 6.9: *Example of an electron temperature profile as derived for comet 67P/Churyumov-Gerasimenko*

explanation. These effects will be neglected in this work when modeling the plasma environment for simplicity.

An electron temperature profile with the following properties is used in this work: a constant electron temperature inside the thermal electron collisionopause (TEC, see Section 6.4.9), a steep temperature increase (with r^2 dependency) within 5000 km to a level of 10^4 K, and a constant temperature at this level further out (neglecting a slow increase to solar wind levels of the electron temperature). This profile is shifted along the comet-sun axis with the position of the TEC.

The increase of the electron temperature is assumed to have a r^2 dependency, corresponding to the decreasing importance of collisions with neutral particles, which have a r^{-2} dependency of the number density (see Equation (6.7)). The scale size of the increasing part of the profile is adopted from the 1P/Halley results, since it has not been modeled in more detail in this work. This assumption results in a steeper electron temperature profile for comets with a higher gas production. An example of the derived electron temperature profile for comet 67P/Churyumov-Gerasimenko at 1.3 AU is plotted in Figure 6.9. The calculated position of the TEC is at $\sim$ 30 km cometocentric distance in this example.

6.4.9 Thermal Electron Collisionopause

In order to match conditions at various heliocentric distances, the electron temperature profile has to be scaled. *Gan and Cravens* [1990] link the sharp jump in the electron temperature to the fading of the main cooling process for electrons: the collisions between the cometary neutrals and the electrons. This boundary is named the *thermal electron collisionopause* (TEC) [*Gan and Cravens*, 1990]. Transport processes such as heat conduction or plasma convection dominate outside this boundary, while inside the TEC collisional processes like electron-neutral cooling are more important. In order to estimate the cometocentric distance

of the inner edge of the TEC the same procedure as with the estimation of the collisionopause is applied here (see Section 6.6.3). A spherically symmetric distribution of the neutral gas density is assumed, ignoring depletion due to ionization:

$$R_{TEC} = \frac{\sigma_{el}\, Q_g(r_h)}{4\,\pi\, v_n}, \tag{6.13}$$

with the gas production rate $Q_g(r_h)$ derived from Equations (4.27) for 67P/Churyumov-Gerasimenko or Equation (4.26) for 46P/Wirtanen, respectively. For electron energies between 0.1 eV and 10^2 eV, the effective total inelastic electron impact cross-section for water is in the range $\sigma_{el} = 10^{-17} - 10^{-14}$ cm^2, as *Gan and Cravens* [1990] provide from their study of the rotational, vibrational and electronic excitation cross sections and cooling rates by water vapor.

Using $\sigma_{el} = 10^{-15}$ cm^2, which is applicable for electrons with a temperature of the order of 10^4 K [*Gan and Cravens*, 1990] and for the conditions at 1P/Halley at 1 AU (Q_g = 10^{30} s^{-1} and $v_n = 1000$ m/s), the derived cometocentric distance of the TEC is $R_{TEC} \approx 8000$ km. This corresponds very well with the position at which the steep increase in the electron temperature is modeled, as can be seen in Figure 6.8.
Therefore the derived cometocentric distance of the TEC from Equation (6.13) is used to estimate the cometocentric distance at which the electron temperature increases as described in Section 6.4.8.

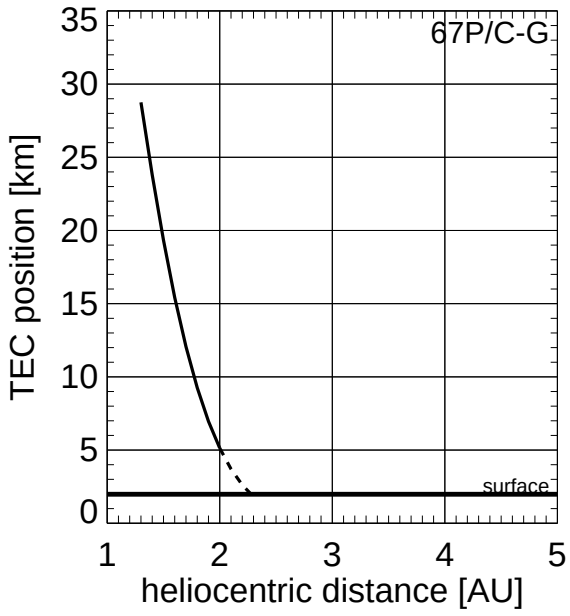

Figure 6.10: *Cometocentric distance of the thermal electron collisionopause (TEC) as derived from Equation (6.13). The horizontal line indicates the surface of the nucleus*

The cometocentric distance of the inner edge of the TEC as derived for comet 67P/Churyumov-Gerasimenko is plotted with respect to the heliocentric distance in Figure 6.10. The respective gas production rate Q_g is derived from the results of the thermal model (Equation (4.27)). The surface of the comet is indicated by the horizontal line at 2 km distance in Figure 6.10. The line indicating the TEC is dashed for standoff distances closer than 3 km from the comet surface. The TEC does separate significantly from the surface of the comet only inside approximately 2.0 AU. A temperature increase that starts at the surface is assumed for heliocentric distances larger than 2 AU. The effect of the electron temperature on the density of ions within the coma is expected to be minor for larger heliocentric distances. The decrease of the recombination rate due to the increase of the electron temperature is expected to have a significant effect in a photochemically controlled regime. The assumption of photochemical equilibrium within the inner coma is only valid under certain conditions, which will be discussed in the next section.

6.5 Stationary Plasma Model 1D

In order to estimate the plasma parameters in the cometary environment, a stationary one-dimensional model along the comet-sun axis is applied. Two scenarios are studied: photochemical equilibrium is assumed in the first case. This has been applied successfully at comet 1P/Halley, where the conditions in the coma justified this assumption (e.g. *Cravens* [1989]). However, it is not necessarily applicable at smaller comets. Therefore the continuity equation for ions is solved without assuming photochemical equilibrium in the second case.
Effects caused by the solar wind are neglected in these models for simplicity. The respective gas production rates of comets 67P/Churyumov-Gerasimenko and 46P/Wirtanen at the corresponding heliocentric distance are derived from the results of the thermal modeling of the comets (Equations (4.27) and (4.26)).

6.5.1 Case 1: with Assumption of Photochemical Equilibrium

For simplicity, the ionosphere is assumed to consist of one single charged ion species. Quasi-neutrality is assumed for the plasma. The one-dimensional continuity equation for the ion (or electron) density n_i in spherical coordinates then is (e.g. *Cravens* [1989]):

$$\frac{\partial n_i}{\partial t} + \mathrm{div}(n_i \mathbf{v}) = P_i(r) - L_i(r) \quad , \tag{6.14}$$

with the cometocentric distance r, the plasma velocity $\mathbf{v} = v_r \mathbf{e}_r$, the local production rate $P_i(r)$ and the local loss rate $L_i(r)$.
If photochemistry is more important than transport processes, the transport terms can be neglected and the ion continuity equation (6.14) reduces to:

$$\frac{\partial n_i}{\partial t} = P_i - L_i \quad . \tag{6.15}$$

Steady state conditions are assumed for studies at particular heliocentric distances. The number density of ions in the cometary environment can then be found by equating the local ion production rate $P_i(r)$ to the local ion loss rate $L_i(r)$. The spatial asymmetry of the distribution of the neutral gas within the coma is neglected and Equation (6.7) is applied to estimate the local number density of the neutral gas $n_n(r)$. The local ion loss rate is calculated from Equation (6.12) and the ion production rate is $P_i = I_i\, n_n$, with the total ionization rate I_i (see Section 6.4.5). The number density of cometary ions then is ($P_i = L_i$):

$$n_i(r) = \sqrt{\frac{I_i\, n_n(r)}{\alpha(r)}} \quad , \tag{6.16}$$

with the recombination rate α as defined in Equation (6.11). Therefore the number density of ions follows in principle a cometocentric $1/r$ dependency, if the assumption of photochemical equilibrium is applicable. Deviations from this dependency are expected where the recombination rate α is not constant, or if variations of the ionization rate I_i are considered. A general $1/r$ dependency has been observed at 1P/Halley for distances up to approximately 10^4 km [*Altwegg et al.*, 1993].

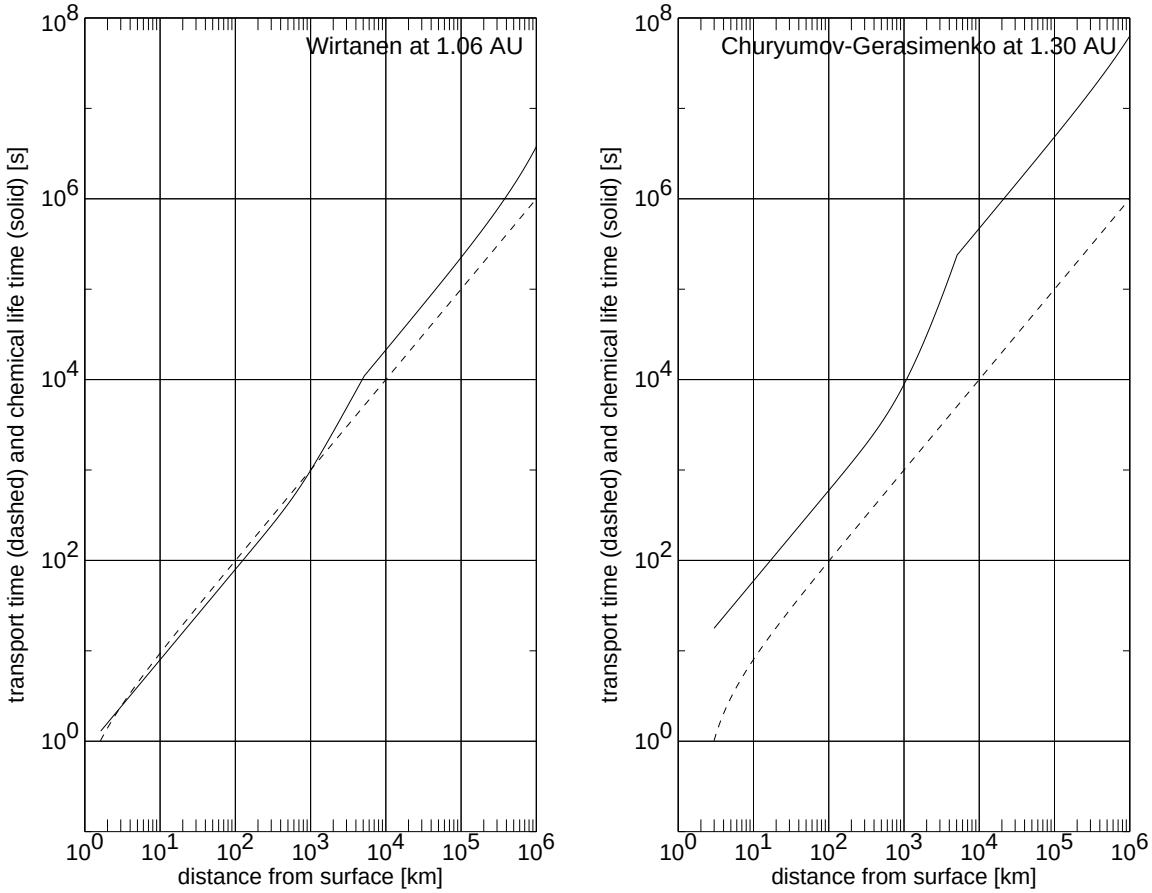

(a) time-scales at 46P/Wirtanen ; solar maximum conditions

(b) time-scales at 67P/Churyumov-Gerasimenko ; solar minimum conditions

Figure 6.11: *Characteristic time scales for ions at 46P/Wirtanen (a) and 67P/Churyumov-Gerasimenko (b) at their respective perihelion distance. Photochemical equilibrium can be assumed when the chemical lifetime of ions (indicated by the solid line) is less than the transport time (indicated by the dashed line).*

Characteristic scales for the chemical lifetime of ions are compared with the transport time of ions in Figure 6.11, in order to estimate the size of the region, where the assumption of photochemical equilibrium can be applied. The chemical lifetime of an H_3O^+ ion is $\tau_c = 1/\alpha n_i$. The transport time in the radial flow is estimated as $\tau_t \approx r/v$, with the cometocentric distance r and the plasma velocity v [*Cravens*, 1989]. The plasma velocity is assumed to be controlled by collisions with the neutral particles. It is therefore assumed to equal the velocity v_n of the neutral gas particles, which is of the order of $v \approx v_n \approx 1$ km/s. The assumption of photochemical equilibrium is applicable, if the photochemical lifetime is shorter than the transport time. In Figure 6.11 the time-scales at 46P/Wirtanen and 67P/Churyumov-Gerasimenko are compared at the respective perihelion of the comets.

It can be generally concluded that the assumption of photochemical equilibrium is not necessarily applicable at comets 67P/Churyumov-Gerasimenko and 46P/Wirtanen. The characteristic transport time of ions at comet 67P/Churyumov-Gerasimenko is always shorter than

their chemical lifetime (see Figure 6.11(b)). At comet 46P/Wirtanen at perihelion, the chemical lifetime of ions just reaches the same order of magnitude as their transport time (Figure 6.11(a)). An ionization rate that corresponds to solar maximum conditions is assumed for the 46P/Wirtanen case.

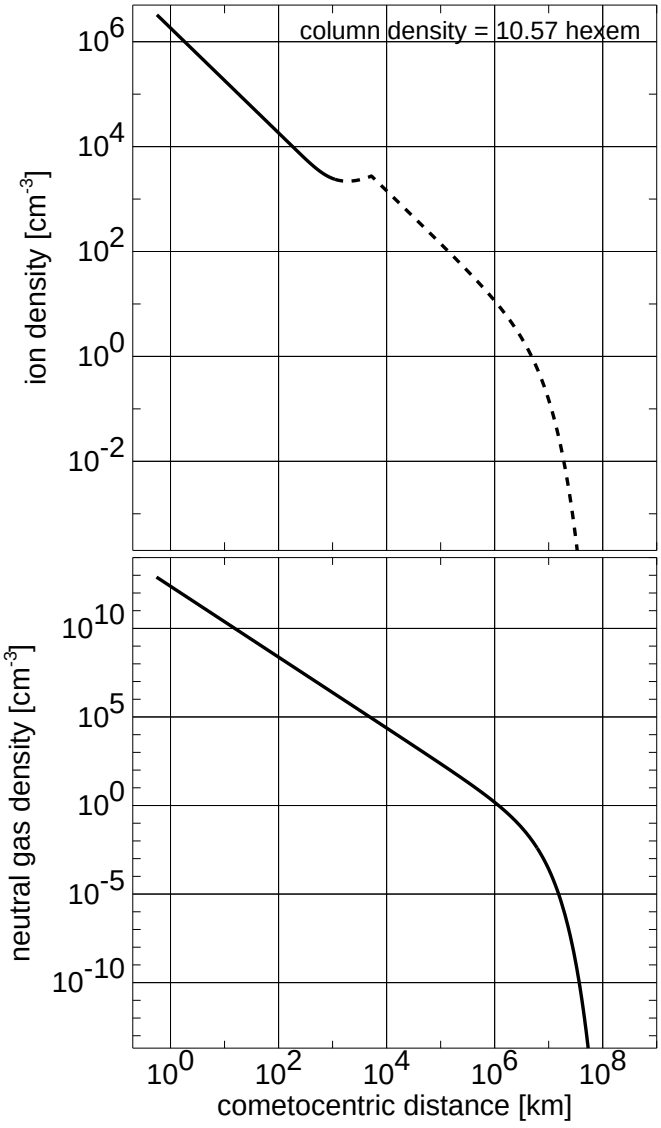

Figure 6.12: *Stationary one-dimensional model of a photochemical controlled coma; Top: ion density, dashed line for results outside the regime where photochemically equilibrium can be assumed; Bottom: Neutral gas density of a spherically symmetric coma; 46P/Wirtanen at perihelion*

In principle, the following is applicable to the coma of comet 46P/Wirtanen at perihelion inside approximately 1000 km (see Figure 6.11(a)). Transport processes are neglected and photochemical equilibrium in the coma is assumed ($P_i = L_i$). The assumed ionization rate I_i at 1 AU is taken from Section 6.4.5, the ion production rate then is $P_i(r) = I_i n_n(r)$, with the number density of neutral gas $n_n(r)$ as derived from Equation (6.7). The dissociative recombination rate of ions is determined as described in Section 6.4.7. With these assumptions the number density of ions in the inner coma can be derived from Equation (6.16).

In Figure 6.12 the resulting ion and neutral gas number densities are plotted. At the ionization scale length of $\sim 10^6$ km the number density of the neutral particles shows the drop off due to the exponential term in Equation (6.7). The ion number density generally follows the same pattern with the exception of the region where the electron temperature rises, which leads to the local maximum at $r \approx 5 \times 10^3$ km. In this region the recombination rate decreases due to increasing electron temperature. The ion number density has the largest values close to the surface, because the coma is assumed to remain optically thin. The assumption of photochemical equilibrium is, in the case studied here, not applicable beyond $r \approx 10^3$ km (see Figure 6.12) and the ion densities at larger distances are therefore not correctly estimated. This is indicated by using a dashed line for larger distances.

6.5.2 Case 2: Numerical Solution of the 1D Continuity Equation

The assumption of photochemical equilibrium is not applicable, if the transport terms in the continuity equation (6.14) can not be neglected. The full 1D continuity equation then has to be solved in order to derive the ion density within the cometary coma. Interaction with the solar wind is neglected and it is again assumed that the radial velocity of the plasma is the same as the outflow speed of the neutral gas ($v_r \approx v_n \approx 1$ km/s), due to collisions between ions and neutral particles. This is applicable in the collision dominated inner coma and at larger distances if other possible acceleration mechanisms (such as e.g. external magnetic fields) are neglected. The continuity equation for the neutral gas is used to to write:

$$\begin{aligned} \operatorname{div} \mathbf{v} &\approx -\frac{1}{n_n}\frac{dn_n}{dt} \\ &= -\frac{1}{n_n}\left(\frac{\partial n_n}{\partial t} + v_n \frac{\partial\, n_n}{\partial r}\right) \quad , \end{aligned} \tag{6.17}$$

with the radial velocity of the neutral gas $\mathbf{v} = v_n \mathbf{e}_r$. By combining Equations (6.14) and (6.17), and assuming stationarity one gets:

$$\frac{v_r}{n_i}\frac{\partial n_i}{\partial r} - \frac{v_r}{n_n}\frac{\partial n_n}{\partial r} = \frac{P_i(r) - L_i(r)}{n_i} \quad . \tag{6.18}$$

The application of this scenario is limited to inside 10^6 km cometocentric distance, which is approximately similar to the ionization scale length. Therefore the exponential term in Equation (6.7) is neglected. When also applying $P_i(r) = I_i\, n_n$ and $L_i(r) = \alpha\, n_i^2$ one gets:

$$\frac{\partial n_i}{\partial r} = \frac{I_i Q_g}{4\pi v^2 r^2} - \frac{\alpha n_i^2}{v_r} - \frac{2n_i}{r} \quad . \tag{6.19}$$

In order to numerically solve this equation, a Runge-Kutta scheme is applied (see e.g. *Press et al.* [1986]). The solutions for various heliocentric distances are plotted in Figure 6.13. The gas production rate of comet 67P/Churyumov-Gerasimenko with respect to the heliocentric distance was derived from Equation (4.27), the ionization and recombination rates were determined as described in Sections 6.4.5 and 6.4.7. The dashed line represents the case 1 scenario (photochemical equilibrium assumed) for a heliocentric distance of 1.3 AU. The corresponding solution of Equation 6.19 at 1.3 AU has much lower ion densities and does not feature the local peak at 6×10^3 km, because the second term on the right-hand side is not strong enough to have any visible effect in this scenario. At the surface, the initial ion density is assumed to be very small ($n_{i0} = 10^{-6}$ cm^{-3}). Therefore the density rises at first then follows an $1/r$ dependency. The same pattern is visible at all heliocentric distances studied out to 4 AU, with decreasing absolute values due to the decreasing gas production rate with increasing heliocentric distance.

A more comprehensive model including the interaction with the solar wind and the interplanetary magnetic field is needed in order to model a more realistic ion density distribution within the cometary ionosphere. The above approximation at least gives reasonable orders of magnitude of the cometary contribution to the ion column density, which is the quantity that can be measured with the RSI experiment, if the ion densities are large enough.

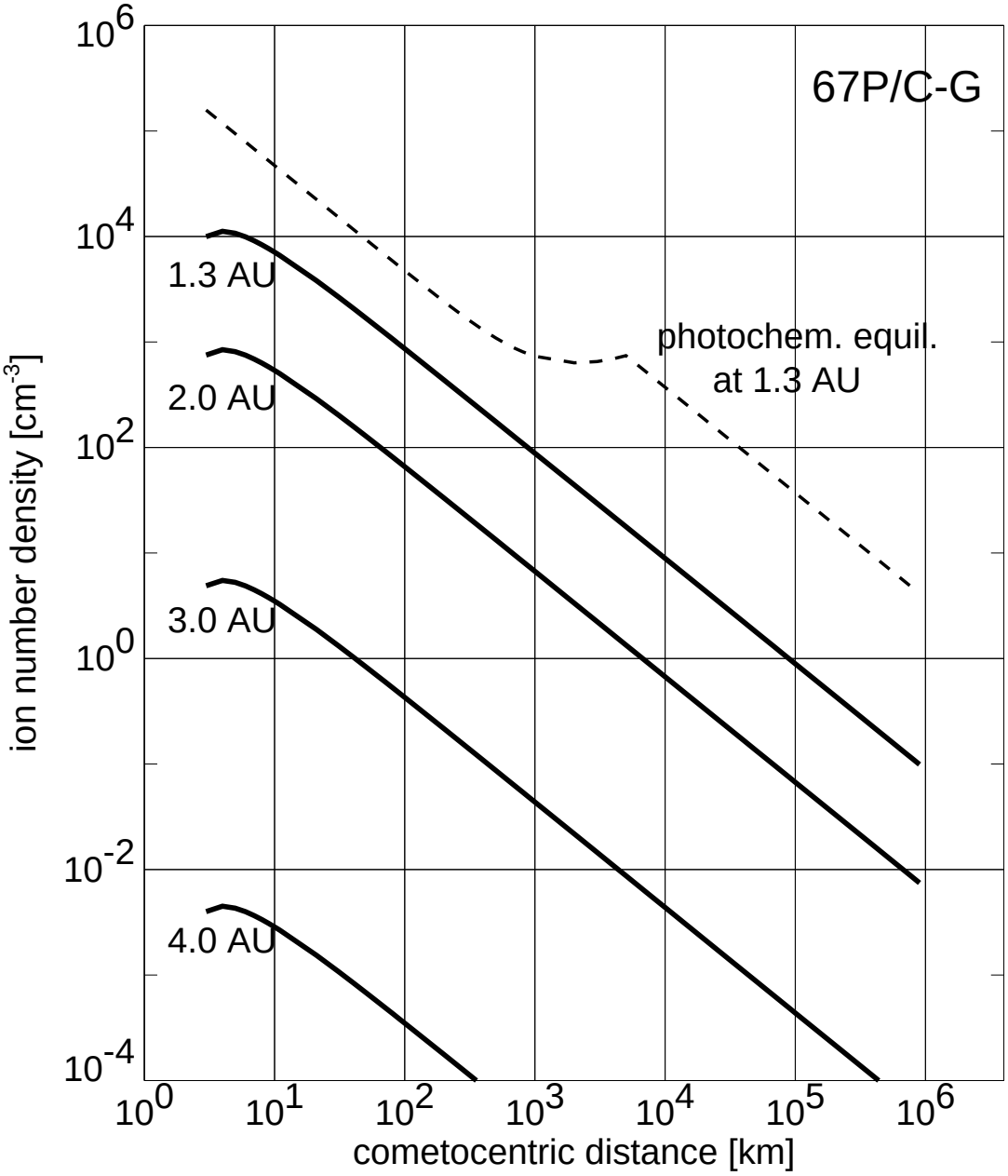

Figure 6.13: *Number density of ions at various heliocentric distances; Numerical solution of Equation (6.19)*

6.5.3 Conclusions

In relation to the ion pile-up region observed at 1P/Halley one can conclude from these calculations that a similar pile-up of ions at 67P/Churyumov-Gerasimenko or 46P/Wirtanen is not expected. The steep rising of the electron temperature profile at the TEC does not result in a significant change of the ion density. The full solution of the continuity equation without the assumption of photochemical equilibrium does not feature this pile-up. If at comets 67P/Churyumov-Gerasimenko or 46P/Wirtanen an ion pile-up is observed at all then other explanations, like locally enhanced ionization processes or dynamic effects, will be needed. The electron temperature profiles considered here have only a very minor effect on the ion distribution within the coma for the scenario of case 2.

The total column density along the comet-sun axis as derived from the results in Section 6.5.2 are listed in Table 6.3. These are integrated densities from the surface out to 10^6 km cometocentric distance, which is a rough estimate of the cometary contribution to the plasma content along the comet-sun axis.

r_h [AU]	column density [cm^{-2}]
1.3	9.1×10^{10}
1.5	4.6×10^{10}
2.0	6.9×10^{09}
2.5	7.0×10^{08}
3.0	4.5×10^{07}
3.5	1.7×10^{06}
4.0	3.7×10^{04}

Table 6.3: *Estimated column densities of ions (electrons) from the surface along the comet-sun axis for various heliocentric distances, see text for details*

No strong effects on the carrier signal are expected in relation to RSI in general. The sensitivity of RSI for variations of the electron content in the line of sight is of the order of 10^{-2} hexem at one second integration time [*Pätzold et al.*, 2000], with 1 hexem $= 10^{12}$ cm^{-2}. The sensitivity of RSI to determine the total electron content in the line of sight is of the order of 1 hexem. The relative velocity between spacecraft and comet is relatively low (of the order of m/s [*Pätzold et al.*, 2001]) when compared with flyby velocities of other cometary missions (of the order of km/s). The variation of the electron content in the line of sight is therefore expected to result from the variation of the plasma density in the cometary coma and not from the changing observational geometry. The variation of the electron content in the line of sight of the carrier signal can be obtained with RSI, if the orbit of the spacecraft has a favorable geometry for this objective. Eclipses of the spacecraft are the most promising scenarios to determine column densities.

Apart from the simplifying assumption of spherical symmetry, the global gas production rate Q_g may also vary with time. With the assumed radial outflow velocity of $v_n \approx 1$ km/s, the distribution of the neutral gas at 10^6 km distance reflects the gas production of ~ 10 days earlier. The variation of Q_g with time may therefore have an effect on in-situ measurements of the ion density which is not accounted for in the model. This problem has also been noted by e.g. *Huddleston et al.* [1993].

A three-dimensional MHD-model would be required to cover the ionosphere in more detail without many of the limiting assumptions. This is beyond the scope of this work. Since the detectability of the ionosphere with RSI will be a challenging task, the detailed structure of the ionosphere is not studied here.

6.6 Interaction with the Solar Wind

The comet - solar wind interaction is studied in this section. The solar wind is mass loaded and various plasma features in the cometary environment are formed. Standoff distances for the bow shock, the collisionopause and the cavity surface are derived. They strongly depend on the heliocentric distance and cometary activity. A one-fluid MHD approach is used to estimate the size of the interaction regions, although this approach simplifies the multi-fluid environment, as has been pointed out by e.g. *Sauer et al.* [1990]. However, with

the MHD approach an estimate of the size of the main plasma boundaries is possible, as has been shown at comets 1P/Halley and 26P/Grigg-Skjellerup. More detailed simulations of the plasma environment with a multi-fluid model can be found in e.g. *Sauer et al.* [1996] or *Sauer and Dubinin* [1999].

6.6.1 Cometary Pick-up Ions in the Solar Wind

Neutral cometary particles are ionized by solar UV radiation and added to the ambient solar wind plasma. These freshly ionized cometary particles modify density, momentum and energy of the plasma flow. This process is called *mass loading* or *pick-up*. In a reference frame at rest with the interplanetary magnetic field the pick-up process depends on the orientation of the velocity of the cometary ions. For a perpendicular orientation, the pick-up is controlled by the macroscopic fields and an adiabatic approximation with a ratio of the specific heat of $\gamma = 2$ can be adopted. If the orientation is oblique, the distribution of the injected particles is isotropized and plasma instabilities dominate the coupling between cometary and solar wind ions. The ratio of specific heats becomes $\gamma = 5/3$ in that scenario (see e.g. *Flammer* [1991] for more details).

The pick up process is handled as simple as possible in this work, i.e. that the ions are immediately embedded in the solar wind flow, with a perpendicular orientation between the solar wind velocity and the interplanetary magnetic field. Only the contribution of the mass of the ionized particle is considered.

The mass flux ratio is denoted here as $\hat{x} = \rho\mathbf{v}/\rho_{sw}\mathbf{v}_{sw}$, with the unperturbed mass flux of the solar wind $\rho_{sw}\mathbf{v}_{sw}$. *Biermann et al.* [1967] determined a critical value of $\hat{x}_c = 4/3$ for the mass flux ratio, at which the *mass loaded* or *contaminated* solar wind forms a shock. From numerical models values of $\hat{x}_c = 1.185$ for $\gamma = 2$ and $\hat{x}_c = 1.323$ for $\gamma = 5/3$ were obtained for a sonic Mach number of $M \approx 2$ at the shock front [*Flammer*, 1991].

Following *Cravens* [1989] and *Huddleston et al.* [1990], a single species of ions moving radially outward from the nucleus at a constant velocity v_i is assumed. The velocity of the ions v_i is assumed to be similar to the outflow velocity of the neutral gas $v_n \approx 1$ km/s. A constant photoionization rate, depending on the solar activity, and constant charge exchange and collisional ionization rates, which depend on the instantaneous solar wind flux, are applied. The total ionization rate I_i is given in Section 6.4.5. The density of cometary neutral particles n_n is given in Equation (6.7).

Since $v_i \ll v_{sw}$, only the mass of the freshly ionized cometary particles contributes significantly to the mass flux. The cometary ion flux along the comet-sun axis at point x_0 can then be derived by integrating the ion production rate back along the axis, which is assumed to be the trajectory of the implanted ions:

$$n_i v_i = \int_{x_0}^{\infty} \frac{Q_g\, I_i}{4\,\pi\, v_n\, r^2} \;\; exp\left(-\;\frac{I_i\;r}{v_n} \right) \;\; dS \;\; , \tag{6.20}$$

where dS is the integration path.

The total ion mass flux along the comet-sun axis is then given by the solar wind component and the cometary pickup ion source:

$$\rho v = \rho_{sw} v_{sw} + \rho_i v_i \ , \tag{6.21}$$

or in terms of the mass flux ratio (or normalized mass flux):

$$\frac{\rho v}{\rho_{sw} v_{sw}} = 1 + \frac{n_i v_i}{n_{sw} v_{sw}} \ \frac{m_i}{m_{sw}} \ , \tag{6.22}$$

where the ions of the comet are assumed to be of the water group with an effective mass $m_i = 20$ amu, and the solar wind protons plus alpha particles are taken as $m_{sw} = 1.15$ amu [*Huddleston et al.*, 1992]. The mass flux ratio along the comet-sun axis can now be determined by applying Equations (6.20) and (6.22).

6.6.2 Bow Shock / Bow Wave

Biermann et al. [1967] predict steady-state mass loading with cometary ions as long as the normalized mass flux stays below a critical value. When the critical value is reached, a shock forms upstream of the comet, which diverts the flow around the comet. Numerical simulations by e.g. *Schmidt and Wegmann* [1982] show that a shock wave with the Mach number $M \approx 2$ forms in the contaminated solar wind at a cometocentric distance that corresponds to a critical value of $\hat{x}_c = 1.185$. In a MHD model applied to comet 26P/Grigg-Skjellerup the results for the Mach number vary between $M \approx 1.4$ and $M \approx 1.7$ [*Schmidt et al.*, 1993]. The resulting critical value for the mass flux is $\hat{x}_c = 1.09$ for a specific heat ratio of $\gamma = 2$ for the plasma.
Wallis [1973] discusses a weakly-shocked plasma flow and argues that photoionization and charge exchange can gradually and smoothly decelerate the solar wind without the formation of a shock in certain configurations. The term *bow wave* or *bow wave transition* appeared as a description of crossings of a spacecraft into the magnetic sheath region without clear identifications of a shock, as observed at the inbound trajectory of GIOTTO at comet 26P/Grigg-Skjellerup, for example [*Neubauer et al.*, 1993; *Rème et al.*, 1993]. In the work of *Sauer et al.* [1990] the transition at 1P/Halley is described with a multi-fluid approach, which agrees well with the measurements. The plasma interaction of weakly outgassing comets ($Q_g \leq 5 \times 10^{26}$ 1/s) with the solar wind is also modeled by *Bogdanov et al.* [1996], who conclude that no bow shock will appear under such conditions. This would apply to comet 67P/Churyumov-Gerasimenko beyond ~ 2 AU (see Figure 4.7).

In the simplified model of the bow shock used in this work, it is assumed that the solar wind flow is one-dimensional. It is therefore not deflected from its original direction, and the speed is determined by the ions picked up along the streamline and not by the flow on neighboring streamlines.

The density of the neutral gas is derived from Equation (6.7) with the assumption of spherical expansion and constant radial outflow velocity v_n of the neutral particles, taking into account a loss due to photoionization with a rate of I_i. The normalized mass flux is then calculated by

combining Equations (6.20) and (6.22) [*Galeev et al.*, 1985]:

$$\begin{aligned} \hat{x} &= 1 + \frac{Q_g\ m_i\ I_i}{4\pi\ v_n\ \rho_{sw} v_{sw}} \int_r^{\infty} \frac{1}{r'^2}\, exp\left(\frac{-r' I_i}{v_n}\right) dr' \\ &= 1 + \frac{Q_g\ m_i\ I_i}{4\pi\ v_n\ \rho_{sw} v_{sw}} \left[\frac{1}{r} exp\left(\frac{-r I_i}{v_n}\right) - \frac{I_i}{v_n} E_1\left(\frac{r I_i}{v_n}\right)\right] \quad , \end{aligned} \tag{6.23}$$

where the exponential integral $E_1(x) = -Ei(-x)$ can be found in standard mathematical tables, e.g. *Abramowitz and Stegun* [1970]. A solution of Equation (6.23) for the standoff distance of the bow shock R_B can not be expressed in a simple form. The standoff distance R_B can be found by deriving the distance at which $\hat{x} = \hat{x}_c$ for a given shock strength.

If the standoff distance of the bow shock R_B is assumed to be much less than the ionization scale length ($\mathcal{L} = v_n / I_i$), the exponential term in Equation 6.7 can be neglected and Equation (6.23) reduces to [*Biermann et al.*, 1967]:

$$\hat{x} = 1 + \frac{Q_g\ m_i\ I_i}{4\pi\ v_n\ \rho_{sw} v_{sw}}\ \frac{1}{r} \quad . \tag{6.24}$$

The standoff distance of the bow shock R_B can now be found for a specified value of $\hat{x}_c$ in Equation (6.24):

$$R_B = \frac{Q_g\ m_i\ I_i}{4\pi\ v_n\ \rho_{sw} v_{sw}\ [\hat{x}_c - 1]} \quad . \tag{6.25}$$

The condition for a fully developed quasi-perpendicular shock is that R_B is larger than at least an ion gyroradius at the shock front. A typically gyroradius is of the order of 10^3 km at 1 AU and 10^4 km at 4 AU [*Flammer*, 1991].

The variation with heliocentric distance of R_B depends on the heliocentric distance variations of Q_g, I_i and $\rho_{sw} v_{sw}$, which are described in earlier sections. The results for comet 67P/Churyumov-Gerasimenko are plotted in Figure 6.14. The applied critical value of the normalized mass flux is $\hat{x}_c = 1.185$, which is the recommended value for a shock Mach number of $M \approx 2$ and a specific heat ratio of $\gamma = 2$ [*Flammer*, 1991].

6.6.3 Collisionopause and Magnetic Pile-Up Boundary

Three plasma discontinuities were expected prior to the first encounters at comets. The bow shock/bow wave, the cavity surface, and an inner shock, at which deflection of the outflowing cometary plasma toward the downstream region occurs [*Wallis and Dryer*, 1976]. These features are also shown in Figure 6.1. An inner shock has not been observed at 1P/Halley, which was theoretically explained later on. A piling up of cometary ions just inside the cavity surface resulting in an enhanced electron - ion recombination rate with the plasma being neutralized instead of flowing downstream has been suggested by *Cravens* [1989] as an explanation. See e.g. *Flammer* [1991] for more details. An additional boundary was detected at $r \approx 10^5$ km distance by *Gringauz et al.* [1986*b*;*a*], which was named the *cometopause*, and seems to coincide with the predicted so called *collisionopause* (e.g. *Mendis et al.* [1986; 1989]). The data from VEGA observations were interpreted as indicating an increase in cometary ion density, decrease of proton density, heating of protons, and change of flow direction. *Goldstein*

et al. [1992] point out that observations by GIOTTO are inconclusive concerning this boundary layer. A *magnetic pile-up boundary (MPB)* has been observed by the magnetometer in this region [*Neubauer*, 1987], which was referred to as the cometopause by e.g. *Rème et al.* [1987]. After arguments against the 'VEGA-like' concept of a cometopause [*Rème et al.*, 1994], at least the MPB seems to be an established intrinsic cometary feature [*Mazelle et al.*, 1995], since it was also observed by GIOTTO at comet 26P/Grigg-Skjellerup [*Neubauer et al.*, 1993]. It is therefore distinguished only between a collisionopause and a MPB and the name *cometopause* is not used in this work. The region of the collisionopause was modeled with a multi-fluid approach by e.g. *Sauer et al.* [1990], who are able to explain many observations and argue that cometary shocks in the ideal MHD sense do not exist.

However, the collisionopause can be viewed as a transition from the collisionless plasma flow to a flow dominated by collisions with the outflowing neutrals. The strong deceleration of the solar wind is expected to occur at a cometocentric distance along the comet-sun axis of [*Mendis et al.*, 1986]:

$$R_{cl} = \frac{\sigma\, Q_g}{4\,\pi\, v_n}, \tag{6.26}$$

where σ is the collision cross-section. Thus, at R_{cl} the total momentum transfer collision mean free path between the average ion in the inflowing contaminated solar wind and the outflowing cometary neutrals is equal to the radial distance. The distance of the collisionopause may be chemically separated for different species, since the momentum transfer collision cross-sections σ are different for different ions [*Gringauz et al.*, 1986*b*]. The range for typical values of σ given by *Mendis et al.* [1986] is $\sigma \approx (2-3.5)\times 10^{-15}$ cm^2. The subsolar distance of a collisionopause is estimated by applying a value of $\sigma \approx 3\times 10^{-15}$ cm^2.

The collisionopause is supposed to be relatively sharp, associated with the increasing efficiency of the momentum transfer between the ions and the neutrals due to the continuously decreasing relative velocity at the collisionopause [*Ip*, 1989]. However, during the GIOTTO observations this transition was not as sharp as during the Vega observations [*Balsiger et al.*, 1986] and also a sudden jump in the magnetic field was observed [*Neubauer et al.*, 1986], which was not observed by the VEGA 1 and 2 spacecraft [*Riedler et al.*, 1986]. It has also been noted by various authors before the 1P/Halley missions that the charge exchange effect may play a major role in this interaction region [*Wallis and Ong*, 1975; *Ip and Axford*, 1982; *Galeev et al.*, 1985].

The MPB was observed by GIOTTO at comets 1P/Halley and 26P/Grigg-Skjellerup (e.g. *Neubauer* [1987]; *Neubauer et al.* [1993]). It appears as a sharp increase in the magnetic field magnitude, and marks the outer boundary of the induced magnetosphere of the comet where the field line draping becomes efficient in addition to the pile-up effect [*Mazelle et al.*, 1995]. The sharpness was different in inbound and outbound crossings, therefore the detailed nature of this boundary is still under discussion and there seems to be no simple way to estimate the standoff distance of this feature at other comets. At comet 26P/Grigg-Skjellerup, which had an estimated gas production rate of 6.7×10^{27} s^{-1}, the magnetic pile-up region was observed at a length of 2500 km along the GIOTTO trajectory [*Neubauer et al.*, 1993] (the closest approach was at less than 200 km [*Grensemann and Schwehm*, 1993]). If comet 67P/Churyumov-Gerasimenko reaches the same gas production rate around perihelion, a

magnetic pile-up region of comparable size has to be expected. For larger heliocentric distances a more sophisticated model has to be developed to predict the size of the magnetic pile-up region.

6.6.4 Cavity Surface / Ionopause

Inside the collisionopause, the solar wind is rapidly decelerated and chemical reactions and dissociative recombination become important. This also leads to an increase of the magnetic field strength and the magnetic barrier region is formed where the solar wind plasma pressure is converted to magnetic pressure. When the outgassing is strong enough the build up of the magnetic barrier terminates at the cavity surface, where the dominant radial forces on a plasma element in this region are balanced, namely the inward directed magnetic $J \times B$-force and the outward ion-neutral frictional force (e.g. *Cravens* [1991*b*]). A region of plasma particles of purely cometary origin is created inside the cavity surface. As a non-magnetized body, the inner region of the cometary coma has no magnetic field and is called magnetic cavity. In the real 3D case, slippage of magnetic flux tubes across the flanks of the cavity attenuates the build up of the magnetic barrier and therefore Ohmic dissipation of currents is expected to be important in this region [*Mendis et al.*, 1986]. The inner edge of the magnetic barrier has been named *contact surface, cavity surface* or *ionopause*. As *Neubauer* [1988] points out, the name contact surface may be misleading, since this boundary can be described as tangential discontinuity and not as contact discontinuity (see e.g. *Landau and Lifschitz* [1967]). The term cavity surface will be used in this work. A number of models study the plasma environment of comets and derive the important processes that lead to the magnetic cavity, see e.g. *Mendis et al.* [1986]; *Baumgärtel and Sauer* [1987]; *Ip and Axford* [1990]; *Cravens* [1989; 1991*b*].

Neubauer [1988] suggests that a pressure gradient at the cavity surface may also contribute to the equilibrium of forces. A possible increase of the sum of the ion and electron temperatures $T_e + T_i$ would create such a gradient. Magnetic field reconnection as discussed by e.g. *Niedner, Jr.* [1984] is mentioned as a possible heating mechanism.

When adding the momentum equations for all species, neglecting mass loading and gravity, one obtains a single fluid momentum equation for the bulk flow velocity $\mathbf{v}$ (e.g. *Cravens* [1991*b*]):

$$\rho \frac{d\,\mathbf{v}}{dt} = \mathbf{J} \times \mathbf{B} - \nabla(p_e + p_i) - \rho \nu_{in}(\mathbf{v} - \mathbf{v_n}) \quad , \tag{6.27}$$

where $\rho = m_i n_i + m_e n_e$ is the plasma mass density, ν_{in} is the ion-neutral momentum transfer collision frequency, p_e and p_i the electron and ion pressure and v_n the outflow velocity of the neutrals. Using Ampére's law, $\nabla \times \mathbf{B} = \mu_0 \mathbf{J}$, the $J \times B$-force can be separated into a magnetic pressure gradient force $-\nabla(B^2/2\mu_0)$ and a curvature force $(\mathbf{B} \cdot \nabla \mathbf{B}/\mu_0)$, with the permeability of space $\mu_0 = 4\pi\,10^{-7}$ H/m (e.g. *Cravens* [1991*b*]). The ion-neutral momentum transfer collision frequency can be written as $\nu_{in} = k_D\, n_n$, where k_D is the ion-neutral collision rate coefficient. The H_2O drag on H_3O^+ is estimated by *Mendis et al.* [1989] to be $k_D \approx 10^{-9}$ cm^3/s. They also estimate that this drag is comparable to or even larger than that between H_2O and H_2O^+. An additional mass loading term was included in the momentum balance

equation by *Haerendel* [1987], which produces only secondary effects [*Cravens*, 1991*b*] and will be neglected here.

The aim here is an estimate of the cometocentric distance of the cavity surface with respect to the heliocentric distance of the comet. A region of stagnant cold plasma in which the magnetic field is amplified and all of the solar wind ram pressure is converted to magnetic pressure is assumed, neglecting curvature effects and obtaining the magnetic field strength B_s in that region as (e.g. [*Ip and Axford*, 1990]):

$$\frac{B_s^2}{2\mu_0} = n_{sw} m_{sw} v_{sw}^2 \quad . \tag{6.28}$$

Analytical expressions for the field strength $B(r)$ at the cavity surface and the cometocentric distance of the cavity surface have been obtained by several authors by integrating the simplified form of the momentum equation (6.27) and usually by assuming photochemical equilibrium at the corresponding distance to derive ion number densities, see e.g. *Mendis et al.* [1989]; *Flammer* [1991]; *Cravens* [1991*b*]. Since the assumption of photochemical equilibrium is not necessarily applicable at comets 67P/Churyumov-Gerasimenko and 46P/Wirtanen, as has been shown in Section 6.5.1, the discussion of *Ip and Axford* [1990] is adopted and the location of the cavity surface R_{CS} is derived as follows:
At the point where B_s reaches its maximum ($dB_s/dr = 0$) it is assumed that the frictional momentum on the plasma due to the radial outflowing neutrals has to be balanced by the curvature force [*Ip and Axford*, 1990]:

$$\frac{B_s^2}{\mu_0 R_{CS}} \approx k_D \, n_i \, m_i \, n_n \, v_n \quad . \tag{6.29}$$

The radius of the curvature is assumed to be similar to the radial distance. The number density of the neutrals n_n is derived from Equation (6.7) with neglection of the exponential term for simplicity, since it is expected that $R_{CS} \ll v_n/I_i$. It follows:

$$R_{CS} \approx \frac{\mu_0 \, k_D \, Q_g \, m_i \, n_i}{4 \, \pi \, B_s^2} \quad , \tag{6.30}$$

with the mean mass of a cometary ion m_i and the ion number density n_i as derived in Section 6.5.2. The condition for a well defined cavity surface is that R_{CS} is larger than the gyroradius of the ions in that region, which is of the order 10^2 km [*Flammer*, 1991].

One main concern about the cavity surface is the stability of this feature. Various authors argue that the ion-neutral frictional force can be destabilizing and that MHD instabilities might occur at the cavity surface (e.g. *Mendis and Houpis* [1982]; *Ip and Axford* [1988]; *Cravens* [1991*b*]). On the other hand, as *Ershkovich et al.* [1989] point out, recombination of ions results in a plasma momentum loss and causes stabilization, although this effect may not be strong enough to quench the instability completely. In an analysis of the stability of the cavity surface, *Ershkovich et al.* [1989] conclude that the cavity surface at 1P/Halley should remain stable and that no effective penetration of magnetic field into the cavity should occur, although possible destabilizing mechanisms do exist. *Ip and Axford* [1990] conclude that the cavity surface is stable when photoionization and recombination effects are accounted for. At comet 67P/Churyumov-Gerasimenko it will therefore be interesting to study the development of a stable cavity surface.

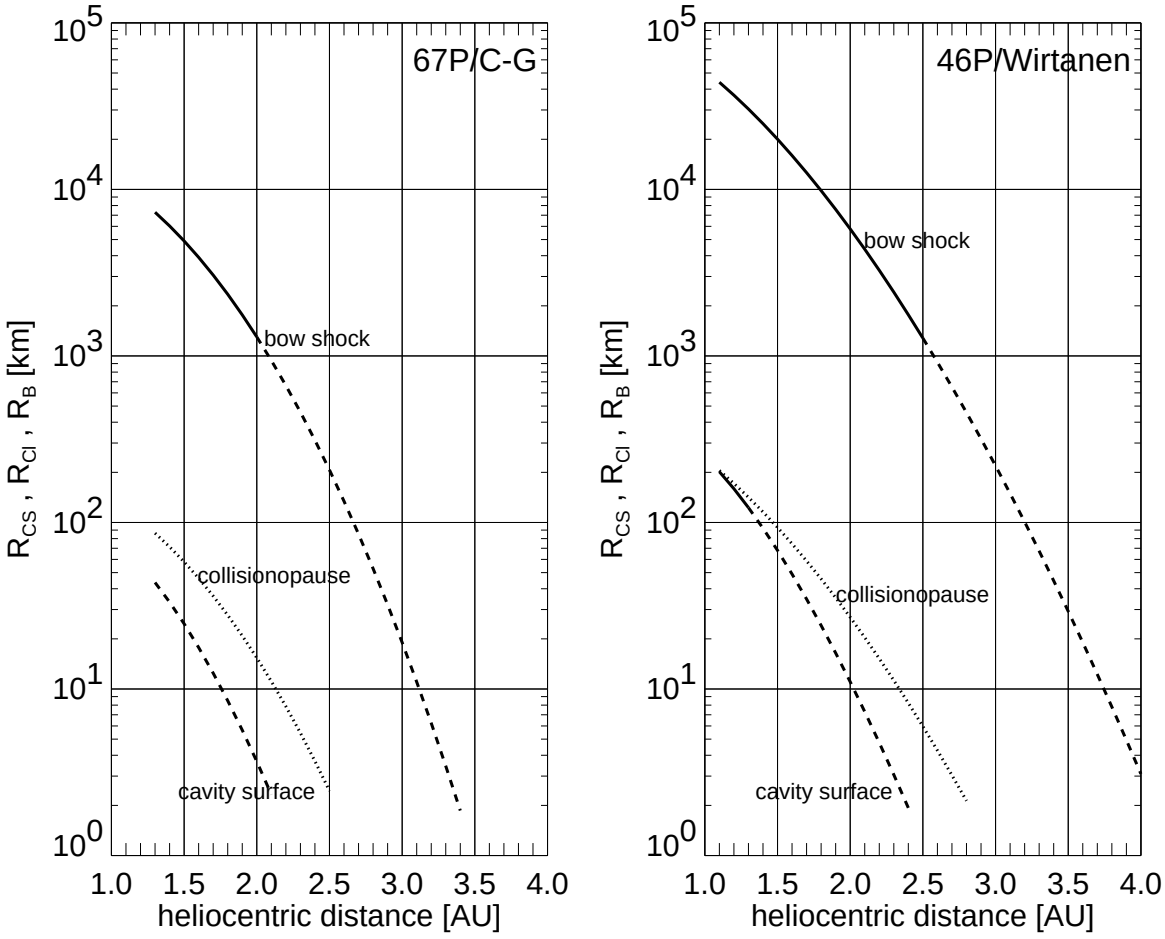

(a) 67P/Churyumov-Gerasimenko

(b) 46P/Wirtanen

Figure 6.14: *Standoff distances of the interaction regions with the solar wind at comets 67P/Churyumov-Gerasimenko and 46P/Wirtanen*

6.6.5 Results for 67P/Churyumov-Gerasimenko and 46P/Wirtanen

The resulting sizes along the comet-sun axis of the main interaction regions for comets 67P/Churyumov-Gerasimenko and 46P/Wirtanen are plotted in Figure 6.14. The sizes are derived as described in the Sections 6.6.2, 6.6.3 and 6.6.4. The differences between the comets appear due to different gas production rates (see Section 4.5) and different ionization rates (solar minimum conditions at 67P/Churyumov-Gerasimenko and maximum conditions at 46P/Wirtanen , see Section 6.3).

The collisionopause depends only on cometary parameters, it therefore does not vary with solar wind conditions and should remain relatively stable at particular heliocentric distances. It is plotted with dotted lines in Figure 6.14. The bow shock and the cavity surface depend on solar wind conditions. The plotted standoff distances therefore are distances expected for average solar wind conditions in the ecliptical plane. The solar wind parameters at 1 AU adopted here are $n_0 = 5$ cm^{-3} and $v_{sw} = 350$ km/s, see Section 6.2 for reference. Dashed lines indicate unrealistic sizes of the features, i.e. when the standoff distance is larger than

the respective estimate of the ion gyroradius. Particularly the size of the magnetic cavity is so small at both comets that it remains questionable whether this feature will fully develop at all.

Comet 67P/Churyumov-Gerasimenko :
At 1.3 AU, the cavity surface is nominally located at $R_{CS} \approx 40$ km subsolar distance (Figure 6.14(a)), which makes its appearance questionable. This standoff distance is slightly less than the estimated cavity surface standoff distance at comet 26P/Grigg-Skjellerup at 1.01 AU: $60 - 80$ km [*Huddleston et al.*, 1992]. This is probably caused by the larger perihelion distance of 67P/Churyumov-Gerasimenko and smaller ion densities at the cavity surface, since *Huddleston et al.* [1992] use a formula for R_{CS}, where photochemical equilibrium is assumed.
The estimated subsolar standoff distance of the bow shock at 1.3 AU is $R_B \approx 7 \times 10^3$ km, slightly less than the observed distance at 26P/Grigg-Skjellerup ($R_B \approx 2 \times 10^4$ km [*Neubauer et al.*, 1993]). This is a result of the weaker gas production of 67P/Churyumov-Gerasimenko and probably also due to differences in the assumed solar wind conditions. The standoff distance is clearly less than the ionization scale length and it is therefore reasonable to apply Equation (6.25).
The standoff distances of the cavity surface and the bow shock decrease quickly with increasing heliocentric distances. An appearance of a fully developed bow shock is therefore not expected outside ~ 2 AU. Bow shock and cavity surface are therefore not expected at the time when ROSETTA is planned to reach comet 67P/Churyumov-Gerasimenko at ~ 3.5 AU heliocentric distance.

Comet 46P/Wirtanen :
The features at 46P/Wirtanen appear at larger cometocentric distances at the corresponding heliocentric distance (Figure 6.14(b)). As mentioned above, this is caused by larger gas production rates and different solar conditions. The features therefore have a better chance to fully develop at comet 46P/Wirtanen. The bow shock might appear inside ~ 2.5 AU and is located at $R_B \approx 4.5 \times 10^4$ km at perihelion. The cavity surface has a subsolar standoff distance of $R_{CS} \approx 200$ km at perihelion. A larger gas production rate and ion number density are the main reasons for the larger standoff distance when compared with the result for comet 67P/Churyumov-Gerasimenko. The standoff distances of the cavity surface and the collisionopause have similar values close to perihelion at 46P/Wirtanen. This is an artificial result, because the ion number density at perihelion of comet 46P/Wirtanen was derived with the maximum of the observed gas production rates, while the gas production rate for the estimation of the distance of the collisionopause was derived from Equation (4.26).

A variation of the solar wind parameters changes the position of the bow shock and the cavity surface. Increasing the number density in the solar wind by a factor of two halves the standoff distances of bow shock and cavity surface. A variability of at least a factor of 2 must be expected in the parameters of the solar wind in the ecliptical plane for the heliocentric distances considered here. The indicated distances in Figure 6.14 are therefore estimates for average solar wind conditions.

6.7 Transient Solar Events

In this section the effects on the cometary environment of some transient solar events are discussed. Solar flares enhance the radiative solar output and the ionization frequency respectively, and therefore can change the interaction pattern with the solar wind due to enhanced cometary plasma densities, which will be briefly discussed below. The effects of enhanced flux of energetic particles in the solar wind due to solar flares on the cometary environment will not be studied in this work. Interplanetary coronal mass ejections usually feature enhanced plasma densities, larger plasma velocities and enhanced magnetic field strength, which has an effect on the global interaction pattern of the comet with the solar wind, as will be presented below. Flares and CMEs occur more often during the maxima of the solar activity cycle. Therefore the mission scenario at comet 46P/Wirtanen would be more convenient for observations than the mission scenario at comet 67P/Churyumov-Gerasimenko (see Section 6.3).

6.7.1 Solar Flares

Solar flares are generally described as transient energy releases in sunspot regions. They feature enhanced radiation across the electromagnetic spectrum and release energetic particles into the interplanetary space. It is distinguished between impulsive and gradual flares. Fully developed flares combine these basic types and feature a brightness increase (typically several minutes long, the 'impulsive' or 'flash' phase), with bursts in γ-rays, *x*-rays, EUV and microwave radiation, followed by a slow decay (30 minutes to hours long, 'main' or 'decay' phase). Large flares may be visible in the optical range as 'white-light' flares [*Stix*, 1989].

Satellite observations of flare emissions are made in different spectral bands: usually *x*-ray, EUV, UV and optical. The EUV and UV bands are interesting in the context of enhanced ionization frequencies at comets. Typically, the energy flux of flares peaks with a normalized value of $1.1 - 1.6$ [*Horan et al.*, 1983]. Some flares might even reach a factor of $2 - 3$ of the normal energy flux, which has been observed at different heliocentric distances [*Horan et al.*, 1982; *Kazachevskaya et al.*, 1990; *Neidig et al.*, 1994].

When modeling effects of solar flares on the cometary environment, the ionization rate can be increased by a factor of $2 - 3$ for a particular time period in the order of the flare duration. This results in transient increased ion densities. The increased ion densities would mainly effect the standoff distance of the cavity surface and the column density of ions and electrons. Since the appearance of the cavity surface is questionable, and the timescales of the activity of flares is relatively short, further studies were not carried out. Effects on RSI are expected to be minor.
The enhanced ionization rate can also increase the standoff distance of the bow shock, which is plotted in Figure 6.15 for an ionization rate increased by a factor of three. The real effect of a flare on the bow shock distance is expected to be much smaller, due to the small timescale of the flare.

6.7.2 Coronal Mass Ejections

Coronal Mass Ejections (CMEs) are large explosion-like events in the solar corona that usually have curvilinear shapes, suggesting magnetically closed regions that are eruptively blown out. They apparently result from a restructuring process of magnetic fields in the low corona. Their spatial distribution varies with solar activity, occurring at all solar latitudes during solar maximum and mainly in equatorial regions during solar minimum. The rate of CMEs depends on the sensitivity of the coronograph used. Observations by the SOHO LASCO instrument indicate a rate of about 0.8 CMEs per day at solar minimum and about an order of magnitude larger during a solar activity maximum [*Lang*, 2001].
When ICMEs (Interplanetary CMEs) are observed in situ, they are usually identified from several plasma signatures, e.g. the presence of bidirectional halo electrons, high alpha/proton density ratios or low proton temperatures. They are often coincident with magnetic clouds, which feature high magnetic field intensities and a rotation of the IMF by $\sim 180^{\circ}$ [*Smith et al.*, 2001]. A large event with a high level of transient activity was observed e.g. around 14 July 2000, which was named *The Bastille Day Event*. The observed transit speed of the Bastille Day shock at 1 AU was 1480 km s^{-1} [*Watari et al.*, 2001].
In order to model effects of ICMEs on the cometary environment (see Section 6.7.3), the number density of the solar wind plasma is enhanced by a factor of ten and the solar wind velocity by a factor of two, which is consistent with observations of CMEs at 1 AU (see e.g. *Smith et al.* [2001]). For larger heliocentric distances the jump in the velocity has decreased, as is noted by e.g. *Burlaga et al.* [2001]. Since the model is only applied to the comet - solar wind interaction inside ~ 2.5 AU, this effect is neglected. Results are included in Figure 6.15.

6.7.3 Possible Effects on Radio Science

The transient events discussed here are expected to occur with a higher probability at comet 46P/Wirtanen, since the proposed mission scenario takes place during or shortly after solar maximum, while the proposed mission scenario at comet 67P/Churyumov-Gerasimenko is expected to take place in solar minimum conditions (see Section 6.3).
ICMEs are known to have an effect on the carrier signal and they should therefore be carefully monitored. However, the effects on the cometary environment that are measurable with RSI are expected to be small, so that special strategies are needed to detect them. Since ROSETTA is intended to have a relatively low orbit velocity, fluctuations of the plasma boundaries will only be visible when the considered feature (e.g. cavity surface or bow wave) sweeps across the carrier signal in a favourable observational geometry. This is not expected to happen when the spacecraft is in low orbit around the nucleus. Orbits with a large cometocentric distance might be a possibility to detect plasma boundaries with RSI.

In Figure 6.15 the derived standoff distances of the bow shock are plotted. The line in the center (solid + dashed) is the same as in Figure 6.14. It indicates the average position of the bow shock during undisturbed solar wind conditions. The additional nominal standoff distances of the bow shock during ICME conditions in the solar wind (the lower dotted line) and during conditions produced by a solar flare (the upper dotted line) are plotted. With ICME

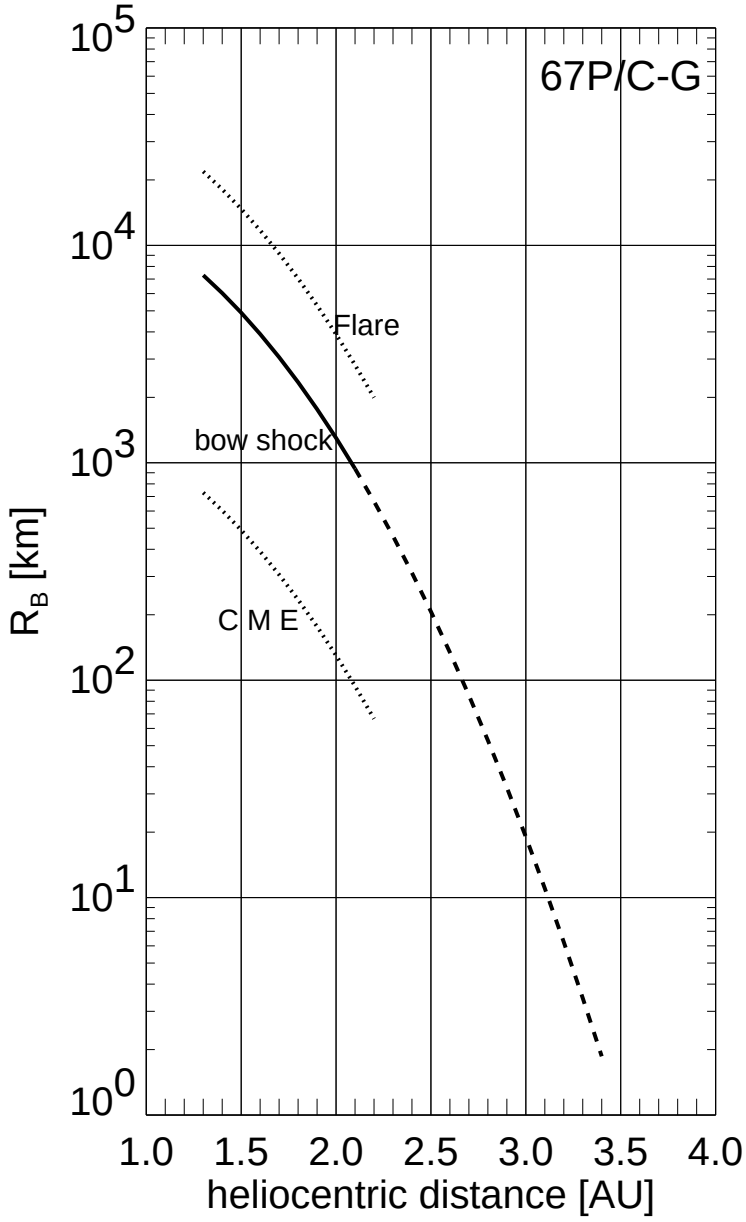

Figure 6.15: *Nominal standoff distances of the bow shock at comet 67P/Churyumov-Gerasimenko (solid + dashed line), additional standoff distances of the bow shock during flare conditions (upper dotted line), and with CME conditions (lower dotted line)*

conditions, the bow shock shifts closer to the comet by about an order of magnitude, which is mainly due to the factor ten enhancement in assumed plasma densities. Such conditions are only applicable during a particular (small) time frame. The lower dotted line therefore represents the standoff distance of the bow shock for a short time period only. After the ICME has passed the comet, the bow shock will return to the average standoff distance that matches undisturbed solar wind conditions. The cavity surface would also shift about an order of magnitude and then reaches the surface of the comet, which is therefore not included in Figure 6.15.

When the ionization rate at the comet incerases due to a solar flare, the standoff distance of the bow shock also increases. Effects of a factor of 3 increased ionization rates are represented by the upper dotted line in Figure 6.15. The standoff distance of the bow shock therefore has

the ability to shift by more than an order of magnitude with the assumed variability in the solar wind conditions.

Transient solar events will be interesting to study, but their effects on the cometary environment may be difficult to detect by radio science alone. If no other measurements at earth are able to monitor the solar CME activity, RSI may be able to report such events in the line of sight.

CHAPTER 7

DISCUSSION AND OUTLOOK

The comprehensive model of a comet and its environment developed here allows the estimate of many physical parameters that can be expected when approaching comet 67P/Churyumov-Gerasimenko with the ROSETTA spacecraft. The main focus of this work is the variation of the physical conditions with the variation of the heliocentric distance of the comet. Many involved parameters have large uncertainties, the results are therefore general estimates of the physical conditions to be expected. The special requirement to predict effects on the radio science experiment RSI on ROSETTA led to the simplification of some involved physical processes.

The modeling of the heat diffusion within the cometary nucleus is needed for the characterization of the physical conditions on the surface with respect to the heliocentric distance of the comet. The focus of the modeling is the determination of local and global gas production rates of the comet. The possible variation of the involved parameters leads to a wide range of possible results. The variation of the composition of the nucleus, its porosity and the effective thermal conductivity within reasonable limits leads to a wide range of possible gas production rates. The model results are compared with remote observations of gas production rates of comets 67P/Churyumov-Gerasimenko and 46P/Wirtanen in order to evaluate the applicability of the considered set of parameters. It is shown that a particular set of parameters does not result in a unique behavior of the sublimation rate with heliocentric distance. In particular the obliquity of the spin axis of the cometary nucleus might have an important effect on the thermal behavior of the cometary nucleus. The thermal model is restricted to spherical shapes of cometary nuclei, since the shapes of comets 67P/Churyumov-Gerasimenko or 46P/Wirtanen are not known to date. Another constraint is the homogeneity of the material, which has the advantage of minimizing computational resources, but which probably has to be changed in future work. The thermal model provides temperatures and local sublimation rates on the assigned grid points on the surface of the nucleus. These grid points match the longitude

and latitude position of the grid point at the inner boundary of the hydrodynamic model of the neutral gas coma. The results are in principle agreement with results from other thermal models, although published model results vary over a wide range. The variation of the gas production rate of comets 67P/Churyumov-Gerasimenko and 46P/Wirtanen with heliocentric distance is described with a fit to the respective model results. This allows a fast first order approximation of physical conditions in the environment of these comets.

The collision dominated regime of the neutral gas coma of the comet is modeled with a hydrodynamic approximation. A fully time dependent, three-dimensional hydrodynamic code, the ZEUS-code, is applied. The size of the hydrodynamic regime is estimated by assuming a spherically symmetric coma. The de-facto applicability is confirmed a-posteriori by comparing the resulting mean free path of the gas particles with their respective cometocentric distance. It turns out that the hydrodynamic regime probably does not enclose the complete cometary nucleus at heliocentric distances of approximately 3AU. The extent of the hydrodynamic regime becomes much larger when the comet approaches the sun, although it is still possible that the night-side coma of a comet remains collisionless (see Appendix D.1). The conditions at the inner radial boundary, at a distance of a few mean free paths above the surface of the nucleus, are determined in accordance with the proposed proceeding by e.g. *Crifo and Rodionov* [1997*a*]. One important difference to the cited work is that the reference pressure used here is not the saturation pressure above a surface of pure ice $p_s(T)$, but the saturation pressure adjusted with the icy area fraction A_0 in order to account for the dust-ice mixture present on the surface.
The model results correspond to the general appearance of cometary comae as a radial expanding gas with velocities of the order of a few hundred meter per second to ~ 1 km/s. A restriction of the gas production to particular areas on the cometary surface might produce discontinuities in the flow that separate regions of different conditions. This applies to the difference between the day-side and the night-side coma, as the scenarios at 67P/Churyumov-Gerasimenko studied in this work indicate. It can also be an effect of areas of different activity (varying the amount of ice available for sublimation), as e.g. the work of *Crifo and Rodionov* [1997*a*] implies.
The gas mass flux within the coma yields an acceleration of a spacecraft in orbit around the considered comet. This acceleration results in orbit perturbations that put the safety of the ROSETTA mission at risk [*Schwinger*, 2001]. It can also perturb the measurement of the higher order gravity coefficients, as e.g. *Pätzold et al.* [2001] point out. The developed model of the inner coma does provide an estimate of this perturbing force with respect to the position of the spacecraft within the coma and with respect to the heliocentric distance. At a heliocentric distance of 3 AU the resulting acceleration of the spacecraft is comparable to or larger than the acceleration due to solar radiation pressure, even if only water ice is assumed as ice component in the nucleus. The difference between day-side and night-side coma can reach many orders of magnitude. At smaller heliocentric distances the gas mass flux will probably perturb orbits with small orbital distances ($\leq$ 10 km) in a way that the orbit can become unbound.

The RSI experiment can also be affected by the ionized component of the cometary coma. The absolute value of the total electron content in the line of sight can be determined from the differential propagation delay of a carrier signal in a two-way mode. A phase shift of the fre-

quency of the carrier signal is expected when the radio wave propagates through an ionized medium. The number density of ions (and electrons) is estimated with a one-dimensional model of the cometary ionosphere in order to evaluate the effect on the carrier signal. The neutral gas coma is assumed to be spherically symmetric in this model. The variation of the solar radiation with the solar activity cycle is taken into account. The state of solar activity is estimated for the mission scenarios at comets 46P/Wirtanen and 67P/Churyumov-Gerasimenko. Since the assumption of photochemical equilibrium is not necessarily applicable at comets 67P/Churyumov-Gerasimenko and 46P/Wirtanen, a one-dimensional continuity equation for the plasma density is solved, neglecting the interaction with the solar wind and assuming quasi-neutrality of the plasma. The electron temperature profile along the comet-sun axis is assumed to be similar to the profile derived at comet 1P/Halley, but scaled to a smaller comet and to larger heliocentric distances. This is done by determining the position of the thermal electron collisionopause (TEC). The electrons are cooled to temperatures of the order 10^2 K inside the TEC by collisions with neutral gas particles. Photoionization and solar wind electrons produce an electron fluid in excess of 10^4 K outside the TEC. The scale size of the transition between these regimes is assumed to be similar to the estimates of the scale size at 1P/Halley.
The resulting ion (end electron) densities in the cometary environment are low so that the possibility of a survey with RSI remains questionable. A special orbit strategy is needed for the determination of the electron content, with a transient occultation of the spacecraft by the comet probably being the most promising scenario.

The standoff distances of various plasma boundaries that appear in the interaction with the solar wind are also estimated. The distances of the bow shock and the cavity surface are derived with magneto-hydrodynamic principles, as successfully applied e.g. at comet 1P/Halley and at 26P/Grigg-Skjellerup (only the bow shock has been detected here). The variation of the standoff distances with heliocentric distance is calculated. The variation of the solar wind parameters with heliocentric distance is also taken care of. The results indicate a much smaller scale size of the interaction pattern when compared with comet 1P/Halley, and a similar or slightly smaller size when compared with comet 26P/Grigg-Skjellerup. A detection with the RSI experiment might be possible when transient solar events, such as solar flares or coronal mass ejections, move these boundaries across the position of the spacecraft or across the line of sight between spacecraft and ground station. In such a scenario it might be challenging to distinguish between the effect of the transient solar event itself and the effect of the cometary contribution on the carrier signal.

The general conclusion concerning RSI is that the neutral coma will have the largest effect on the carrier signal, probably masking the effects of the higher order gravity coefficients. The orbit strategy for ROSETTA needs to be carefully developed not only to accomplish the scientific objectives of RSI, but also to minimize the resulting risk for the complete mission. The effect of the ionized coma is expected to be very small and therefore also needs a favorable orbital strategy to be surveyed.

Future work should include different shapes of cometary nuclei. The effort for the heat diffusion model of the nucleus probably involves mainly the consumption of more computational resources. The effect on the model of the neutral gas coma is then accounted for by applying

the results of the nucleus model as inner radial boundary conditions. A three-dimensional grid that matches the actual shape of the nucleus then needs to be defined. The effect of gas jets within the cometary coma needs also to be evaluated. This can also be achieved by modifying the heat diffusion model of the nucleus. The conditions at each position of a one-dimensional model can therefore be varied.

Detailed models of the conditions at 67P/Churyumov-Gerasimenko or 46P/Wirtanen are only possible when many parameters of their nuclei are determined in greater detail. The knowledge of the shape of the nucleus, as well as the composition of the nucleus and the orientation of the spin axis and spin period will improve the accuracy of the existing models. This will probably not be possible until ROSETTA reaches its target. At this time the real challenge for the modeling begins, because many parameters will be defined with a much better accuracy and the model results can be verified or discarded by measurements. Up to then the models can be used to develop an optimized orbital strategy for ROSETTA.

CHAPTER 8

ZUSAMMENFASSUNG

Das in dieser Arbeit entwickelte Modell eines Kometen und seiner Umgebung ermöglicht die Einschätzung der in der Kometenumgebung zu erwartenden physikalischen Verhältnisse. Motiviert ist diese Arbeit durch die derzeitige Vorbereitung der ROSETTA Mission und insbesondere des Experimentes zur Radiosondierung am Kometen (RSI = Radio Science Investigations). ROSETTA wird nach dem für Februar 2004 geplanten Start den Kometen 67P/Churyumov-Gerasimenko ansteuern und diesen auf seiner Umlaufbahn über mehrere Monate begleiten. Der Komet 46P/Wirtanen ist als Ersatz-Ziel vorgesehen, falls es bei dem Starttermin erneut Probleme geben sollte.
Die prinzipielle Motivation der ROSETTA Mission ist die Untersuchung des Ursprunges von Kometen, der Bedeutung von Kometen bei der Entstehung des Sonnensystems und der Beziehung zwischen Kometen und der interstellaren Materie. Die wichtigsten wissenschaftlichen Ziele des RSI-Experimentes beinhalten die Bestimmung des kometaren Gravitationsfeldes, Untersuchung des Kometenkerns, der Neutralgas-Koma, sowie der Plasmaumgebung des Kometen. In dieser Arbeit wird mit der globalen Modellierung des Kometen die Grössenordnung der zu erwartenden Effekte auf das Radioträgersignal abgeschätzt. Dies dient nicht nur der Einschätzung der Wichtigkeit der einzelnen Effekte, sondern liefert auch die Möglichkeit eine sinnvolle Strategie bei der konkreten Missionsplanung zu entwickeln.

Viele der involvierten Parameter sind derzeit nur sehr ungenau bekannt, da Kometen bisher nicht direkt untersucht werden konnten. Die wichtigsten Ergebnisse sind vom Kometen 1P/Halley bekannt, der 1986 von mehreren Raumfahrzeugen untersucht wurde. Die größte Annäherung erfolgte dabei durch die Mission GIOTTO, die in einer Entfernung von unter 600 km den Kometenkern vorbei geflogen ist.

Die Ergebnisse der Modellrechnungen können nur eine generelle Einschätzung der physikalischen Verhältnisse liefern. Der Schwerpunkt dieser Arbeit liegt auf der Ermittlung der Verhältnisse bei Variation des heliozentrischen Abstandes des Kometen. Die Kometenumge-

bung wird im Wesentlichen durch das Sublimationsverhalten des Kometenkerns bestimmt. Dieses Verhalten wird mit einem eindimensionalen Wärmediffusionsmodell simuliert, welches unter Anderem lokale und globale Gasproduktionsraten berechnet. Die mögliche Variationsbreite der zu berücksichtigenden Parameter erzeugt eine entsprechend große Variationsbreite in den Ergebnissen. So führt zum Beispiel die Variation der chemischen Zusammensetzung des Kometenkerns, der Porosität des Materials oder der effektiven Wärmeleitfähigkeit zu Unterschieden in der sich ergebenden Gasproduktionsrate, die durchaus mehr als einen Faktor 10 betragen können. Um diese Unsicherheiten zu minimieren, wird die simulierte Gasproduktionsrate des Kometen mit Beobachtungsdaten von 67P/Churyumov-Gerasimenko und 46P/Wirtanen verglichen. Mit diesem Vergleich wird also die Anwendbarkeit der gewählten Parameter überprüft. Dabei wird gezeigt, dass ein Satz von gewählten Parametern keine einmaligen Ergebnisse in Bezug auf das Sublimationsverhalten liefert, sondern dass ein ähnliches Verhalten auch auf andere Weise simuliert werden kann. So kann zum Beispiel auch die Neigung der Rotationsachse gegen die Bahnebene des Kometen das Sublimationsverhalten stark beeinflussen. In dieser Arbeit wird das Wärmediffusionsmodell des Kometen nur auf sphärisch geformte Kometenkerne angewendet, da die tatsächliche Form der Kometenkerne von 67P/Churyumov-Gerasimenko und 46P/Wirtanen noch nicht bekannt ist. Eine weitere Vereinfachung stellt die Annahme der Homogenität des Materials dar, welche den Vorteil einer effizienten Nutzung der zur Verfügung stehenden Computer-Ressourcen für zahlreiche Parameter-Studien bietet. Diese Vereinfachung wird mit steigender Entwicklungsstufe der Modelle in Zukunft nicht mehr sinnvoll sein.

Mit dem Wärmediffusionsmodell werden Temperaturen und Sublimationsraten an diskreten Gitterpunkten auf der Oberfläche des Kometenkernes berechnet. Diese Gitterpunkte entsprechen in ihrer Position bezüglich lokaler Längen- und Breitengrade den innersten Gitterpunkten des hydrodynamischen Modells der inneren Neutralgas-Koma. Die Ergebnisse der Kernmodellierungen stimmen mit den Ergebnissen anderer Modelle prinzipiell überein. Dabei ist zu berücksichtigen, dass die bisher veröffentlichten Modelle große Unterschiede in den Ergebnissen aufweisen.
Die Abhängigkeit der Gasproduktionsrate der Kometen 67P/Churyumov-Gerasimenko und 46P/Wirtanen vom heliozentrischen Abstand wird jeweils mit einer Formel beschrieben, die den Ergebnissen der modellierten Gasproduktionsraten angepasst ist. Mit einer solchen Abschätzung lassen sich viele weitere physikalische Bedingungen in den Umgebungen dieser Kometen zumindest grob einschätzen.

Der stoßdominierte Bereich der Neutralgas-Koma wird mit einem hydrodynamischen Modell simuliert. Dabei wird ein numerisches Modell verwendet, das die hydrodynamischen Gleichungen in drei Dimensionen voll zeitabhängig löst. Dieses Modell hat den Namen *Zeus* und wurde an der *University of Illinois,* im *Laboratory of Computational Astrophysics, National Center for Supercomputing Applications* entwickelt. Der innere Rand des simulierten Gebietes liegt dabei nicht unmittelbar auf der Oberfläche des Kometenkernes, sondern befindet sich wenige mittlere freie Weglängen der abströmenden Partikel oberhalb, da die Geschwindigkeitsverteilung der Teilchen in dieser Grenzschicht nicht einer Maxwell-Verteilung entspricht. Erst wenn die Verteilung einer Maxwell-Verteilung entspricht, lässt sich der Bereich mit den makroskopischen Parametern der Hydrodynamik beschreiben.

Die Größe des in dieser Arbeit simulierten Volumens ist variabel und wird abhängig vom Sublimationsverhalten des Kometenkerns gewählt. Die Ausdehnung des hydrodynamischen Regimes wird dazu zunächst, unter der Annahme einer sphärisch symmetrischen Koma mit vorgegebener Gasproduktionsrate, abgeschätzt. Dabei geht man von einem stoßdominierten Bereich aus, solange die mittlere freie Weglänge der einzelnen Teilchen kleiner ist, als der jeweilige Abstand vom Kometenkern. Ob der simulierte Bereich tatsächlich mit einer hydrodynamischen Näherung beschrieben werden kann, lässt sich erst am Ende einer Simulation bestimmen, wenn die Verteilung des Gases in dem Volumen bekannt ist. Dabei ergibt sich für die untersuchten Fälle, dass das hydrodynamische Regime bei einem heliozentrischen Abstand von 3 AE den Kometenkern noch nicht notwendigerweise umschließt, sondern nur ein Teil der Koma auf der Tagseite des Kometen stoßdominiert ist. Bei der Annäherung eines Kometen an die Sonne wird die Ausdehnung des stoßdominierten Bereiches aufgrund der zunehmenden Gasproduktionsrate größer. Auch bei einem Abstand von 1.3 AE kann es vorkommen, dass die Nachtseite der Koma nicht von Stößen dominiert wird, wie aus einem Beispiel im Anhang (D.1) erkennbar ist.

Die jeweiligen Randbedingungen am Übergang vom Kometenkern in die Koma werden entsprechend der vorgeschlagenen Vorgehensweise aus der Arbeit von z.B. *Crifo und Rodionov* [1997*a*] bestimmt. Im Gegensatz zu der zitierten Arbeit wird hier aber nicht der lokale Sättigungsdruck des Gases als Referenzdruck an einem Oberflächenelement verwendet, sondern der Sättigungsdruck wird noch durch einen Faktor modifiziert, der den Anteil an sublimierendem Eis in einem Oberflächenelement beschreibt. Der Flächenanteil von Eis in dem Staub-Eis Gemisch wird dabei aus den Parametern des Kernmodelles berechnet.

Die Ergebnisse der hydrodynamischen Simulation stimmen mit der allgemeinen Vorstellung der inneren kometaren Koma überein. Das sublimierte Gas strömt mit Geschwindigkeiten von einigen hundert Metern pro Sekunde bis ~ 1 km/s im Wesentlichen radial vom Kometen weg. Bei einer Sublimation von diskreten Gebieten auf der Oberfläche können Diskontinuitäten im Gas entstehen, die unterschiedliche physikalische Bedingungen in der Koma räumlich trennen. Dies kann zum Beispiel für Unterschiede zwischen der Koma auf der Tagseite und der Nachtseite zutreffen, wie die Beispiele für den Kometen 67P/Churyumov-Gerasimenko in dieser Arbeit zeigen. Solche Diskontinuitäten können auch auftreten, wenn Gebiete unterschiedlicher Aktivität auf der Oberfläche scharf begrenzt aneinander liegen, wodurch sogenannte Gas-Jets entstehen können (z.B. *Crifo und Rodionov* [1997*a*]).

Der Massenfluss des Staub-Gas Gemisches in der Koma erzeugt eine Beschleunigung eines Raumfahrzeuges, das sich in der Umgebung des Kometen befindet. Die Beschleunigung kann je nach den Ausmaßen des Raumfahrzeuges und der Gasproduktionsrate so groß werden, dass ein gebundener Orbit um den Kometen nicht ohne Weiteres möglich ist. In Bezug auf ROSETTA wird festgestellt, dass die gesamte Mission durch die Möglichkeit eines Absturzes auf den Kometenkern gefährdet ist [*Schwinger*, 2001]. Desweiteren können auch die Messungen des Gravitationsfeldes durch das RSI Experiment gestört werden [*Pätzold et al.*, 2001]. Mit dem hier entwickelten Modell der inneren Koma lassen sich die Kräfte, die durch die Strömung des Neutralgases auf ROSETTA ausgeübt werden abschätzen. Dabei kann die Position des Raumfahrzeuges innerhalb der Koma berücksichtigt werden. Die Abhängigkeit der Größenordnung der Störung vom heliozentrischen Abstand des Kometen wird durch die

Betrachtung unterschiedlicher Fallstudien berücksichtigt. Bei einem heliozentrischen Abstand von 3 AE kann die Beschleunigung von ROSETTA durch den Gasfluss die gleiche Größenordnung erreichen, wie die Beschleunigung durch den Strahlungsdruck der Sonne. Das trifft auch zu, wenn ausschließlich Wasser als Eiskomponente im Kometen angenommen wird. Der Unterschied in der Beschleunigung durch den Gasdruck zwischen Tag- und Nachtseite der Koma kann dabei viele Größenordnungen betragen. Bei größerer Annäherung an die Sonne kann die Beschleunigung durch den Gasfluss erheblich zunehmen.

Der ionisierte Anteil des Gases in der Kometenumgebung hat auch einen Effekt auf das Radioträgersignal von ROSETTA. Der Elektroneninhalt im Sehstrahl kann aus der Bestimmung der differentiellen Laufzeitverzögerung des Radiosignals berechnet werden (z.B. *Pätzold et al.* [2000]). Eine Phasenverschiebung des Signals tritt zudem auf, wenn sich das Radiosignal durch ein ionisiertes Medium ausbreitet. Um die diesbezüglichen Effekte der Kometenumgebung für das RSI Experiment einzuschätzen, wird ein eindimensionales Modell der kometaren Ionosphäre entlang der Achse Komet-Sonne entwickelt. Dabei wird der Einfachheit halber angenommen, dass das Neutralgas eine sphärisch symmetrische Verteilung hat. Die Änderung der solaren Strahlung im UV-Bereich im Verlauf des solaren Aktivitäts-Zyklus wird in dem Modell berücksichtigt. Entsprechend der aktuell verfügbaren Vorhersagen für die Entwicklung des Aktivitätszustandes der Sonne wird angenommen, dass die Sonne im für 67P/Churyumov-Gerasimenko geplanten Missionszeitraum im Aktivitätsminimum ist. Das geplante Szenario für 46P/Wirtanen lässt einen Aktivitätszustand nahe eines solaren Maximums erwarten. Es wird gezeigt, dass für 67P/Churyumov-Gerasimenko und 46P/Wirtanen die Annahme eines photochemischen Gleichgewichtes in der inneren Koma nicht gerechtfertigt ist. Daher wird die Anzahldichte der Ionen in der Koma mit einer Kontinuitätsgleichung für die Ionendichte berechnet. Dabei wird der Einfluss des Sonnenwindes vernachlässigt und Quasi-Neutralität des Plasmas angenommen.

Bei der Berechnung der Plasmadichte geht die lokale Temperatur des Elektronen-Fluids mit ein. Diese kann, wie Messungen bei 1P/Halley andeuten, stark variieren. Ein Profil der Elektronentemperatur entlang der Achse Komet-Sonne wird dazu modelliert. Dabei wird angenommen, dass das Profil im Prinzip dem Temperaturverlauf entspricht, wie er bei 1P/Halley bestimmt wurde, nur dass es entsprechend des Größenunterschiedes zwischen 1P/Halley und 67P/Churyumov-Gerasimenko bzw. 46P/Wirtanen skaliert werden kann. Auch die Variation in Abhängigkeit vom heliozentrischen Abstand des Kometen wird berücksichtigt. Dies wird erreicht, indem die Ausdehnung des Bereiches bestimmt wird, in dem Stöße mit Neutralteilchen die Elektronen effektiv kühlen können. Die äußere Grenzfläche, bis zu der dieser Prozess möglich ist, wird *thermal electron collisionopause* (TEC) genannt. Innerhalb der TEC werden die Elektronen durch die Stöße mit den Neutralteilchen auf Temperaturen von der Größenordnung 10^2 K gehalten. In größeren Entfernungen vom Kometen erreichen die Temperaturen der Elektronen durch den Photoionisationsprozess und durch den Beitrag von Elektronen aus dem Sonnenwind eine Größenordnung von 10^4 K - 10^5 K. Es wird angenommen, dass die Ausdehnung des Überganges zwischen diesen beiden Regionen von den Abschätzungen bei 1P/Halley übernommen werden kann.

Das Modell der kometaren Ionosphäre ergibt Anzahldichten für Ionen (und Elektronen), die so niedrig sind, dass eine Untersuchung mit dem RSI Experiment aufgrund des Auflösungs-

vermögens schwierig werden dürfte. Eine günstige Orbitstrategie wird nötig sein, um den kometaren Beitrag zum Elektroneninhalt im Sehstrahl überhaupt bestimmen zu können. Am vorteilhaftesten erscheint diesbezüglich eine Bahn, die eine vorübergehende Bedeckung der Raumsonde durch den Kometen beinhaltet, da in diesem Fall Regionen mit unterschiedlichen Eigenschaften mit dem Sehstrahl relativ schnell durchlaufen werden können.

Bei der Wechselwirkung des kometaren Plasmas mit dem Sonnenwind und dem interplanetaren Magnetfeld treten Grenzflächen auf, die mit den Methoden der Magneto-Hydrodynamik beschrieben werden können. Die kometozentrischen Abstände dieser Grenzflächen werden hier dementsprechend abgeschätzt. Dieses Vorgehen lieferte bereits bei dem Kometen 1P/Halley und 26P/Grigg-Skjellerup sinnvolle Ergebnisse. In dieser Arbeit werden die Abstände der Bugstoßwelle, der Ionopause und der sogenannten *Collisionopause*, die den Übergang vom stoßfreien Bereich in den von Stößen mit kometaren Neutralteilchen dominierten Bereich markiert, in Abhängigkeit vom heliozentrischen Abstand des berücksichtigten Kometen berechnet. Dabei geht die Variation der Parameter des Sonnenwindes in Bezug auf den Abstand von der Sonne mit ein. Die Ergebnisse zeigen, dass der Bereich der Wechselwirkung mit dem Sonnenwind bei den Kometen 67P/Churyumov-Gerasimenko und 46P/Wirtanen kleiner ist, als bei 1P/Halley. Die Größenordnung ist vergleichbar mit den beobachteten und modellierten Verhältnissen beim Kometen 26P/Grigg-Skjellerup. Eine Erkennung der Grenzflächen mit dem RSI Experiment scheint möglich, wenn transiente solare Ereignisse, wie zum Beispiel Effekte durch solare *Flares* oder koronale Massenauswürfe, diese Grenzflächen über das Raumfahrzeug hinweg oder durch den Radiostrahl bewegen. In einem solchen Fall dürfte allerdings auch die Trennung von der interplanetaren Störung und dem kometaren Beitrag im Radioträgersignal anspruchsvoll sein.

Mit Bezug auf das RSI Experiment lässt sich zusammenfassen, dass der größte Effekt auf das Radioträgersignal durch die Neutralgas-Koma erwartet wird. Die Bestimmung des Gravitationsfeldes des Kometenkerns kann dabei beeinträchtigt werden. Eine Strategie für die Umlaufbahn um den Kometenkern muss unter diesem Gesichtspunkt entwickelt werden. Dieser Schluss bezieht sich nicht nur auf die wissenschaftlichen Ziele des RSI Experimentes, sondern zusätzlich auf die Sicherheit der gesamten ROSETTA Mission. Es wird nur ein kleiner Einfluss des kometaren Plasmas auf das Radioträgersignal erwartet, daher wird auch hierfür eine günstige Strategie bei der Wahl der Umlaufbahnen nötig sein.

In künftigen Arbeiten sollte der Einfluss von anders geformten Kometenkernen genauer analysiert werden. In Bezug auf das Modell der Wärmediffusion im Kometenkern wird der Arbeitsaufwand nach der Festlegung sinnvoller Randbedingungen im Wesentlichen einen höheren Rechenaufwand bedeuten. Der Effekt auf die Neutralgasumgebung geht dann direkt über die Bestimmung der Randbedingungen ein. Der Aufwand bei der hydrodynamischen Simulation besteht dann im Wesentlichen darin, ein der Form des Kometen angepasstes Gitter zu definieren.
Der Effekt von Jets in der Koma sollte ebenso genauer untersucht werden. Auch das kann erreicht werden, indem das Modell des Kometenkerns modifiziert wird. Dazu können die Modellparameter an jedem Oberflächenelement einzeln variiert werden.

Detailliertere Modelle der Kometen 67P/Churyumov-Gerasimenko und 46P/Wirtanen sind voraussichtlich erst möglich, wenn viele der Modellparameter besser bestimmt sind. Die

genauere Kenntnis der Form des Kometenkerns, seiner chemischen Zusammensetzung, der Lage der Rotationsachse und der Rotationsperiode wird die Genauigkeit der derzeit existierenden Modelle deutlich verbessern können. Dies wird vermutlich erst möglich sein, sobald ROSETTA den Zielkometen erreicht. Erst dann werden die Ergebnisse der gegenwärtigen Modelle wirklich bewertet werden können. Bis dahin müssen die heutigen Kenntnisse zur Optimierung der Orbit-Strategie für ROSETTA verwendet werden.

APPENDIX **A**

PHYSICAL CONSTANTS

S_0	solar constant at 1 AU	1367.0	[W m^{-2}]
AU	astronomical unit	1.4959787×10^{11}	[m]
σ	Stefan-Boltzmann constant	5.670400×10^{-8}	[W m^{-2} K^{-4}]
k_B	Boltzmann constant	$1.3806503 \times 10^{-23}$	[J K^{-1}]
R_g	molar gas constant	8.314472	[J K^{-1} mol^{-1}]
N_A	Avogadro constant	$6.02214199 \times 10^{23}$	[mol^{-1}]
amu	atomic mass unit	$1.66053873 \times 10^{-27}$	[kg]
eV	electron volt	$1.602176462 \times 10^{-19}$	[J]
c	speed of light in vacuum	2.99792458×10^{8}	[m/s]

Table A.1: *Physical constants used in the calculations*

The solar constant is assumed to be constant in the considered time period. It is known that the solar energy output varies slightly with the solar cycle and a small trend is suspected from the available measurements[1]. The implied uncertainty is of the order of 1%.
The other physical constants in Table A.1 are the values recommended by the NIST Physics Laboratory[2].

[1] see e.g. http://remotesensing.oma.be/solarconstant/solar.html for more details
[2] http://physics.nist.gov/cuu/index.html

APPENDIX **B**

FINITE DIFFERENCE SCHEME FOR THE HEAT DIFFUSION EQUATION

The numerical scheme applied to solve Equation (4.22) is a FTCS (Forward Time Centered Space) finite difference approximation. Since Equation (4.22) corresponds to a nonlinear diffusion problem, due to the dependence of the thermal conductivity on temperature, the approximation proposed by *Press et al.* [1986] is used.

$$c_1 \frac{\partial T}{\partial t} = \frac{\partial}{\partial z} D(T) \frac{\partial T}{\partial z} \tag{B.1}$$

is approximated as:

$$c_1 \frac{T_j^{i+1} - T_j^i}{\Delta t} = \frac{D_{j+1/2}\left(T_{j+1}^i - T_j^i\right) - D_{j-1/2}\left(T_j^i - T_{j-1}^i\right)}{(\Delta z)^2} , \tag{B.2}$$

with the subscript i indicating the time steps and the subscript j indicating the discretized space domain, and with

$$D_{j\pm1/2} = \frac{1}{2}\left[D\left(T_{j\pm1}^i\right) + D\left(T_j^i\right)\right] . \tag{B.3}$$

In this formulation D corresponds to the thermal conductivity $k_{\text{eff}}(T)$ and c_1 is $\rho_n c(T)$.

The stability criterion for the scheme (B.2) is [*Press et al.*, 1986]:

$$\Delta t \leq \min_j \left[\frac{(\Delta z)^2 c_1}{2 D_{j\pm1/2}}\right] . \tag{B.4}$$

APPENDIX C

THE THERMAL MODEL APPLIED TO 1P/HALLEY

In Figure C.1 the resulting gas production rates from a thermal model applied to comet 1P/Halley are plotted. The parameter settings are (notation as in Chapter 4) $\rho_n = 800$ kg, $R_{di} = 100$, $h = 10^{-3}$, $A = A_0/r_h$, and $\omega = 0^\circ$. The observed gas production rates are taken from *Fink and DiSanti* [1990] and *Schloerb et al.* [1987]. Production rates derived at the inbound part of the orbit are plotted with diamonds, the outbound measurements are plotted as stars. The dashed line is a fit to the data from *Fink and DiSanti* [1990]. The solid line is the resulting gas production rate from the model run. The effective radius of the spherical model comet is assumed to be $R_c = 5.6$ km. This value and the orbital parameters for comet 1P/Halley are taken from the JPL DASTCOM database[1].

Since no data are available for heliocentric distances larger than $r_h = 2.9$ AU, the large deviation between model results and fit can not be judged. However, since the fit is based on observations alone, it should not be extrapolated beyond $r_h = 2.9$ AU. Inside $r_h \approx 2.0$ AU the model result overestimates the gas production rate. The icy area fraction on the surface is ~ 5 % at perihelion distance. Treating the evolution of the icy area fraction with heliocentric distance differently or taking a possible obliquity $\omega \neq 0^\circ$ into account might produce even better results.
The magnitude of observed gas production rates for comet 1P/Halley can be reproduced with reasonable model parameter settings.

[1] http://ssd.jpl.nasa.gov/dastcom.html

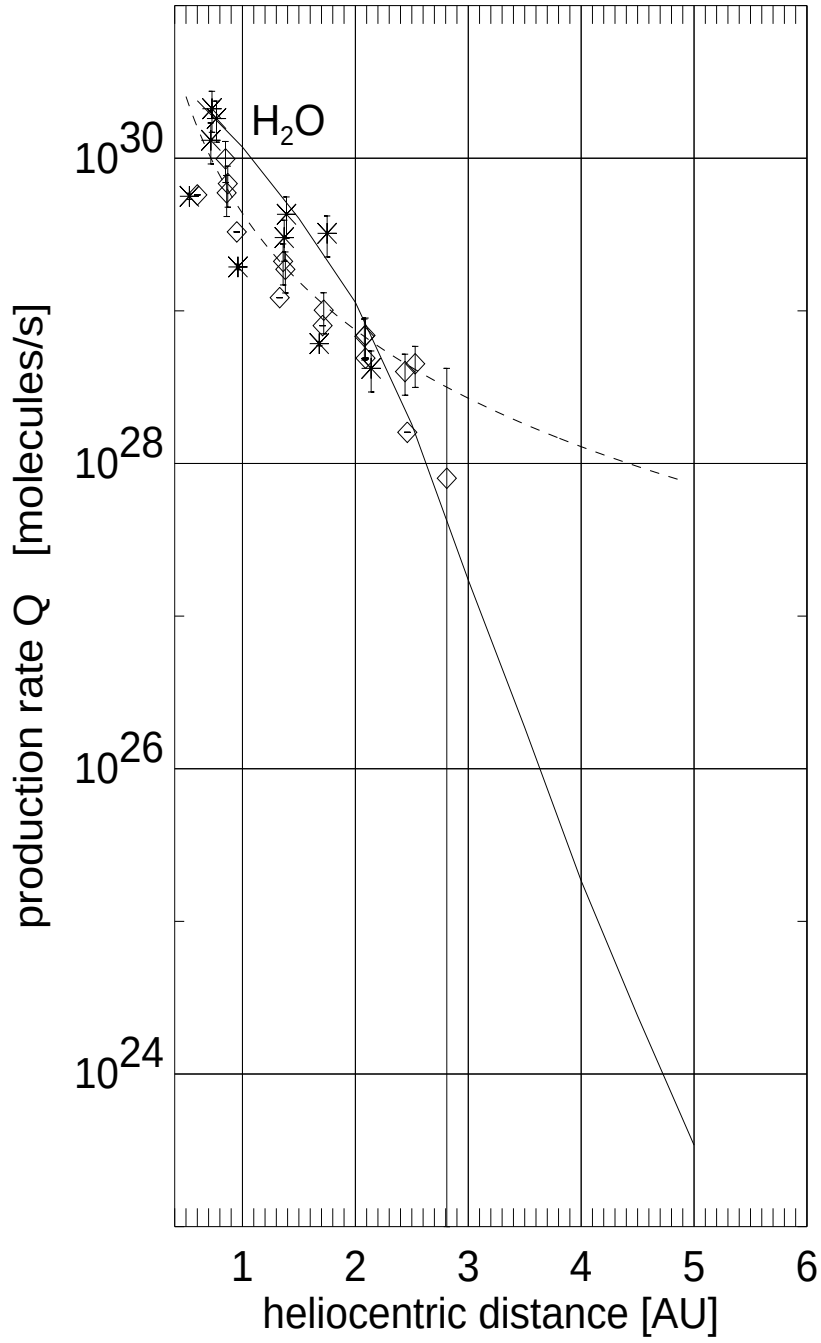

Figure C.1: *Results from the thermal model applied to 1P/Halley. Some observed production rates (diamonds = inbound, stars = outbound), fit to a data-subset (dashed line) [Fink and DiSanti, 1990], and model results (solid line) are plotted.*

APPENDIX **D**

ADDITIONAL RESULTS OF THE COMA MODEL

Two additional results from the hydrodynamic modeling are presented here. The coma of comets 67P/Churyumov-Gerasimenko and 46P/Wirtanen at approximately their respective perihelion distance is modeled. The inner radial boundary conditions are derived from the heat diffusion models of the comets. At comet 46P/Wirtanen an additional constant source of gas is added, accounting for possible sublimating ices from below the surface.

D.1 67P/Churyumov-Gerasimenko at 1.3 AU

Results from the hydrodynamic modeling of the neutral coma of comet 67P/Churyumov-Gerasimenko at 1.3 AU are presented here. The conditions at the inner radial boundary are derived from the results of model M3 of the heat diffusion model of the nucleus. In Figure D.1 isolines of the number density and vectors of the velocity are plotted. The vectors of the velocities are projected in the equatorial plane. The sun is to the left of the chart and the comet spins in an anti clockwise sense. The gas production is almost symmetric to the comet-sun axis. It is dominant on the day-side of the nucleus. The appearance is jet-like caused by the sharp transitions to the night-side coma. This is a result of the large difference of the appearing temperatures between the day-side and the night-side on the surface of the nucleus (see Figure 4.8(c)). The dominant gas expansion on the day-side is bounded by a discontinuity in the terminator region, and therefore the gas is not expanding spherically symmetric. The result is a night-side inner coma that is not dominated by collisions. The velocities in the day-side coma remain at a constant level and the expansion is purely radial. The night-side coma has very low number densities, since no lateral flow from the denser region on the day-side exists.

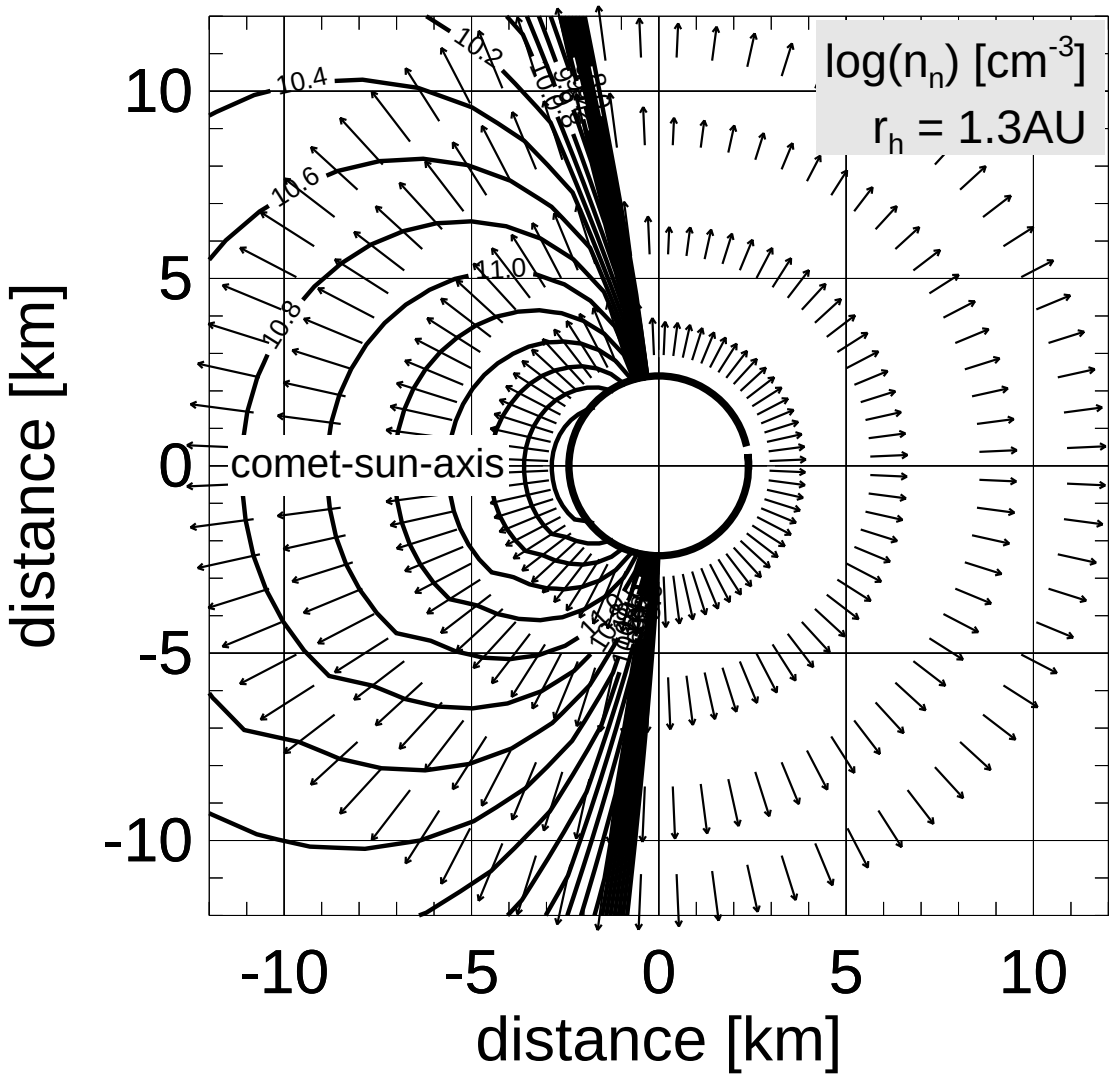

Figure D.1: *Logarithmically scaled number density n_n [cm^{-3}] of the neutral gas. Isolines indicate the distribution of the number density at levels spaced by an uniformly distance of* 0.2*. Velocities are projected in the equatorial plane. The respective length of the plotted arrows indicates the velocity in units of (km/s)*$\times$4*. Exemplary result for 67P/Churyumov-Gerasimenko at* 1.3 *AU.*

The general appearance of the resulting coma is comparable to a spherically symmetric coma on the day-side that is not centered on the origin of the cometocentric coordinate system, but has an offset in the sun direction by about the radius of the comet.

A radial profile at the comet-sun axis of the number density n_n, mean free path of particles mfp, radial velocity v_r, and the resulting acceleration of the spacecraft is plotted in Figure D.2. The dashed lines represent the corresponding number density of a spherically symmetric coma with the same gas production rate (first panel), the cometocentric distance (second panel) and the speed of sound (third panel).

It can be concluded that the gas expands supersonically, that the number density depends on the cometocentric distance with the inverse square, and has larger number densities than a

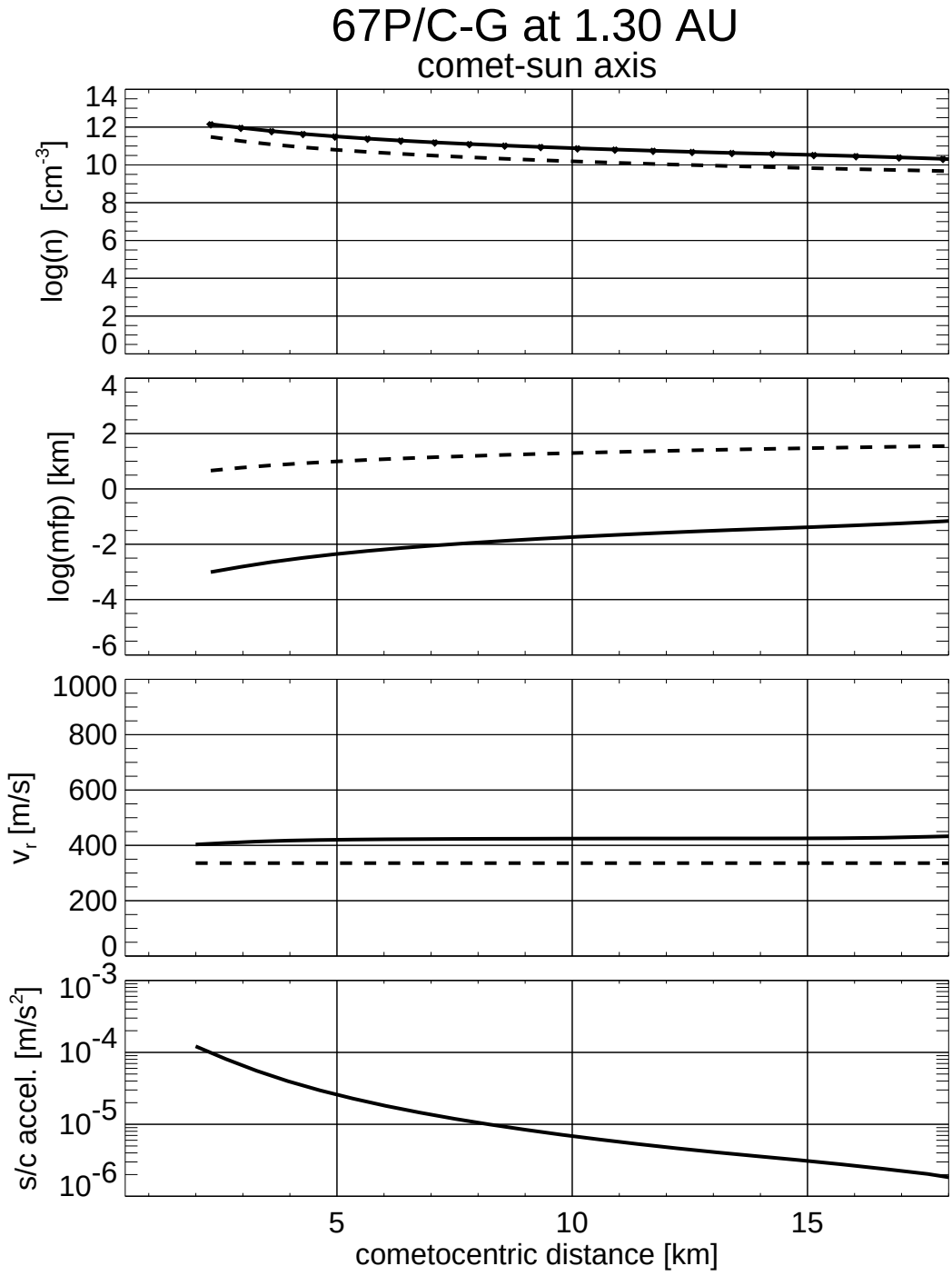

Figure D.2: *Radial profile at comet-sun axis of the logarithmically scaled number density n_n and mean free path of particles mfp, the radial velocity v_r and the resulting acceleration of the spacecraft. Exemplary result at a heliocentric distance of* 1.3 *AU for 67P/Churyumov-Gerasimenko .*

spherically symmetric coma in the day-side part of the coma. The velocity remains at $v_r \approx$ 400 m/s in the inner coma. The resulting absolute of the acceleration of the spacecraft caused by gas drag exceeds the radiation pressure by about 3 orders of magnitude at a cometocentric distance of $r \approx 5$ km.

Profiles on a virtual orbit at a cometocentric distance of 5 km in the equatorial plane are plotted in Figure D.3. Included in the plot are the number density, the radial component of the velocity, and the resulting acceleration of the ROSETTA spacecraft. The number density

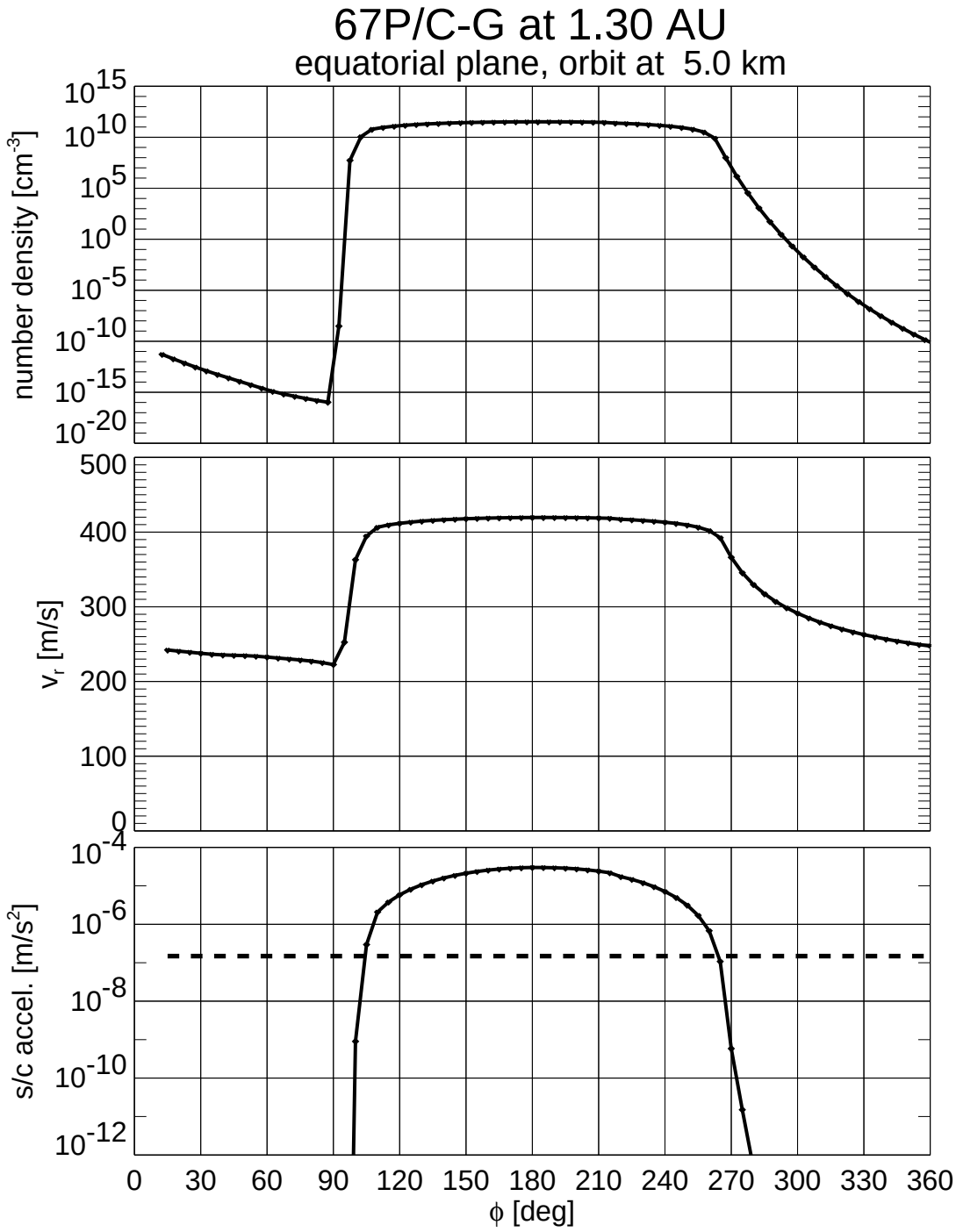

Figure D.3: *Profile in the equatorial plane of 67P/Churyumov-Gerasimenko of the number density n_n, the radial velocity component v_r and the resulting acceleration of the spacecraft. Exemplary result at a heliocentric distance of* 1.3*AU.*

differs many orders of magnitude between the day-side and the night-side coma. The more gradual decrease on the evening side $\Phi = 270^\circ$ results from the temperature distribution on the surface. The radial gas velocities on the day-side coma are also larger than on the night-side. The acceleration of the spacecraft exceeds the acceleration caused by the radiation pressure (indicated by the dashed line in the third panel of Figure D.3) by about two orders of magnitude. The radiation pressure is dominant for this scenario on the night-side part of the orbit.

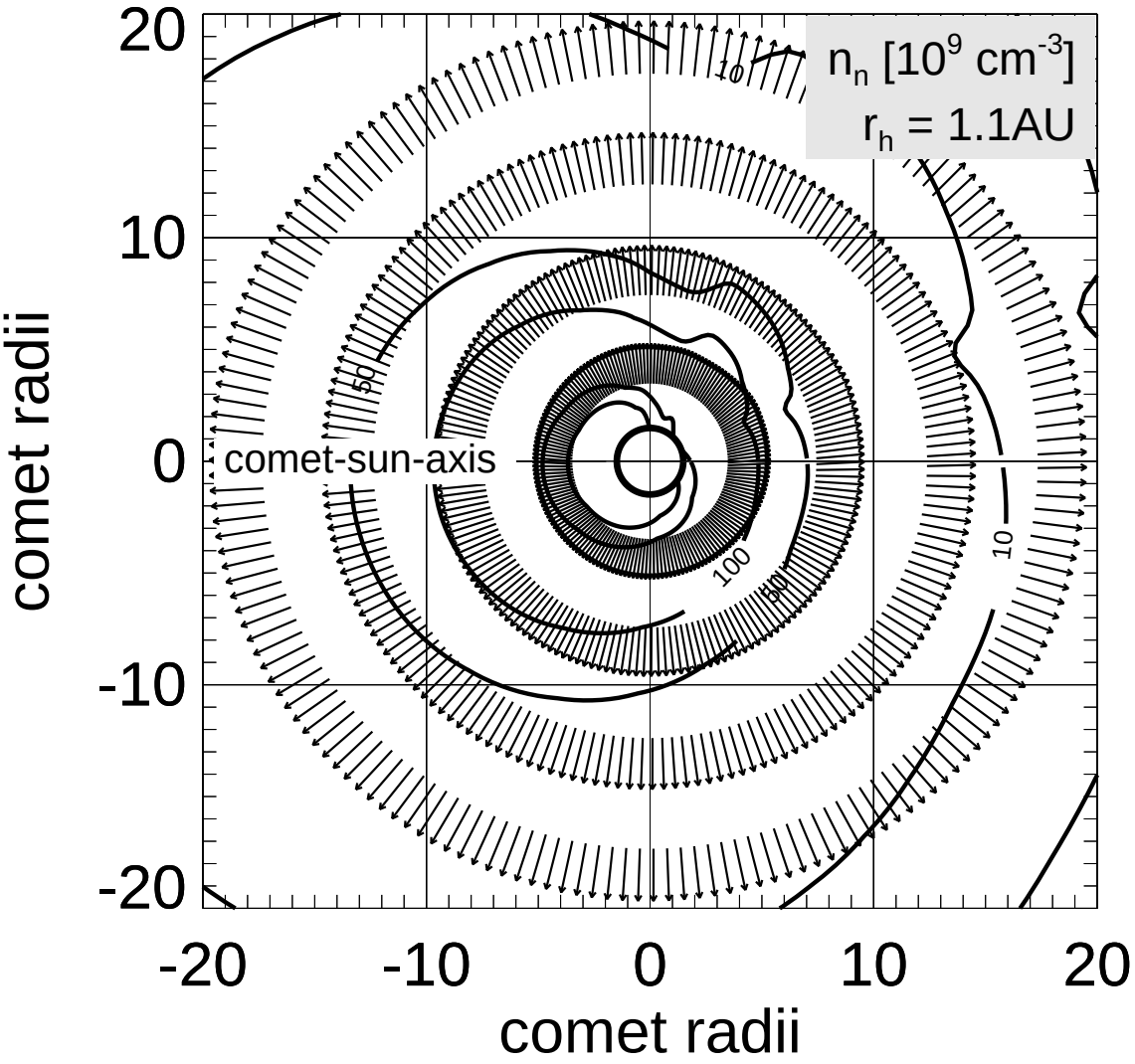

Figure D.4: *Isolines of the number density n_n of the neutral gas at levels 1,5,10,50,100,500,1000 in $10^9 cm^{-3}$. The projected vectors of the velocities are normalized to a length of [(km/s)×4]. Exemplary result in the equatorial plane of 46P/Wirtanen at* 1.1 *AU.*

D.2 46P/Wirtanen at 1.1 AU

The inner radial boundary in this scenario is determined from model W2 of the heat diffusion model of the nucleus. An additional constant source of gas of the order of 10^{26} molecules/s is added in order to account for the possible sublimation of more volatile species from sublimation fronts below the surface.

The number density and the projected velocity components in the equatorial plane of comet 46P/Wirtanen at 1.1 AU heliocentric distance are plotted in Figure D.4. Isolines of the number densities are plotted. The arrows indicate direction and strength of the velocity. The sun is to the left and the comet is rotating in anti clockwise direction in this chart.

The appearance of the inner coma is similar to a spherically symmetric coma with an offset of the center in the sun direction. This is a result of the stronger sublimation on the day-side of the nucleus.

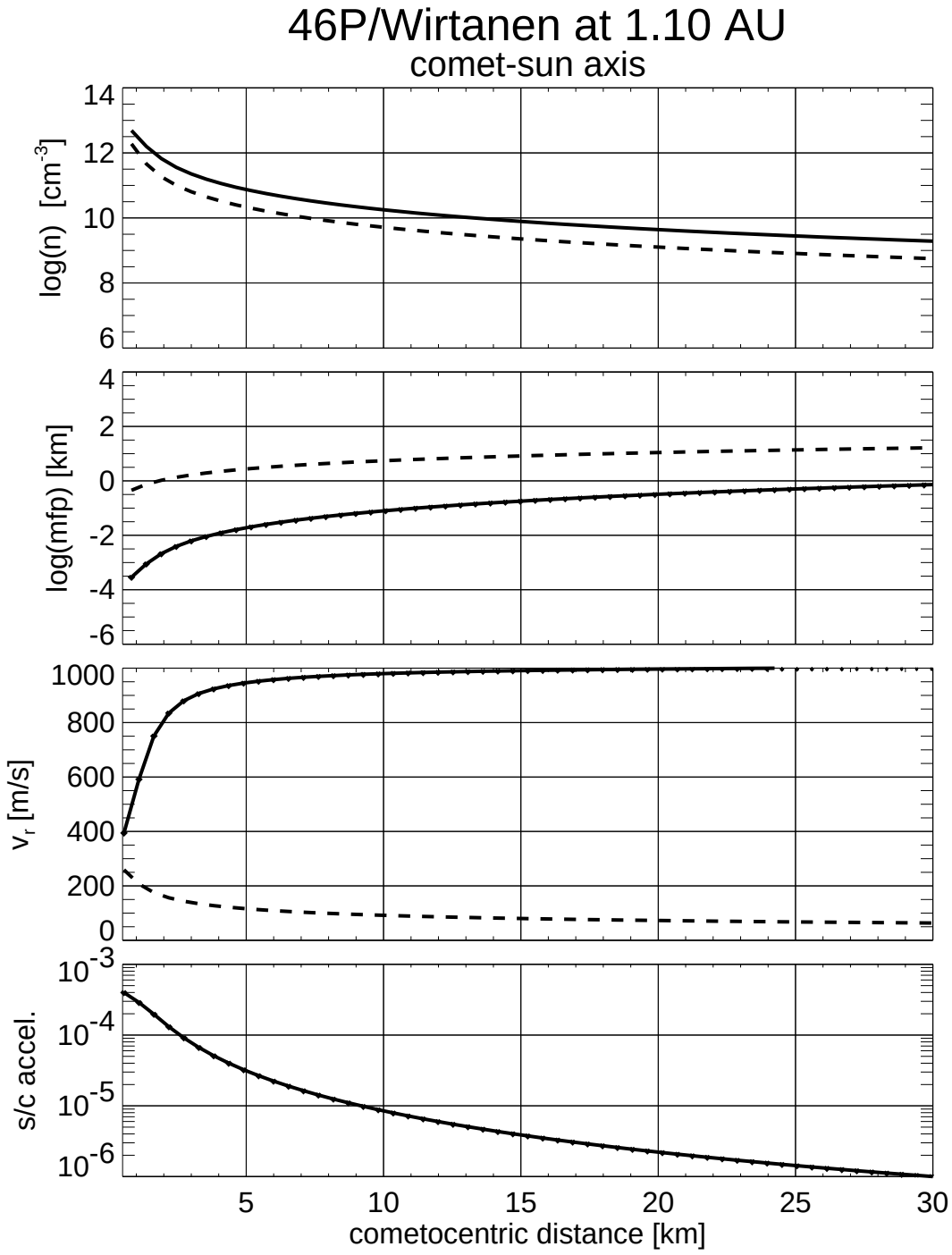

Figure D.5: *Radial profile at the comet-sun axis of the logarithmically scaled number density n_n and mean free path of particles mfp, the radial velocity v_r and the resulting acceleration of the spacecraft [m/s^2]. Exemplary result at a heliocentric distance of* 1.1 *AU for 46P/Wirtanen .*

Radial profiles along the comet-sun axis of the number density, mean free path of particles, radial velocity, and the resulting acceleration of the spacecraft due to gas drag are plotted in Figure D.5. The included dashed lines represent the corresponding number density of a spherically symmetric coma with the same gas production rate (first panel), the cometocentric distance (second panel) and the speed of sound (third panel). It can be concluded that this region of the coma expands supersonically, has a larger number density than a spherically symmetric coma, and remains collision dominated in the considered range.

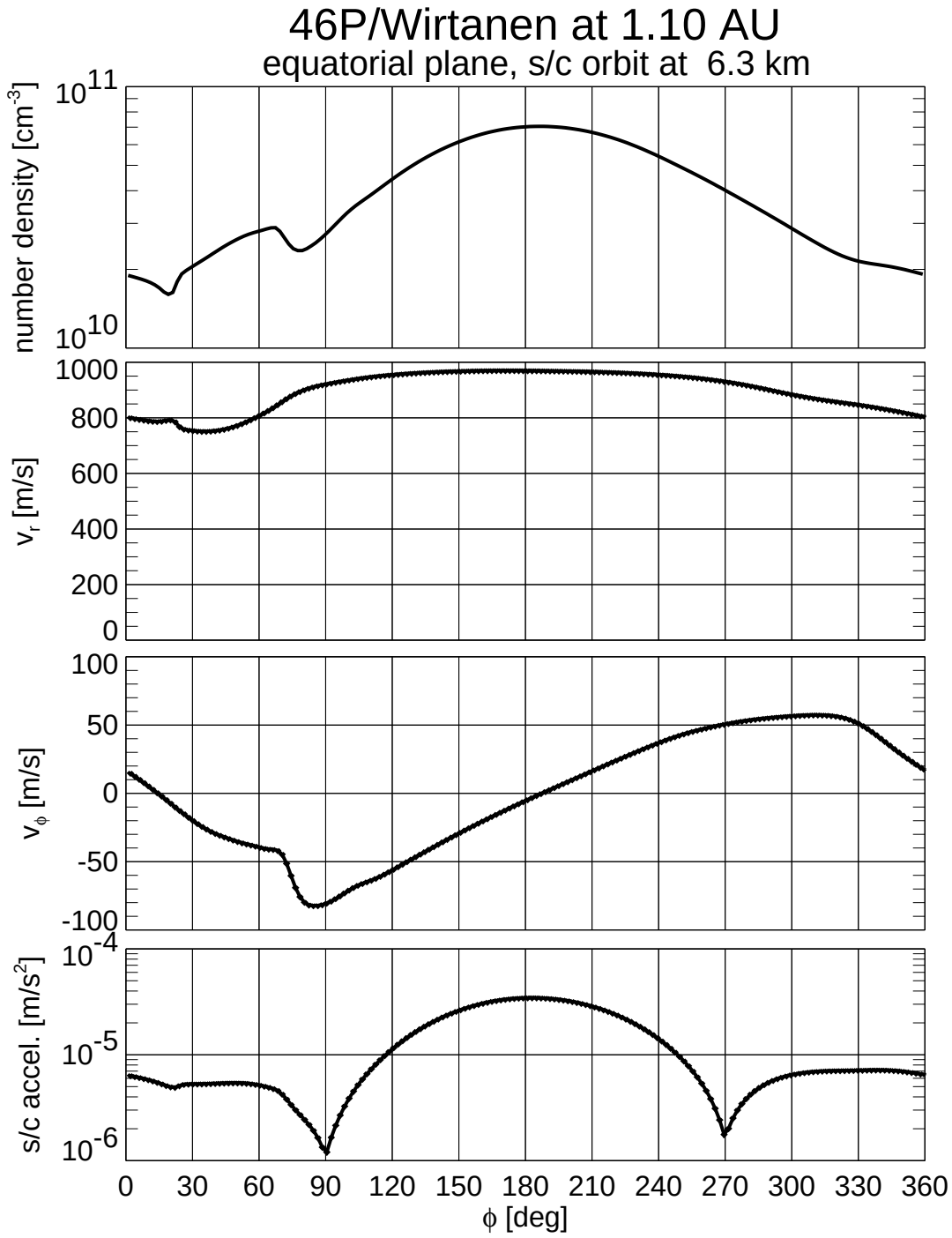

Figure D.6: *Profile in the equatorial plane of 46P/Wirtanen of the number density n_n, the radial velocity component v_r, the longitudinal velocity component v_Φ and the resulting acceleration of the spacecraft. Exemplary result at a heliocentric distance of* 1.1*AU.*

Profiles on a virtual orbit at a cometocentric distance of $r \approx 6$ km in the equatorial plane are plotted in Figure D.6. Included in the plot are the number density, the radial and longitudinal components of the velocity, and the resulting acceleration of the ROSETTA spacecraft. The number density differs about a factor of 3 between the day-side and the night-side coma. The radial gas velocities on the day-side coma are approximately similar to the values on the night-side. The longitudinal velocity component indicates a gas flow component away from the dense subsolar region. The gas flux remains mainly radial. The acceleration of the ROSETTA spacecraft with such an orbital distance has values between 10^{-6} m/s^2 and

10^{-4} m/s^2. The orientation of the solar panels is assumed to be perpendicular to the comet-sun axis throughout the complete orbit.

APPENDIX **E**

OBSERVATIONAL GEOMETRY FOR 67P/CHURYUMOV-GERASIMENKO

In Figure E.1(a) the earth orbit projected on the orbital plane of comet 67P/Churyumov-Gerasimenko is plotted. Cometocentric coordinates are applied, and the comet-sun axis is fixed. The time frame from June 2014 to December 2015 is plotted. An solar opposition and a solar conjunction occur during early phases of this time frame. The kink in the projected path of the earth does occur close to the perihelion passage of the comet (see also Figure 3.1).

The corresponding absolute angle between the line-of-sight (between earth and comet) and the comet-sun axis is shown in Figure E.1(b).This angle becomes larger than 30 degrees approximately ± 3 months around the perihelion passage. It can be concluded that the received radio signals will propagate through the interaction pattern that develops between the solar wind and the comet on the upwind side. This is of particular interest for the considerations of the plasma environment (see Chapter 6).

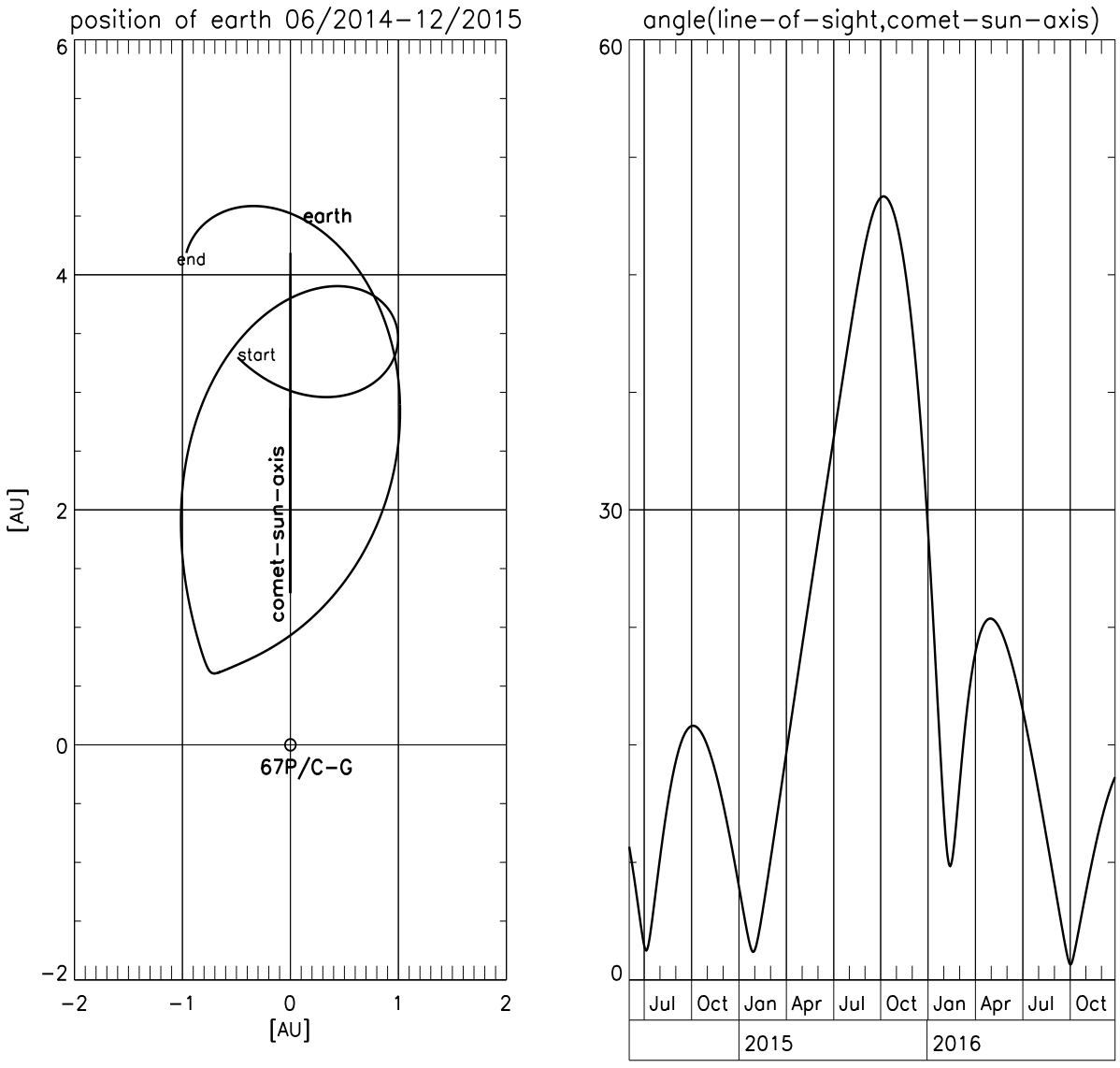

Figure E.1: *The orbit of earth in cometocentric coordinates, projected in the orbital plane of 67P/Churyumov-Gerasimenko (left). Absolute of the angle between the line of sight and the comet-sun axis during the time frame of the proposed prime mission (right).*

Bibliography

Abramowitz, M. and I. Stegun, *Handbook of Mathematical Functions*, Dover Publ., 1970.

A'Hearn, M. F. and M. C. Festou, The neutral coma, in *Physics and Chemistry of Comets*, edited by W. F. Huebner, A+A Library, chapter 3, 69–112, Springer, Berlin New York, 1990.

Altwegg, K., H. Balsiger, J. Geiss, R. Goldstein, W.-H. Ip, A. Meier, M. Neugebauer, H. Rosenbauer and E. Shelley, The ion population between 1300 km and 230 000 km in the coma of comet P/Halley, *Astron. Astrophys.*, *279*, 260–266, 1993.

Andreev, V. E. and A. L. Gavrik, Radio transmission measurements of the plasma shell of comet Halley, *Astron. Lett.*, *19*, (6), 437–440, 1993.

Balsiger, H. et al., Ion composition and dynamics at comet Halley, *Nature*, *321*, (6067), 330–334, 1986.

Bar-Nun, A. and D. Laufer, First experimental studies of large samples of gas-laden amorphous "cometary" ices, *Icarus*, *161*, 157–163, 2003.

Bar-Nun, A., G. Herman, D. Laufer and M. L. Rappaport, Trapping and release of gases by water ice and implications for icy bodies, *Icarus*, *63*, 317–332, 1985.

Baumgärtel, K. and K. Sauer, Fluid simulation of comet P/Halley's ionosphere, *Astron. Astrophys.*, *187*, 307–310, 1987.

Benkhoff, J., Energy balance and the gas flux from the surface of comet 46P/Wirtanen, *Planet. Space Sci.*, *47*, (6/7), 735–744, 1999*a*.

Benkhoff, J., On the flux of water and minor volatiles from the surface of comet nuclei, *Space Sci. Rev.*, *90*, (1/2), 141–148, 1999*b*.

Benkhoff, J. and D. C. Boice, Modeling the thermal properties and the gas flux from a porous, ice-dust body in the orbit of P/Wirtanen, *Planet. Space Sci.*, *44*, (7), 665–673, 1996.

Benkhoff, J. and W. F. Huebner, Influence of the vapor flux on temperature, density, and abundance distributions in a multicomponent, porous, icy body, *Icarus*, *114*, 348–354, 1995.

Benkhoff, J. and W. F. Huebner, Modeling the gas flux from a Jupiter-family comet nucleus, *Planet. Space Sci.*, *44*, (9), 1005–1013, 1996.

Biermann, L., B. Brosowski and H. U. Schmidt, The interaction of the solar wind with a comet, *Sol. Physics*, *1*, 254–283, 1967.

Boehnhardt, H. et al., VLT observations of comet 46P/Wirtanen, *Astron. Astrophys.*, *387*, 1107–1113, 2002.

Bogdanov, A., K. Sauer, K. Baumgärtel and K. Srivastava, Plasma structures at weakly outgassing comets - results from bi-ion fluid analysis, *Planet. Space Sci.*, *44*, (6), 519–528, 1996.

Budzien, S. A., M. C. Festou and P. D. Feldmann, Solar flux variability and the lifetimes of cometary H_2O and OH, *Icarus*, *107*, 164–188, 1994.

Burlaga, L. F., N. F. Ness, J. D. Richardson and R. P. Lepping, The Bastille day shock and merged interaction region at 63 AU: Voyager 2 observations, *Sol. Physics*, *204*, 399–410, 2001.

Capria, M. T., F. Capaccioni, A. Coradini, M. C. De Sanctis, S. Espinasse, C. Federico, R. Orosei and M. Salomone, A P/Wirtanen evolution model, *Planet. Space Sci.*, *44*, (9), 987–1000, 1996.

Cochran, A. L., A re-evaluation of the Haser model scale lengths for comets, *Astrophys. J.*, *90*, (12), 2609–2614, 1985.

Combi, M. R. and W. H. Smyth, Monte Carlo particle-trajectory models for neutral cometary gases: I. Models and equations, *Astrophys. J.*, *327*, 1026–1043, 1988*a*.

Combi, M. R. and W. H. Smyth, Monte Carlo particle-trajectory models for neutral cometary gases. II. The spatial morphology of the Lyman-alpha coma, *Astrophys. J.*, *327*, 1044–1059, 1988*b*.

Combi, M. R., K. Kabin, D. L. De Zeeuw, T. I. Gombosi and K. G. Powell, Dust-gas interrelations in comets: Observations and theory, *Earth, Moon and Planets*, *79*, 275–306, 1997.

Coradini, A., F. Capaccioni, M. T. Capria, M. C. De Sanctis, S. Espinasse, R. Orosei and M. Salomone, Transition Elements between comets and asteroids: I. Thermal Evolution Models, *Icarus*, *129*, 317–336, 1997.

Cravens, T. E., A magnetohydrodynamical model of the inner coma of comet Halley, *J. Geophys. Res.*, *94*, (A11), 15025–15040, 1989.

Cravens, T. E., Collisional processes in cometary plasmas, in *Cometary Plasma Processes*, edited by A. D. Johnstone, vol. 61 of *Geophysical Monograph*, 27–35, Amer. Geophys. Union, Washington D.C., 1991*a*.

Cravens, T. E., Plasma processes in the inner coma, in *Comets in the Post-Halley Era*, edited by R. L. Newburn, Jr., M. Neugebauer, and J. Rahe, vol. 2, 1211–1255, Kluwer Academic, 1991*b*.

Cravens, T. E. and A. Körösmezey, Vibrational and rotational cooling of electrons by water vapor, *Planet. Space Sci.*, *34*, (10), 961–970, 1986.

Cravens, T. E., J. U. Kozyra, A. F. Nagy, T. I. Gombosi and M. Kurtz, Electron impact ionization in the vicinity of comets, *J. Geophys. Res.*, *92*, (A7), 7341–7353, 1987.

Crifo, J. F., Improved gas-kinetic treatment of cometary water sublimation and recondensation: application to comet P/Halley, *Astron. Astrophys.*, *187*, 438–450, 1987.

Crifo, J. F., Hydrodynamic models of the collisional coma, in *Comets in the Post-Halley Era*, edited by R. L. Newburn, Jr., M. Neugebauer, and J. Rahe, vol. 2, 937–989, Kluwer Academic, Dordrecht, 1991.

Crifo, J. F., Note: The correct evaluation of the sublimation rate of dusty ices under solar illumination, and its implication on the properties of P/Halley nucleus, *Icarus*, *130*, (2), 549–551, 1997.

Crifo, J. F. and A. V. Rodionov, The dependence of the circumnuclear coma structure on the properties of the nucleus I. Comparison between a homegeneous and an inhomogeneous spherical nucleus, with application to P/Wirtanen, *Icarus*, *127*, 319–353, 1997*a*.

Crifo, J. F. and A. V. Rodionov, The dependence of the circumnuclear coma structure on the properties of the nucleus II. First investigation of the coma surrounding a homogenous, aspherical nucleus, *Icarus*, *129*, 72–93, 1997*b*.

Crifo, J. F. and A. V. Rodionov, Modelling the circumnuclear coma of comets: objectives, methods and recent results, *Planet. Space Sci.*, *47*, (6/7), 797–826, 1999.

Crifo, J. F., A. L. Itkin and A. V. Rodionov, The near-nucleus coma formed by interacting dusty gas jets effusing from a cometary nucleus: I, *Icarus*, *116*, 77–112, 1995.

Crovisier, J., The water molecule in comets: fluorescence mechanisms and thermodynamics of the inner coma, *Astron. Astrophys.*, *130*, 361–372, 1984.

Delsemme, A. H., Chemical composition of cometary nuclei, in *Comets*, edited by L. L. Wilkening, Space Science Series, chapter II, 85–130, Univ. of Ariz. Press, 1982.

Delsemme, A. H., Nature and history of the organic compounds in comets: an astrophysical view, in *Comets in the Post-Halley Era*, edited by R. L. Newburn, Jr., M. Neugebauer, and J. Rahe, vol. 1, chapter III, 377–428, Kluwer Academic, 1991.

Delsemme, A. H. and D. C. Miller, Physico-chemical phenomena in comets – III. The continuum of comet Burnham (1960 II), *Planet. Space Sci.*, *19*, 1229–1257, 1971.

Donn, B., The accumulation and structure of comets, in *Comets in the Post-Halley Era*, edited by R. L. Newburn, Jr., M. Neugebauer, and J. Rahe, vol. 1, 335–359, Kluwer Academic, Dordrecht, 1991.

Eberhardt, P. and D. Krankowsky, The electron temperature in the inner coma of comet P/Halley, *Astron. Astrophys.*, *295*, 795–806, 1995.

Ellsworth, K. and G. Schubert, Saturn's icy satellites: Thermal and structural models, *Icarus*, *54*, 490–510, 1983.

Enzian, A., H. Cabot and J. Klinger, A 2 1/2 D thermodynamic model of cometary nuclei I. Application to the activity of comet 29P/Schwassmann-Wachmann 1, *Astron. Astrophys.*, *319*, 995–1006, 1997.

Enzian, A., H. Cabot and J. Klinger, Simulation of the water and carbon monoxide production rates of comet Hale-Bopp using a quasi 3-D nucleus model, *Planet. Space Sci.*, *46*, (8), 851–858, 1998.

Enzian, A., J. Klinger, G. Schwehm and P. R. Weissman, Temperature and gas production distributions on the surface of a spherical model comet nucleus in the orbit of 46P/Wirtanen, *Icarus*, *138*, 74–84, 1999.

Ershkovich, A. I., J. F. McKenzie and W. I. Axford, Stability of a cometary ionosphere/ionopause determined by ion-neutral friction, *Astrophys. J.*, *344*, 932–939, 1989.

Espinasse, S., J. Klinger, C. Ritz and B. Schmitt, Modeling of the thermal behavior and of the chemical differentiation of cometary nuclei, *Icarus*, *92*, 350–365, 1991.

Espinasse, S., A. Coradini, M. T. Capria, F. Capaccioni, R. Orosei, M. Salomone and C. Federico, Thermal evolution and differentiation of a short-period comet, *Planet. Space Sci.*, *41*, (6), 409–427, 1993.

Fanale, F. P. and J. R. Salvail, An idealized short-period comet model: surface insolation, H_2O flux, dust flux and mantle evolution, *Icarus*, *60*, 476–511, 1984.

Fanale, F. P. and J. R. Salvail, The loss and depth of CO_2 ice in comet nuclei, *Icarus*, *72*, 535–554, 1987.

Fanale, F. P. and J. R. Salvail, The influence of CO ice on the activity and near-surface differentiation of comet nuclei, *Icarus*, *84*, 403–413, 1990.

Fanale, F. P., J. R. Salvail, D. L. Matson and R. H. Brown, The effect of volume phase changes, mass transport, sunlight penetration, and densification on the thermal regime of icy regoliths, *Icarus*, *88*, 193–204, 1990.

Feldman, P. D., Ultraviolet spectroscopy of comae, in *Comets*, edited by L. L. Wilkening, Space Science Series, chapter IV, 461–479, Univ. of Ariz. Press, Tucson, 1982.

Festou, M. C., The density distribution of neutral compounds in cometary atmospheres, *Astron. Astrophys., 95*, 69–79, 1981.

Fink, U. and M. A. DiSanti, The production rate and spatial distribution of H_2O for comet P/Halley, *Astrophys. J., 364*, 687–698, 1990.

Fink, U., M. D. Hicks, R. A. Fevig and J. Collins, Spectroscopy of 46P/Wirtanen during its 1997 apparition, *Astron. Astrophys., 335*, L37–L45, 1998.

Flammer, K. R., The global interaction of comets with the solar wind, in *Comets in the Post-Halley Era*, edited by R. L. Newburn Jr., M. Neugebauer, and J. Rahe, vol. 2, 1125–1144, Kluwer Academic, 1991.

Galeev, A. A., T. E. Cravens and T. I. Gombosi, Solar wind stagnation near comets, *Astrophys. J., 289*, 807–819, 1985.

Gan, L. and T. E. Cravens, Electron energetics in the inner coma of comet Halley, *J. Geophys. Res., 95*, (A5), 6285–6303, 1990.

Goldstein, B. E., R. Goldstein, M. Neugebauer, S. A. Fuselier, E. G. Shelley, H. Balsiger, G. Kettmann, W.-H. Ip, H. Rosenbauer and R. Schwenn, Observations of plasma dynamics in the coma of comet P/Halley by the Giotto ion mass spectrometer, *J. Geophys. Res., 97*, 4121–4132, 1992.

Gombosi, T. I., Charge exchange avalanche at the cometopause, *Geophys. Res. Lett., 14*, (11), 1174–1177, 1987.

Gombosi, T. I., Multidimensional dusty gasdynamical models of inner cometary atmospheres, in *Comets in the Post-Halley Era*, edited by R. L. Newburn Jr., M. Neugebauer, and J. Rahe, vol. 2, 991–1001, Kluwer Academic, 1991.

Gombosi, T. I. and H. L. F. Houpis, An icy-glue model of cometary nuclei, *Nature, 324*, 43–44, 1986.

Gombosi, T. I., T. E. Cravens and A. F. Nagy, Time-dependent dusty gasdynamical flow near cometary nuclei, *Astrophys. J., 293*, 328–341, 1985.

Gombosi, T. I., A. F. Nagy and T. E. Cravens, Dust and neutral gas modeling of the inner atmospheres of comets, *Rev. Geophys., 24*, (3), 667–700, 1986.

Gombosi, T. I., D. L. D. Zeeuw and R. M. Haeberli, Three-dimensional multiscale MHD model of cometary plasma environments, *J. Geophys. Res., 101*, (A7), 15233–15253, 1996.

Green, R. M., *Spherical Astronomy*, Cambridge Univ. Press, Cambridge, 1985.

Greenberg, J. M., What are comets made of? A model based on interstellar dust, in *Comets*, edited by L. L. Wilkening, Space Science Series, chapter II, 131–163, Univ. of Ariz. Press, 1982.

Grensemann, M. G. and G. Schwehm, Giotto's second encounter: The mission to comet P/Grigg-Skjellerup, *J. Geophys. Res., 98*, (A12), 20907–20910, 1993.

Gringauz, K. I. et al., Detection of a new ”chemical” boundary at comet Halley, *Geophys. Res. Lett.*, *13*, (7), 613–616, 1986*a*.

Gringauz, K. I. et al., First in situ plasma and neutral gas measurements at comet Halley, *Nature*, *321*, 282–285, 1986*b*.

Grün, E. and E. K. Jessberger, Dust, in *Physics and Chemistry of Comets*, edited by W. F. Huebner, A&A Library, chapter 4, 113–176, Springer, 1990.

Grün, E. et al., Laboratory simulation of cometary processes: Results from first KOSI experiments, in *Comets in the Post-Halley Era*, edited by R. L. Newburn, Jr., M. Neugebauer, and J. Rahe, vol. 1, 277–311, Kluwer Academic, Dordrecht, 1991.

Gutiérrez, P. J., J. L. Ortiz, R. Rodrigo and J. J. López-Moreno, Effects of irregular shape and topography in thermophysical models of heterogenous cometary nuclei, *Astron. Astrophys.*, *374*, 326–336, 2001.

Gutiérrez, P. J., R. Rodrigo, J. L. Ortiz and B. Davidsson, An investigation of errors in estimates of the cometary nuclei active area fractions, *Astron. Astrophys.*, *401*, 755–761, 2003.

Häberli, R. M., K. Altwegg, H. Balsiger and J. Geiss, Physics and chemistry of ions in the pile-up region of comet P/Halley, *Astron. Astrophys.*, *297*, 881–891, 1995.

Häberli, R. M., K. Altwegg, H. Balsiger and J. Geiss, Heating of the thermal electrons in the coma of comet P/Halley, *J. Geophys. Res.*, *101*, (A7), 15579–15589, 1996.

Häberli, R. M., M. R. Combi, T. I. Gombosi, D. L. De Zeeuw and K. G. Powell, Quantitative analysis of H_2O^+ coma images using a multiscale MHD model with detailed ion chemistry, *Icarus*, *130*, 373–386, 1997.

Haerendel, G., Plasma transport near the magnetic cavity surrounding comet Halley, *Geophys. Res. Lett.*, *14*, (7), 673–676, 1987.

Hagermann, A., Messung des Temperaturprofils unter der Oberfläche eines Kometenkerns, Diplomarbeit, Westfälische-Wilhelms-Universität Münster, February 1996.

Heppner, R. A., F. L. Walls, W. T. Armstrong and G. H. Dunn, Cross-section measurements for electron-H_3O^+ recombination, *Phys. Rev. A*, *13*, (3), 1000–1011, 1976.

Herman, G. and P. R. Weissman, Numerical Simulation of cometary nuclei: III. Internal Temperatures of cometary nuclei, *Icarus*, *69*, 314–328, 1987.

Hodges Jr., R. R., Monte Carlo simulation of nonadiabatic expansion in comety atmospheres: Halley, *Icarus*, *83*, 410–433, 1990.

Horan, D. M., R. W. Kreplin and G. G. Fritz, Direct measurements of impulsive extreme ultraviolet and hard x-ray solar flare emission, *Astrophys. J.*, *255*, 797–805, 1982.

Horan, D. M., R. W. Kreplin and K. P. Dere, Direct measurements of the gradual extreme ultraviolet emission from large solar flares, *Sol. Physics*, *85*, 303–312, 1983.

Horányi, M., T. I. Gombosi, T. E. Cravens, A. Körösmezey, K. Kecskemetey, A. F. Nagy and K. Szego, The friable sponge model of a cometary nucleus, *Astrophys. J.*, *278*, 449–455, 1984.

Houpis, H. L. F., W.-H. Ip and D. A. Mendis, The chemical differentiation of the cometary nucleus: The process and its consequences, *Astrophys. J.*, *295*, 654–667, 1985.

Huddleston, D. E., A. D. Johnstone and A. J. Coates, Determination of comet Halley gas emission charcteristics from mass loading of the solar wind, *J. Geophys. Res.*, *95*, (A1), 21–30, 1990.

Huddleston, D. E., A. J. Coates and A. D. Johnstone, Predictions of the solar wind interaction with comet Grigg-Skjellerup, *Geophys. Res. Lett.*, *19*, (8), 837–840, 1992.

Huddleston, D. E., A. J. Coates, A. D. Johnstone and F. M. Neubauer, Mass-loading and velocity diffusion modells for heavy pickup ions at comet Grigg-Skjellerup, *J. Geophys. Res.*, *98*, (A12), 20995–21002, 1993.

Huebner, W. F. and J. Benkhoff, From coma abundances to nucleus composition, *Space Sci. Rev.*, *90*, 117–130, 1999.

Huebner, W. F. and J. J. Keady, First-flight escape from spheres with R^{-2} density distribution, *Astron. Astrophys.*, *135*, 177–180, 1984.

Huebner, W. F. and W. J. Markiewicz, Note: The temperature and bulk flow speed of a gas effusing or evaporating from a surface into a void after reestablishment of collisional equilibrium, *Icarus*, *148*, (2), 594–596, 2000.

Huebner, W. F., D. C. Boice, H. U. Schmidt and R. Wegmann, Structure of the coma: Chemistry and solar wind interaction, in *Comets in the Post-Halley Era*, edited by R. L. Newburn, Jr., M. Neugebauer, and J. Rahe, vol. 2, 907–936, Kluwer Academic, Dordrecht, The Netherlands, 1991.

Huebner, W. F., J. J. Keady and S. P. Lyon, Solar photo rates for planetary atmospheres and atmospheric pollutants, *Astrophys. Space Sci.*, *195*, 1–294, 1992.

Huebner, W. F., J. Benkhoff, M. T. Capria, A. Coradini, M. C. De Sanctis, A. Enzian, R. Orosei and D. Prialnik, Results from the comet nucleus model team at the international space science institute, Bern, Switzerland, *Adv. Space Res.*, *23*, (7), 1283–1298, 1999.

Hughes, D. W., The interior of a cometary nucleus, *Planet. Space Sci.*, *44*, (7), 705–710, 1996.

Ip, W.-H., On charge exchange effect in the vicinity of the cometopause of comet Halley, *Astrophys. J.*, *343*, 946–952, 1989.

Ip, W.-H. and W. I. Axford, Theories of physical processes in the cometary coma and ion tails, in *Comets*, edited by L. L. Wilkening, 588–634, Univ. of Ariz. Press, Tucson Arizona, 1982.

Ip, W.-H. and W. I. Axford, The formation of a magnetic-field-free cavity at comet Halley, *Nature*, *325*, 418–419, 1987.

Ip, W.-H. and W. I. Axford, Cometary plasma physics, in *Physics of Comets in the Space Age*, edited by W. F. Huebner, Springer, New York, London, Berlin, Heidelberg, 1988.

Ip, W.-H. and W. I. Axford, The plasma, in *Physics and Chemistry of Comets*, edited by W. F. Huebner, A+A Library, chapter 5, 177–233, Springer, Berlin, 1990.

Jockers, K., T. Credner and T. Bonev, Water ions, dust and CN in comet 46P/Wirtanen, *Astron. Astrophys.*, *335*, L56–L59, 1998.

Johnstone, A. D., A. J. Coates, D. E. Huddlestone, K. Kockers, B. Wilken, H. Borg, C. Gurgiolo, J. D. Winningham and E. Amata, Observations of the solar wind and cometary ions during the encounter between Giotto and comet P/Grigg-Skjellerup, *Astron. Astrophys.*, *273*, L1–L4, 1993.

Kazachevskaya, T. V., L. L. Bukusova, D. A. Gonyukh, A. I. Lomovskii and Y. N. Tsigel'nitskii, Ultraviolet observations of solar flares from the orbit of Mars, *Sov. Astron. Lett.*, *16*, (2), 145–146, 1990.

Kehse, U., Modellrechnungen zur thermischen Evolution von Kometen, Diplomarbeit, Westfälische-Wilhelms-Universität Münster, 1994.

Keller, H. U., The nucleus, in *Physics and Chemistry of Comets*, edited by W. F. Huebner, A+A Library, chapter 2, 13–68, Springer, Berlin New York, 1990.

Keller, H. U. et al., First Halley multicolour camera imaging results from Giotto, *Nature*, *321*, 320–326, 1986.

Keller, H. U. et al., Comet P/Halley's nucleus and its activity, *Astron. Astrophys.*, *187*, 807–823, 1987.

Keller, H. U., R. Kramm and N. Thomas, Surface features on the nucleus of comet Halley, *Nature*, *331*, 227–231, 1988.

Keller, H. U., M. L. Marconi and N. Thomas, Hydrodynamic implications of particle fragmentation near cometary nuclei, *Astron. Astrophys.*, *227*, L1–L4, 1990.

Kitamura, Y., Axisymmetric dusty gas jet in the inner coma of a comet, *Icarus*, *66*, 241–257, 1986.

Kittel, C. and H. Krömer, *Physik der Wärme*, R. Oldenbourg, München, 4. Auflage, 1993.

Klinger, J., Some consequences of a phase transition of water ice on the heat balance of comet nuclei, *Icarus*, *47*, (3), 320–324, 1981.

Klinger, J., Classification of cometary orbits based on the concept of orbital mean temperature, *Icarus*, *55*, 169–176, 1983.

Klinger, J., A.-C. Levasseur-Regourd, N. Bouziani and A. Enzian, Towards a model of cometary nuclei for engineering studies for future space missions to comets, *Planet. Space Sci., 44*, (7), 637–653, 1996.

Kömle, N. I. and W.-H. Ip, Anisotropic non-stationary gas flow dynamics in the coma of comet P/Halley, *Astron. Astrophys., 187*, 405–410, 1987.

Körösmezey, A. and T. I. Gombosi, A time-dependent dusty gas dynamic model of axisymmetric cometary jets, *Icarus*, *84*, 118–153, 1990.

Körösmezey, A., T. E. Cravens, T. I. Gombosi, A. F. Nagy, D. A. Mendis, K. Szegö, B. E. Gribov, R. Z. Sagdeev, V. D. Shapiro and V. L. Shevchenko, A new model of cometary ionospheres, *J. Geophys. Res., 92*, (A7), 7331–7340, 1987.

Krankowsky, D., The composition of comets, in *Comets in the Post-Halley Era*, edited by R. L. Newburn Jr., M. Neugebauer, and J. Rahe, vol. 2, 855–877, Kluwer Academic, 1991.

Krankowsky, D. et al., In situ gas and ion measurements at comet Halley, *Nature*, *321*, (6067), 326–329, 1986.

Kührt, E. and H. U. Keller, The formation of cometary surface crusts, *Icarus*, *109*, 121–132, 1994.

Lämmerzahl, P. et al., Expansion velocity and temperatures of gas and ions measured in the coma of comet P/Halley, *Astron. Astrophys., 187*, 169–173, 1987.

Lamy, P. L., I. Toth, L. Jorda, H. A. Weaver and M. A'Hearn, The nucleus and inner coma of comet 46/P Wirtanen, *Astron. Astrophys., 335*, L25–L29, 1998.

Landau, L. D. and E. M. Lifschitz, *Elektrodynamik der Kontinua*, vol. 8, Akademie Verl., Berlin, 3. Auflage, 1967.

Landau, L. D. and E. M. Lifschitz, *Hydrodynamik*, vol. VI of *Lehrbuch der theoretischen Physik*, Akademie Verl., Berlin, 1991.

Lang, K. R., *The Cambridge Encyclopedia of the Sun*, Cambridge Univ. Press, Cambridge, UK, 2001.

Lean, J., M. VanHoosier, G. Brueckner, D. Prinz, L. Floyd and K. Edlow, SUSIM/UARS observations of the 120 to 300 nm flux variations during the maximum of the solar cycle: Inferences for the 11-year cycle, *Geophys. Res. Lett., 19*, (22), 2203–2206, 1992.

Marconi, M. L. and D. A. Mendis, The photochemical heating of the cometary atmosphere, *Astrophys. J., 260*, 386–394, 1982.

Marconi, M. L. and D. A. Mendis, The atmosphere of a dirty-clathrate cometary nucleus: A two-phase, multifluid model, *Astrophys. J., 273*, 381–396, 1983.

Mariani, F. and F. M. Neubauer, The interplanetary magnetic field, in *Physics of the Inner Heliosphere*, edited by R. Schwenn and E. Marsch, vol. 1, Springer, Berlin Heidelberg, 1990.

Markiewicz, W. J., Y. V. Skorov, H. U. Keller and N. I. Kömle, Evolution of ice surfaces within porous near-surface layers on cometary nuclei, *Planet. Space Sci.*, *46*, (4), 357–366, 1998.

Mazelle, C., H. Réme, F. M. Neubauer and K.-H. Glaßmeier, Comparison of the main magnetic and plasma features in the environments of comets Grigg-Skjellerup and Halley, *Adv. Space Res.*, *16*, (4), 41–45, 1995.

McDonnell, J. A. M. et al., The dust distribution within the inner coma of comet P/Halley 1982i: Encounter by Giotto's impact detectors, *Astron. Astrophys.*, *187*, (1-2), 719–741, 1987.

McDonnell, J. M. A., P. L. Lamy and G. S. Pankiewicz, Physical properties of cometary dust, in *Comets in the Post-Halley Era*, edited by R. L. Newburn, Jr., M. Neugebauer, and J. Rahe, vol. 2, 1043–1073, Kluwer Academic, 1991.

McKay, C. P., S. W. Squyres and R. T. Reynolds, Methods for computing comet core temperatures, *Icarus*, *66*, 625–629, 1986.

Mekler, Y., D. Prialnik and M. Podolak, Evaporation from a porous cometary nucleus, *Astrophys. J.*, *356*, 682–686, 1990.

Mendis, D. A. and H. L. F. Houpis, The cometary atmosphere and its interaction with the solar wind, *Rev. Geophys. Space Phys.*, *20*, (4), 885–928, 1982.

Mendis, D. A., E. J. Smith, B. T. Tsurutani, J. A. Slavin, D. E. Jones and G. L. Siscoe, Comet-solar wind interaction: dynamical length scales and models, *Geophys. Res. Lett.*, *13*, (3), 239–242, 1986.

Mendis, D. A., K. R. Flammer et al., On the global nature of the solar wind interaction with comet Halley, *Ann. Geophysicae*, *7*, (2), 99–106, 1989.

Montenbruck, O. and E. Gill, *Satellite Orbits*, Springer, New York, Berlin, 2000.

Mul, P. M., J. W. McGowan, P. Defrance and J. B. A. Mitchell, Merged electron-ion beam experiments: V. Dissociative recombination of OH^+, H_2O^+, H_3O^+ and D_3O^+, *J. Phys. B At. Mol. Phys.*, *16*, 3099–3107, 1983.

Müller, M., *A model of the inner coma of comets with applications to the comets P/Wirtanen and P/Wild 2*, Dissertation, Rupertus Carola University of Heidelberg, Heidelberg, 1999.

Neidig, D. F., H. Grosser and M. Hrovat, Optical output of the 24 April 1984 white-light flare, *Sol. Physics*, *155*, 199–202, 1994.

Neubauer, F. M., Giotto magnetic field results on the boundaries of the pile-up region and the magnetic cavity, *Astron. Astrophys.*, *187*, 73–79, 1987.

Neubauer, F. M., The ionopause and boundary layers at comet Halley from Giotto magnetic field observations, *J. Geophys. Res.*, *93*, (A7), 7272–7281, 1988.

Neubauer, F. M. et al., First results from the Giotto magnetometer experiment at comet Halley, *Nature, 321*, (6067), 352–355, 1986.

Neubauer, F. M. et al., First results from the Giotto magnetometer experiment during the P/Grigg-Skjellerup encounter, *Astron. Astrophys., 268*, (2), L5–L8, 1993.

Niedner, Jr., M. B., Magnetic reconnection in comets, in *Magnetic Reconnection in Space and Laboratory Plasmas*, edited by E. W. Hones, Jr., Geophys. Monogr. Ser., 79–89, AGU, Washington, 1984.

Ogilvie, K. W., M. A. Coplan, P. Bochsler and J. Geiss, Ion composition results during the international cometary Explorer encounter with Giacobini-Zinner, *Science, 232*, 374–377, 1986.

Oppenheimer, M., Gas phase chemistry in comets, *Astrophys. J., 196*, 251–259, 1975.

Oppenheimer, M. and C. J. Downey, The effect of solar-cycle ultraviolet flux variations on cometary gas, *Astrophys. J., 241*, L123–L127, 1980.

Orosei, R., F. Capaccioni, M. T. Capria, A. Coradini, M. C. De Sanctis, C. Federico, M. Salomone and J.-P. Huot, Numerically improved thermochemical evolution models of comet nuclei, *Planet. Space Sci., 47*, 839–853, 1999.

Osip, D. J., D. G. Schleicher and R. T. Millis, Comets: Groundbased observations of spacecraft mission candidates, *Icarus, 98*, 115–124, 1992.

Özgüc, A., T. Atac and J. Rybák, Flare index variability in the ascending branch of solar cycle 23, *J. Geophys. Res., 107*, (A7), SSH 11–1 – SSH 11–8, 2002.

Parker, E. N., Dynamics of the interplanetary gas and magnetic fields, *Astrophys. J., 128*, (3), 664–676, 1958.

Pätzold, M., F. M. Neubauer, V. E. Andreev and A. L. Gavrik, Detection of the inner plasma pileup region at comet Halley during the Vega 1 flyby by the radio sounding experiment, *J. Geophys. Res., 102*, (A2), 2213–2222, 1997.

Pätzold, M. et al., Rosetta Radio Science Investigations (RSI), Forschungsberichte 4, Institut für Geophysik und Meteorologie, Köln, February 2000.

Pätzold, M. et al., Gravity field determination of a comet nucleus: Rosetta at P/Wirtanen, *Astron. Astrophys., 375*, 651–660, 2001.

Podolak, M. and G. Herman, Numerical simulations of comet nuclei: II. The effect of the dust mantle, *Icarus, 61*, 267–277, 1985.

Press, W. H., S. A. Teukolsky, W. T. Vetterling and B. P. Flannery, *Numerical Recipes in Fortran*, Cambridge Univ. Press, Cambridge, 2. Auflage, 1986.

Prialnik, D., Crystallization, sublimation and gas release in the interior of a porous comet nucleus, *Astrophys. J., 388*, 196–202, 1992.

Reisenfeld, D. B. et al., Deep Space 1 encounter with comet Borrelly: Composition measurements by the PEPE ion mass spectrometer, 33rd Annual Lunar and Planetary Science Conference, Abstract no. 1840, March 2002.

Rème, H. et al., General features of comet P/Halley: solar wind interaction from plasma measurements, *Astron. Astrophys.*, *187*, 33–38, 1987.

Rème, H. et al., Electron plasma environment at comet Grigg-Skjellerup: General observations and comparison with the environment at comet Halley, *J. Geophys. Res.*, *98*, (A12), 20965–20976, 1993.

Rème, H., C. Mazelle, C. d'Uston, A. Korth, R. P. Lin and P. Chaizy, There is no "cometopause" at comet Halley, *J. Geophys. Res.*, *99*, (A2), 2301–2308, 1994.

Richards, P. G., J. A. Fennelly and D. G. Torr, EUVAC: A solar EUV flux model for aeronomic calculations, *J. Geophys. Res.*, *99*, (A5), 8981–8992, 1994.

Richardson, J. D., K. I. Paularena, A. J. Lazarus and J. W. Belcher, Radial evolution of the solar wind from IMP 8 to Voyager 2, *Geophys. Res. Lett.*, *22*, (4), 325–328, 1995.

Rickman, H., The thermal history and structure of cometary nuclei, in *Comets in the Post-Halley Era*, edited by R. L. Newburn, Jr., M. Neugebauer, and J. Rahe, vol. 2 of *Astrophysics and space science library*, 733–760, Kluwer Academic, Dordrecht, 1991.

Riedler, W., K. Schwingenschuh, Y. G. Yeroshenko, V. A. Styashkin and C. T. Russell, Magnetic field observations in comet Halley's coma, *Nature*, *321*, (6067), 288–289, 1986.

Rodionov, A. V., J.-F. Crifo, K. Szegö, J. Lagerros and M. Fulle, An advanced physical model of cometary activity, *Planet. Space Sci.*, *50*, (10-11), 983–1024, 2002.

Rousselot, P., J. Clairemidi and G. Moreels, Radial distribution of the OH radical in Halley's inner coma, *Astron. Astrophys.*, *277*, 653–665, 1993.

Sagdeev, R. Z., P. E. Elyasberg and V. I. Moroz, Is the nucleus of comet Halley a low density body?, *Nature*, *331*, 240–242, 1988.

Sauer, K. and E. Dubinin, Bi-ion fluid simulations of solar wind massloading, Workshop on Massloaded Plasmas, September 1998 MPAE-W-100-99-02, MPI, Katlenburg-Lindau, Germany, 1999.

Sauer, K., U. Motschmann and T. Roatsch, Plasma boundaries at comet Halley, *Ann. Geophysicae*, *8*, (4), 243–250, 1990.

Sauer, K., A. Bogdanov, K. Baumgärtel and E. Dubinin, Plasma environment of comet Wirtanen during its low-activity stage, *Planet. Space Sci.*, *44*, (7), 715–728, 1996.

Schatten, K. H. and W. D. Pesnell, An early solar dynamo prediction: cycle 23 - cycle 22, *Geophys. Res. Lett.*, *20*, (20), 2275–2278, 1993.

Schloerb, F. P., M. J. Claussen and L. Tacconi-Garman, OH radio observations of comet P/Halley, *Astron. Astrophys.*, *187*, 469–474, 1987.

Schmidt, U. and R. Wegmann, Plasma flow and magnetic fields in comets, in *Comets*, edited by L. L. Wilkening, 538–560, Univ. of Ariz. Press, Tuscon, 1982.

Schmidt, H. U., R. Wegmann, W. F. Huebner and D. C. Boice, Cometary gas and plasma flow with detailed chemistry, *Comp. Phys. Comm., 49*, 17–59, 1988.

Schmidt, H. U., R. Wegmann and F. M. Neubauer, MHD modeling applied to Giotto encounter with comet P/Grigg-Skjellerup, *J. Geophys. Res., 98*, (A12), 21009–21016, 1993.

Schulz, R. and G. Schwehm, Coma composition and evolution of Rosetta target comet 46P/Wirtanen, *Space Sci. Rev., 90*, 321–328, 1999.

Schunk, R. W., Mathematical structure of transport equations for multispecies flows, *Rev. Geophys. Space Phys., 15*, (4), 429–445, 1977.

Schunk, R. W. and A. F. Nagy, *Ionospheres - Physics, Plasma Physics, and Chemistry*, Cambridge Atmospheric and Space Science Series, Cambridge Univ. Press, Cambridge, UK, 2000.

Schwenn, R., Large - scale structure of the interplanetary medium, in *Physics of the Inner Heliosphere I*, edited by R. Schwenn and E. Marsch, Springer, 1990.

Schwenn, R., Der Sonnenwind, in *Plasmaphysik im Sonnensystem*, edited by K.-H. Glaßmeier and M. Scholer, BI Wiss. Verl., Mannheim, 1991.

Schwenn, R., W.-H. Ip, H. Rosenbauer, H. Balsiger, F. Bühler, R. Goldstein, A. Meier and E. G. Shelley, Ion temperature and flow profiles in comet P/Halley's close environment, *Astron. Astrophys., 187*, 160–162, 1987.

Schwinger, J., Simulation von Umlaufbahnen um einen Kometenkern, Diplomarbeit, Universität zu Köln, 2001.

Sekanina, Z., Cometary activity, discrete outgassing areas, and dust-jet formation, in *Comets in the Post-Halley Era*, edited by R. L. Newburn Jr., M. Neugebauer, and J. Rahe, vol. 2, 769–823, Kluwer Academic, 1991.

Sello, S., Solar cycle activity: A preliminary prediction for cycle 24, *Astron. Astrophys., 410*, 691–693, 2003.

Shelley, E. G. et al., Charge exchange of solar wind ions in the coma of comet P/Halley, *Astron. Astrophys., 187*, 304–306, 1987.

Shimizu, M., The hydrogen clouds of comets, in *Comets in the Post-Halley Era*, edited by R. L. Newburn, Jr., M. Neugebauer, and J. Rahe, vol. 2, 897–905, Kluwer Academic, 1991.

Sittler Jr., E. C. and J. D. Scudder, An Empirical Polytrope Law for Solar Wind Thermal Electrons Between 0.45 and 4.76 AU: Voyager 2 and Mariner 10, *J. Geophys. Res., 85*, (A10), 5131–5137, 1980.

Skorov, Y. V. and H. Rickman, A kinetic model of gas flow in a porous cometary mantle, *Planet. Space Sci., 43*, (12), 1587–1594, 1995.

Skorov, Y. V. and H. Rickman, Simulation of gas flow in a cometary Knudsen layer, *Planet. Space Sci., 46*, (8), 975–996, 1998.

Skorov, Y. V. and H. Rickman, Gas flow and dust acceleration in a cometary Knudsen layer, *Planet. Space Sci., 47*, 935–949, 1999.

Skorov, Y. V., N. I. Kömle, W. J. Markiewicz and H. U. Keller, Mass and energy balance in the near-surface layers of a cometary nucleus, *Icarus*, *140*, 173–188, 1999.

Smith, C. W. et al., ACE observations of the Bastille day 2000 interplanetary disturbances, *Sol. Physics*, *204*, 229–254, 2001.

Smoluchowski, R., Heat content and evolution of cometary nuclei, *Icarus*, *47*, (3), 312–319, 1981.

Smoluchowski, R., Heat transport in porous cometary nuclei, *J. Geophys. Res.*, *87*, (S1), A422–A424, 1982.

Soderblom, L. A. et al., Observations of comet 19P/Borrelly by the miniature integrated camera and spectrometer aboard Deep Space 1, *Science*, *296*, 1087–1091, 2002.

Spohn, T. and J. Benkhoff, Thermal history models for KOSI sublimation experiments, *Icarus*, *87*, 358–371, 1990.

Squyres, S. W., C. P. McKay and R. T. Reynolds, Temperatures within cometary nuclei, *J. Geophys. Res.*, *90*, (B14), 12381–12392, 1985.

Steiner, G. and N. I. Kömle, Thermal budget of multicomponent porous ices, *J. Geophys. Res.*, *96*, (E3), 18897–18902, 1991.

Stern, S. A., J. W. Parker, M. C. Festou, M. F. A'Hearn, P. D. Feldman, G. Schwehm, R. Schulz, J.-L. Bertaux and D. C. Slater, HST mid-ultraviolet spectroscopy of comet 46P/Wirtanen during its approach to perihelion in 1996-1997, *Astron. Astrophys.*, *335*, L30–L36, 1998.

Stix, M., *The Sun*, Springer, Berlin, 1989.

Stone, J. M. and M. L. Norman, Zeus-2D: A radiation magnetohydrodynamics code for astrophysical flows in two space dimensions. I. The hydrodynamic algorithms and tests, *Astrophys. J. Suppl. Ser.*, *80*, 753–790, 1992.

Szegö, K., J.-F. Crifo, A. V. Rodionov and M. Fulle, The near-nuclear coma of comet Halley in march 1986, *Earth, Moon and Planets*, *90*, 435–443, 2002.

Tancredi, G., H. Rickman and J. M. Greenberg, Thermochemistry of cometary nuclei, I. The Jupiter family case, *Astron. Astrophys.*, *286*, 659–682, 1994.

Thompson, W. R., B. G. Murray, B. N. Khare and C. Sagan, Coloration and darkening of methane clathrate and other ices by charged particle irradiation: Applications to the outer solar system, *J. Geophys. Res.*, *92*, (A13), 14933–14947, 1987.

Vaisberg, O. L. et al., Spatial distribution of heavy ions in comet P/Halley's coma, *Astron. Astrophys.*, *187*, 183–190, 1987.

Wallis, M. K., Weakly-shocked flows of the solar wind plasma through atmospheres of comets and planets, *Planet. Space Sci.*, *21*, (10), 1647–1660, 1973.

Wallis, M. K., Hydrodynamics of the H_2O comet, *Mon. Not. R. Astr. Soc.*, *166*, 181–189, 1974.

Wallis, M. K. and M. Dryer, Sun and comets as sources in an external flow, *Astrophys. J.*, *205*, 895–899, 1976.

Wallis, M. K. and R. S. B. Ong, Strongly-cooled ionizing plasma flows with application to Venus, *Planet. Space Sci.*, *23*, 713–721, 1975.

Watari, S., M. Kunitake and T. Watanabe, The Bastille day (14 July 2000) event in historical large sun-earth connection events, *Sol. Physics*, *204*, 423–436, 2001.

Wegmann, R., H. U. Schmidt, W. F. Huebner and D. C. Boice, Cometary MHD and chemistry, *Astron. Astrophys.*, *187*, 339–350, 1987.

Wegmann, R., K. Jockers and T. Bonev, H_2O^+ ions in comets: Models and observations, *Planet. Space Sci.*, *47*, (6/7), 745–763, 1999.

Weissman, P. R., Are cometary nuclei primordial rubble piles?, *Nature*, *320*, 242–244, 1986.

Weissman, P. R. and H. H. Kieffer, Thermal modeling of cometary nuclei, *Icarus*, *47*, (3), 302–311, 1981.

Whipple, F. L., A comet model. I. The acceleration of comet Encke, *Astrophys. J.*, *111*, 375–394, 1950.

White, O. R., *The Solar Output and its Variation*, Colorado Associated University Press, Boulder, 1977.

Xie, X. and M. J. Mumma, Monte Carlo simulation of cometary atmospheres: Application to comet P/Halley at the time of the Giotto spacecraft encounter. I. Isotropic model, *Astrophys. J.*, *464*, 442–456, 1996.

Young, D. T. et al., Solar Wind interactions with comet 19P/Borrelly, submitted to Icarus, 2003.

VIELEN DANK!

Meinen Dank möchte ich aussprechen:

Herrn Prof. Dr. F. M. Neubauer,
für die Möglichkeit diese Arbeit am Institut für Geophysik und Meteorologie der Universität zu Köln durchzuführen, und für Seine hilfreiche und ideenreiche Betreuung. Die zahlreichen wissenschaftlichen Diskussionen waren immer sehr anregend.

Herrn Hochsch.-Doz. Dr. M. Pätzold,
für die Gelegenheit in dem Projekt ROSETTA aktiv mitarbeiten zu können und für die Unterstützung bei der wissenschaftlichen Ausrichtung der Promotion. Die Möglichkeit meine Arbeit auf nationalen und internationalen Tagungen und Team-Meetings vorzustellen und zu diskutieren haben mich sehr motiviert.

Den Kollegen und Freunden, die die Entstehung der Arbeit mit Interesse begleitet und sich die Zeit genommen haben konstruktive Kritik zu üben, insbesondere auch bei der Durchforstung der Arbeit nach Schwachstellen: Heiko Backes, Eike Brandt, Michael Commer, Axel Hagermann, Walter Heibey, Joachim Saur, Sascha Schieke, Nico Schilling und Greg Terrill (thanx for some aussie slang).

Den Administratoren unseres Rechnernetzwerkes unter Leitung von Dr. A. Wennmacher, für den unermüdlichen Einsatz bei der Aufrechterhaltung des reibungslosen Betriebes im Institut.

Allen weiteren Mitgliedern des Instituts für Geophysik, insbesondere allen Eties, für eine stets freundschaftliche und wissenschaftlich anregende Atmosphäre.

Und ganz besonders meiner Frau Barbara, meiner Tochter Nina und allen weiteren Mitgliedern meiner Familie, für den Rückhalt und die Motivation, die nie nachgelassen haben. Und für die ständig verbreitete Lebensfreude und Energie, die mir sehr viel bedeuten.

Erklärung

Ich versichere, dass ich die von mir vorgelegte Dissertation selbständig angefertigt, die benutzten Quellen und Hilfsmittel vollständig angegeben und die Stellen der Arbeit - einschliesslich Tabellen, Karten und Abbildungen -, die anderen Werken im Wortlaut oder dem Sinn nach entnommen sind, in jedem Einzelfall als Entlehnung kenntlich gemacht habe; dass diese Dissertation noch keiner anderen Fakultät oder Universität zur Prüfung vorgelegen hat; dass sie - abgesehen von unten angegebenen Teilpublikationen - noch nicht veröffentlicht worden ist sowie, dass ich eine solche Veröffentlichung vor Abschluss des Promotionsverfahrens nicht vornehmen werde. Die Bestimmungen dieser Promotionsordnung sind mir bekannt. Die von mir vorgelegte Dissertation ist von Prof. Dr. F. M. Neubauer betreut worden.

Teilpublikation:

Pätzold, M., B. Häusler, A. Wennmacher, K. Aksnes, J. D. Anderson, S.W. Asmar, J.-P. Barriot, H. Boehnhardt, W. Eidel, F. M. Neubauer, O. Olsen, J. Schmitt, J. Schwinger and N. Thomas, Gravity field determination of a Comet Nucleus: ROSETTA at P/Wirtanen, *Astronomy&Astrophysics* **375**, 651-660, 2001

Jörg von Oertzen